UNIVERSITÀ
DEGLI STUDI
DI PADOVA

UNIVERSITÀ DEGLI STUDI DI PADOVA

DIPARTIMENTO DI FISICA E ASTRONOMIA

SCUOLA DI DOTTORATO DI RICERCA IN ASTRONOMIA
XXV CICLO

Multi-band Emission of Active Galactic Nuclei: the Relationship of Stellar and Gravitational-Accretion Activity

Director of the School
Ch.mo Prof. Giampaolo Piotto
Università degli studi di Padova
Supervisor
Ch.mo Prof. Alberto Franceschini
Università degli studi di Padova
Co-Supervisor
Dott. Evanthia Hatziminaoglou
European Southern Observatory

Ph.D. Student: Anna Feltre

To Matelda and Giovanni

... "Se tu segui tua stella
Non puoi fallire a glorioso porto, ..."

..."If thou thy star do follow,
Thou canst not fail thee of a glorious port,..."

DANTE, Inferno, Canto XXV, vv. 55-56

Sommario

Una delle questioni ancora aperte nell'ambito dell'analisi dei nuclei galattici attivi riguarda il fatto che l'accrescimento gravitazionale nucleare é spesso accompagnato da una concomitante attività di formazione stellare . Qual é, in questo contesto, il ruolo assunto dalla polvere oscurante che circonda il nucleo e cosa può dirci lo stato dell'arte dei modelli a riguardo? Riescono i dati infrarossi dei satelliti *Spitzer* e *Herschel* a permettere uno studio approfondito di entrambi i fenomeni e, in tal caso, come e con quali limitazioni? La presenza di un nucleo attivo ha effettivamente un impatto sulle proprietà medio e lontano infrarosse delle galassie ospiti? Quali sono gli effetti della simultaneità dell'accrescimento gravitazionale nella regione nucleare e dell'attività di formazione stellare in queste stesse galassie?

In questa Tesi viene esposto il nostro contributo al tentativo di rispondere a queste domande. Vengono presentati i risultati di uno studio comparativo tra diversi approcci usati per modellare i nuclei galattici attivi, focalizzandosi soprattutto sulla questione, attualmente ancora molto dibattuta, relativa alla morfologia della distribuzione della polvere nella struttura toroidale che circonda il centro del nucleo. Viene mostrato in maniera esaustiva che le proprietà della polvere dei nuclei attivi, ottenute dal confronto tra modelli e osservazioni (sia fotometria infrarossa a banda larga che spettro medio infrarosso), dipendono fortemente dalle assunzioni sulla distribuzione della polvere.

Viene fornita, inoltre, una descrizione dettagliata della tecnica di sintesi spettrofotometrica sviluppata allo scopo di ricavare contemporaneamente le proprietà fisiche dei nuclei attivi a delle coesistenti galassie *starburst*. Tale procedura é stata sviluppata per sfruttare al meglio le osservazioni medio e lontano infrarosse dei satelliti *Spitzer* e *Herschel*. In questo contesto, tali dati giocano un ruolo cruciale fornendo vincoli molto più forti sui modelli rispetto alle precedenti strutture osservative. Il codice di sintesi spettrofotometrica è stato usato su un vasto campione di sorgenti extragalattiche rappresentanti la popolazione della *Herschel/Multi-tiered Extragalactic Survey* per le quali erano disponibili sia lo spettro medio infrarosso di *Spitzer* che un pletora di dati multi-banda (SDSS, *Spitzer* e *Herschel*/SPIRE). L'obiettivo di tale lavoro é quello di studiare l'impatto che l'eventuale presenza di un nucleo attivo potrebbe avere sulle proprietà delle galassie ospiti. Infine, vengono presentati i principali risultati ottenuti, con particolare attenzione all'analisi del tasso di formazione stellare in relazione alla presenza di un nucleo attivo e al confronto delle proprietà della polvere calda, riscaldata dal nucleo attivo stesso, e fredda, riscaldata dalla formazione stellare.

Abstract

One of the remaining open issues in the context of the analysis of active galactic nuclei is the evidence that nuclear gravitational accretion is often accompanied by a concurrent starburst activity. What is, in this picture, the role played by the obscuring dust around the nucleus and what does the state of the art models have to say? Can the infrared data provided by *Spitzer* and *Herschel* help us in extensively investigate both phenomena and, if so, how and with what limitations? Does the presence of an active nucleus have an impact in the mid- and far-infrared properties of galaxies? Which are the effects of simultaneous nuclear gravitational accretion and starburst activities in these same galaxies?

This Thesis presents our contribution to the efforts of answering these questions. I report on results coming from a comparative study of various approaches adopted while modelling active galactic nuclei, focusing mostly on the much-debated issue about the morphology of the dust distribution in the toroidal structure surrounding their nuclear centre. We largely illustrate that properties of dust in active galactic nuclei as measured by matching observations (be it broad band infrared photometry or infrared spectra) with models strongly depend on the choice of the dust distribution.

Further, I describe a spectral energy distribution fitting tool appositely developed to derive simultaneously the physical properties of active nuclei and coexisting starbursts. The procedure was developed to make the best use of *Spitzer* and *Herschel* mid- and far-infrared observations. Such data play a crucial role in this context, providing much stronger constraints on the models with respect to the previous observing facilities. The tool has been applied to a large sample of extragalactic sources representing the *Herschel*/Multi-tiered Extragalactic Survey population with mid-infrared spectra from *Spitzer* and with a plethora of multi-wavelength data (SDSS, *Spitzer* and *Herschel*/SPIRE). The goal of such work is to study the impact of a possible presence of an active nucleus on the host galaxy's properties. Finally, I present the main results obtained. In particular, I focus on the analysis of the star formation rate in connection to the presence of an active nucleus and on the comparison of the properties of the hot, heated by the active nucleus, and cold, starburst heated, dust components.

Contents

List of Figures

List of Tables

Introduction

During their lifecycle Active Galactic Nuclei (AGN) undergo transient processes, referred to as "galaxy activity", in which a great amount of energy is produced. In such processes stars are being formed at very high rates in a "starburst phase", and supermassive nuclear black holes residing at the centres of galaxies accrete mass, in an "AGN phase". These two main activity phases of galaxies have been studied separately for decades and until relatively recently, when evidence that the two phenomena are linked and, most frequently, coexistent began to accumulate. Indeed, in the context of the analysis of the spectral energy distributions (SEDs) of AGN, one of the most important recent results is the evidence that the nuclear gravitational accretion happens, more often than not, concomitantly with intense star formation. Quantifying the relative importance of these two emission mechanisms was, till recently, extremely difficult, as they both happen in dusty environments, producing thus a lot of infrared (IR) photons. It is the IR regime where efforts to investigate these two coeval phenomena should be concentrated. The large amount of high quality data available nowadays provides an unprecedented IR coverage of the extragalactic sources. In particular, *Spitzer* provides the mid-infrared (MIR) coverage of the extragalactic sources, where the peak of the hot dust, AGN heated, emission is expected and *Herschel*, with its unprecedented angular resolution, samples the far-infrared (FIR) peak of cold dust emission which is a powerful tracer of star formation.

The hot dust emission is usually attributed to ultraviolet (UV) radiation reprocessed by the dust surrounding the AGN. The AGN unified scheme (Urry & Padovani, 1995) asserts that all active nuclei comprise the same components, such as a central black hole, an accretion disk, a region emitting broad lines, a more external one emitting narrow lines and a dusty structure historically believed to be in a toroidal shape. From this last comes the name "AGN dusty torus". According to this scenario the differences between type 1 and type 2 AGN are due to the orientation of the line of sight with respect to the dusty structure surrounding the central source of the AGN. The first class of objects, observed "face-on", shows broad band emission lines in their optical/UV spectrum, while the second shows only narrow lines because of dust obscuration along the line of sight towards the broad line region. This dusty structure plays a crucial role, not only in the unification scenario, but in a broader context, in understanding the fueling of the

central black hole and the formation and evolution of active galaxies and galaxies in general. The main open question in this context is: "how is the dust distributed around the central source?". Since the discovery of the the first quasar, 50 years ago, scientists are still trying to address this question. But direct investigations of the dust distribution are still seriously hampered by observational limitations and the inner parsecs of an AGN are still out of reach. Moreover, the exact origin and evolution of the black hole, the accretion disk and the material surrounding the AGN are still a matter of debate. Making a step forward in one of these topics is essential because it would also help in advancing the others. A large part of this Thesis focuses on a very detailed modelling study of the configuration of the dust distribution inside the aforementioned toroidal structure. The models that have been developed over the last decades can be mainly divided into two classes on the basis of the dust distribution. The first class is characterized by a "smooth" distribution inside the toroidal structure while the second presents a "clumpy" distribution, with the dust concentrated in clumps or clouds. The comparison between these two classes of models is exactly the topic on which part of my PhD work has focused on. In particular, a thorough comparison between two of the most popular grids of models present in the literature, each one representative of one of the two classes, is being presented in this Thesis. Namely, the models used are a revisited grid of the smooth models of Fritz et al. (2006) and the grid of clumpy models of Nenkova et al. (2008a,b). Both classes of models are quite successful in fitting different parts of the observed AGN broad band SEDs making the discrimination between the two dust configurations even harder. The comparison comprises the analysis of the geometrical and physical similarities and differences resulting from the two approaches of dust distribution and the resulting model SEDs. Furthermore, models are compared with MIR spectra information as well as photometric observations.

The contribution from starburst-heated dust can not be neglected while studying the IR emission of AGN. Indeed, there is mounting evidence that the nuclear gravitational accretion onto super-massive black holes is related and, most frequently, concomitant with episodes of star formation. Indications of this coexistence have been found both from the theoretical and the observational point of view, beginning with the need of AGN feedback to suppress star formation in cosmological simulations and semi-analytical models, and ending with the correlation found between the mass of the black hole and that of the host galaxy. Here another main question arises: "Are these correlations the results of an existing causal relation between the AGN and starburst phenomena?". Another big part of my PhD Thesis is dedicated to this issue. The possible mutual connection is likely to provide important clues for models of AGN and galaxy evolution. It is, in fact, a very hot topic, as a lot of controversy has been generated from very recent results from deep field surveys, which report the quenching of star formation in the presence of a very energetic AGN (e.g. Page et al., 2012). Since both AGN and starburst mechanisms emit strongly in the IR, the main problem is to quan-

tify the relative contribution of the two. *Spitzer* has provided a full coverage of the wavelengths between 3.6 and 160 μm, with the IRAC and MIPS cameras and the IRS spectrograph, in a way never done before. The unprecedented angular resolution and spectral coverage of the *Herschel* Space Observatory allowed us to overcome previous limitations, to study the FIR peak of the cold dust emission, a powerful star formation tracer, and to extend our studies on the concomitant AGN and starburst activities. As more and more data become available for the study of the AGN-starburst connection, the need for a more customised tool is pressing. With this goal in mind, an *ad hoc* multi-wavelength SED fitting technique has been developed in order to reproduce the emission of active galaxies from the optical/UV to the FIR accounting for both the AGN and host galaxies emission. This is a very powerful tool as it allows us to derive various physical properties of each of the components, such as the accretion luminosity, the contribution of the AGN and starburst to the total IR luminosity, the optical depth of the hot dust, the size and the mass of the torus, the stellar masses and the star formation rate (SFR). This procedure has been already applied in various published works (Hatziminaoglou et al., 2010; Vignali et al., 2011; Rodighiero et al., 2011; Pozzi et al., 2012) and extensively tested with all the different options within the *Herschel Multi-tiered Extragalactic Survey (HerMES) SED Modelling* and the *IRS Spectra Working* groups. Moreover, with the aim of investigating the effects of simultaneous AGN and starburst activity on the MIR and FIR properties of the host galaxy, the SED fitting tool has been applied to a very large sample of 250 μm selected sources in the HerMES fields with a plethora of multi-wavelength data from the optical/UV to the FIR. The photometry along with the IRS spectra information, fitted together for the first time, allows an extensive analysis of the various physical properties (and eventually their relations), such as the SFR estimates, the total IR luminosity, the AGN and starburst contributions to the total IR luminosity and, finally, the properties of the host and cold dust emissions.

The outline of this Thesis is organized as follows:

◇ **Chapter 1 - Galaxy Activity** is a review of the physical mechanisms taking place during nuclear accretion and starburst activities.

◇ **Chapter 2 - Extragalactic Surveys in the Infrared** is an overview of the most important IR surveys up to date, focusing on the main results achieved in the field of active galaxies and AGN-starburst connection. A deeper look at the HerMES data products and their multi-wavelength coverage is also presented.

◇ **Chapter 3 - Modelling Multi-Wavelength Data** describes the various components of emission contributing to the SED of galaxies over all the electromagnetic spectra. This Chapter also summarizes some of the main models and tools developed to study the information coming from such multi-band data, which carry a lot of information on the underlying physics.

◇ **Chapter 4 - An *ad hoc* SED fitting tool** illustrates in detail the full operation of the SED fitting code used in this Thesis and the new options introduced during my PhD. This includes examples of the main applications of the aforementioned SED fitting procedure and its comparison with others commonly used in the literature.

◇ **Chapter 5 - Dust Distribution in AGN** reports on the very detailed comparative study performed between smooth and clumpy torus models, both from the pure modelling point of view and from the side of comparison with both photometric and spectroscopic observations. This Chapter presents an extended version of Feltre et al. (2012).

◇ **Chapter 6 - AGN and Star Formation in 250 μm Selected HerMES Sources with IRS Spectra** presents the work carried out within the context of the HerMES consortium, in which the SED fitting procedure, presented in Chap. 3, is applied to a large sample of 250 μm selected source with IRS spectra. This Chapter is an extended version of Feltre et al. (2013).

◇ **Conclusions** summarizes results and discussions of this Thesis, along with the new perspectives for the future.

1 | Galaxy Activity

During their evolution galaxies undergo some extreme phases in which transient processes take place producing great amounts of energy, phenomena that are usual referred to as "galaxy activity". These concern both processes of gas accretion in the nucleus (AGN phase), due to the intense gravitational field produced by a central black hole, and stellar activity (starburst phase) due to starburst phenomena in which stellar populations are formed. The interplay between these phenomena and the surrounding environments plays a crucial role in understanding the above processes and the galaxy evolution.

The review in this Chapter is aimed at providing a complete overview of AGN and the physical mechanisms that come into play. An historical review of the AGN phenomenon will be followed by the descriptions of AGN properties over all the electromagnetic spectrum and their classification, along with an illustration of the models unifying all their variety. Further, a description of starburst galaxies and the properties of their SED is provided. To conclude, a long section is dedicated to the putative AGN-starburst connection, where evidence supporting this link and the methodologies to study it are extensively presented.

1.1 Active Galactic Nuclei

We discuss in this Section *bona-fide* Active Galactic Nuclei, that is objects in which the phenomena occurring in the nuclear regions can be safely ascribed to the presence of a nuclear supermassive black hole. Later, in Section 1.2 we will discuss the category of Active Galaxies dominated by star-formation.

The term Active Galactic Nuclei (AGN) refers to objects characterized by a strong emission over all the electromagnetic spectrum, from the radio to the gamma regime. Their luminosity can not be attributed to the normal components of galaxies such as stars, dust and gas. Moreover, variability measurements of these sources tightly constrain the size of the region from which the radiation comes to be quite compact. As a consequence of this, different hypothesis proposed along the years to explain the energetic emission of such extragalactic sources has been excluded, such as the presence of a superdense stellar cluster or the explosion of a large number of supernovae. The most probable explanation considers the presence of a supermassive black hole, residing in the central region of the galaxies,

responsible for the observed large energy release.

AGN are among the most powerful energy sources of the Universe and with their high luminosity, hundreds or thousands times higher than the ones characterizing normal galaxies, AGN have been for decades the only objects detectable at the larger distances. AGN have been for a long while the most luminous and most distant objects known in the Universe, and for this reason they have been used to study the intergalactic medium existing between them and the observer. They constitute, nowadays, a very important laboratory to understand and investigate the physical processes concerning the formation and evolution of galaxies and the Universe itself.

Black holes, ultra-relativistic particles and magnetic fields, complex hydrodynamic processes and radiative transfer modelling come into play when attempting to develop theories of AGN.

The intent of this Section is to give a complete and clear description of the properties of these objects in order to provide a general view before to undergo on a detailed analysis of their IR emission.

1.1.1 A Brief Historical Overview of Active Galactic Nuclei

Despite the fact that emission lines from galactic nuclei had already been found at the beginning of XX century, half of a century had to pass before the AGN became the cornstore of various studies. These sources have been the target of many research groups since 50 years. Let us briefly review the main steps through which the current knowledge on AGN has accumulated.

- At the beginning of the XX century, Fath (1909) carried out a series of observations at the Lick Observatory where one spectrum, over all those taken for the various objects, was peculiar: NGC1068 showed a composite spectrum with both absorption and emission lines. At later stage, the presence of these was confirmed by Slipher (1917) with the spectra taken at the Lowell Observatory in 1913.

- The systematic study of nuclear emission lines of galaxies starts in 1943 with a student at the Monte Wilson Observatory, Carl Seyfert, who discovered the high excitation emission lines coming from the centre of some spiral galaxies. However his work was not enough to promote the study of AGN as one of the biggest research fields. Indeed, for this it was necessary to wait for the progress of radioastronomy.

- From the end of the Second World War, radio sources have been detected by various groups of physicists. In the early 1950s there were further improvements on radio observations, positions determinations, optical identifications and radio sources measurements. In the late 1950s the first double radio-lobed sources were discovered, allowing the community to reach the conclusion that galaxies were capable of extremely energetic phenomena.

- During the 1950s and 1960s elliptical galaxies with luminous, variable and radio-emitting nuclei have been detected. The studies of Minkowski on radio-galaxies culminated with the identification of 3C295 as a member of a galaxy cluster with an unprecedented redshift, z, of 0.46 (Minkowski, 1960). By 1959 three catalogues of radio sources were published by the Cambridge group of radio astronomers (Edge et al., 1959). Unluckily, the resolution was not enough to determine the position of 3C273 with the accuracy needed to identify the optical counterpart. The necessary method to achieve this goal was that of lunar occultation (Hazard et al., 1963).

- Allan Sandage in 1960, at the Palomar and Monte Wilson Observatory, obtained an image of 3C48 showing a stellar aspect within a weak nebulousity. Its spectrum showed intense emission lines at unusual wavelengths and an excess of UV emission respect to the normal stars, while the photometry revealed the presence of variability.

- With the purpose of identifying stellar-like optical counterparts of strong radio sources, Schmidt (1963) and Greenstein (1963) carried out spectroscopic observations of 3C273 and 3C48, respectively, and estimated their redshfit (0.16 and 0.37, respectively).

- Shortly later, others quasars up to redshift 2.2 were discovered and found to be variable in intensity on short timescales (weeks/months), implying very small (light months $\sim$ a few 10^3 Schwarzschild radii) emitting volumes.

Despite the fact that the pieces of the puzzle were all there, it took quite some time to put everything together and to relate Seyfert galaxies and quasars as essentially the same type of objects. Moreover, the idea of a galaxy hosting a quasar was yet quite vague and there was no explanation for the origin of that amount of energy.

With years, the study of AGN acquired more and more importance. In particular, their high redshift made quasars powerful tool to analyse cosmological questions and investigate the high-redshift universe. Indeed, Hoyle (1966), Bondi, Sciama and collaborators abandoned the steady-state cosmological model, most "in vogue" at that time, after the statistical analyses of extragalactic radio-sources. Further, the study of the chemical abundances in high-redshift quasars enabled to know the chemical composition in the younger Universe. The analysis of the absorption lines (called "Lyman forest"), especially for distant quasars, at shorter wavelengths than that of the Lyα line, was of particular interest for cosmology. Indeed, these lines, generated by the absorption due to the presence of hydrogen clouds along the line of sight between the source and the observer (Gunn & Peterson, 1965), provided us information about the nature of the absorbing clouds and the intergalactic medium.

With the progress of the studies, various AGN properties have been discovered. Most of the astronomers accepted the cosmological redshift of quasars and the

parallelism between Seyfert galaxies and quasars. The nature of the power source, the structure of the regions emitting the continuum and emission lines and the reasons originating the AGN phenomena in some galaxies rather than in other, were, and mostly are, still open questions.

1.1.2 AGN and their Properties

It is useful to group the variety of AGN into classes of objects with their own peculiarities, as a first step towards a better understanding.

High Bolometric Luminosity

AGN are characterized by high luminosity spanning from 10^{42} erg/s for the weaker classes up to 10^{48} erg/s for the most powerful ones, or even more. Various factors need to be taken into account in this context. First, there are some active nuclei which are still unknown because weaker than the host galaxy. Second, many AGN are believed to be obscured by the surrounding dusty structure making difficult the estimates of the exact luminosity value. The observed SED is due to "primary" emission associated with particles that receive their energy from the central source, such as the synchrotron emission of relativistic particles and the thermal emission of the accretion disc surrounding the central black holes. AGN SEDs are also characterized by a "secondary" emission due to the presence of dust and gas which re-radiate the primary one.

Very Small Angular Size

The very small angular size of a typical quasar make the objects to appear, in optical images, as a spot more luminous than what predicted by the luminosity profile of the host galaxy. In some cases the difference in luminosity between the nucleus and the host galaxy is so high that the emission of the first, seen like a point source, overwhelms that of its host galaxy, with this last being below the flux limit.

Wide Multi-band Emission

The SEDs of most AGN reveal a continuum emission over more than 16 decades in frequency, from the radio to the Gamma and sometimes the TeV domain. This differs from that of a typical galaxy which is mostly due to black body-like emission of stars emitting in a range that is not wider than one order of magnitude in frequency (Padmanabhan, 2002). Different emission mechanisms, both thermal and non-thermal, coming from different regions of the active nucleus, come into play in different wavelength domains.

- The **Radio** emission of AGN, as already explained in Section 1.1.1 allowed their discover and the resulting recognition of them as a unique class of astronomical objects. Only 10% of AGN, referred to as "radio-loud" AGN, present a

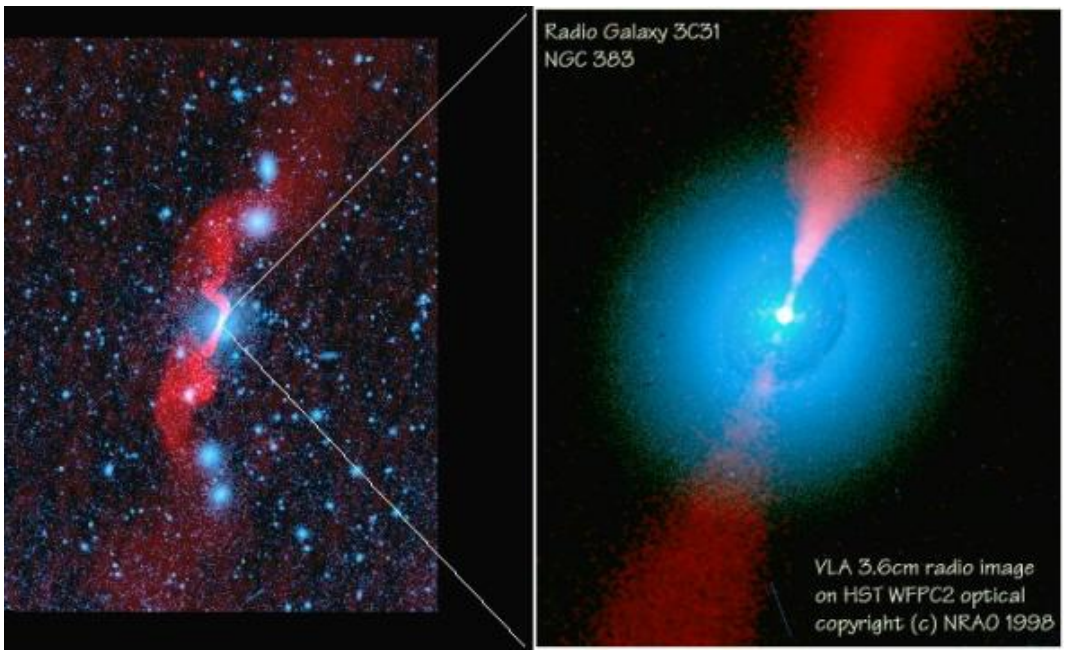

Figure 1.1: Optical and radio morphology of the powerful radio source 3C31 (NGC 383). Red colors depict the radio emission measured with the VLA, and blue colors depict the optical emission from starlight. The right-panel shows the center of the galaxy with its conical radio jets. These last develop into wiggling jets and irregularly shaped plumes, which stretch to a distance of 300 kpc from the center of the galaxy, as can be seen the large-scale morphology and the surrounding optical field (optical image from the Digitized Sky Survey) in the left-panel. The optical image is an HST WFPC2 image, and shows prominent dust features in the host galaxy. Image from Alan Bridle & Robert Laing. HST image from Martel et al. (1999). Copyright by NRAO 1998.

strong radio emission showing double radio lobes extended up to kpc scale with a galaxy in the centre. The rest of the active nuclei, called "radio-quiet" AGN, show a decreasing SED starting from submillimetric wavelengths, referred to as "submillimetric break". The radio morphology of quasars if often described in terms of a "compact" and an "extended" component (see Fig. 1.1) both due to synchrotron emission of rapidly accelerated charged particles (Beckmann & Shrader, 2012). For an homogenous source with a constant magnetic field, such synchrotron mechanism generates a spectra that can be described with a power law:

$$F_\nu \propto \nu^{-\alpha}, \tag{1.1}$$

where F_ν is the flux expressed in ergs s^{-1} cm^{-2} Hz^{-1}. This emission can be

related to an initial power law distribution of electron energies E of the form

$$N(E)dE = N_0 E^{-s} dE, \tag{1.2}$$

where $\alpha = (s-1)/2$. For an extended component, the typical observed power law index is roughly 0.7 for higher frequency where the synchrotron self-absorption is not important, while at lower frequency the gas is optically thick and the spectra have been found to be $F_\nu \propto \nu^{5/2}$ (Peterson, 1997). The compact component shows, in general, a flatter spectrum ($\alpha \leq 0.5$) due to the fact that different parts of the compact region become thick at different frequencies. In addition to these two componets, radio AGN show also jets which, originated from the central compact source, lead out to extended lobes (see Fig. 1.1).

- The **Infrared** spectra of AGN shows a rise of emission at wavelengths greater than 1 μm, where most of the AGN SEDs present a local minimum. IR radiation spans the range of 1-300 μm and can be either thermal and/or no-thermal according to the AGN type. In fact, in radio-loud AGN the same synchrotron emission process producing the radio continuum is the predominant source of IR radiation. The spectra of Seyfert galaxies and low luminosity AGN show the presence of multiple thermal components: a thermal radiation from dust in a compact region surrounding the nucleus, dust in star-forming regions and additional contribution coming from emission lines of molecular, atomic and ionic species. Moreover, the presence of silicate dust grains in the dusty structure surrounding the centre and of PAH molecules in star-forming regions can give rise to absorption or emission features in the AGN MIR spectrum.

- In the **Optical** band we find the most common distinguishing signatures. It is still the best domain for the AGN identification and for the measurement of redshift and distance. For objects allowing a direct view of the central source, the nuclear continuum shows a power law dependence increasing with photon energy. This excess of emission extends well into the UV band and goes under the name of "big blue bump". And additional but less accentuated feature, due to blended iron (Fe) emission lines and Balmer continuum, corresponds to the "small blue bump". Then, AGN appear bluer with respect to "inactive" galaxies. Moreover, the optical spectra of AGN are populated by various emission lines. The broad emission lines are originated by material close to the central black hole and mostly consist in Lyα and Balmer series lines and high-ionization transitions from helium, carbon and magnesium. The narrow lines come from colder material, lie at much larger distance from the centre and present almost no variability.

- The **UV** and optical part of the electromagnetic spectrum are characterized by the aforementioned "big blue bump" and its maximum in the SED is com-

monly believed to be associated with thermal emission from the accretion disc (Shields, 1978). AGN can present rich atomic emission and absorption lines spectra with UV spectroscopy having provided the highest precision dynamical measurements in the inner region. UV lines and continuum can be used to investigate the emission due to hot plasma with a temperature of 10^4-10^5 K (Beckmann & Shrader, 2012). The UV imaging have also facilitated studies of recent star formation histories of early-type galaxies in the local Universe and the investigation of their possible evolutionary connection with AGN activity.

- The **X-ray** emission spans between about $\sim$ 100 eV and 100 keV. In the region of lower energy there is an excess of X-ray emission called "soft X-ray excess". This is usually interpreted as the emission due to accretion processes around the black hole in the centre of the host galaxy. The soft X-ray spectra can be affected by the presence of absorbing material in the vicinity of the central engine. The observed short term variation ($\sim$ 1 day) indicates small emission region of X-rays. The low energy photons of the thermal spectrum produced by the accretion disc are scattered to higher energy by relativistic electrons through inverse Compton processes (Haardt & Maraschi, 1993). Spectra are characterized by broad emission lines of Fe at low-ionization stage due to the absorption of cold ($T < 10^6$ K) optically thick material (George & Fabian, 1991). Low energy absorption and Comptonization processes are responsible for the broad "hump" in the hard X-ray spectra with a maximum around 20-30 keV (Beckmann & Shrader, 2012).

- γ**-ray** radiation characterizes the spectra of a particular class of AGN, called BLAZARs. At MeV energies the Compton scattering becomes the predominant photon-matter interaction. At higher energies the dominant process is the pair-production which is most efficient above 100 MeV. At these energies neither Seyfert galaxies nor radio quite AGN are expected to be detected. Instead, the emission regions of BLAZARs' jets have much higher energy particles than the thermal electrons close to the accretion disc, and fluxes are further amplified by relativistic bulk motions towards the observer.

Emission Lines

AGN spectra are characterized by very intense emission lines allowing a straightforward distinction with the spectra of most of the stars and normal galaxies. It is almost always possible to observe the Lyα lines, Balmer series, the pair of CIV 1549, [OIII] 5007, and the Kα Fe line in the X-rays around 6.4 keV (Padmanabhan, 2002). It has been noticed an important distinction based on the line widths: most of the object lines present wide wings corresponding to thousands of km/s, while other objects show lines narrower than hundreds of km/s. The lines can be both permitted or forbidden, with these latter usually having a narrow profile.

High Variability

Differently from normal galaxies, AGN are highly variable, with the optical luminosity varying roughly 10% on a year timescale (Krolik, 1999). Evidence suggests an increase of the variability amplitude at decreasing wavelengths. The variability in some AGN can be strictly connected with a high polarization, a compact radio structure and a powerful high energy γ-ray emission.

The variability of the SED is a basic tool to understand emission processes and the origins of their variations. Different mechanisms can give rise to different variation in different bands of the electromagnetic spectra. This is also the reason why, for a more detailed description of all the mechanisms playing part in the life of an AGN, is necessary to resort to multi-wavelengths study (Zitelli et al., 2004).

1.1.3 Taxonomy of Bona-fide Active Galactic Nuclei

AGN have been classified in a variety of ways on the basis of their spectra and of their properties shown at the different wave-bands. As usual, on the basis of the properties considered it is also possible to associate the same object to different classes. As a matter of fact, the AGN classification presented below is not being considered univocal.

Radio Galaxies

Radio-galaxies are usually identified with giant elliptical galaxies and associated with the presence of radio-emitting jets and lobes extending from tens of kpc to more than 1 Mpc from the central region. As already mentioned, the radio emission is due to synchrotron emission associated with the relativistic motion of electrons immerse in very strong magnetic fields.

On the basis of the properties of the AGN radio SED we can find different classifications. The simplest one is based on the luminosity at 1.4 GHz, $L_{1.4}$:

- Weak Radio Galaxies (WRGs) with $L_{1.4} \lesssim 10^{25}$ W/Hz and associated with elliptical galaxies characterized by being luminous in the optical with strong emission lines in their spectra.

- Powerful Radio Galaxies (PRGs) with $L_{1.4} \gtrsim 10^{25}$ and associated with less luminous elliptical galaxies in the optical domain. Emission lines in these objects are weak or absent.

Another one is based on the spectral index α, defined as $F_\nu \propto \nu^\alpha$, around 1 GHz:

- Steep spectrum sources are characterized by a radio-band spectrum described by a power law with a spectral index $\alpha \gtrsim 0.4$. They are, in general, more extended and optically thin.

- Flat spectrum sources with $\alpha \lesssim 0.4$ are compact, variable and in part optically thick to the synchrotron radiation.

A further criterion is based on the ratio, q, between the lobes separation and the total size of the source at 178 MHz:

- $q \lesssim 0.5$ radio galaxies are called Faranoff-Riley I, FRI, or edge-darkened sources. They present double lobes radio with relatively smooth surface brightness distribution.

- $q \gtrsim 0.5$ radio galaxies are called Faranoff-Riley II, FRII, or edge-brightned sources. The extreme of the lobes have some emission region characterized by high surface brightness.

Quasars

Quasars have been discovered around 1950s with the first radio surveys, when the angular resolution of radio imaging became good enough to allow astronomers reliable identifications with optical counterparts. The name itself of Quasar comes from Quasi-Stellar Radio-Source, whose terminology has remain to indicate all classes of such objects. It has been understood soon that Quasars were not stars and assuming their redshift was due to universal expansion, then they should be very far away and extremely luminous. As of today, no doubts about a quasar being the active nucleus of a very distant galaxy. The classical partition is:

- Radio-loud quasars, characterized by a strong radio emission and an unresolved luminous nucleus ($M_V < -23$). Their optical spectra show very broad emission lines.

- Radio-quiet quasars, constituting 90% of the total and being very similar to the radio-loud in the optical. Instead, in the radio band the emission from these objects is observed to be much weaker but this last does not mean they present a lack of radio emission. While the radio emission in radio-loud sources is associated with relativistic jets, the origin of radio emission in radio-quiet objects has not been clearly established yet. A likely explanation of this last have been found to be synchrotron emission of electrons accelerated in shocks (Ishibashi & Courvoisier, 2011).

This dichotomy is based on the radio loudness parameter, $R = F_r/F_o$, defined as the ratio of monochromatic luminosities at 5 GHz and optical B band at 4400 Å. The classical threshold value used to distinct the two populations is formally set at $R \sim 10$ (Kellermann et al., 1994).

Seyfert Galaxies

Seyfert galaxies are objects of relatively low luminosity, taking their name from the scientist who discovered them in 1943. They appear as a quasar-like nucleus, but with the host galaxy clearly detectable (Peterson, 1997). Their optical spectra show strong emission lines due to the hydrogen recombination and forbidden transitions of elements at a different ionization level (typically: oxygen, iron, nitrogen and sulphur).

They are divided in:

- Type 1 Seyfert (Sy1) galaxies which are characterized by both broad permitted and narrow forbidden emission lines with an optical spectrum close to that of quasars. This class includes most of the spiral galaxies which, indeed, look like radio-quiet quasars with a lower intrinsic nuclear luminosity.

- Type 2 Seyfert (Sy2) are analogous of Sy1, with the difference that their spectra present only narrow emission lines.

The narrow lines, with widths of several hundreds of km/s, are typical of emission from ionized gas at low density ($n_e \simeq 10^3 - 10^6$ cm^{-3}). The broad lines in Sy1 have widths up to 10^4 km/s, but they are seen in the permitted lines only. The lack of forbidden-broad lines in Sy2 suggests that these are originated in high density region ($n_e \simeq 10^9$ cm^{-3}) where the non-electric-dipole transitions are collisionally suppressed Peterson (1997).

Osterbrock (1981) introduced the notation Seyfert 1.5, 1.8, 1.9, where the classification in intermediate sub-classes from 1 to 2 is based lonely on the optical spectra. Those with an higher number present weaker broad lines than narrow lines. High excitation lines have been discovered, thanks to X-ray observations, in Seyfert galaxies with relatively low luminosity. These objects, which actually are Seyfert galaxies with a strongly reddened optical spectrum and extinguished by the dust inside the galaxy, are called Narrow-line X-ray galaxies.

Blazars

AGN of this class are characterized by a high level of polarization of the continuum and very rapid variability, usually with a daily time scale. In this class the following are included:

- BL Lacertae objects which are very luminous sources similar to the radio-loud quasar, but presenting a lack of emission and absorption lines in their spectra. They are highly variable in optical, radio and X-ray bands with a time scale lower than a day. Their optical radiation can be highly polarized with a polarization degree between 5% and 40%. The host galaxy is usually a giant elliptical.

- Optically Violent Variables - OVV are highly variable objects with properties close to that of the BL Lacearte objects, but with spectra showing broad emission lines, although weaker than those of quasars.

LINERS

LINERS, or Low Ionization Nuclear Emission-line Region, are a class of galaxies with a nuclear region of low luminosity. Their spectra show, apart from the Balmer series emission lines, strong emission lines originated by low ionization elements, such as oxygen and sulphur. They also present a very intense [OIII] $\lambda(4363)$ line, indicative of an electronic temperature of $\simeq$ 40000 K. The amplitude of the emission lines correspond to a velocity of only 200-400 km/s. LINERs are close to Seyfert, but the narrow lines present a lower level of ionization. They represent the low luminosity tail of AGN population and are, at the same time, the most common active nuclei. Diagnostic diagrams, proposed by Veilleux & Osterbrock (1987), comparing the intensity ratio between lines conveniently chosen and belonging to different elements but with close by wavelength, are used to distinguish Seyfert galaxy from LINERs. For example, a distinction is made between objects with the ratio of [OIII(λ5007)/Hβ(λ4861)]. When this ratio is higher than 3 we are dealing with classical Sy2, while objects with a lower value of this ratio are classified as LINERs.

1.1.4 The Unified Model of AGN and new Issues

After the establishment of AGN as a new class of objects and the discovery of the various AGN sub-classes, a question emerged, i.e. whether it was possible to explain the AGN zoo with a unified theory. To start with, on the basis of the UV and optical spectra, the AGN are divided in:

- Type 1 AGN characterized by a luminous continuum and spectra with both narrow and broad emission lines.

- Type 2 AGN charaterized by a weaker continuum and spectra only with narrow lines.

Rowan-Robinson (1977) found an excess of dust emission in the IR continuum of Sy2 with respect to Sy1. From this discovery he concluded that the central region should be surrounded by dust which attenuates the broad wings of the spectra giving rise to the distinction between type 1 and 2. Rowan-Robinson (1977) also argued about the possibility that this difference could be due to an orientation effect. The main issue to understand was the reason for the lack of broad lines in the spectra of Sy2. A step forward was made by Antonucci & Miller (1985) while studying NGC1068, the prototype of Sy2 galaxies. The discovery of polarized broad lines in its spectra let to pose the basis for a unified model explaining with a common physical mechanism the two class of objects (Antonucci, 1984; Antonucci

& Miller, 1985; Antonucci, 1993). Indeed, the light reflected by the dust (and for this reason polarized) can be indirectly observed, as a consequence of reflection, in type 2 objects for which the direct view of the central source is prevented by the presence of dust along the line-of-sight. The key for this scenario concerns the dust geometry. The ideal dusty shape able to explain the observed differences between type 1 and 2 was a toroidal structure. This dusty "doughnut" would be such as that type 1 objects would be observed face-on, with a direct view of the central source. In this case the central region, where the broad lines are believed to come from, is not obscured and both narrow and broad lines are visible. When the object is observed "edge-on", the line of sight intersects the toroidal dusty structure which prevents the view of the region where the broad lines originate and, consequently, no broad lines are observed in the spectra of type 2 objects. This unification scenario is graphically represented in Fig. 1.2, showing that all the various AGN are supposed to be intrinsically the same objects (Urry & Padovani, 1995), with the differences between the various subclasses due to the orientation with respect to the observer.

1.1.5 Main AGN Structural Components

The components of an AGN can be summarized as follows.

- A **Super Massive Black Hole** (SMBH) with masses between 10^6 and a few 10^9 $M_\odot$. It is believed to be the central engine, with its gravitational potential energy being the source of the AGN luminosity. Measurements of black hole masses involve the most sensitive instruments, operating in optical and NIR, as well as different techniques. Among these we find: maser measurements (Miyoshi et al., 1995), rotational curves of circumnulcear medium using the high resolution of satellites (*Hubble Space Telescope*, HST, Marconi et al., 2006) and ground based adaptive optic systems (Very Large Telescope, VLT, Häring-Neumayer et al., 2006).

- An **accretion disc** producing the AGN primary emission and the corona of ionized hot gas surrounding the SMBH. The matter lying in this region is subject to a loss of angular momentum through viscous and turbulent processes. The high luminosity characterizing the AGN could not be attributed to stellar emission only, therefore an efficient mechanism of energy production has to be sought. Currently, the most accepted scenario foresees the power source being the same within all AGN and consisting of gravitational potential energy of the surrounding material accreting on the SMBH. A famous model of accretion disc is that assuming a geometrically thin and a optically thick disc (Shakura & Sunyaev, 1973), with the efficiency of energy production during the accretion processes able to reach the maximum allowed from the gravitational potential in general relativity: 5.7% for no-rotating black holes (or Schwartzschild's black holes) and 45% for the rotating ones (or

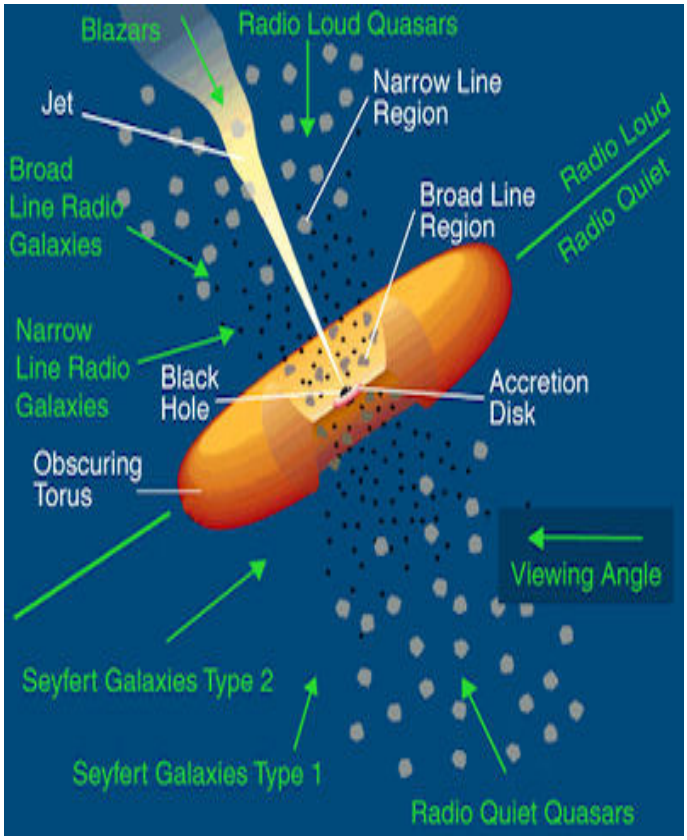

Figure 1.2: Illustration of the AGN Unified Model by Urry & Padovani (1995). In this scenario AGN are constituted of the same components with the difference of the various sub-classes associated with an orientation effect.

kerr's black holes) (Shapiro, 1993). The disc, heated by magnetic and/or viscous processes, emits mostly at optical and UV wavelengths, with a steep cut at the higher energies. It is surrounded by a hot gas corona explaining the observed emission at hard X-ray wavelengths (Haardt & Maraschi, 1993).

- High velocity gas in the so-called **broad-line region** (BLR) arranged in several clouds (10^7-10^8) (Arav et al., 1998; Dietrich, 1999). The region extends up to 0.1-1 pc from the centre and is characterized by density ($n_e \simeq 10^9 - 10^{10}$ cm^{-3}) high enough to generate the broad (permitted) lines observed in type 1 AGN. The broad lines emitted in this region are due to recombination or deexcitation of photoionized atoms, while the effects of the thermal processes are negligible. The broad emission-line clouds (BELC) could have a spherical geometry, following the standard model, or rather asymmetric, as suggested from Maiolino et al. (2001).

- Low velocity gas in the **narrow-line region** (NLR) constitued by clouds of ion-

ized gas, extended in a region of some hundreds of pc or more and characterized by lower densities ($n_e \simeq 10^4 - 10^5$ cm^{-3}) with respect to those of the BLR, is able to generate forbidden lines. The widths of the lines are $\lesssim 1000$ Km/s (Antonucci, 1993). The spatial distribution of the narrow emitting line clouds (NELC) is another important property. Indeed, the NLR corresponds to the widest spatial scale in which the ionizing radiation, coming from the central source, is able to excite the surrounding medium. Moreover, this is the only AGN component to be partially resolved in the optical band and, in some cases, it is also possible to map the physical and kinematic distributions. In general, it has been found the morphology of the NLR being axi-symmetric rather then spherically symmetric, and making a kind of two opposite ionizing cones centered into the nuclear source.

- An **obscuring torus** of dust and gas which, for certain lines of sights, can prevent the observer's view of the BLR. Antonucci & Miller (1985) have been the first to verify the existence of this dusty structure by observing the broad lines of the polarized spectra of NGC1068, the prototype of Sy2 galaxies. The detection of broad polarized lines made possible to infer the presence of the BLR also in type 2 AGN. In fact, since type 2 objects are obscured by the intervening medium material, broad lines are visible only in polarized light. The presence of a torus is supported also by optical, UV and X-ray data, since the optical/UV continuum is much weaker in Sy2 than in Sy1 (for the same luminosity of the central source) and the X-ray spectra show a cut due to photo-electric absorption. The torus is not only responsible for the obscuration of the type 2 sources but also of the IR continuum produced by the warm dust emission which reprocess the photons coming from the primary source. Geometry and composition of the dusty structure in question are currently still not well known. The dusty structure can not have spherical symmetry in order to allow a direct view of the central source for type 1 objects and it has to be constituted of gas, to produce X-ray absorption, and dust, to explain the extinction of the optical/UV continuum and the IR emission. Finally, it needs to be outside the BLR to allow the broad-line polarized emission in type 2 sources. The main current issues concern how the dust is distributed inside this dusty structure (smooth or clumpy distribution), the grain sizes distribution, the chemical composition and its distance from the centre.

- **Relativistic jets** are supposed to form within 100 Schwarzschild's radius from the black hole and extend up to tens of kpc, and, in some cases, up to Mpc. Jets are present in all radio-loud AGN even if with different energetics. The weaker ones decelerate closer to the central engine, often still inside the host galaxy, while the most powerful jets propagate into the interstellar and intergalactic medium before to originate large scale radio lobes. Currently, as already pointed out in Section 1.1.3, AGN are divided in radio-quiet and

radio-loud essentially depending on the power of the radio jets.

The physical origin of the radio jets and the reason why they are so powerful in some AGN and absent in others is one of the fundamental problems of high-energy extragalactic astrophysics. The most obvious interpretation is that associating the extraordinary collimation of jets to the direction defined by a fast rotating nuclear SMBH on which gas is accreting. The differentiation of radio-loud and radio-quiet AGN would then be related to the angular momentum and rotational power of the SMBH and the prominence or weakness of the accretion disc. Then radio galaxies might be conceived as late stages in the "activation" process, when the SMBH has already acquired large amounts of rotational energy from the accretion disc during a preceding radio-quiet phase, and is dissipating this energy in the form of radio emitting jets made of particles and electromagnetic radiation.

With the exclusion of relativistic jets, AGN unification requires the presence of all the other aforementioned components, even though some differences from case to case are possible on the basis of the mass of the black hole, the ionization parameters and the luminosity. According to the unified model, most of the main observable AGN properties, e.g. the global SED and the broad and narrow emission lines, are due to an orientation effect rather than intrinsic differences of the sources (Urry & Padovani, 1995).

The phenomena of obscuration of local AGN due to the presence of dust has been very well studied, starting with the spectropolarimetric observations of Antonucci (1984). These last suggested the obscuration to concern a significant solid angle within which the view of the BLR and even of the accretion disc is prevented. There is still some controversy about this simple scenario, in particular concerning the luminosity dependence of the phenomenon and how the starburst activity is associated with type 2 objects. At higher redshifts the situation is even less clear: low luminosity type 2 objects have been found at z$\sim$2-3 (see e.g. Stern et al., 2002; Norman et al., 2002), but certainly not as much as type 1 quasars found by optical/UV surveys at such redshift.

It is worth noting that there are two different schemes of unification, one for the optically selected AGN and the other for the radio selected ones. In the first unification scheme the dependence by the viewing angle is due to the optical depth and by the obscuring structure of dust and gas. In the second one the dependence on orientation is related to the direction of the radio jets and depend on the Doppler factor from relativistic plasma clouds (Urry, 2004). The optical scheme explains the presence or absence of broad emission lines as due to the orientation with respect to the obscuring torus. If we consider an unification scenario with a fixed geometry for the torus, all the properties of the respective classes and orientation-independent should statistically hold for the whole population, and consequently, all the differences should be caused by dust absorption. The radio scheme explains the difference between flat-spectrum (core-dominated) radio-loud AGN and the steep-spectrum (lobe-dominated) as due to the orientation between relativistic jets and the axis of symmetry. Some radiogalaxies show outflowing

jets only in one side (one-sided), some others on both (two-sided). The reason of this is believed to be the Doppler effect of the material in relativistic motion which amplify the closer jet and weaker the other. This relativistic effect introduces a strong anisotropy and, consequently, the aspect of the source with one jet would strongly depend on the angle between the axis of the jet and the line of sight.

1.2 Starburst Galaxies

After the previous brief introduction to the phenomenon of *bona-fide* AGN, we discuss in the present one active galaxies dominated by stellar activity, and with typically an enhanced rate of formation of stars.

The study of global star formation properties, such as the star formation rate, gas content, mass, bar structure and dynamical environment, allow to identify and classify systematically galaxies along the Hubble sequence[1] (see Fig. 1.3) and better understand their formation and evolution. The identification of starburst sources dates back to late 1970s (Rieke & Lebofsky, 1979; Weedman et al., 1981). The interest in these sources has been stimulated by the discovery by the Infrared Astronomical Satellite (IRAS) in mid-1980s of a large population of ultra luminous IR starburst galaxies. Moreover, the interest increased after the detection of star-forming galaxies at high redshift. This made possible to extend the star formation studies on starburst diagnostics also for distant galaxies and to be able to study the evolution of the Hubble sequence with cosmological time.

There is not a a rigorous and unique definition of a starburst galaxy (Kennicutt & Evans, 2012). However, all the definitions of starburst galaxies have some common parameters:

- the star formation rate (SFR) which is the rate at which the galaxy convert gas into stars, usually expressed in $M_{\odot}/yr$;
- the quantity of gas available to form stars;
- a comparison between the time scale in which all the gas is consumed by star formation processes and the age of the galaxy.

Indeed, we usually refer to starburst galaxies as those systems forming stars at such high rates that can not be sustained over the entire lifetime of a galaxy (Harwit & Pacini, 1975; Weedman et al., 1981). If we consider the Milky Way, a common spiral galaxy, its SFR is of few solar masses per year with a life cycle of gas-stellar mass conversion of about one billion years of duration. Starburst galaxies show SFR one, two or even three orders of magnitude greater with respect to

[1]The Hubble is sequence is a morphological classification scheme for galaxies introduced by Edwin Hubble in 1926. The shape if that of a tuning fork diagram. Galaxies are divided into classes on the basics of their appearance, namely ellipticals, lenticulars and spirals and a fourth one of galaxies with irregular appearance, refer to as peculiar galaxies.

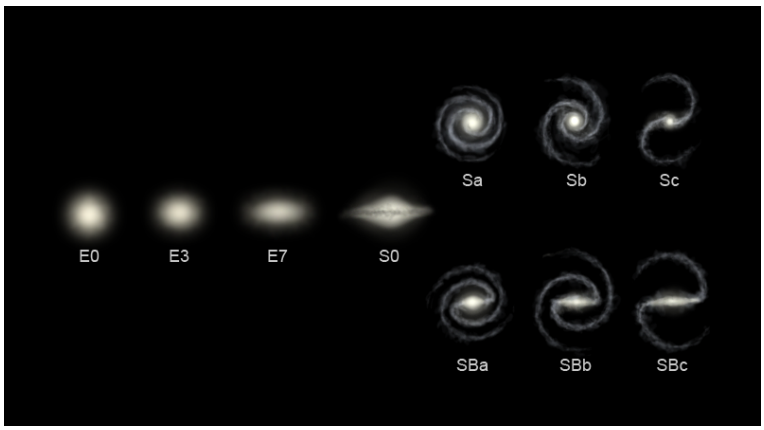

Figure 1.3: Schematic Hubble morphological classification of galaxies, i.e. the so-called "tuning fork diagram" illustrating ellipticals (denoted with E), lenticulars (S0), spirals with (SBa,.,.,d) and without (Sa,.,.,d) bar.

the common spiral galaxies and they are able to supply the observed strong star formation only for 10^7-10^8 years. If such sources continue to form stars at their current rate, the gas reservoir would be exhausted in much less than the age of the Universe (the Hubble time). The intense starburst activity lasting for such a short period of time gave rise to the general idea that all the galaxies likely pass through such starburst phase. Episodes of intense star formation were invoked to explain very high infrared luminosity, which were consistent with thermal emission associated with dust heated by the UV emission of young, newly formed populations of massive stars (Rieke et al., 1980). In the local Universe starburst activity interests the circumnuclear region which extends up to few kpc. The most intense starburst phase are associated with gas-rich disc galaxies characterized by a large amount of molecular gas concentration in their central kpc regions with gas-mass densities comparable to stellar densities in ellipticals (Bryant & Scoville, 1999; Downes & Solomon, 1998).

The on-going star formation is measured with the SFR, that is, as already mentioned, the number of stellar masses formed per year. The star formation history (SFH) is the number of stellar masses formed at any epoch, t, and includes the current and the past star formation. As already mentioned, the Hubble sequence can be seen as a sequence of SFH in which the star formation peak moves from elliptical to spiral galaxies when going towards later epochs (see Fig. 1.4, Sandage, 1986).

The radiation mechanisms taking place in starburst galaxies can be related to the number and the properties of the massive stars involved in the starburst. One of the basic parameter to describe star formation is the initial mass function (IMF), which define the number N of stars formed as a function of their mass m:

$$dN \propto m^{-x} dm, \tag{1.3}$$

where the index x, describing the shape of the IMF, is determined from observations ($1.5< x <3.5$ for star-forming regions, Weedman, 1988). Eq. 1.3 needs to be integrated over the mass between a lower and a upper limits of the masses range. The lower limit, M_i, is usually chosen to be 0.1 $M_\odot$, as suggested form the minimum mass to activate the hydrogen burning ($\sim$0.07 $M_\odot$). The upper limit can be determined by observations and it is usually chosen to be $\sim$100 $M_\odot$.

The IMF of stars more massive than our sun was first quantified by Edwin Salpeter in 1955, with x=-2.35 (Salpeter, 1955). In later times, various alternatives were explored, including a multisegment power law (Kroupa et al., 1993), where the slope of the IMF at lower masses was found to be shallower than the Salpeter value obtained at higher masses. Further, Chabrier (2003) presented a new formulation of IMF while reviewing numerous observational constraints. This IMF resembles a two-part power law and, hence, distinguishing between a Kroupa or Chabrier IMF is difficult (Dabringhausen et al., 2008).

The observed mass function is affected by the different evolution rates of stars of different mass. In fact, the more massive stars have a quicker life cycle and, consequently, they would progressively disappear as the starburst aged.

1.2.1 Multi-wavelength SED

The SEDs of starburst galaxies span a wide range of wavelengths. As purpose of illustration, Fig. 1.5 shows an example of a typical starburst SED, namely the spectra of M82 from the UV to the radio from Kennicutt et al. (2003). In starburst galaxies the X-ray emission is associated with accretion in binary stars and supernova remnants. Young and massive stars dominate the optical and UV continuum and give rise to emission lines originated from gas ionized by the hot stars themselves. The optical and NIR emission is due to intermediate and old stars which contribute both with continuum emission and spectral features, such as the Balmer absorption lines or molecular bands. This optical/UV emission is re-radiated by the dust in the star-forming regions giving, then, rise to the observed intense IR continuum. The most intense emission manifests itself with a prominent FIR peak located between 80 and 200 μm. The NIR and MIR wavelengths are characterized by emission features associated with the presence of Polycyclic Aromatic Hydrocarbon (PAH) molecules at some specific wavelength, namely 3.3, 6.2, 7.7, 8.6, 11.3 and 12.7 μm. Finally, radio continuum is due to the free-free emission of gas photoionized by massive stars or to synchrotron radiation emitted by electrons that are generated by supernova explosion.

1.2.2 Star Formation Tracers

One of the main properties that define galaxies and their evolution is the SFR. Severals are the SFR indicators, affecting different wavelengths, that have been

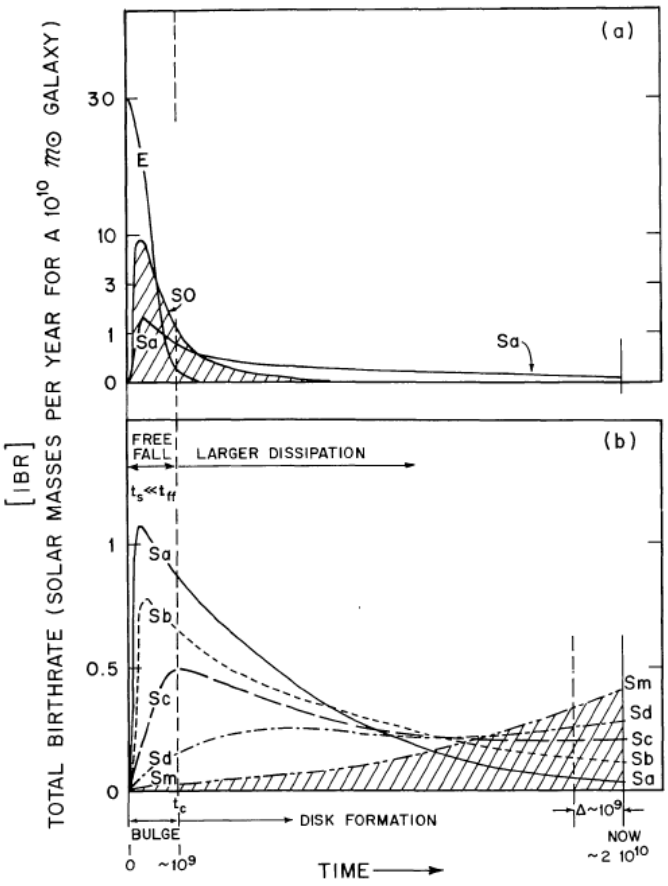

Figure 1.4: Schematic curves of the behaviour of the SFR with the time for galaxies of types E, S0, and Sa (top) and for later Hubble types, Sa,.,.,.,m (bottom) from Sandage (1986).

used over the past decades. Between these we find the UV luminosity (Madau et al., 1998), the H_α line luminosity (Kewley et al., 2002; Erb et al., 2006; Salim et al., 2007), the O[II] and H_α lines luminosities in the optical regime (Kennicutt, 1992) and the IR luminosity. This last concerns both monochromatic luminosity, NIR and FIR continuum as well as the PAH features luminosity.

In this section we focus only on the last two tracers which are those actually used in this Thesis. We remind to the previous references for the other methods to derive the SFR and to Kennicutt (1998) for a review.

IR Luminosity as Star Formation Tracer

The absorption cross section of the interstellar dust, absorbing the UV emission mainly due to massive stars, strongly peaks in the UV. The bulk of the re-emitted radiation is then expected in the FIR which is, for this reason, considered a sensi-

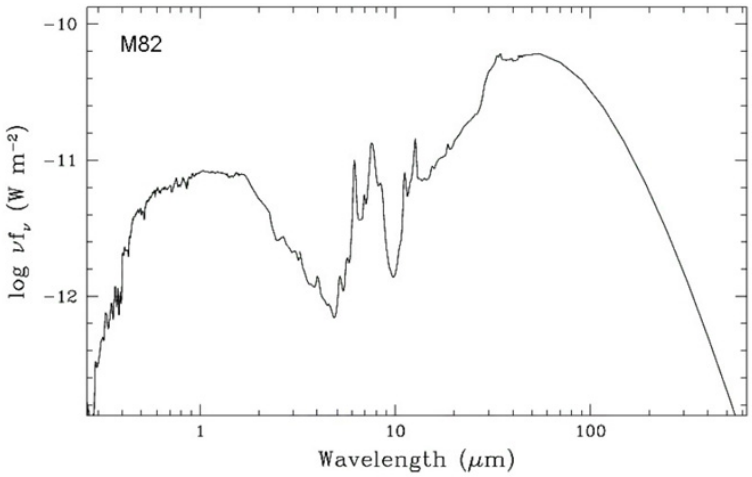

Figure 1.5: On purpose of illustration, a panchromatic view of an SED of the typical starburst galaxy M82, from the UV to the radio, taken from Kennicutt et al. (2003).

tive SFR tracer. In the ideal situation of optical/UV emission dominated by that of the newly formed stars and of star-forming regions characterized by a high dust opacity, as in dense circumnuclear starbursts powering many IR-luminous galaxies, the FIR luminosity provides an estimates of the bolometric luminosity of the starburst. Consequently, it can be consider an ultimate tracer of the on-going star formation. The real physical situation is more complex (Lonsdale & Hacking, 1987; Cox & Mezger, 1989; Rowan-Robinson & Crawford, 1989), with both a "warm" dust component, around young star-forming regions ($\sim$60 μm), and an "infrared cirrus" component ($\sim$ 100 μm), due to more extended dust heated by the interstellar radiation field, contributing to the observed spectra. FIR emission is considered a better tracer of SFR than that in the NIR and MIR, especially for AGN-hosting galaxies. In fact, NIR and MIR wavelengths can be affected by a significant contribution associated with AGN emission (e.g. Daddi et al., 2007; Mullaney et al., 2011), while it has been shown that FIR emission suffers a minimum contamination from the AGN (e.g. Netzer et al., 2007; Hatziminaoglou et al., 2010; Mullaney et al., 2011; Kirkpatrick et al., 2012).

In this Thesis, to derive the SFR from the FIR, SFR_{FIR} (see Section 6.4.2), we make use of the calibration of Kennicutt (1998). Such calibration was obtained by applying the models of Leitherer & Heckman (1995) for continuous bursts of age between 10 and 100 Myr and adopting the Salpeter IMF with a mass range between 0.1 and 100 $M_\odot$:

$$SFR_{FIR} = 4.5 \times 10^{-44} \times L_{SB}, \tag{1.4}$$

where L_{SB} is the IR starburst luminosity integrated between 8-1000 μm.

Several calibrations based on different assumptions on the star formation time scale have been published by different authors (e.g. Hunter et al., 1986; Lehnert & Heckman, 1996; Meurer et al., 1997). Most of these calibrations lie within 30% of that of Kennicutt (1998) (Kennicutt & Evans, 2012).

Various are the issues to take into account when using the relation between the global FIR luminosity and SFR. First of all, not all the luminous energy produced by newly formed massive stars is reprocessed by dust. This strongly depends on the amount of dust and, therefore, on the level of obscuration. Second, evolved stellar populations also contribute in dust heating with a consequent FIR emission (Kennicutt, 1998; Poggianti et al., 2001). This would imply that the FIR luminosity is not always a good tracer of the on-going star formation (e.g. Bendo et al., 2012; Lo Faro et al., 2013). It follows that a fully energy census needs to be included. Finally, besides old stars, a potential presence of an AGN can also contribute to the FIR emission. These ambiguities can affect the calibration of the relation and it is, indeed, well known that there probably is no single calibration that applies to all galaxy types (Kennicutt, 1998).

PAH Features as Star Formation Tracers

The MIR spectra of starburst galaxies clearly show features attributed to emission due to the vibration modes of PAH (Peters, 2002). These molecules are pumped by the far-UV (FUV) emission due to young stars and emit at some specific wavelengths (3.3, 6.3, 7.7, 8.6, 11.3 and 12.7 μm). PAH emission arises from photodissociation regions at the inner edge of the dusty molecular clouds surrounding the starburst. In fact, various authors have found the presence of PAH to correlate with the presence of starburst as classified in other parts of the spectra (Genzel et al., 1998; Rigopoulou et al., 1999; Brandl et al., 2006). The relative strength of the PAH features changes as a consequence of variations of the radiation field but Sargsyan & Weedman (2009) showed that these changes are not great in the integrated spectra of the starburst.

In this context, MIR spectra allow us to measure the PAH features and luminosities and, hence, provide an estimates of the SFR. In particular, *Spitzer* IRS spectra, with its unprecedented resolutions, have been used to measure the SFR based on PAH measurements and to derive empirical calibrations between PAH luminosities and bolometric luminosities (Brandl et al., 2006; Pope et al., 2008; Houck et al., 2007; Weedman & Houck, 2008). Indeed, it is well known that a correlation between the luminosity of the PAH, L_{PAH}, and the IR total luminosity, L_{IR}, exists (Rigopoulou et al., 1999; Brandl et al., 2006). The ratio between these two depends on the type of extragalactic source and on the interstellar medium (ISM) and, hence, on its luminosity. Indeed, Smith et al. (2007) found normal galaxies with quiescent star formation to show a higher L_{PAH}/L_{IR} ratio respect to starburst galaxies. The lowest ratio has been found in local ULIRGs with massive star formation (Rigopoulou et al., 1999; Lu et al., 2003; Netzer et al., 2007).

In this work we measure the luminosity of the PAH (see also Section 6.2.2) with the method of Hernán-Caballero et al. (2009) which use a lorentzian or drude profile for the PAH features (Laurent et al., 2000; Sajina et al., 2007; Smith et al., 2007). Then, the calibrations for the PAH features at different wavelengths is obtained by applying the Kennicutt (1998) calibration (Eq. 1.7 and under the assumption that AGN activity does not alter significantly the PAH emission. In this specific case, the calibrations of Hernán-Caballero et al. (2009) used are:

$$\mathrm{SFR_{PAH}} = 1.4 \times 10^{-8} \times \mathrm{L_{PAH[6.2]}} \tag{1.5}$$

$$\mathrm{SFR_{PAH}} = 4.65 \times 10^{-9} \times \mathrm{L_{PAH[7.7]}} \tag{1.6}$$

$$\mathrm{SFR_{PAH}} = 1.52 \times 10^{-8} \times \mathrm{L_{PAH[11.3]}} \tag{1.7}$$

for the PAH features at 6.2, 7.7 and 11.3 μm, respectively .

1.2.3 The ULIRGs case

Ultra Luminous Infrared Galaxies, ULIRGs, discovered by the IRAS satellite, are among the brightest objects in the Universe, with $\mathrm{L_{IR}} > 10^{12}\mathrm{L_{\odot}}$. The nature of their peculiar luminosity have been fascinating scientists since their discovery. ULIRGs are relatively rare in the local Universe and mostly found in major disc mergers. Indeed, the mergers themselves are believed to trigger the ULIRG activity process. Local ULIRGs are mainly found in low density environments and expected to evolve into spheroidal systems (Lonsdale et al., 2006). The compactness of the IR emitting region suggests two possible origins for the high ULIRGs luminosities: a compact circumnuclear starburst or a highly obscured AGN. Of particular interest is understanding the nature of the source powering these objects, which emission is believed to be composite of contributions both from a large population of hot young stars and a rapid rate accretion of matter onto a very massive black hole. Early effort was dedicated to determine which one of the two was the dominat phenomena. There is evidence now for ULIRGs to be powered by starburst but frequently with a significative nuclear activity. Nowadays, starburst and AGN emissions are frequently found to manifest themselves concomitantly in luminous galaxies. Therefore, the interest on ULIRGs moved from determining which of the two was the dominant mechanism for investigating their coexistence and a possible mutual connection.

1.3 AGN-Starburst Connection

As already mentioned in the Introduction, there is growing evidence of intense star formation phenomena coexisting with nuclear accretion. This suggests the existence of an intimate link between the two emission mechanisms. The study of AGN-starburst connection is directly related to our understanding of the early

Universe and plays a crucial role in studying the history of metal enrichment (Ferrara et al., 2000; Pettini, 2000) and the importance of feedback processes in the primordial phases of our Universe. We refer to "AGN feedback" to denote the mutual influence between the accretion onto a SMBH and star formation processes. This mutual influence can be in the form of a positive AGN feedback when the presence of an AGN trigger the SF, while a negative one would result in the quenching of the star formation, as well as of the gas fueling into the SMBH, due to photoionization/excitation of the ISM heated up by SMBH and by Compton heating mechanisms (Springel et al., 2005; Farrah et al., 2012; Cano-Díaz et al., 2012; Pope et al., 2012). In the regions very close to the SMBH the gas in the ISM is heated by the AGN and the collapse of the gas into stars is prevented. Moreover, a part of this gas can be driven out by radiation pressure resulting in a lack of fuel for further star formation. Moving outwards, the material expelled from the inner regions can heat the gas of the ISM and its kinetic pressure can drive the gas out of the galaxy, inhibiting then the star formation processes. To simplify, AGN feedback can be divided in two paradigms. A short time ($\sim 10^8$ yr) "quasar" mode feedback which assumes that the star formation in the host galaxy is suppressed by radiation from the accretion disc while the quasar is in rapid accretion. Second, a "radio" mode feedback which occurs over longer time scales ($\sim 10^9$ yr) and requires only low accretion rate to produce radio jets powerful enough to affect the ISM.

The putative AGN-starburst connection is still currently under the spotlight because its origin is not certain yet. Here, we summarize the most relevant evidence favouring the link between the two phenomena, both from the theoretical and observational point of view:

- Empirical correlations between the mass of the black holes residing at the centre of both active and inactive nearby galaxies and the mass of their bulges (Kormendy & Richstone, 1995; Faber et al., 1997; Magorrian et al., 1998; Marconi & Hunt, 2003), or the velocity dispersion of their stars (Ferrarese & Merritt, 2000; Gebhardt et al., 2000) or the Sersic index of the spheroid (Graham et al., 2001; Graham & Driver, 2007) could imply a direct link between the bulges formation and the black hole growth.

- Negative feedback from AGN to suppress star formation is required in cosmological simulations and semi-analytical models (e.g. Bower et al., 2006; Croton et al., 2006; Booth & Schaye, 2009).

- The peak of the quasar number density has been found to coincide with that of the SFH of the Universe (e.g. Madau et al., 1998; Heavens et al., 2004).

- Genzel et al. (1998) and Schweitzer et al. (2006) find presence of circumnuclear starburst in an accreting number of local AGN. Indeed, simultaneous star formation and AGN activity has been found in bright local AGN and

QSO (e.g. some well-known objects, such us NGC1068, NGC6240, Mrk231, Arp299 and Circinus).

- There is evidence of both star formation downsizing (Thomas et al., 2005; De Lucia et al., 2006) and AGN downsizing (Fiore et al., 2003; La Franca et al., 2005) where most massive galaxies and most luminous AGN tend to have formed earlier.

- Evidence for AGN luminosity to correlate with FIR luminosity of the host-galaxies (e.g. Netzer et al., 2007; Lutz et al., 2008; Netzer & Marziani, 2010) and with the strength of PAH features (e.g. Schweitzer et al., 2006; Lutz et al., 2008), which are, as already mentioned, star formation tracers, further suggests a link between star formation and gravitational accretion.

Various authors proposed different scenarios to explain and connect the evidence of an intimate link between AGN and star formation activity. One of the most popular is the merger scenario proposed by Hopkins et al. (2008) (see Fig. 1.6). In the early stages of this scenario the merger between gas rich galaxies is believed to drive the gas which fuels both star formation and black hole accretion. The merger gives rise to massive inflows of gas which triggers violent starburst episodes (ULIRGs) along with heavily obscured black hole accretion. Then, galaxies go through a coalescence phase characterized by an accretion peak with the SMBH becoming X-ray and optically visible. To follow, a QSO phase with AGN winds blowing out gas and with starburst consuming most of the nuclear gas. In later times, star formation and black hole growth are quenched due to gas consuming and dispersion. The result is a dead quasar hosted in red galaxies characterized by a passive evolution and satisfying the observed correlations between black holes and spheroid properties. In this scenario the growth of the black hole and star formation processes occur simultaneously with the quenching of the last requiring the action of the so-called "AGN-feedback" in which the radiation pressure, from a black hole accreted to the Eddington limit, can drive the gas outwards. This, would prevent a further growth and the gas expelled would influence the surrounding environment through winds and jets as well as radiation. The question, wether this AGN evolution would eventually quench the star formation and its impact of the host galaxies of different types is still matter of debate.

Despite the mounting evidence supporting an AGN-starburst connection, there is also indication of it being not valid for all the systems. This gave rise to a sort of crisis of the merger scenario. Among such indication we find:

- Observations of discs at z$\sim$2, indicating that a population of galaxies evolved without mergers does clearly exist (e.g. Genzel et al., 2006, 2008; Elbaz et al., 2011; Rodighiero et al., 2011).

- Kormendy et al. (2011) found no correlation between the mass of the black holes and the properties of the disc or the pseudobulge.

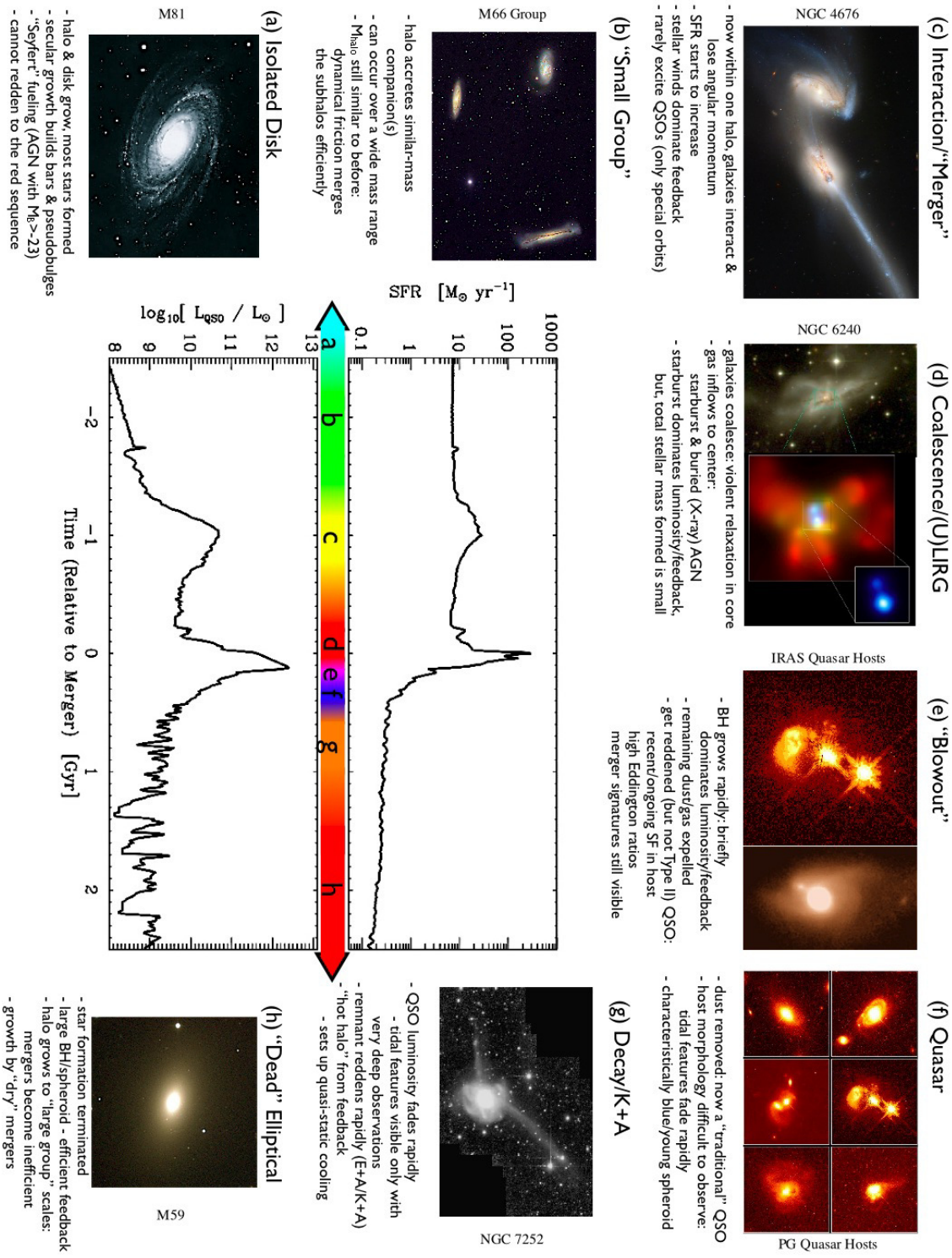

Figure 1.6: Schematic outline from Hopkins et al. (2008) illustrating the various phases of a galaxy evolution after a gas rich major merger. The cycle starts from isolated galaxies undergoing to merger process, passing through starburst and quasar phases and ending up with an elliptical galaxy.

- Jahnke & Macciò (2011) found no need of AGN feedback to explain the bulge-SMBH mass relation.
- Lutz et al. (2010) found no simple inverse relation between SFR and AGN luminosity in X-ray selected AGN.
- A dichotomy in the formation history of galaxies have been found, giving rise to a open debate between merger scenario and the secular accretion. Indeed, the stochastic/secular accretion can explain some classes of low-luminosity low-z AGN, such as the Narrow Line Seyfert 1 (NLS1).

Over the years, various observables and key tests have been proposed in order to investigate the putative AGN-starburst connection and the most suitable evolutionary scenario. There may be a dependence of the effectiveness of the feedback with the star formation mode. Indeed, in spatially compact bulges the star formation is easier to turn off than in spatially extended discs. In the merger scenario the AGN is expected to regulate/influence the star formation and, therefore, a correlation between SFR and the luminosity of the AGN is expected. Instead, in the scenario in which AGN and starburst are not coeval, as that of Cen (2012), the aforementioned correlation is not expected. Further, the merger scenario predicts an increase of SFR in AGN hosts (and AGN colors) but this is time-dependent. Morever, in this same scenario the morphologies of the AGN hosts should differ from those of the secular accretion scenario, with the host galaxies expected to be elliptical or disturbed systems for the first and discs for the latter. SFR should also differ between type 1 and type 2 obscured AGN at high-z since they are expected to be more star-forming than unobscured AGN. Another important point is to disentangle among positive (enhance of star formation) and negative (quench of star formation) AGN feedback. Studies in this context are still on-going and the evolutionary effect associated with the two types of AGN feedback is not certain yet.

In the literature, we find mountain works dedicated to study the star formation in AGN hosts galaxies. In particular, since obscured AGN are expected to be more star-forming, an extensive series of works have been dedicated to such sources. Brusa et al. (2009) and Xue et al. (2010) studied obscured AGN matching together X-ray and IR observations and found that these sources are red, but not particularly redder or more luminous than inactive galaxies of the same mass. Similarly, Cardamone et al. (2009) and Lusso et al. (2011) found AGN to have the same colors expected for galaxies of their masses. Moreover, 50% of obscured AGN, being not all ULIRGs or starburst galaxies, have been found to actively form stars with a rate greater than 20 $M_{\odot}$/yr, at almost all redshifts (Brusa et al., 2009; Lusso et al., 2011). Mainieri et al. (2011) found obscured AGN associated with star-forming galaxies to do not significantly scatter from the main sequence of star-forming galaxies. Indeed, these sources have been found to follow the well known tight correlation between SFR and stellar mass typical of star-forming galaxies (e.g. Noeske et al., 2007; Daddi et al., 2007; Elbaz et al., 2007; Rodighiero et al., 2010).

About the possible enhancement of star formation in galaxies hosting an active nucleus, Santini (2011) found, for AGN with low X-ray luminosity in the GOODS field, a SFR broadly consistent with that observed in "inactive" galaxies, with a modest enhancement. Instead, the SFR of high X-ray luminosity AGN host galaxies in the COSMOS (*Cosmic Evolution Survey*) field have been found to be $\sim$ 0.6 dex higher than in "inactive" galaxies, at all redshift and masses (Santini, 2011). This difference in the enhancement of star formation at low and high AGN luminosities is consistent with the two different modes of star formation and black hole growth. Indeed, high luminosity sources are believed undergoing to major mergers while the low luminosity ones are associated either with a scenario of smooth accretion or mergers with delay between the starburst and AGN phases.

Another way to investigate the AGN-starburst connection is to analyse the morphologies of the host galaxies. One of the first results in this direction goes back to Sanders et al. (1988), which found local QSO and ULIRGs to be hosted in highly distributed systems, providing evidence in support of mergers. Cisternas et al. (2010), while studying AGN host at z$>$ 1, found the 85% of them to do not show distortions or enhancement in mergers fraction among the different AGN morphologies with respect to the normal galaxies population (see also Grogin et al., 2003; Pierce et al., 2007; Georgakakis et al., 2009; Gabor et al., 2009). These results do not support the major merger scenario. Moreover, Kocevski et al. (2011) and Schawinski et al. (2011) found no significant excess of distorted morphologies in AGN at z between 1 and 3. Indeed, a large fraction of AGN has been found to reside in late-type galaxies and fueling by stochastic accretion of cold gas. A dependence on the X-ray luminosity has also been found. In fact, low X-ray luminosity AGN are mostly hosted in discs, while those with high X-ray luminosity mostly in elliptical or relaxed systems. An high disc fraction (and no distortion) is at odds with predictions that merger driven accretion is the dominant AGN fueling mode.

It is worth noting that the time delay between AGN activity, phase of intense star formation and merger, predicted by the simulations involving AGN feedback (e.g. Hopkins et al., 2006; Wild et al., 2010) can explain the SFR enhancement observed in systems with low X-ray luminosity or low masses but not the disc morphologies. The observed morphologies of AGN host galaxies fit better with a scenario of secular evolution or smooth accretion than the major merger one, with this last suffering a crisis also for moderate and high luminosity (Di Matteo et al., 2011; Bournaud et al., 2011).

Finally, having seen the time scale problem, the merger path does not seem to be the rule of AGN and starburst connection or, even, a casual relation does not exist. This last is represented by the scenario of Cen (2012) in which the star formation and the growth of the black hole are self regulated and independent. In this scenario the reason responsible of the starting of star formation, being it due to mergers or secular process, does not play an important role and the time scale is much longer with respect to Hopkins et al. (2008).

In the picture in which intense starburst activity coexists with nuclear accretion processes, the main issue is to qualify the relative importance between the two emission mechanisms. Both such main activity phases of galaxies happen in dusty environment producing a lot of IR photons and it is exactly in the IR where we should concentrate our efforts to investigate the putative AGN-starburst connection. The unprecedented resolution of *Spitzer* and *Herschel* satellites allows us to built the IR SED of extragalactic sources up to 500 μm, sampling both the peak of the hot (AGN heated) and cold (starburst heated) dust. In contrast to single band observations, a multi-wavelength approach can provide extensive information on the incidence of AGN and star formation and in the manner in which the two phenomena coexist. Moreover, IR selections favour sources with intense AGN and starburst activity as the IR SEDs are likely to be dominated by these two processes.

2 | Extragalactic Surveys in the Infrared

A thorough study of the energy absorbed by dust and reprocessed in the IR, loosely defined as the wide spectral interval from 1 to 1000 μm, is essential to understand galaxy evolution and formation. IR observations allow, in some sense, to see, throughout the dust, what in the visible is "not visible". They allow us to deeply investigate all the complex physical processes taking placing in the dusty phases of the life cycle of galaxies. In particular, as already pointed out in Chapter 1, IR studies are essential for investigating the very rich ISM of star forming systems in the early phases of their evolution, along with the emission of host dust surrounding the nucleus of active galaxies.

The contribution of the IR emission of the galaxies to the total energy budget evolves with redshift. Such contribution is around one third for the local Universe (Soifer & Neugebauer, 1991) and about half of the total energy produced by extragalactic sources for the distant Universe, as inferred from the *Cosmic Infrared Background* (CIRB, Dole et al., 2006). This increase reflects a more frequent heavily obscured star formation and/or gravitational activity in the distant Universe (Dole et al., 2006; Puget et al., 1996; Hauser & Dwek, 2001).

Ground based IR telescopes suffer of contamination due to thermal emission associated with the environment surrounding the telescopes and the instrumentations itself. The Heart's atmosphere also represents a problem because, with the exception of some narrow windows of the electromagnetic spectrum, it is able to block most of the IR radiation. Indeed, Heart's atmosphere is contaminated by the presence of water vapor, carbon dioxide, ozone absorption and thermal continuum and molecular lines emissions. IR ground based telescopes require a certain number expedients to avoid this contamination and the space, therefore, results the best place to observe the IR universe. Indeed, the kick-off of the IR extragalactic astrophysics dates back 30 years ago with the launch of the first IR satellite, IRAS.

More recently, the need of a large amount of observations and source monitoring in order to fully understand extragalactic sources got off to surveys on larger and larger fields, with wider and wider wave-band coverage and at higher and higher redshift. This allow astronomers to observe the full SEDs of galaxies at

wavelengths from the X-ray to the radio.

Since it is beyond of the aims of this Thesis to give a complete overview of all the surveys over all the electromagnetic spectrum, this Chapter will focus on the IR observatories and surveys. The first part presents a brief overview of the main IR satellites and their scientific achievements. This is followed by a description of the data used in this Thesis, along with the problem of handling and analysing multi-wavelength data.

2.1 IRAS

The Infrared Astronomical Satellite, IRAS [1], launched on the 25th of January 1983 and realized by a collaboration between the space agencies of USA, United Kingdom and Netherlands, was the first space based IR observatory to scan the entire sky. The "all-sky survey" lasted 10 months mapping the 96% of the sky four times. The IR pass bands are 12, 25, 60 and 100 μm with a resolution ranging between 30 arcsec and 2 arcmin from the first to the last band. The completeness limit is of 0.5 Jy at 12, 25 and 60 μm and 1.5 Jy at 100 μm.

IRAS explored for the first time the IR sky providing the FIR flux of about 25000 galaxies, of which ellipticals, Seyfert galaxies and quasars. It revealed the nucleus of our galaxy for the first time, finding IR cirrus in most of the space directions. Moreover, IRAS data have shown that our galaxy is a spiral with bars. In the field of extragalactic astronomy, the most important goal achieved by IRAS is the discovery of a new class of galaxies which SED is dominated by IR emission: LIRGs (i.e. Soifer et al., 1987) and ULIRGs (Sanders et al., 1986). These sources were characterized by intense star formation and embedded in a large amount of dust. LIRGs and ULIRGs are classified on the basics of their IR luminosity, L_{IR}, with $10^{11} L_{\odot} \leq L_{IR} \leq 10^{12} L_{\odot}$ and $L_{IR} \geq 10^{12} L_{\odot}$ for the first and the latter, respectively (Sanders & Mirabel, 1996). Then, an intense debate arose about the origin of the high luminosity of such sources, focusing on whether an intense star formation or an AGN (Sanders & Mirabel, 1996; Joseph, 1999) were dominating the observed emission. Indeed, their spectra showed evidence of high optical depth, implying high obscuration, but also high excitation lines (Lagache et al., 2005). It was necessary to wait for the ISO satellite in order to have further progress in this direction.

Among the main catalogues produced within the IRAS survey we find:

- The *Point Source Catalogue* (PSC, Bidelman, 1988), containing 250000 sources.
- The *Point Source Redshift Catalogue* (PSCz, Saunders et al., 2000) which is a further developed version of PSC through spectroscopic studies.
- The *Faint Source Catalogue* (FSC, Moshir et al., 1990), containing point sources

[1] http://irsa.ipac.caltech.edu/Missions/iras.html

with flux densities typically above 0.2 Jy at 12, 25 and 60 μm and above 1 Jy at 100 μm.

IRAS survey led off to statistical studies of IR selected galaxies in mostly local sources, allowing to systematically investigate star formation and AGN activity. Moreover, it allowed, for the first time, to look for evidence of evolution of extragalactic sources (Saunders et al., 1990; Lonsdale et al., 1990; Fisher et al., 1992; Oliver et al., 1992; Franceschini et al., 1988).

One of the most relevant discovers refers to Rowan-Robinson et al. (1991) which found a high (for the epoch) z (2.286) source, IRASF10214, showing high emission lines in its spectrum. The source have been found to be embedded in dust and emitting most of its energy in the FIR. The interpretation of the nature of this source was either a galaxy undergoing to its formation process or a heavily obscured quasar within a dust cloud.

Franceschini et al. (1994) carried out a pioneering study of the photometric properties of distant galaxies. The results of such work suggested the starburst phenomena to occur in regions heavily embedded in dust and, then, obscured at optical/UV wavelengths. This was consistent with the lack of optically luminous galaxies in optical surveys at $z \geq 0.5$.

In the context of AGN candidates selection, one of the first work was carried out by Miley et al. (1985) which showed, studying a sample of Seyfert galaxies of the IRAS catalogue, how the FIR colour could be used as diagnostic between AGN and IRAS galaxies. Fig. 2.1 reports the colour-colour diagram made by Miley et al. (1985), with the spectral index $\alpha(100, 60)$ between 100 and 60 μm versus the spectral index $\alpha(60, 25)$ between 60 and 25 μm. The spectral index α is defined as $F_\nu \propto \nu^\alpha$, where F_ν is the flux density at a certain frequency ν. Note that, even if the lower part of the diagram is populated by three types of galaxies, the upper part is mostly populated by Sy1. The same diagnostic diagram have been used by de Grijp et al. (1985) and de Grijp et al. (1987) to select AGN from normal galaxies. An example is shown in Fig. 2.2 which shows the colour-colour diagnostic diagram obtained by de Grijp et al. (1987) for galaxies characterized by strong emission lines in their spectra. Note that different types of objects occupy different regions of the diagram.

2.2 ISO

The Infrared Space Observatory, ISO[2] (Kessler et al., 1996), was the first cryogenic space mission operating as an observatory. It was realized by ESA with the participation of ISAS (part of JAXA from 2003) and NASA. ISO was launched in November 1995 and lasted until May 1998, 8 months longer than the time expected for the consuming of the superliquid helium.

[2] http://iso.esac.esa.int

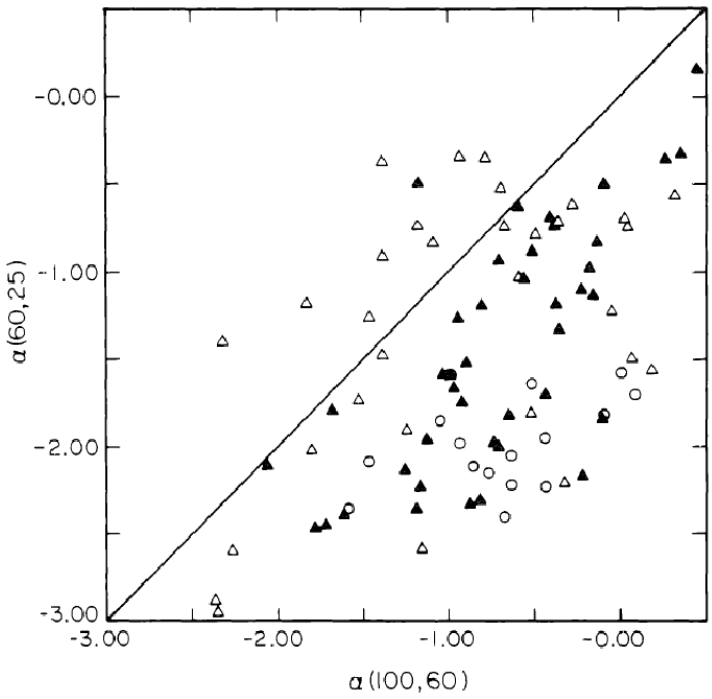

Figure 2.1: MIR and FIR colour-colour diagram from Miley et al. (1985) for galaxies with high nuclear emission lines. The spectral index between 100 and 60 μm, $\alpha(100, 60)$, is reported versus the spectral index between 60 and 25 μm , $\alpha(60, 25)$. Open(filled) triangles refer to Sy1(2) and the open circles to HII regions.

ISO observed all the active galaxies known at that time providing images, spectra and photometric data with unprecedented wavelength and quality coverage. 1000 times more sensitive in the MIR than IRAS, ISO provided much more detailed images along with high quality spectra in the range between 2.5-200 μm (Moorwood, 1999). The limiting flux density were pushed down to about 0.1 mJy at 6.7 μm and 0.5 mJy at 15 μm (Oliver et al., 2002).

The satellite was equipped with:

- ISOPHOT, an imaging polarimeter composed of 3 sub-systems to be used once per time, ISOPHOT-P (multi-band photo-polarimeter in the range 3-120 μm), ISOPHOT-C (photometric camera for the range 40-200 μm) and ISOPHOT-S (two spectrometers operating simultaneously in the range 2.5-12 μm, excluding the interval 5-6 μm);

- ISOCAM, a NIR and MIR camera to map the sky at wavelengths between 2.5 and 17 μm;

- SWS which comprises two independent spectrometers covering together the

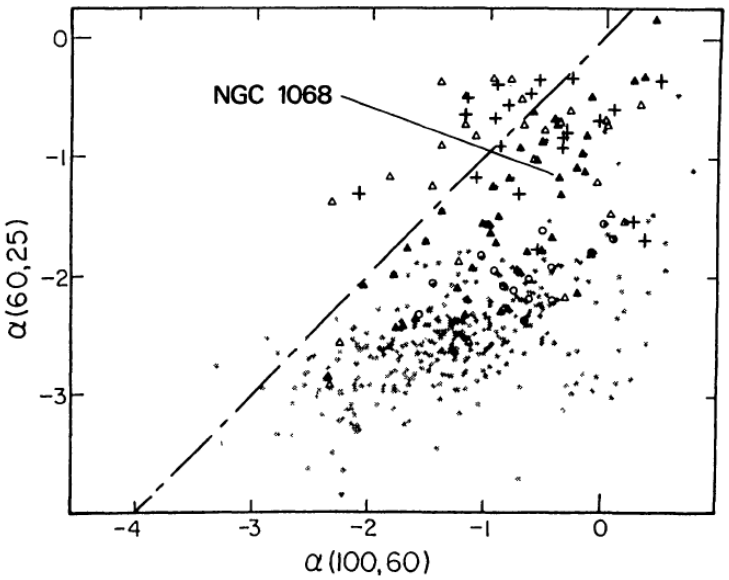

Figure 2.2: Another example of MIR and FIR colour-colour diagram with IRAS data by de Grijp et al. (1987). Open(filled) triangles refer to Sy1(2), open circles to HII regions and crosses to quasars.

range between 2.4 and 45 μm;

- LWS, a spectrometer covering the range between 45 and 200 μm.

Among the ISO surveys, we find those performed in the *Hubble Deep Field North* (HDFN) and *South* (HDFS) areas (Aussel et al., 1999; Oliver et al., 2002). The largest project is the *European Large Area ISO Survey* (ELAIS) which mapped an area of 12 deg^2 at 15 μm with ISOCAM and at 90 μm with ISOPHOT (Oliver et al., 2002).

One of the main results obtained exploring ISO data, in particular from the ISOCAM Cosmological survey, is the evidence for an excess of the number counts at 15 μm, indicating a strong evolution (Aussel et al., 1999). Evidence for strong evolution dominated by a population of star-forming or post starburst galaxies have been found also by Pearson & Rowan-Robinson (1996); Guiderdoni et al. (1997); Elbaz et al. (1998); Franceschini et al. (2001); Roche & Eales (1999). With this in mind, it became clear that observations in optical and UV regimes alone do not provide all the info about the SFH but that the SFR is underestimate while considering only optical data (by a factor 3 at z$\sim$ 0.6, Flores et al., 1998)

The SEDs provided by ISO were found to be essential for the unified model of AGN, both for testing the presence of dust and the orientation dependence. Haas et al. (1998) studied a subsample, composed of 10 objects, from the program

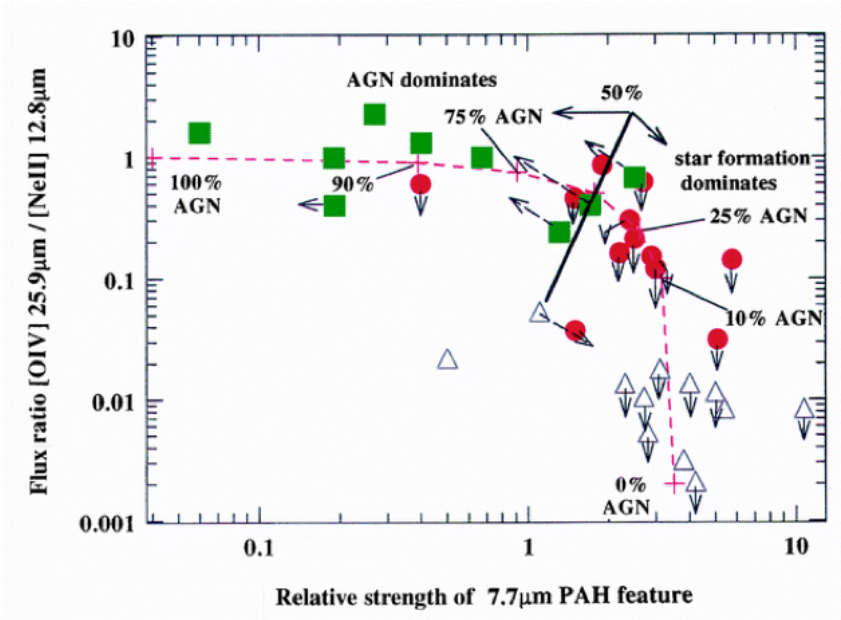

Figure 2.3: l
ine and that of [Ne v] line as a function of the strength of the PAH features at 7.7 μm.]Diagnostic diagram from Genzel et al. (1998) using the ratio between the intensity of [O IV] line and that of [Ne v] line as a function of the strength of the PAH features at 7.7 μm. In this diagram AGN are represented with green squares, ULIRGs with red circles and classical starburst galaxies with open triangles.

European Central Quasar finding steep-spectrum radio-quiet quasars having an enhanced emission around 60 μm and a decline above 100 μm steeper than what expected from self-absorption of synchrotron radiation. This increase was then attributed to thermal emission due to dust in a wide range of temperature, from 30 to 600 K.

The spectrographs on board on ISO were definitely more sensitive than those of IRAS and with a wider wavelengths coverage with respect to those ground based. This allowed the first observations of the PAH features. Schulz et al. (1998) carried out a statistical study on low resolution ISOPHOT-S spectra of 26 Sy1 and 28 Sy2 obtaining evident differences between the two types. In general, Sy2 showed a strong PAH features and a weak continuum, while Sy1 showed a power law continuum and weak PAH features. This difference was attributed to the continuum emission which is not attenuated in Sy1 and therefore can affect the PAH emission diminishing it. Such result was consistent with unification schemes predicting the torus to be optically thick in the radial direction.

Note that no evidence for silicate emission in Sy1 have been found with ISOPHOT-

S within the program *MPE Central Galaxy* (P.I.: R. Genzel) and also in the sample of Schulz et al. (1998). This lack of observations constituted for years one of the biggest problems related to the AGN unification scenario (see Section 5.0.1).

Furthermore, the spectrometers SWS and LWS enabled to detect a wide number of emission lines, both of hydrogen recombinations and molecular lines, providing information on the shape of the ionizing continuum in the extreme UV (Moorwood, 1999).

Various are the diagnostics suggested to distinguish between AGN and star formation activities using ISO data. High excitation lines, such as [O IV](25.9 μm) and [Ne V](14 and 24 μm), are typical of the AGN spectra, while the photoionization due to hot stars in starburst galaxies is enough to give rise to extremely strong lines of low excitation, such as [Ne II](12.8 μm). IR lines are less sensitive to the extinction, and therefore this represents an advantage while studying the dust material surroundings the AGN and the star-forming regions. Moreover, the ratio between the PAH features (at 7.7 μm) and the continuum, with this last being high in starburst galaxies and low in AGN, can be used as diagnostic between the two mechanisms (Moorwood, 1999). Fig. 2.3 reports the diagnostic diagram obtained by Genzel et al. (1998). ISO allowed to understand the source powering the ULIRGs, which are composite objects, dominated by heavily obscured intense star formation. Indeed, from Fig. 2.3, the contribution of star formation to the MIR emission in ULIRGs have been estimated to be 70-80 %, with the remaining 20-30 % due to the AGN (Genzel et al., 1998).

2.3 *Spitzer*

Enormous steps forwards in the IR astronomy were made with the *Spitzer* Space Telescope[3], constructed by NASA and *California Institute of Technology*. With its launch on August 25th, 2003, the mission lasted for more than five years until the depletion of the liquid helium on May 15th, 2009. Numerous were the goals of the mission, spanning planetology, star formation processes, ISM of our Galaxy and evolution of local and distant galaxies including AGN.

Three were the instruments on board on *Spitzer*:

- IRAC, the *Infrared Array Camera* (Fazio et al., 2004), a four channels IR camera providing simultaneously 5.2′×5.2′ images (with 256×256 pixel detectors) at four NIR and MIR bands, such as 3.6, 4.5, 5.8 and 8.0 μm. IRAC bands, being only weakly affected by dust, are well suited to detect elliptical/spheroidal galaxies (Surace et al., 2005).

- MIPS, the *Multiband Imaging Photometer* for *Spitzer* (Rieke et al., 2004), a camera providing images and photometric measurements in three MIR and FIR

[3] http://www.spitzer.caltech.edu

bands, such as 27, 70 and 160 μm. These bands were sensitive to on-going star formation and cold dusty regions.

- IRS, the *InfraRed Spectrograph* (Houck et al., 2004), a spectrograph comprising four separate modules (Short-Low, SL, Short-High, SH, Long-Low, LL, Long-high, LH) and providing low (R$\sim$ 60-130) and moderate (R$\sim$600) resolution spectroscopy from 5.2 to 38 μm. IRS provided also imaging in two filters, 13-18 μm and 18-26 μm.

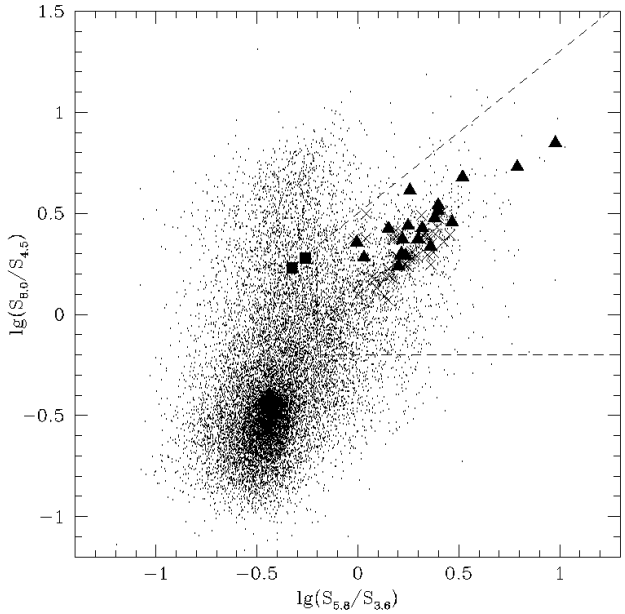

Figure 2.4: Colour-colour diagram obtained Lacy et al. (2004) using IRAC data from a sample AGN candidates of sources in the FLS. Dots indicate the 16000 sources detected in the four IRAC bands. Radio selected SDSS quasars are represented with crosses, SDSS Sy1 galaxies with squares and the obscured AGN of the sample (with flux at 8 μm, $S_{8.0} \geq 1$ mJy) with triangles.

Much of the extragalactic information from *Spitzer* comes form various surveys. Most of such surveys cover the same areas observed by other observatories, providing in this way a unique multi-wavelength view of the extragalactic sources. Among the most relevant we find[4]:

- SWIRE, the *Spitzer Wide-Area Infrared Extragalactic Survey* (Lonsdale et al., 2003), which carried out observations of six separate regions of the sky, selected for

[4] http://irsa.ipac.caltech.edu/data/SPITZER/docs/spitzermission/observingprograms/legacy/

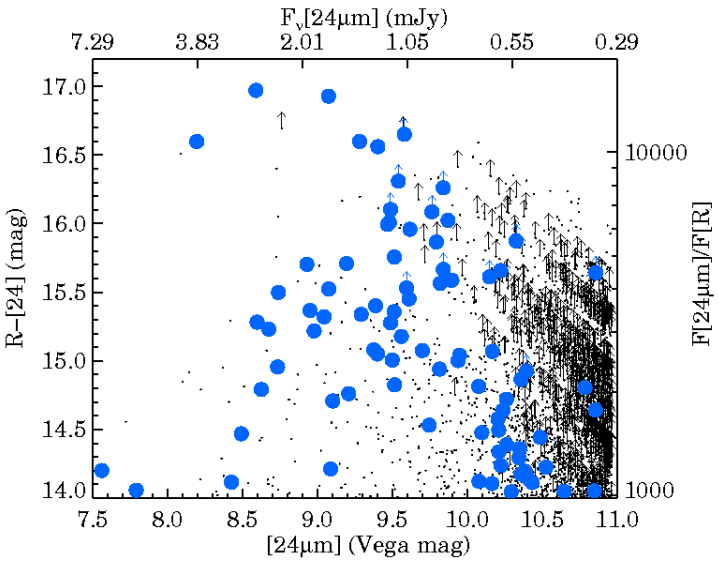

Figure 2.5: Diagram from Dey et al. (2008) with the difference, $(R - [24]) \geq 14$ mag, between the magnitudes in R band and at 24 μm as a function of that at 24 μm. Dots represent the entire sample, filled blue circles galaxy for which the spectroscopic redshift measurements are available and the upwards arrows the sources with upper limits on the R band magnitude.

their low levels of dust obscuration, for a total sky area of $\sim$50 deg^2, with both IRAS and MIPS.

- FLS, the *First Look Survey*, which observed 4 deg^2 with IRAC and MIPS.
- SDWFS, the *Spitzer Deep Wide-Field Survey*, which provided observations of an area of 8.5 deg^2 in the *NOAO Deep-Filed Survey Bootes* area with IRAC, following major Guaranteed Time Observer (GTO) prorates using both IRAC and MIPS.
- S-COSMOS, the *Spitzer Cosmic Evolution Survey* which observed an area of 2 deg^2 in the *Cosmic Evolution Survey* field (COSMOS) with IRAC and MIPS.
- SPUDS, the *Spitzer Ultra Deep Survey* which was an extension of the 1 deg^2 field *UKIDSS Ultra Deep Survey* with an IRAC and MIPS deep imaging survey.
- SIMPLE, the *Spitzer IRAC/MUSYC Public Legacy* in the E-CDFS (*Extended Chandra Deep Filed South*), which provided images of 0.25 deg^2 around the CDFS with IRAC.
- GOODS, the *Great Observatories Origins Deep Survey* which observed an area of 320 arcmin^2 on the *Hubble Deep Field North* and the CDFS fields with IRAC and MIPS (at 24 μm). The deepest *Spitzer* observations have been

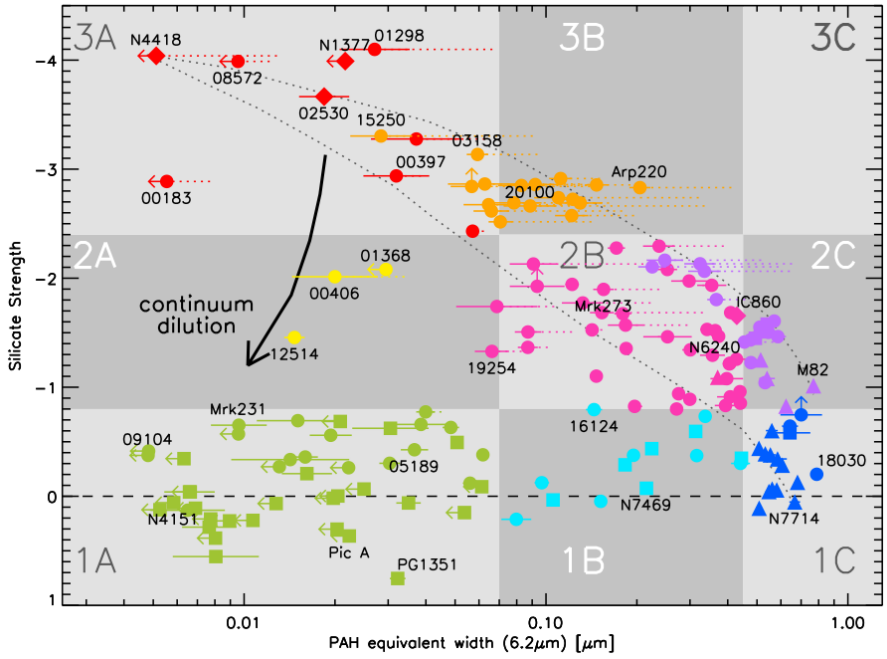

Figure 2.6: Diagnostic diagram from Spoon et al. (2007) showing the equivalent width of the PAH feature at 6.2 μm versus the strength of the silicate feature at 9.7 μm. Arrows denote upper and lower limits. On the basis of the region occupy in the diagram the sources have been divided in 9 classes, colors refer to different classes. The different symbols represent different type of galaxies: ULIRGs (filled cyrcles), starburst galaxies (filled triangles), Sy and quasars (filled squares) and other IR galaxies (diamonds).

done over portions of the GOODS field. A number of General Observer (GO) programmes and the *Far-Infrared Deep Extragalactic Legacy Survey* extends, in part, this imaging to 70 μm.

- SINGS/LVLS: the *Spitzer Infrared Nearby Galaxies Survey* which provided imaging and spectroscopic study of 75 nearby galaxies with IRAC, MIPS and IRS.

Two examples of Other Exploratory Science projects, that have allowed to better sample the IRAC depth-area parameter space, are the *Spitzer Extended Deep Survey* (SEDS) of a few very small fields observed by *Hubble Space Telescope* (HST) and the *Spitzer Extragalactic Representative Volume Survey* (SERVS) of about 1/3 of the SWIRE footprint.

The common goal of such ambitious extragalactic observing programmes was to expand the knowledge and the understanding of galaxy evolution, mapping various types of extragalactic sources, such as AGN, starburst, spiral and spheroidal galaxies out to high redshift. The aims comprised the study of the influence of the

environment on all scales, the history of star formation, the assembly of stellar mass and the role of gravitational accretion in the nuclei. *Spitzer* increased sensitivity respect to ISO allowed to detect sources at higher redshift and, therefore, to carry a more detailed analysis of galaxy evolution and on the physical mechanisms ruling the evolution itself.

Science achievements made with *Spitzer* span a wide variety of astronomical fields. Indeed, one of the most important award reached by the satellite is the first detection of radiation associated with an extrasolar planet (Werner et al., 2006). *Spitzer* observations dramatically improved the number counts of extragalactic sources, with e.g. Elbaz et al. (2007) finding a population of objects dominated by spiral galaxies, while carrying out number counts at 24 μm. In regard to the fraction of AGN, Charmandaris et al. (2004) and Smith et al. (2007), while investigating the strength of the PAH features, found the 50% of local galaxies to harbor a low-luminosity AGN. Moreover, deep observations with *Spitzer* enabled direct measurements of the star formation in galaxies up to z$\sim$3. In this context, results have shown a dependence of starburst activity with redshift, with a peak at z$\sim$1 and approximatively constant up to z$\sim$2.5 with a possible decrease in the SFR per volume moving to higher redshift.

Since the peak of the host dust emission heated by the AGN is expected to be in the MIR, *Spitzer* observations turned out to be very useful to look for AGN candidates and to estimates the number of the obscured AGN. Lacy et al. (2004) used a sample of sources in the FLS field to identify the fraction of AGN, missing in the previous optical surveys due to dust obscuration, with MIR luminosities comparable to those of quasars. The authors used the *Sloan Digital Sky Survey*, SDSS, database to identify 54 quasars within the 4 deg^2 FLS field. Lacy et al. (2004) selected a sample of obscured AGN candidates with a flux density $\geq$ 1 mJy at 8 μm. Fig. 2.4 shows the IRAC colour-colour diagram obtained by Lacy et al. (2004) where most of the obscured AGN candidates lie in the same region of the SDSS quasars. This is in agreement with the fact that the SEDs are dominated by the emission of the hot dust surroundings the AGN (Lacy et al., 2004).

Another interesting work aimed to select new AGN is that by Donley et al. (2007) where the authors used the power law of the emitted spectra as a selection criteria. In fact, the properties of this last can be used to identify luminous AGN (Neugebauer et al., 1979; Elvis et al., 1994). The authors selected galaxies with emission resembling that of a power law with a signal-to-noise ratio, $S/N \geq 6$, in each of the four IRAC bands and with an IRAC spectra well reproduced by a spectral index $\alpha \leq -0.5$ ($F_\nu \propto \nu^\alpha$). Donley et al. (2007) studied the properties of the sample at various wavelengths and compared them with the selected AGN using also other selection colour-colour criteria with *Spitzer* data (e.g. Lacy et al., 2004; Stern et al., 2005). Only the 55% of the galaxies under analysis were detected in the X-ray catalogue obtained by *Chandra Deep Field-North*, but most of the remaining galaxies likely hosted heavily X-ray obscured AGN (Donley et al., 2007). The selection criteria is based on the shape of the power law, and therefore this requires

the AGN to dominate the emission in the NIR and MIR. The galaxies in the sample of Donley et al. (2007) comprised a significative fraction of AGN detected with *Spitzer* at high redshift and luminosity. The AGN fraction revealed at 24 μm also showed evidence for a luminous population. Accounting only for objects of the sample identified also in the X-ray catalogue, Donley et al. (2007) found a fraction of obscured AGN of 68% ($<$ 81% when considering all the objects).

Spitzer revealed also a significant fraction of dusty obscured galaxies at high redshift (z$\sim$2) with an high ratio between the observed flux in the MIR at 24 μm and the flux in the R band. Dey et al. (2008) used such ratio as criteria to select obscured objects at high z. The sample considered comprises objects in the region of 8.140 deg^2 of the Bootes field with both MIPS data at 24 μm and KPNO (*Kitt Peak National Observatory*) data in R band. They selected the objects applying two selection criteria: flux at 24 μm larger than 0.3 mJy and a difference in magnitude between the R band and 24 μm $\geq$ 14. One of the main results of this work is the estimate of the contribution of such obscured galaxies to the IR luminosity density.

An interesting diagnostic diagram for MIR spectra of IR sources is that of Spoon et al. (2007), shown in Fig. 6.10. It reports the equivalent width of the PAH feature at 6.2 μm versus the strength of the silicate feature at 9.7 μm. The position of the sources in the diagram enables to classify them in 9 classes ranging from those with the spectra dominated by the continuum of the AGN host dust and starburst-dominated by PAH to those deeply obscured dominated by absorption. Spoon et al. (2007) noticed that the objects were distributed in two different branches of the diagram: one occupied by AGN- and starburst- dominated objects and the other by deeply obscured nuclei and starburst. The interpretation was associated with a difference in dust geometry: clumpy or not clumpy. Moreover, ULIRGs have been found in both branches, indicating, once again, the composite nature of such sources.

2.4 *Herschel*

The *Herschel* Space Observatory[5] is, so far, the largest IR telescope ever launched. Built by the European Space Agency (ESA) with the participation of NASA, *Herschel*, launched on May 2009, successfully fulfilled its operation lasted until April 29th, 2013. It carried a single mirror of 3.5 m along with instrumentation sensitive to FIR and sub-mm regime (55-672 μm). *Herschel* enabled to probe the earliest epoch proto-galaxies, allowing to investigate the co-evolution of AGN and starburst and the complex physics mechanisms involved in star and planet formation. The main aim of *Herschel* was to observe the coldest and dustiest objects in the Universe, unveiling the hidden details of the formation of stars and galaxies and the interrelation between the two. In the field of extragalactic astrophysics, thanks to its unprecedented high resolution and spectral coverage, *Herschel* brought incred-

[5] http://herschel.esac.esa.int/, http://herschel.cf.ac.uk/

ible improvements allowing accurate SED fitting de-composition of large sample of objects and statistical analysis to investigate AGN-starburst coevolution.

Herschel instrumentations provided broad band imaging in six bands with centre at 70, 100, 160, 250, 350 and 500 μm and imaging spectroscopy over the entire *Herschel* coverage. Three were the instruments on board on *Herschel*, namely:

- PACS, the *Photodetector Array Camera and Spectrometer*, (PI: A. Poglitsch, Max-Planck-Institut für extraterrestrische Physik (MPE), Garching, Poglitsch et al., 2010), a camera and a slow to medium resolution spectrometer for wavelengths in the range between 55 and 210 μm. It comprises four detector arrays: two bolometer arrays dedicated to wide-band photometry and two Ge:Ga photoconductor arrays employed exclusively for spectroscopy.

- SPIRE, the *Spectral and Photometric Imaging REceiver*, (PI: M. J. Griffin, Cardiff University, Griffin et al., 2010), a camera and a low to medium resolution spectrometer complementing PACS for wavelengths in the range between 194 and 672 μm. It employes an imaging photometer and a Fourier Transform Spectrometer (FTS), both of which using bolometer detector arrays. The total number of arrays is five, three of which dedicated to photometry and the remaining two for spectroscopy.

- the HIFI *Heterodyne Instrument for the Far Infrared*, (PI: T. de Graauw, in late 2008 succeeded by F. Helmich, SRON Netherlands Institute for Space Research, Groningen, de Graauw et al., 2010), is a very high resolution heterodyne spectrometer covering the 490-1250 GHz and 1410-1910 GHz bands. It was not an instrument dedicated to imaging but it observed a single pixel of the sky at a time using low noise detection through superconductor-insulator-superconductor (SIS) and hot electron bolometer (HEB) mixers, along with acousto-optical and autocorrelation spectrometers.

Among the most important *Herschel* observing programmes we find [6]:

- H-ATLAS, the *Astropysical Teraherz Large Area Survey*[7] (P.I.: S. Eales, Eales et al., 2010) which covered the largest total area, such as 550 deg^2 of the sky (i.e. one eightieth of the sky) in five bands in FIR and sub-mm. Five are the main science programmes, with the main one being a survey to investigate the dust emission of 50000 nearby galaxies with observations done both with SPIRE and PACS in parallel mode. The goal of such project is to investigate the heavily hidden objects and the gas in the star forming region.

- HerMES, the *Herschel Multi-Tiered Extragalactic Survey*[8] (P.I.: S. Oliver, Oliver et al., 2012) is aimed to study galaxy evolution in the distant Universe ex-

[6] http://herschel.cf.ac.uk/mission/key-programmes/
[7] http://www.h-atlas.org/
[8] http://hermes.sussex.ac.uk/

ploring sub-mm wavelength. It is the biggest project on *Herschel*. Observations are done with both SPIRE and PACS instruments, surveying $\sim$70 deg^2 from $20' \times 20'$ to $3.6^\circ \times 3.6^\circ$ (for a total of 900 hours observing time) and 12 clusters.

- PEP, the *PACS Evolutionary Probe*[9] (P.I.: D. Lutz, Lutz et al., 2011) was developed to study the rest-frame FIR emission of galaxies up to redshifts $\sim$3 as a function of environment. The survey enabled to investigate the constituents of the cosmic IR background and their nature, as well as the AGN and starbursts co-evolution. The observations are carried out with PACS only, but observations of common fields between PEP and HerMES have been coordinated in order to have also SPIRE observations. It observed 2.7 deg^2 from $10' \times 10'$ to $85' \times 85'$ (550 hours of observing time) and 10 clusters.

- the *Dusty Young Universe*[10] (P.I.: K. Meisenheimer) observed in the FIR some of the highest redshift quasars, which origin date back to the first billion years after the Big Bang, embedded in a substantial amount of dust. The bulk of this emission was not yet observed before SPIRE and PACS. The project consists in the observations of over 100 quasars with the aim of analysing their properties. In addition, PACS spectroscopy of four of the brightest quasars was proposed to disentangle the different origins of the FIR emission.

- GOODS, the *Great Observatories Origins Deep Survey* (P.I. D. Elbaz, Elbaz et al., 2011), which observed the GOODS fields. Such fields occupy small regions of the sky but they have been observed very deeply over all the electromagnetic spectrum, from the X-ray to the radio regime, by many of the greatest space observatories, including Hubble, Chandra and *Spitzer*. The sky area, a total of 300 acrmin^2, was observed both with PACS (very deep imaging of both GOODS-N and GOODS-S for a total of 330 hours of observations) and SPIRE (deep imaging of the GOODS-N field for a total of 30 hours of observations). The goal of the project was to study the faintest objects and the early stages of galaxies.

In particular, the work presented in Chapter 6 was carried out within the HerMES consortium of which I am a working member. For this reason more details about this survey are provided later in this chapter (see Section 2.4.1).

The first *Herschel* results are published in two *Astronomy and Astrphysics* special issues, one dedicated to the achievements reached with PACS and SPIRE (Walmsley et al., 2010a) and the other to those obtained by HIFI (Walmsley et al., 2010b).

Mounting are the *Herschel* accomplishments but it is beyond the scope of this Thesis to review all of them. I will briefly mention some among the most im-

[9] http://www.mpe.mpg.de/ir/Research/PEP/index.php

[10] http://www.mpia.de/Public/Forschung/Instrumentation/DustyYoungUniverse/index.html

portant, focusing to those related to galaxy evolution and AGN-starburst connection. Notwithstanding the success of IRAS, ISO and *Spitzer*, before *Herschel* the wavebands from 60 to 500 μm were still unexplored (see Fig. 2.7). The advent of *Herschel* enabled for the first time to probe the Universe at FIR and sub-mm wavelengths, allowing to study that half of radiation which is re-emitted in such range (Dwek et al., 1998; Fixsen et al., 1998; Driver et al., 2008). More than 75% of the *Cosmic Infrared Background* (CIRB) radiation is now resolved both in PACS (Altieri et al., 2010; Berta et al., 2010, 2011; Rigby et al., 2011; Magnelli et al., 2013; Sibthorpe et al., 2013) and SPIRE bands (Oliver et al., 2010; Béthermin et al., 2012) from studies of number counts. This increase to more than $\sim$ 89% when applying the "probability of deflection" P(D) approach which considers even more fainter objects (Berta et al., 2011; Glenn et al., 2010, for PACS and SPIRE, respectively). Morover, a very detailed analysis of the luminosity function of galaxy both for local and more distant objects in all the *Herschel* bands (Vaccari et al., 2010; Sargent et al., 2012, 2013; Gruppioni et al., 2013; Magnelli et al., 2013, and Marchetti et al. in prep) shows a strong evidence of downsizing in the SFH.

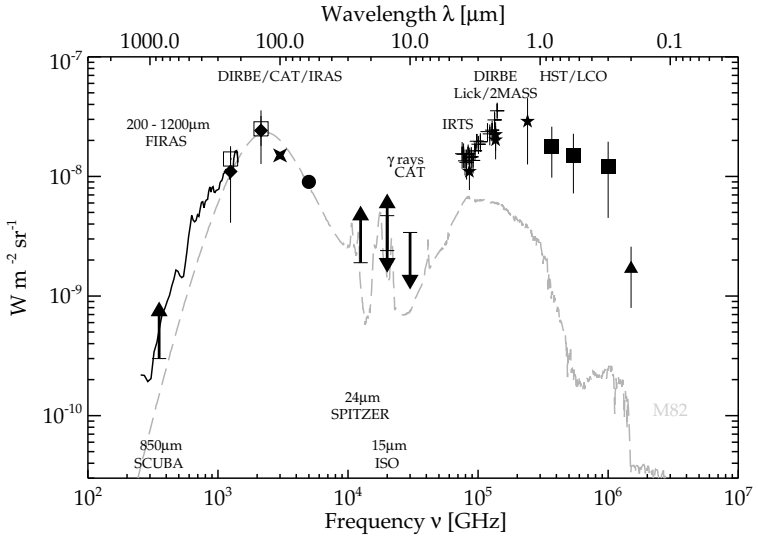

Figure 2.7: Extragalactic background radiation as a function of wavelength (Dole et al., 2006).

In addition, it has been found that starburst galaxies, driven by mergers, at z$\sim$2 have a minor role in contributing to the LIR (Rodighiero et al., 2011; Sargent et al., 2012, 2013). Indeed, galaxy growth is ruled by two main modes: one in which stars are formed in disc-like galaxies following the SFR-stellar mass sequence and another, referred to as starburst mode, in outliers to such a sequence. This last is believed to be driven by mergers. Investigation of the relative contribution of the two modes with PACS and/or SPIRE data have found the merger-driven starburst to play a relatively lesser role in the formation of stars in galaxies. Rodighiero

et al. (2011), using a combination of BzK- and PACS-selected star forming galaxies at 1.5<z<2.5 from the whole COSMOS and GOODS-South fields, found starburst galaxies with SFR four times greater than those of the main sequence to represent only 2% of the star forming galaxies. Rodighiero et al. (2011) found these sources to contribute only 10% to the SFR density at z∼2 . Concurring, Sargent et al. (2012), while observing the IR luminosity functions, found the contribution form starburst galaxies to the SFR density to be constant or weakly dependent on redshift, with a value around 8-14%.

Pozzi et al. (2012), while doing accurate SED fitting decomposition of 24 ULIRGS at z∼2 of the sample of Fadda et al. (2010) using PACS data, found the 35% of them to harbor an AGN with only 10% of this being AGN dominated (i.e. AGN contribution to the $L_{IR} > 50\%$). Sajina et al. (2012), while investigating ∼200 with infrared luminosity between 10^{11} and 10^{12} $L_{\odot}$ (24 μm sources in the FLS field), found the 53% to harbor an AGN, with the 23% having the AGN contributing for more than 50% to the L_{IR} and 30% being starburst dominated (with AGN contributing to the L_{IR} for less than 20%). The remaining 47% comprises composites sources, including starbursts with AGN-like MIR spectra.

Rosario et al. (2012) analyzed a sample of X-ray selected AGN using a combination of deep FIR and X-ray data in the GOODS-South, GOODS-North and COSMOS fields. They found accretion luminosity and SFR to do not correlate at all redshifts for low AGN luminosities, while high AGN luminosities showed a significant correlation but only among AGN at low and moderate redshifts (z<1). These observations are consistent with the scenario where most low-luminosity AGN are primarily fueled by secular processes, while moving to higher AGN luminosities the major mergers, driving both the accretion onto SMBHs and star formation processes, become more and more important. These findings are in agreement with those of Santini (2011) (see also Section 1.3). Rosario et al. (2012) also found evidence for the enhancement of SFR in luminous AGN to become weaker or to disappear at high redshifts (z> 1) suggesting that the role of mergers is less important at these epochs.

Conflicting results have been found for what concerns the possible enhancement of star formation with the increasing of AGN luminosity. Page et al. (2012) studied X-ray selected AGN with SPIRE data in the CDF-N field, finding the mean SFR of AGN with a X-ray luminosity $> 10^{44}$ erg s^{-1} at z between 1 and 3 to be significantly lower than those of moderate luminosity AGN. Contrary, Harrison et al. (2012) investigating the COSMOS and CDF-N fields using also SPIRE data, found SFR of the AGN to be constant over the broad X-ray luminosity range ($10^{43} - 10^{45}$ erg s^{-1}).

The most important results connected with this Thesis is that of Hatziminaoglou et al. (2010) which investigated a large sample of type 1 and type 2 AGN in the HerMES fields finding the need of a starburst component to fully account for the total FIR emission of the objects in the sample. Fig. 2.8 shows the colour-colour diagrams from Hatziminaoglou et al. (2010). When using MIPS-

SPIRE colours, S_{250}/S_{70} vs S_{70}/S_{24} (top panel of Fig. 2.8) AGN are distinct from star-forming galaxies, instead when using only longer wavelength SPIRE data, S_{500}/S_{350} vs S_{350}/S_{250} (bottom panel), AGN and starburst galaxies are indistinguishable.

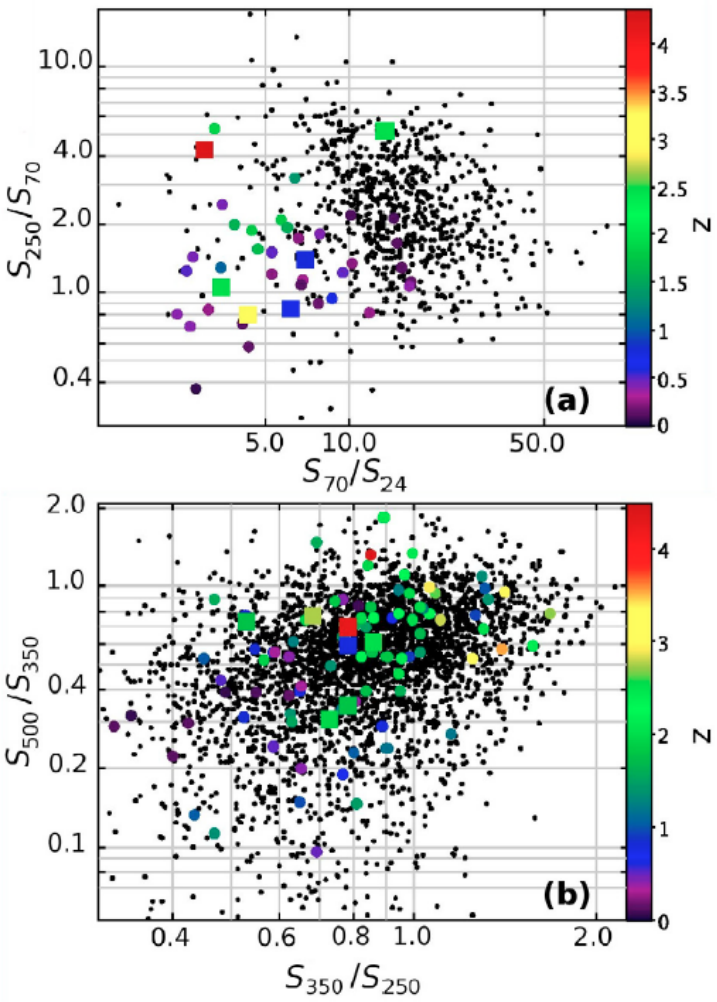

Figure 2.8: Colour-colour diagrams from Hatziminaoglou et al. (2010) showing S_{250}/S_{70} vs S_{70}/S_{24} (top panel) and S_{500}/S_{350} vs S_{350}/S_{250} (bottom panel). Diagrams are color-coded on the basis of the redshift. Type 1 (circles) and Type 2 (large squares) are over plotted on the IR sources of the entire SPIRE catalogues (black dots).

Very recently, Kirkpatrick et al. (2013) proposed a new diagnostic to disentangle high-redshift AGN and starburst galaxies combining sub-mm wavelength SPIRE photometry with MIR Spitzer data (see Fig. 2.9). They found the S_{250}/S_{24} vs $S_8/S_{3.6}$ and S_{100}/S_{24} vs $S_{8.0}/S_{3.6}$ to be optimal color selections for their 151 high-

redshift (z between 0.5 and 4) galaxies selected to have flux greater that 100 μJy at 24 μm in the GOODS-N and ECDFS.

2.4.1 HerMES

HerMES, the *Herschel Multi-tiered Extragalactic Survey*, is a legacy survey aimed to study the evolution of galaxies in the distant Universe. It is the largest project on ESA's Herschel Space Observatory. HerMES was designed to map fields ranging in size from 0.01 to $\sim$20 deg^2 for a total area of $\sim$ 380 deg^2 using SPIRE (at 250, 350 and 500 μm) and PACS (at 100 and 160 μm), with a wider component of 270 deg^2 with SPIRE alone (Oliver et al., 2012). The key science goal of this project is to investigate star forming galaxies in the part of the electromagnetic spectrum in which the emission of galaxies and the CIRB are expected to peak. HerMES observations have been partly combined with the PEP survey (Lutz et al., 2011) in order to obtain a sample optimized to probe the peak of star forming galaxies and, therefore, to obtain very accurate measurements of the IR luminosity. The need of multi-wavelength data in order to achieve the major objectives of the programme was satisfied choosing to monitor fields among the richest in the sky for multi-band coverage (see Fig. 2.11). HerMES observations were divided in six nominal levels with different depths and areas. These go from Level 1 to Level 6, moving from deeper observations in narrower areas to shallower observations in wider areas. The structure of fields and observations results to be distributed as a "wedding cake structure" as shown in Fig. 2.10. Higher rare bright luminosity objects are observed in wide shallow tiers, while the lower luminosity sources, faint but very numerous, in the deep narrow tiers. For a complete census of fields and their correspondent levels, areas and confusion limits we refer to tables 2.1 and 2.2 reported here, as purpose of clarification, and corresponding to tables 1 and 2 of Oliver et al. (2012), respectively.

2.4.2 Multi-wavelength Data and Database

As already mentioned HerMES fields (Fig. 2.11) boast of a plethora of multi-wavelength data, including: radio (VLA, WRST, GMRT,ATCA); sub-mm (SCUBA, Bolocam, AzTEC, MAMBO); MIR and FIR (*Spitzer*, ISO, AKARI); NIR (UKIRT, VISTA); optical (HST, Subaru SuprimeCAM, CFHT Mega-CAM, KPNO MOSAIC1, CTIO MOSAIC2, INT WFC); UV (GALEX) and X-ray (XMM-Newton, Chandra). The main problem when dealing with multi-wavlength data is that these often come in separate database and a unique and homogenous dataset is necessary when the purpose of the work is to pursue multi-band studies. The main issue connected with the realization of such datasets is the source identification which is a complex and time consuming process. Matching catalogue of sources observed with different observatories means also to deal with different aperture and exposure.

In the context of the HerMES survey the need of a multi wavelength catalogue

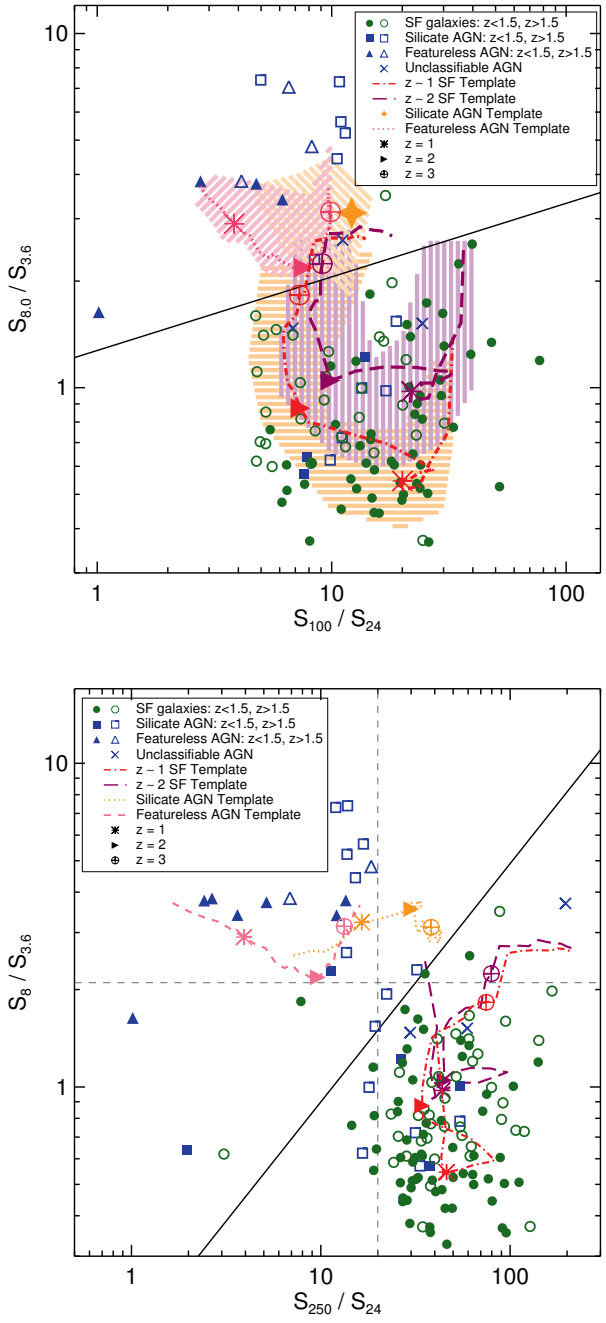

Figure 2.9: Color-color diagram from Kirkpatrick et al. (2013) combining FIR PACS (top) and SPIRE (bottom) photometry photometry with MIR *Spitzer* data. The dark line divides the star forming galaxies (green) from the AGN (blue). All sources are plotted according to redshift (filled symbol: z < 1.5; open symbol: z > 1.5). Redshift tracks, form z∼0.5 and 4.0, of high redshift templates of Kirkpatrick et al. (2012) are also plotted. In the left panel, the silicate AGN composite shows a negligible redshift evolution and is plotted as the orange star. In the right panel, the dashed gray lines shows the color thresholds that can be used to separate AGN from star forming sources if only one color is available.

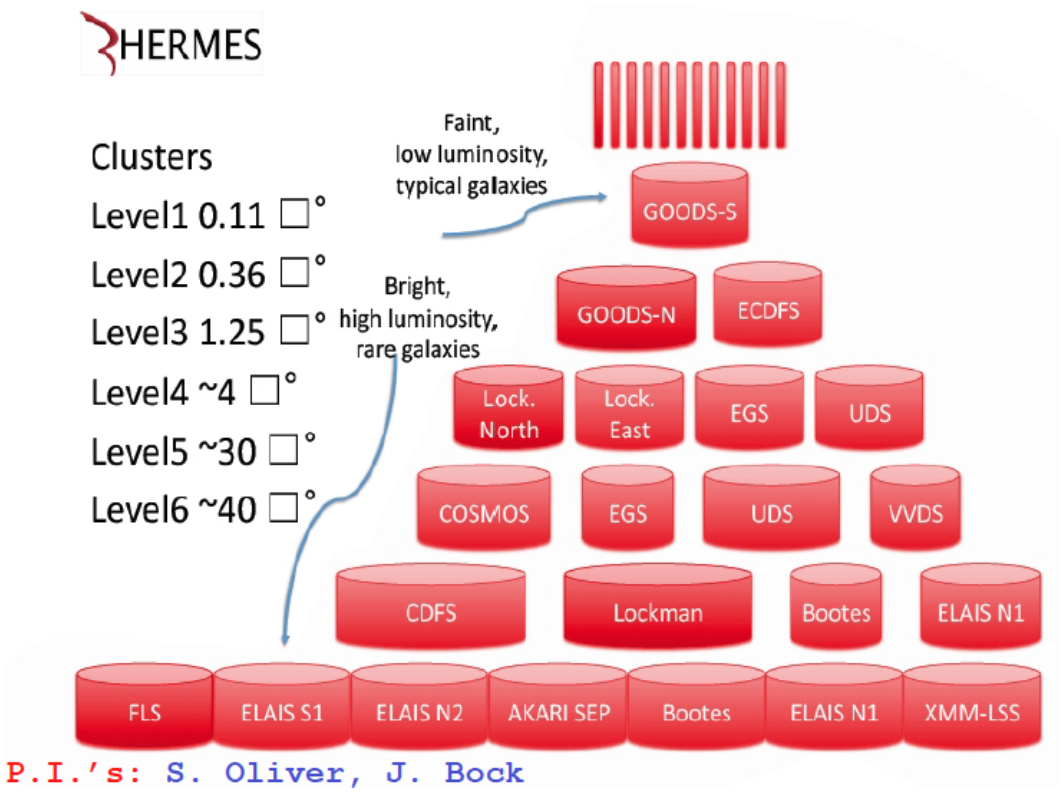

Figure 2.10: The "wedding cake" structure of HerMES fields.

has been supplied with the creation of the *Spitzer-Selected Multi-Wavelength Wide-Area Data Fusion* which is also the guide to the XID source extraction of Roseboom et al. (2010). In particular, in Chapter 6 we made use of data coming from the first data release of HerMES (published on April 3rd 2012 through the Herschel Database in Marseille, HeDaM[11], realized on the basis of Data Fusion catalogue and the XID method source catalogue. For this reason I dedicated a part of this Section to described the ancillary data available, the HerMES XID method and the Data Fusion assembling.

XID method, source extraction and cross-identification

A very serious issue and the dominant source of noise in deep imaging is the confusion noise, i.e. fluctuations in the telescope background. This can dramatically increase the uncertain on the position of the source making the cross-identifications with other wavelengths problematic (Hogg, 2001).

The XID catalogue was created by Roseboom et al. (2010) processing SPIRE

[11] http://hedam.oamp.fr/HerMES/

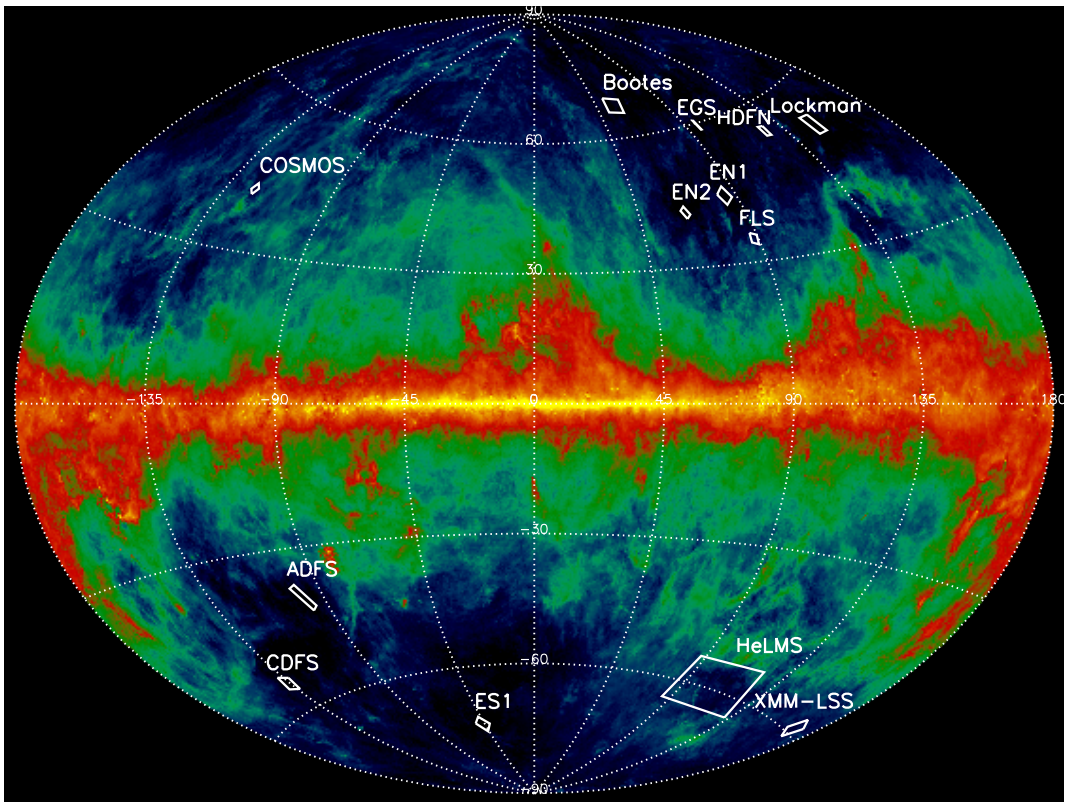

Figure 2.11: HerMES fields overlaid on IRAS/COBE sky maps by Schlegel et al. (1998) in Galactic coordinates. Most fields were chosen on the basis of their largest sizes, for being characterized by very-low FIR background and for being far from bright IRAS sources. A few were chosen on the basis of the availability of multi-wavelength data at non-IR wavelengths and/or to being observable from both hemispheres.

imaging taken as part of HerMES. The approach is statistical and ignore the single sources. Indeed, Roseboom et al. (2010) looked at the aggregate properties of the sources using a combination of methods: both stacking (Dole et al., 2006; Pascale et al., 2009) and statistics maps using the pixel intensity distribution (e.g. Patanchon et al., 2009). The method made use of a combination of linear inversion and model selection techniques to produce reliable cross-identification catalogues based on MIPS 24 μm source positions. Note that this method has been developed in parallel with other techniques (i.e. Smith et al., 2012; Levenson et al., 2010) which have been used in the first papers of the Science Demonstration Phase from HerMES. Comparison between the different methods provided good agreement (Roseboom et al., 2010).

Ancillary datasets and *Spitzer* Data Fusion

Spitzer Data Fusion combines HerMES XID catalogue with datasets coming from the most popular multi-wavelength survey wide-area fields and extends from the FUV to the FIR. The goal of such work, carried out by Mattia Vaccari (MV) and Lucia Marchetti (LM) (see also Vaccari et al. in prep) was to provide an homogeneous database of FUV to FIR photometry for *Spitzer*-selected sources in the, as we already mentioned, most well observed wide-areas of the sky.

MV and LM collected *Spitzer* data from both MIR and FIR imaging surveys: SWIRE (Lonsdale et al., 2003; Rowan-Robinson et al., 2008), which covers 50 deg^2 spread over six fields (ELAIS-S1, XMM, CDFS, Lockman Hole, ELAIS-EN1, ELAIS-EN2) selected for their low levels of obscuration due to dust, the SDWSurvey (PI: D. Stern) in Bootes field of $\sim$9 deg^2 and the FLS (PI: T. Soifer) in the Extragalactic FLS (XFLS) field of $\sim$4 deg^2 (see also the previous Section 2.3 for a more detailed description of these surveys). All these catalogues are IRAC selected and have MIPS data always available. After having selected catalogues from such surveys, MV ad LM crossed correlate them with a plethora of ancillary datasets. These last include both photometry from the FUV to the NIR and optical spectroscopy, namely:

- The *Galaxy Evolution EXplorer* (GALEX) mission (Martin et al., 2005) which was conceived to carry out a wide-ranging set of imaging, in FUV (1350-1750 Å) and near-UV (NUV, 1750-2800 Å) and a spectroscopic survey (1350-1800 Å).

- Photometry and Spectroscopy from the *Sloan Digital Sky Survey* [12](SDSS, York et al., 2000) which is one of the major and most successful surveys in the history of astronomy. It is a deep multi-color imaging and spectroscopic survey covering more than a quarter of the sky and providing maps in five bands (u, g, r, i and z) having average wavelength of 355.1, 468.6, 616.5, 748.1 and 893.1 nm. Each filter has a 95% completeness in typical seeing to magnitudes of 22.0, 22.2, 22.2, 21.3, and 20.5, respectively (Abazajian et al., 2004).

- The Two Micron All Sky Survey, 2MASS (Skrutskie et al., 2006), which uniformly scanned the entire sky in 3 NIR bands to detect and characterize point sources brighter than about 1 mJy in each band, with SNR greater than 10, using a pixel size of 2.0 arcsec. The three bands are J, H and K_s centered at 1,24 μm, 1.66 μmand 2.16 μm, respectively, with K_S differing from the classical definition by Johnson (1962). Wavelengths longward of 2.31 μm were excluded to reduce the thermal background.

- The United Kingdom Infrared Deep Sky Survey (UKIDSS) is a set of five public surveys of complementary combination of depth and area, all using *Wide Field Camera* (WFCAM) on the United Kingdom Infrared Telescope (UKIRT).

[12] http://www.sdss.org

The wavelength range is between 0.83−2.37 μm in up to five filters Z,Y,J,H, and K.

The Data Fusion have been also complemented with photometric and spectroscopic redshift information (whenever available), collected from the SDSS as well as from many different available public works (e.g. the SWIRE photometric redshift catalogue by Rowan-Robinson et al., 2008). Moreover, thanks to this data collection, new photometric redshift estimates and validations have been made within the HerMES consortium. In addition, to complement the SDSS spectroscopic database, the NASA Extragalactic Database (NED) [13] was searched for spectroscopic redshifts, so as to complement the SDSS spectroscopic database.

Multi-band catalogues, as the Data Fusion, have revolutionized the modern observational cosmology and astrophysics allowing for a proper characterization of the sources. The physical mechanisms occurring in the extragalactic sources contribute to different parts of the electromagnetic spectrum. Indeed, a multi-wavelength approach is the most suitable to investigate the complex physics imprinted in the galaxy SEDs.

[13] http://nedwww.ipac.caltech.edu/

Set	Level	Target	Mode	N_{AOR}	T [hr]	N_{rep}	N_{samp}	l_1 [']	l_2 [']	θ [deg]	Ω_{nom} [deg^2]	Ω_{max} [deg^2]	Ω_{good} [deg^2]	DR
1	CD	Abell 2218	Sp. Nom.	2	9.29	100	1118	4	4	84		0.14	0.10	SDP
2	CD	Abell 1689	Sp. Nom.	8	1.97	48	235	4	4	18		0.11	0.08	
3	CD	MS0451.6-0305	Sp. Nom.	8	1.97	48	235	4	4	5		0.11	0.08	DR1
4	CS	RXJ13475-1145	Sp. Nom.	8	1.97	48	234	4	4	17		0.11	0.08	
5	CS	Abell 1835	Sp. Nom.	8	1.97	48	236	4	4	16		0.11	0.08	
6	CS	Abell 2390	Sp. Nom.	8	1.97	48	235	4	4	81		0.11	0.08	
7	CS	Abell 2219	Sp. Nom.	8	1.97	48	234	4	4	66		0.11	0.08	DR1
8	CS	Abell 370	Sp. Nom.	8	1.97	48	233	4	4	70		0.11	0.08	
9	CS	MS1358+62	Sp. Nom.	8	1.97	48	235	4	4	76		0.11	0.08	
10	CS	Cl0024+16	Sp. Nom.	8	1.97	48	235	4	4	61		0.11	0.08	
11	CH	MS1054.4-0321	Sp. Nom.	8	2.18	16	131	15	10	22		0.24	0.16	
12	CH	RXJ0152.7-1357	Sp. Nom.	8	2.18	16	131	15	10	165		0.24	0.16	
13	L1	GOODS-S	Sp. Nom.	76	20.22	76	730	20	20	14		0.51	0.35	
22	L2	COSMOS	Sp. Nom.	24	50.13	24	388	85	85	70		3.49	2.82	
14	L2	GOODS-N	Sp. Nom.	1	13.51	30	416	30	30	42		0.64	0.55	SDP
15	L2	ECDFS	Sp. Nom.	19	8.78	19	232	30	30	44		0.79	0.58	DR1
17	L3	Groth Strip	Sp. Nom.	7	3.54	7	85	67	10	130		0.82	0.60	DR1
18	L3	Lockman-East ROSAT	Sp. Nom.	7	3.2	7	87	30	30	77		0.77	0.57	
18B	L3	Lockman-East Spitzer	Sp. Nom.	4	4.53	4	32	80	40	149		1.78	1.40	
19	L3	Lockman-North	Sp. Nom.	1	3.91	7	104	35	35	1		0.74	0.65	SDP
23	L4	UDS	Sp. Nom.	7	10.54	7	110	66	66	20		2.46	2.02	
24	L4	VVDS	Sp. Nom.	7	10.39	7	110	66	66	21		2.46	2.02	
22B	L5	COSMOS HerMES	Sp. Nom.	8	25.20	8	128	110	110	70		5.04	4.38	
27	L5	CDFS SWIRE	Sp. Fast	10	41.72	20	81	190	150	99		12.18	11.39	
28	L5	Lockman SWIRE	Sp. Fast	2	13.51	2	16	218	218	2		18.2	17.37	SDP
28B	L5	Lockman SWIRE	Sp. Fast	8	41.26	8	58	220	180	50		15.26	7.63	
42	L7	HeLMS	Sp. Fast	11(10)	103.4	2		1560	750	15	270			
20	L3	Lockman-North	PACS	12	13.96	11		30	30	42	0.25			SDP
20B	L3	Lockman-North	PACS	20	20.89	20		30	30	42	0.25			
21	L3	UDS HerMES	PACS	25	25.93	14		30	30	0	0.25			
25	L4	UDS	PACS	12	40.19	7		57	57	0	0.9			
29	L5	EGS HerMES	Parallel	7	22.68	7	93	150	40	131		3.50	2.67	
30	L5	Bootes HerMES	Parallel	5	20.33	5	70	80	80	0		4.21	3.25	DR1
31	L5	ELAIS N1 HerMES	Parallel	5	20.82	5	72	95	95	38		3.74	3.25	DR1
32	L5	XMM VIDEO1	Parallel	4	13.44	4	65	106	75	107		3.20	2.72	
32B	L5	XMM VIDEO2	Parallel	4	8.88	4	53	106	44	107		2.12	1.74	
32C	L5	XMM VIDEO3	Parallel	4	13.44	4	53	106	75	107		3.19	2.73	
33	L5	CDFS SWIRE	Parallel	4	50.42	4	57	204	170	101		11.87	10.89	
34	L5	Lockman SWIRE	Parallel	4(2)	71.22	4		215	215	154		17.86	16.08	
39B	L5	ELAIS S1 VIDEO	Parallel	4	17.72	4	56	138	80	87		4.42	3.72	
35	L6	ELAIS N1 SWIRE	Parallel	2	28.0	2	28	207	192	55		13.37	12.28	
36	L6	XMM-LSS SWIRE	Parallel	6	45.58	2	29	180	180	82		21.62	18.87	DR1
37	L6	Bootes NDWFS	Parallel	4	27.99	2	30	243	80	145		11.3	10.57	DR1
38	L6	ADFS	Parallel	2	18.11	2	28	190	122	80		8.58	7.47	DR1
39	L6	ELAIS S1 SWIRE	Parallel	2	17.9	2	28	140	81	91		8.63	7.86	
40	L6	FLS	Parallel	2	17.1	2	29	160	138	5		7.31	6.71	SDP
41	L6	ELAIS N2 SWIRE	Parallel	2	17.1	2	26	177	119	147		9.06	7.80	

Table 2.1: Summary of the HerMES observations. The full set of Astronomical Observation Requests (AORs) are available through ESA's Herschel Archive. We have grouped N_{AOR} observations of the same field at the same level made with the same mode and areal size into a 'set' (the number of AORs still to be scheduled after 2011 Dec 21st is indicated in parentheses). The first five columns give: the set identification number; the design level; the target name, the *Herschel* observing mode and the number of AORs in the set. T is the time used or allocated for this set. N_{rep} is the total number of repeats of the observing mode in the set. All our SPIRE nominal (30" s^{-1}) and fast mode (60" s^{-1}) (Sp. Nom. and Sp. Fast) observations include a scan in the nominal and orthogonal direction, so 1 repeat is 2 scans). For SPIRE observations that have been executed N_{samp} is the median number of bolometer samples per pixel in the 250 μm map (6″ × 6″ pixels). The error per pixel in our SPIRE maps as processed by the standard HIPE pipeline are $\sigma^2_{250} = \sigma^2_0/N_{samp}$ with $\sigma^2_0 = 896 \pm 11, 1554 \pm 27$ and ~ 1440 mJy^2 beam^{-2} for Parallel, Sp. Nom. and Sp. Fast modes respectively. l_1, l_2 are sides of a rectangle with near homogenous coverage. θ is the roll angle with short-axis of that rectangle measured East of North. For SPIRE observations that have been executed Ω_{max} is the total area of pixels with any 250 μm coverage and Ω_{good} is the area of pixels where the number of bolometer samples per pixel in the 250 μm map is greater than $N_{samp}/2$. For PACS fields or unobserved SPIRE fields Ω_{nom} gives the nominal area of region. The final column indicates which observations are included in our data releases; observations marked SDP were released in our Early Data Release, observations marked SDP or DR1 have been released through http://hedam.oamp.fr as part of HerMES DR1. Set numbers #16 and #26 were removed from the programme. From Oliver et al. (2012).

Fields	Area			Observations		5-σ noise level (for band in μm)				
	Nominal	Extra	Cummulative	PACS	SPIRE	110	160	250	350	500
		[deg^2]						[mJy]		
Abell 2218	0.0050	0.0050	0.1	P	1	4.1	7.9	6.4	5.3	7.6
Abell 1689	0.0050	0.0050	0.11	P	2	3.6	6.9	9.2	7.7	11.0
8 Targets	0.04	0.04	0.15	P	3-10	5.7	10.9	9.2	7.7	11.0
2 Targets	0.03	0.03	0.18	P	11-12			13.9	11.6	16.7
Various	0.18	0.18	0.36	E	E	6.1	11.7	14.2	11.9	17.1
GOODS-N	0.042	0.042	0.04	G,P	G,14	2.2	4.1	3.8	3.1	4.5
GOODS-S	0.11	0.087	0.13	G,P,33	13,15,27,33	2.1	2.9	4.3	3.6	5.2
GOODS-S	0.012	0.012	0.14	G,P,33	13,15,27,33	1.1	2.1	4.6	3.8	5.5
GOODS-S	0.018	0.0060	0.15	G,P,33	13,15,27,33	1.6	3.0	4.6	3.8	5.5
GOODS-S	0.023	0.0060	0.15	G,P,33	13,15,27,33	2.0	3.8	4.6	3.8	5.5
COSMOS	2.0	2.0	2.15	P	22,22B	7.7	14.7	8.0	6.6	9.5
ECDFS	0.25	0.14	2.29	P,33	15,27,33	7.6	14.5	8.0	6.6	9.6
GOODS-N	0.25	0.208	2.5	P	14	4.7	8.9	8.2	6.8	9.9
Lockman-East	0.25	0.25	2.75	P	18,18B,28B,34,28	6.5	12.3	9.6	7.9	11.5
Lockman-North	0.25	0.25	3.0	20,20B,34	19,28B,34,28	7.4	14.1	10.6	8.8	12.7
Groth Strip	0.25	0.25	3.25	P,29	17,29	7.1	13.6	10.7	8.9	12.8
UDS HerMES	0.25	0.25	3.5	21,25,32,36	23,25,32,36	6.8	12.9	11.2	9.3	13.4
UDS	0.7	0.7	4.2	25,32,36	25,32,36	11.2	21.4	11.2	9.3	13.4
VVDS	2.0	2.0	6.2	25,32C,36	25,32C,36	28.8	54.9	11.2	9.3	13.4
CDFS SWIRE	11.4	11.1	17.3	33	27,33	31.5	60.2	12.7	10.5	15.2
Lockman SWIRE	16.1	15.6	32.9	34	28,28B	35.3	67.3	13.6	11.2	16.2
EGS HerMES	2.7	2.5	35.4	29	29	26.6	50.8	13.8	11.3	16.4
Boötes HerMES	3.3	3.3	38.6	30,37	30,37	26.6	50.8	13.8	11.3	16.4
ELAIS N1 HerMES	3.3	3.3	41.9	31,35	31,35	26.6	50.8	13.8	11.3	16.4
ELAIS S1 VIDEO	3.7	3.7	45.6	39B,39	39B,39	28.8	54.9	14.9	12.2	17.8
XMM-LSS VIDEO	7.7	5.0	50.6	32,32B,32C,36	32,32B,32C,36	28.8	54.9	14.9	12.2	17.8
COSMOS Hermes	4.4	2.4	53.0		22B			15.9	13.3	19.1
ELAIS N2 SWIRE	7.9	7.9	60.9	41	41	49.9	95.1	25.8	21.2	30.8
FLS	6.7	6.7	67.6	40	40	49.9	95.1	25.8	21.2	30.8
ADFS	7.5	7.5	75.1	38	38	49.9	95.1	25.8	21.2	30.8
ELAIS S1 SWIRE	7.9	4.2	79.2	39	39	49.9	95.1	25.8	21.2	30.8
ELAIS N1 SWIRE	12.3	9.1	88.3	35	35	49.9	95.1	25.8	21.2	30.8
Boötes NDWFS	10.6	7.3	95.6	37	37	49.9	95.1	25.8	21.2	30.8
XMM-LSS SWIRE	18.9	15.0	110.6	36	36	49.9	95.1	25.8	21.2	30.8
Various	570.0	570.0	681.0	A	A	86.3	164.0	44.5	37.1	53.0
SPT	100.0	100.0	781.0		S			45.3	37.5	54.1
HeLMS	270.0	270.0	1051.0		42			64.0	53.0	76.5

Table 2.2: HerMES survey with sensitivities in the context of other survey programmes being undertaken by *Herschel*. The "observations" columns refer to the AOR set numbers of Table 2.1 for HerMES or for other Key Programmes we use: "E" for Egami cluster programme, "G" for GOODS-H, "P" for PEP, "A" for H-ATLAS and "S" for SPT (see Table 6 in Oliver et al. (2012) for a summary of the ıHerschel programs). The sensitivities are estimated consistently using HSPOT v5.1.1. These are single pixel sensitivities and ignore the benefits of matched filters, particularly for unconfused fields, e.g. H-ATLAS quote empirical 5-σ sensitivities of 105, 140, 32, 36, 45 mJy for the five wavelengths so the sensitivities in this table should be scaled by 1.22, 0.85, 0.72, 0.97, 0.85 to obtain a consistent comparison with H-ATLAS. The sensitivity of HerMES observations have been calculated including data from shallower tiers as described in the text. Other surveys are treated independently. Cluster observations are listed before blank fields. The fields are ordered in increasing 250 μm flux limit then right ascension. The area is defined by the PACS observations for Levels 1-4 (above the second horizontal line), otherwise we use $\Omega_{\rm good}$ from Table 2.1 or $\Omega_{\rm nom}$ for HeLMS. We tabulate three areas: the nominal area for each field; the 'doughnut' area which excludes any deeper sub-fields within; and the cumulative area of all fields higher in the table. The 5-σ confusion noise (after 5σ cut) from Nguyen et al. (2010) is 24.0, 27.5, 30.5 mJy (at 250, 350 and 500 μm), approximately the Level 6 depth. GOODS-S also has PACS data not listed here at 70 μm over 0.11 deg^2 to a 5-σ depth of 1.9 mJy. From Oliver et al. (2012).

3 | Modelling Multi-Wavelength Data

Multi-band datasets from large surveys provide a lot of information on the underlying complex physics of galaxy SEDs and are the primary source of our knowledge of galaxies themselves. Since different physical mechanisms can manifest themselves at different wavelengths, a multi-band approach is favored to fully understand all the emission processes happening in galaxies with respect to single band studies that can provide constrains only on a single parameter. With a multi-wavelength approach, it is then possible to reach a proper characterization of extragalactic sources. Accurate modelling and analysis should be, in principle, able to provide robust measurements of the fundamental properties of galaxies, such as stellar masses, SFR, gas and dust content. Indeed, all the emission processes coming into play leave characteristic imprints at different wavelengths on the global SED of extragalactic sources.

Stars populating the galaxy emit mostly in the optical/UV regime. This same radiation is reprocessed by the gas and dust composing the ISM. This re-radiation is observed in emission/absorption lines due to gas photoionization/excitation at various wavelengths as well as in the continuum emission and PAH features in the IR regime. When considering active galaxies, the contribution of the AGN to the total emission over all the electromagnetic spectrum can not be neglected. In type 1 AGN the accretion disc contributes most of the emission at X-ray, optical and UV wavelengths, often overwhelming that of the host galaxy. Moreover, the hot dust emission attributed to the AGN torus emits in the IR. The bulk of its energy interests MIR wavelengths, where silicate features at 9.7 and 18 μm, related to the presence of silicate dust grains, are also observed.

The main tool used to investigate galaxy SED is applying appropriate SED fitting techniques along with sophisticated models. In recent years customized tools for SED fitting and sophisticated models have progressed significantly. Various fitting procedures have been introduced to fit data from the UV to the FIR. This progress has benefited from new observing facilities and large surveys at different wavelengths. Appropriate emission models of galaxies across the electromagnetic spectrum are necessary to investigate the energy radiated by the galaxies themselves and to extract information about stellar light and the surrounding medium.

Part of this Thesis (chapters 4 and 6) is dedicated to modelling the emission from optical/UV to the FIR of active galaxies.

To model a galaxy all the mechanisms marking the SED need to be taken into account. Therefore, various models need to enter in the recipe, such as spectrophotometric models, radiative transfer of stellar light through the ISM and the connection of this picture with galaxy evolution and formation.

With this is mind I dedicated this chapter to the description of the different physical emission mechanisms that need to be considered when modelling the galaxy SEDs. This comes along with a summary on the most used models and tools dedicated to model the observed spectra of galaxies from UV to the FIR. Finally, the last part reviews AGN torus models, providing a more detailed description for those used in the next chapters.

3.1 Stars

Stellar emission contributes mostly in the range between ~ 0.3 μm and ~ 5 μm (restframe). The total emission of stars populating a galaxy can be represented as a sum of spectra of simple stellar population models (SSP). Such stellar population synthesis models, under various assumptions, account for the mass and the luminosities of all the stars and for the distributions of their metal content and age. Pioneering works of such method have been made by Tinsley (1972) and Larson & Tinsley (1978).

A SSP is defined as an assembly of coeval, initially chemically homogeneous, single stars and it is described by four parameters: age (t), chemical composition (X, Y, Z)[1] and the IMF (already defined in Section 1.2). The total spectrum of an SSP is the result of the sum of the spectrum of all the stars of a certain mass, M, age, t, and metallicity, Z:

$$\mathrm{L}_\nu(\mathrm{t},\mathrm{Z}) = \int_\mathrm{M} \Phi(\mathrm{M})_{\mathrm{t},\mathrm{Z}} \mathrm{L}_\nu(\mathrm{M},\mathrm{t},\mathrm{Z}) \mathrm{dM} \tag{3.1}$$

in flux emitted per unit frequency per unit mass. $\Phi(\mathrm{M})$ is the IMF, already defined in Section 1.2, which determines the number of stars of certain mass along the isochrone, which is the locus that stars of the same age occupy in the Hertzsprung-Russel (H-R) diagram[2]. Isochrones are built up from evolutionary tracks which determine where a star of given mass M, age t and metallicity Z lies on the H-R diagram. There are two main ingredients to build up an SSP: isochrones and spectral libraries. Isochrones are approximated to series of virtual stars, for each of which we know the spectrum. The construction of isochrones,

[1] A chemical composition of a star is characterized by the hydrogen content, X, the helium component, Y, and all the remaining elements, referred to as "metals", like Carbon, Oxygen, Magnesium, Silicious, Iron (C, O, Mg, Si, Fe, respectively).

[2] This diagram is a plot of luminosity (absolute magnitude) against the spectral type (temperature) of the stars

which determine the place occupied by a star of given M, t and Z in the H-R diagram, required a large grid of evolutionary tracks. These are created by modelling the evolution of stars of a given initial mass and metal content. Various isochrones and evolutionary tracks have been developed over the years, such as those from Padova (Bertelli et al., 1994; Marigo & Girardi, 2007; Marigo et al., 2008), Geneva (Lejeune & Schaerer, 2001), Yale (Demarque et al., 2004) and MPA (Weiss & Schlattl, 2008). The starting point to create evolutionary tracks is a star of the main sequence (Zero Age Main Sequence, ZAMS), which corresponds to the phase in which stars start to burn hydrogen. The evolution of that specific star is then taken into account until an end point, given from the stellar evolution theory, such as supernova or Asymptotic Giant Branch (AGB)[3] phase. Underlying assumptions consist of the parameters to investigate, such as the mass range (usually between $\sim$0.1 and $\sim$ 120 $M_{\odot}$) and the metallicity range (usually between $\sim$0.01 and $\sim$4 $Z_{\odot}$). The requirement to construct a stellar spectral libraries is to have a very wide and uniform coverage of the parameter space, namely of M, t and Z. These stellar spectra can be either empirical, coming from real stars, or theoretical spectra generated by using stellar atmosphere models. Once the flux of each star with certain parameters (thanks to the stellar library) and the number of stars with such parameters (thanks to the isochrones) are known the SSP can be built up. Basically, the contribution to the flux at each wavelength of the spectrum of the star is weighted on the number of stars in it and their luminosity.

The method described above, called "isochrone synthesis" and established by Chiosi et al. (1988), Maeder & Meynet (1988) and, in particular, Charlot & Bruzual (1991), is currently used by the majority of stellar population models (Walcher et al., 2011). Another method is the "fuel consumption" approach which resolve the problem that the previous method had in rapid evolutionary phases (e.g. thermally pulsing asymptotic giant branch stars, TP-AGB[4]). The isochrones are, indeed, calculated in discrete steps in time and models using the fuel consumption theorem circumvent this problem by changing the integration variable above the main sequence (MS) turnoff[5] to the stellar fuel, i.e. the amount of hydrogen and helium used in nuclear burning. The fuel is integrated along the evolutionary track. The main idea is that the luminosity of the post-main sequence stars, which are the most luminous, is directly linked to the fuel available to stars at the turnoff point (for full details, see e.g. Buzzoni, 1989; Maraston, 1998, 2005).

Among widely used SSP models we find:

- BC03 (Bruzual & Charlot, 2003) models which use evolutionary tracks from

[3]The AGB is a phase of stellar evolution undertaken by all low- to intermediate-mass stars (0.6-10 $M_{\odot}$). In such phases helium and hydrogen are burned in two external shells, while the internal core is composed by carbon and oxygen.

[4]The AGB is divided in two phases: the early AGB (E-AGB) where the main source of energy is helium fusion in shell and the thermally pulsing AGB (TP-AGB) which starts after that the helium shell has run out of fuel and where the energy comes from the hydrogen fusion in a thin shell.

[5]The turnoff point of the H-R diagram correspond to the position where the stars leave the MS due to the exhaustion of hydrogen fusion in the core.

PADOVA94 (Alongi et al., 1993; Bressan et al., 1993; Fagotto et al., 1994a,b; Girardi et al., 1996) for metallicity between 0.0001-0.1, from PADOVA2000 (Girardi et al., 2000) for metallicity in the range 0.0004-0.03 and complemented with the Geneva isochrones for solar metallicity (0.02, Schaller et al., 1992; Charbonnel et al., 1996, 1999). The TP-AGB and PAGB[6] phases are treated according to Vassiliadis & Wood (1993, 1994). Both the STELIB (Le Borgne et al., 2003) and BaSEL (Lastennet et al., 2002) stellar libraries can be used.

- PEGASE models (Fioc & Rocca-Volmerange, 1997, 1999) also use stellar tracks from the PADOVA group, and pseudo-tracks for the TP-AGB phase as proposed by Groenewegen & de Jong (1993). The PAGB models of Schoenberner (1983) are also connected to the tracks.

- STARBURST99 (Vázquez & Leitherer, 2005) based on the evolutionary tracks of PADOVA 1994 as well and incorporating TP-AGB stars in a similar manner to BC03. It was appositely developed for the study of young stellar populations. The advantage of this model is the simultaneous treatment of the chemical evolution of gas and the spectra evolution of the stellar content.

- GALEV (Anders & Fritze-v. Alvensleben, 2003) evolutionary synthesis code, developed to study the spectral and chemical evolution of galaxies, also makes use of PADOVA evolutionary tracks.

- SPEED models are described by Jimenez et al. (1995, 2004). They adopt a stellar evolution code based upon Eggleton (1971, 1972) with improvements concerning, in particular, the Horizontal Branch (HB)[7] and AGB phases. A distribution of values of mass-loss parameter μ (Reimers, 1975) is used to model the mass loss during the Red Giant Brach (RGB)[8] phase.

- The Bag of Stellar Tracks and Isochrones (BaSTI) models are based on the work of Pietrinferni et al. (2004) extended to cover TP-AGB stars by Cordier et al. (2007). Model spectra are constructed from the BaSTI isochrones as described by Percival et al. (2009).

- Maraston (2005) models are determined from an evolutionary synthesis code (Maraston, 1998) based upon the tracks of Cassisi et al. (1997a,b, 2000) for MS stars, and upon the fuel consumption theorem (Renzini & Buzzoni, 1986) for post-MS evolution.

[6]The post-AGB (PAGB) is a very brief phase of stellar evolution where the carbon-oxygen core is surrounded by helium with an outer shell of hydrogen. A thermal pulse occurs if the helium is ignited again and the star quickly returns to the AGB phase.

[7]The HB is a stage of stellar evolution where low mass stars burn helium in the core, while hydrogen fusion is in an external shell.

[8]The RGB is the phase of stellar evolution in which the hydrogen fusion in the core is terminated and the helium core starts to contract, while hydrogen starts to burn in shell.

For completeness, the main characteristics of the models listed above are summarized in Tab. from Carter et al. (2009).

Note that it is beyond the aims of this work to carry out a comparison between the various SSP models. Since in this Thesis we do not focus on the investigation of the physical properties of the stellar population of active galaxies, we use household SSP spectra from Bressan et al. (1998) constructed by using Padova (1994) evolutionary tracks (shown in Fig. 3.1, Bertelli et al., 1994) and a Salpeter IMF with mass in the interval between $0.15 \div 120$ $M_{\odot}$. The stellar atmospheres library used to build up the optical spectra ($\sim 3500 \div 7500$ Å) are those from Jacoby et al. (1984) with spectral resolution of 4.5 Å and those from Kurucz (1993) with a spectral resolution of $\sim$ 20 Å in the remaining part of the spectra ($90 \div 3500$ Å and $7500 \div 10^9$ Å). Note that these SSP include the handling of dust emission from AGB stellar envelopes (Bressan et al., 1998).

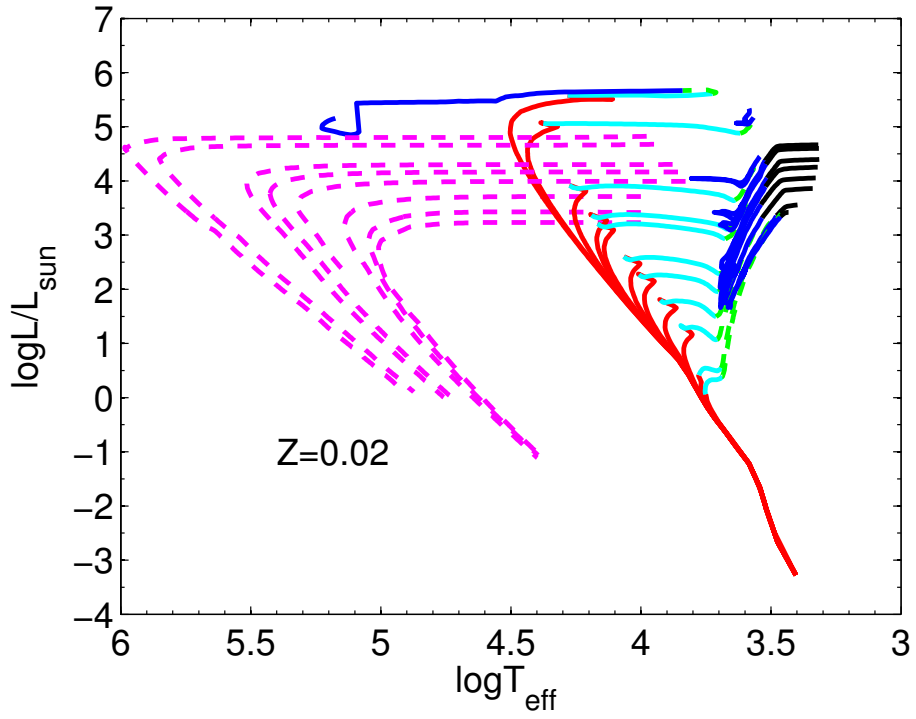

Figure 3.1: Isochrones in the theoretical H-R diagram constructed using the evolutionary tracks from Bertelli et al. (1994) for solar metallicity. Colors refer to different evolutionary phases: MS (red), beginning of RGB (light blue), RGB, (green), tip of RGB and beginning HB (dark blue), AGB (black), planetary nebula phase (dashed magenta). [Courtesy of L. Cassará].

3.2 The ISM around stars

To reproduce the entire SED of a galaxy the SSP spectra is not sufficient because the radiation from stars is absorbed and processed by the gas and dust that lies between the stars, in turn the ISM. This reprocessed radiation contributes to the observed continuum emission and special absorption and emission features, e.g. emission and absorptions lines associated with the presence of gas and PAH features due to the dust. When comparing SSP models with optical/UV observations the effect of the ISM on the observed SED needs to be taken into account. An appropriate treatment of the radiative transfer of the stellar light through the ISM and subsequent ISM emission are necessary to understand the full UV-to-IR SED of galaxies. While gas and dust are in reality intermingled within the ISM, in practice they are often treated as separate components because their absorption properties have a different wavelength dependence (Walcher et al., 2011).

3.2.1 Principle of the Radiative Transfer

The radiation coming from a source, being it a star, an AGN nucleus or a galaxy, passes through the surrounding medium before arriving at the observer. When dealing with a material emitting both thermal and scattered radiation, these two components are described by the absorption (α_ν) and the coherent isotropic scattering (σ_ν) coefficients, respectively. The radiative transfer equation will be then written as follows (see Rybicki & Lightman, 1979):

$$\frac{dI_\nu}{ds} = -\alpha_\nu(I_\nu - B_\nu) - \sigma_\nu(I_\nu - J_\nu) = -(\alpha_\nu + \sigma_\nu)\cdot(I_\nu - S_\nu), \tag{3.2}$$

where I_ν is the specific intensity, B_ν is the Planck function and J_ν is the isotropic intensity. S_ν is the *source function*, also written as:

$$S_\nu = \frac{\alpha_\nu B_\nu + \sigma_\nu J_\nu}{\alpha_\nu + \sigma_\nu}, \tag{3.3}$$

in turn a weighted, by their respective absorption coefficients, average of the two separate source functions. When scattering is present the solution of Eq. 3.2 needs to be partially solved with numerical techniques as it does not have an analytical solution. The detailed treatment of the solution of the radiative transfer problem depends on the exact setup of the dust grains, e.g. single or composite grain and the size of the cells in which the model space is divided. Moreover, various methods are invoked to solve one, two or three dimensional radiative transfer, ranging from analytic solutions to Monte Carlo simulations and ray-tracing techniques. An example of a numerical solution of the radiative transfer problem for AGN dusty torus is described in detail in Appendix C.1.

3.2.2 Interstellar Gas

The ISM can be in both atomic and molecular form. The molecular phase of the ISM has a low filling factor and it rarely contributes to the overall opacity of the galaxy. Consequently, it does not significantly contribute to the overall SED of a galaxy (Young & Scoville, 1991; Hollenbach & Tielens, 1997). For this reason the molecular gas is not considered very often when modelling galaxies. However, its contribution becomes important when dealing with ULIRGs or heavily obscured sources. It emits predominately at NIR wavelengths with the emission coming from photodissociation regions (Walcher et al., 2011).

The dominant source of opacity in the extreme-UV ($\geq$ 13.6eV) is the atomic gas. It is reprocessed into strong lines in optical, UV and IR. The contribution of this gas is particularly important for young actively star-forming galaxies. The hydrogen is ionized by photons, then locally absorbed and finally re-emitted in hydrogen recombination lines. To account for its contribution in the models, a full radiative transfer needs to be taken into account. Among the most widely used code for this we find CLOUDY (Ferland et al., 1998) and MappingsIII (Graves & Schiavon, 2008).

3.2.3 Interstellar Dust

Dust grains compose 1% of the ISM (Ferrière, 2001) lying between the stars. Their exact chemical composition, shape and distribution are currently under study, since the precise extinction varies from one line of sight to another (Williams, 2005). The main information that we have about interstellar grains comes from its interaction with the electromagnetic radiation, namely attenuation (absorption and scattering), polarization of the starlight and emission in the IR.

Direct evidence shows that interstellar dust is composed of:

- graphitic/amorphous carbon grains;
- amorphous silicate grains;
- PAH molecules (see sections 1.2.1 and 1.2.2) with emission bands in the MIR (Leger & Puget, 1984).

These three components are those most used when modelling dust emission. The first ingredient required is the grain size distribution which is usually represented with a power law and with a size range varying from model to model. The general expression for the distribution of the dust grains with spherical radius is:

$$dN(a) = 10^{A_i} a^q da, \tag{3.4}$$

where $dN(a)$ is the number of the grains with size between a and $a + da$, normalized at the number of atoms of hydrogen with the constant A_i (-25.16 for graphite and -25.11 for silicate Draine & Lee, 1984). The exponent q describes

the extinction curves and its value for our Galaxy is -3.5 (Mathis et al., 1977). A distribution with $q = -3.5$ is called MRN distribution, from Mathis, Rumpl & Nordsieck (1977). Theory (Jones et al., 1996) and observations (Mathis et al., 1977; Draine & Lee, 1984; Draine & Li, 2001) have shown that the average cross-section is dominated by small grains. Once the size distribution and the chemical composition of the grains have been fixed, this information is convolved with absorption, emission and scattering cross-sections.

Attenuation by dust

The presence of interstellar dust was first inferred from obscuration, or "extinction", of the starlight (Trumpler, 1930). This attenuation of the radiation emitted by stars is strongly wavelength dependent and, at the same time, it varies from one line of sight to another. As just mentioned the intrinsic flux of the source, $F_{\lambda intr}$, would be attenuated by dust, with a dependence on the wavelength, resulting in an observed flux:

$$F_{\lambda obs} = F_{\lambda intr} 10^{-0.4E(B-V)k(\lambda)}, \tag{3.5}$$

where E(B-V) is the color excess between the B and V band. This is a measure of the "reddening" of a source because of the wavelength dependence of attenuation, which is greater in the blue (short wavelengths) than in the red (longer wavelengths). $k(\lambda)$ is the extinction curve, commonly parametrized as:

$$k(\lambda) = \frac{A_\lambda}{E(B-V)}, \tag{3.6}$$

where $A_\lambda = 2.5 log(F_{\lambda obs}/F_{\lambda intr})$ is the wavelength dependent extinction. It is a measure of the total light absorbed or scattered out of the line-of-sight by dust, either bolometrically or in a single band.

The dust extinction phenomena of a galaxy, referred to as "attenuation", is the result of the interplay between the geometry and the different optical depth characterizing the different regions of a galaxy. It applies to the whole stars and not to the single stars. A measure of the slope of the extinction curve is usually given with a dimensionless quantity:

$$R_V = \frac{A_V}{E(B-V)}, \tag{3.7}$$

which varies from line of sight to line of sight, from values as low as 2.1 (Welty & Fowler, 1992) to value as large as 5.6-5.8 (Cardelli et al., 1989). The attenuation depends on the nature and the geometrical distribution of the dust grains. Attenuation laws have been obtained for the Milky Way, with R_V=3.1 (Savage & Mathis, 1979; Cardelli et al., 1989), and for the Small and Large Magellanic Clouds (SMC and LMC, respectively). Calzetti et al. (1994) derived an empirical curve for starburst galaxies, with R_V=4.5. For purposes of illustration Fig. 3.2 shows the

extinction curve for different attenuation laws. The extinction law of our galaxy and LMC have been found to be less grey than that found by Calzetti et al. (1994) for starburst galaxies, which can be fitted with a simple polynomial as a function of $1/\lambda$.

Note that these extinction curves do not account for the differential geometries and star formation histories within and between galaxies which would result in variation of the optical depth along the line of sight. An improvement over a simple attenuation law has beed made by Silva et al. (1998) and Charlot & Fall (2000) accounting for two sources of attenuation: a "diffuse" dust accounted for as in Eq. 3.5 and an additional "birth cloud" attenuation in which young stars are embedded. In these models, the light of young stars is higher than that of longer-lived stars.

However, all the previous still do not account for differential dust distribution, stellar geometries (such as bulges and discs) and the clumpiness of the ISM. Moreover, light is not only scattered out from the line of sight but it is also scattered into it. This anisotropic light scattering by dust is also not considered (Walcher et al., 2011). All of this need for a proper radiative transfer to be taken into account with iterative methods and Monte Carlo methods (Baes et al., 2010a). In such approaches the emitted and scattered light is broken up into various components, the radiative transfer equation is solved for each one of these and the solution from the previous components is used for the subsequent until the convergence of the equation (see Kylafis & Bahcall, 1987; Xilouris et al., 1998, 1999; Tuffs et al., 2004, e.g.). A simple extinction curve is still the most commonly used way to account for effects of dust on the optical/UV SED because radiative transfer codes require the introduction of several free parameters. In the case of unresolved galaxies with only-broad band photometry available, such parameters would be difficult to determine (Walcher et al., 2011).

Note that the silicate dust grains also contribute to the absorption with two characteristic features at 9.7 and 18 μm. These features are observed in sources with high optical depth and, in general, in galaxies hosting a strong nuclear source (i.e. AGN, see Section 5.0.1). When modelling galaxies, this absorption is usually modelled with a simple absorbing screen, but there are models, e.g. those of the emission torus of AGN (see Section 3.4), which actually account for a self-consistent radiative transfer.

Emission by dust

As already mentioned dust can give rise to some features in the MIR associated with PAH and silicate grains. But the presence of dust can also be observed as a continuum emission, associated with reprocessed optical/UV radiation, at IR and sub-mm wavelengths. The bulk of the contribution of the cold dust emission due to starburst heating is expected to be in the FIR and sub-mm regimes. At such wavelengths the cold dust emission can be modelled in a simplistic way with a

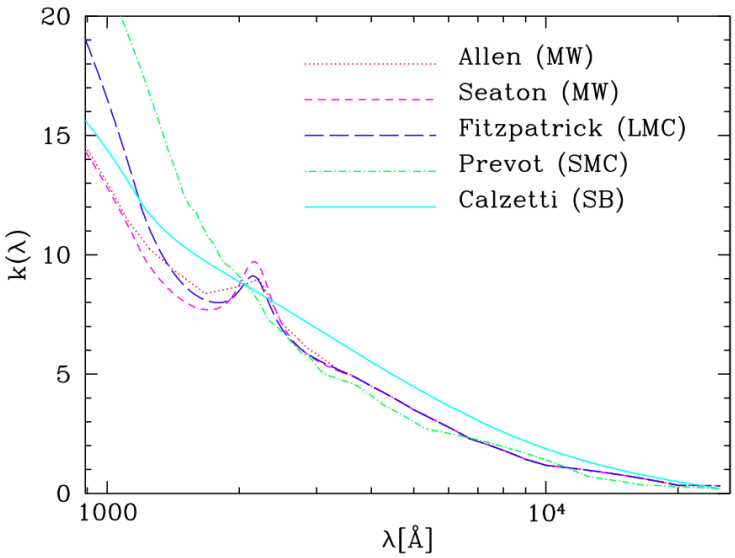

Figure 3.2: Extinction curve $k(\lambda)$ for different attenuation laws (from Hyperz's manual, http://webast.ast.obs-mip.fr/hyperz/).

black body emission or a emissivity modified black body under the assumption of thermal equilibrium.

$$S_\nu(\beta, T) = \frac{M_c k_0}{d^2} \left(\frac{\nu}{\nu_0}\right)^\beta B_\nu(T), \tag{3.8}$$

where M_c is the mass of the (cold) dust, k_0 is the total mass absorption coefficient evaluated at a fixed frequency ν_0, d is the distance to the object, β is the dust emissivity index, and $B_\nu(T)$ is the Planck function. β is 0 for a black body and usually spans the values between 1 and 2 for an emissivity modified black body. β is expected to be a function of grain size, composition and temperature.

To model the MIR emission a simple black body is not enough because, at such wavelengths, the grains have smaller surfaces with a consequent reduction and randomization of the photon incidence, and as a result are statistically less-well represented by a black body (Draine, 2003). There is the need of a model in which the dust has a range of temperatures parametrized with the strength of the radiation field heating it. One possibility is to apply Monte Carlo techniques or a steady-state distribution to solve the radiative transfer equation or to solve, with a more simplistic approach, the steady-state distribution of temperatures for given radiation field, dust size and composition (e.g. Desert et al., 1990; Draine et al., 2007). PAH features, which also contribute to the emission at MIR wavelengths, are generally incorporated in starburst emission models. One way to do this is to assume a template form for the MIR emission (e.g. Desert et al., 1990), another is to model the physical processes in a way analogous to the grains (e.g. Draine

et al., 2007).

Realistic FIR models are, then, those taking into account the various range of temperatures. Once the radiation field and the dust properties have been chosen, the following step, to obtain the total FIR emission of a model is to calculate the emission from each grain and then to integrate over all the dust grains. In all these models, the temperature distribution depends on the dust-gas geometry of the ISM. This information can not be obtained by optical/UV data alone. For this reason, empirical templates of FIR emission of galaxy are often used to reproduce the galaxy SEDs. These templates are, in general, realized taking the aforementioned dust models and matching them with observations of sample of galaxies. The use of such empirical templates (Chary & Elbaz, 2001; Dale & Helou, 2002; Lagache et al., 2004; Rieke et al., 2009) allow for investigation of the galaxy-wide properties.

3.3 Combining Stellar and ISM Emission

When constructed detailed models, the fact that the energy emitted in the optical/UV is re-emitted in the MIR and FIR needs to be taken into account. This requires some assumptions, varying from model to model, for the dust and the radiation field. Over the years, various models have been developed starting from simple representation and arriving to the more complex one.

Leung (1975) was the first to realize a model with a complete solution of the radiative transfer for an optically thick dust clouds using a very detailed grain properties and solving the grain temperature by assuming radiative balance. The interaction between gas and dust has been introduced by Yorke (1977) which models the dynamical evolution of an HII region. A numerical solution of the full radiative transfer equation of a cloud surrounding a star was carried out by Rowan-Robinson (1980). This solution shows that the inner edge of the dust cloud presents bright emission in the MIR. Moreover, this model shows the net emitted spectra to be no longer a black body but to be characterized by absorption bands at wavelengths typical of the dust emission features (Rowan-Robinson & Harris, 1982). In subsequent years, mounting radiative transfer models for starburst galaxies have been developed. For example,Efstathiou & Rowan-Robinson (1991) resolve the radiative transfer problem in an axially symmetric cloud, while Krugel & Siebenmorgen (1994) and Silva et al. (1998) (see later in this section for more details) model star-forming regions through spherically symmetric radiative transfer. A more realistic model in this context is that of Efstathiou et al. (2000) in which the authors follow the evolution of a spherically symmetric HII region within a dense molecular cloud. Other models are those of Takagi et al. (2003), Dopita et al. (2005, 2006b,a) and Groves et al. (2008). Moreover, Siebenmorgen & Krügel (2007) provide a large library of starburst parametrized models.

Nowadays, sophisticated and self-consistent UV to FIR models can be found in the literature:

- STARDUST99 (Devriendt et al., 1999) in which the optical depth of galaxies is computed using SSP models, including simple galaxy chemical evolution. The simple geometrical distribution is represented with an oblate ellipsoid in which dust and sources are homogeneously mixed. The total mass (gas and dust) is kept constant. The SSP models used are constructed using the Geneva tracks and the theoretical spectra of Kurucz (1993).

- MAGPHYS (Multi-wavelength Analysis of Galaxy Physical Properties, da Cunha et al., 2008)[9] in which the SED of the galaxy is constructed computing the absorption of starlight using the aforementioned two-field model of Charlot & Fall (2000). In such model the ISM comprises a diffuse ISM and dust in stellar birth clouds (star-forming regions). The dust in the stellar birth clouds is a sum of three components: PAH molecules, hot grains with temperature T in the range between 130-250 K characterizing the continuum emission in the MIR and a component of grains in thermal equilibrium with a range of T between 30-60 K. The weight of these three components is kept fixed as to reproduce the diffuse cirrus emission of the Milky Way. Further, da Cunha et al. (2008) include also an additional component of cold dust grains (T between 15-25 K) in thermal equilibrium. SSP models of BC03 are used to model the stellar emission. The code then computes the IR emission due to the luminosity absorbed and reprocessed by the ISM.

- CIGALE[10] was developed to reproduce the UV-to-IR SEDs of galaxies. The models created by the code consist of dust-attenuated complex stellar population models, IR dust emission models and spectral line templates. For the stellar components CIGALE allows both PEGASE (Fioc & Rocca-Volmerange, 1997) and Maraston (2005) SSP models to be used. Several dust emission models and templates can be used, such as Chary & Elbaz (2001); Dale & Helou (2002); Draine et al. (2007); Siebenmorgen & Krügel (2007). Dust attenuation and dust emission are related and can be studied simultaneously.

- Efstathiou et al. (2000) models are represented with optically thick giant molecular clouds surrounding recently formed stars. Evolution of both clouds and stellar populations (using SSP models of BC03) are considered. The radiative transfer problem is solved taking into account the effects of both multiple scattering and transiently heated grains/PAHs.

- Siebenmorgen & Krügel (2007) provided a library of ∼7000 SEDs for the nuclei of starburst and ULIRGs. The radiative transfer problem is solved in a spherical symmetric geometry in which stellar clusters are distributed inside a ISM with standard (that is of the Milky Way) dust properties. Two stellar populations are considered, namely old bulge stars and OB stars in dense

[9] http://www.iap.fr/magphys/magphys/MAGPHYS.html
[10] http://cigale.oamp.fr

clouds. The luminosity of the first are distributed continuously over the volume, while the second are embedded in compact clouds contributing to the MIR emission.

- Groves et al. (2008) further developed the work from Dopita et al. (2005) and Dopita et al. (2006b,a). The emission from star-forming regions and the solution of the radiative transfer problem throughout the surrounding gas and dust are calculated simultaneously in a self-consistent way. Empirically calibrated models are used for the evolution of the HII regions over time. This code is very well suited to model starburst galaxies, whose SEDs are dominated by emission coming from young heavily obscured stars, but not for non-star-forming galaxies.

- GRASIL (Silva et al., 1998)[11] is a code in which the spectral evolution of stellar systems is computed taking into account the effects of dust and chemical evolution. The geometry is a cloud-disc-bulge and by changing the ratio between the disc and the bulge is possible to model galaxies from spiral to elliptical. GRASIL accounts for differential extinction suffered by stars of different ages.

Another approach to model the UV-to-IR SEDs of galaxies is to use Monte Carlo radiative transfer methods. These methods include SUNRISE (Jonsson, 2006; Jonsson et al., 2010), DIRTY (Gordon et al., 2001; Misselt et al., 2001), TRADING (Bianchi et al., 1996, 2000; Bianchi, 2008), SKIRT (Baes et al., 2003) and RADISHE (Chakrabarti & Whitney, 2009). Compared to the previous these Monte-Carlo radiative transfer codes allow for complex geometry accounting for spiral arms, dust lanes, bulges and clumpy ISM.

3.4 Models of IR Emission from AGN

All the aforementioned models and codes were developed to reproduce the SED of galaxies, in particular starburst galaxies. None of them account for the presence of an AGN which emission needs to be taken into account while fitting UV-to-IR AGN SEDs.

The various ingredients and steps required to obtain an AGN torus emission model are summarized as follow:

- The choice of the geometry for the toroidal structure surrounding the central source of the AGN. Such structure represents the model space which is usually enclosed between an inner, R_{in}, and an outer, R_{out}, radius. R_{in} depends on the sublimation temperature of the grains and obeys to a scaling law with the luminosity, e.g. $R_{in} \propto L^{1/2}$ (Barvainis, 1987; Suganuma et al., 2006).

[11] http://adlibitum.oat.ts.astro.it/silva/grasil/grasil.html

- Other assumptions concern the dust composition and distribution. As already mentioned, the radial dust grains distribution is usually represented with a power law (see Eq. 3.4). In addition, since the AGN unification scheme require the torus to be geometrically thick, also a vertical distribution need to be considered. This last assumes various shapes in literature, from an homogeneous one with a cut-off height or scale-height to a gaussian or power law distribution. Moreover, appropriate absorption and emission coefficients need to be associated with the dust grains chosen, which are usually only graphite and silicate grains.

- The values of the parameters to explore need to be selected in order to create an *ad hoc* grid of models.

- The last assumptions concerns the luminosity of the primary source, usually represented as a set of power laws (e.g. see Eqs. 3.11 and 3.14).

- Finally, the last step to obtain the final SED models is to solve the radiative transfer of the emission coming from the central source through the dusty torus.

As the state-of-art of UV-to-IR models of galaxies, also AGN models that have been developed over the years are well advanced. In the next section I provide a brief historical review of the of torus models, followed by a more detailed description of the models used in the next chapters.

3.4.1 Brief History of Torus Models: from Smooth to Clumpy

Statements for the interplay between optical/UV emission and dust in AGN arise with Rees et al. (1969) which suggested that the observed IR radiation, between 2.2-22 μm, coming from Seyfert galaxies may be energy originated from an intense optical/UV source at the center of the galactic nucleus and reprocessed by dust grains. The discovery of an excess in the IR continuum of Sy2 with respect to Sy1 by Rowan-Robinson (1977) confirmed the presence of dust around the central region (see also Section 1.1.4). The need for a source contributing to the heating of the dust, and then responsible for its thermal emission, was pointed out also by Neugebauer et al. (1979) when explaining the excess at $\sim$3 μm observed in some quasars. Barvainis (1987) was the first to demonstrate that was possible to reproduce the IR emission of quasars in terms of thermal radiation from dust heated by a primary optical/UV continuum source. This model was able to explain the rise of the bump at $\sim$ 2 μm, wavelength corresponding to a black body emission due to graphite grains at their sublimation temperature ($\sim$ 1550 K).

The designation "obscuring torus", from Krolik & Begelman (1986), reflects exactly the angle-dependent (proposed for the first time by Rowan-Robinson, 1977), geometrically and optically-thick obscuring shape needed to explain the difference

between type 1 and 2 AGN. Over the past decades different torus models with increasing in complexity and using different approaches for the dust distribution have been developed.

Since simpler and faster to compute, especially in terms of CPU use, smooth models were the first ones to appear in the literature. Pier & Krolik (1992) were the first to suggest an emission model from an annular ring of dust. They assumed a common extinction curve for all of the grains, an MRN distribution function of grain composition and sizes and they do not account for light scattering, they solved the radiative transfer problem with the Böhm-Vitense method described in Mihalas et al. (1978). The aim of their work was to explore the main properties of IR emission in AGN.

Granato & Danese (1994) considered a so-called *flared disc*, with dust grain density that was allowed to vary both along the radial and the vertical coordinates and they solved the radiative transfer equation by means of the Λ-*iteration* method (see Appendix C.1) with both graphite and silicate grains, taking into account also radiation scattering. In order to match with the observations, they found the need to add silicate grains depletion due to shocks to weaken the silicate emission at $\sim$ 9.7 μm.

Stenholm (1994) studied a configuration given by an optically thick silicate disc. They did not find the need of silicate grain depletion or the choice of an alternative grain size distribution to weaken the silicate feature around $\sim$ 9.7 μm.

Efstathiou & Rowan-Robinson (1995) analysed three different geometrical configurations for the torus, a flared as well as a tapered disc and an anisotropic sphere, and found that a tapered disc (i.e. a disc whose height increases along with distance from the centre but flattens at a given height in the outer parts) with an opening angle of 45° and with a density distribution proportionally decreasing with the distance from the center r (following a r^{-1} behavior) to be the most successful in satisfying the observational constraints.

Manske & Henning (1998) reproduced the AGN SEDs with thick discs characterized by opening angle of 90° and density distribution following the r^{-1} behavior. They also did not find the need of a silicate depletion.

van Bemmel & Dullemond (2003) suggested that the obscuring torus should be in a conical or flaring shape. Their most reliable models predicted constant density over the whole torus and large values for the inner radius (R_{in} $\sim$10 pc).

The dusty torus of Fritz et al. (2006) is represented by two concentric spheres (see Fig. 3.3) with the polar cones removed and delimited respectively by a inner and outer radius. The spatial distribution could either be constant or vary both

along the radial and vertical coordinate.

Schartmann et al. (2005) presented radiative transfer calculations for an hydrostatic model of a dusty torus using the so-called Turbulent Torus Model, introduced by Camenzind (1995) and, for the sake of simplicity, they treated the torus as a continuous medium in which the interaction between the clouds were neglected.

Smooth models faced two main problems when trying to match the observations. First, many of the model SEDs could not fit the MIR and FIR parts of the observed SEDs because they were too narrow (Dullemond & van Bemmel, 2005). Second, the 9.7 μm silicate feature (see Section 5.1.1) was often observed in absorption in type 2 sources, but had barely been seen in emission in type 1 sources (Dullemond & van Bemmel, 2005), as predicted by the models, until recent observations with *Spitzer* IRS (Siebenmorgen et al., 2005; Sturm et al., 2005; Hao et al., 2005; Buchanan et al., 2006; Shi et al., 2006).

With the aim to solve these problems, Nenkova et al. (2002) developed a torus model in which dust was distributed in clumps. They solved the radiative transfer for each clump by means of the radiative code DUSTY (Nenkova et al., 1999) and then computed the final emission as the sum of clumps' emission calculated using a ray-tracing approach. They suggested that the behaviour of the silicate feature around 9.7 μm could be explained with the dust being contained in approximately five to ten clouds along the radial coordinate through the torus.

Rowan-Robinson (1995) made the first attempts to model a clumpy torus. Their approach was based on the dust-shell approach by cutting "hole" into the spheres. Such shells were geometrically thin but optically thick. The resulting SEDs showed a range of temperature narrower than that of smooth models and a very weak silicate feature at 9.7 μm.

Hönig et al. (2006) modelled NIR and MIR emission of 3-dimensional clumpy tori using Monte Carlo simulations. The properties of the individual clouds and their distribution within the torus are determined from a theoretical approach of self-graviting clouds close to the shear limit in a gravitational potential.

Schartmann et al. (2008) developed a new three-dimensional model in which the AGN tori are modelled as a wedge-shaped disc. Dusty clouds are randomly distributed throughout the volume occupied by the torus with a dust density distribution of the corresponding continuos model of Schartmann et al. (2005). To realize the SED and the surface brightness at various wavelengths they used radiative transfer calculation as well as a three-dimensional Monte Carlo radiative transfer code MC3D. They analyzed the difference between their continuos and clumpy models in terms of the temperature and the surface brightness distribu-

tions, interferometric visibilities and spectral energy distributions. They directly compare them also to observations concluding that clumpy models posses more fine structure to explain MIR interferometric observations performed with MIDI (Jaffe et al., 2004; Tristram et al., 2007).

More recently, Stalevski et al. (2012), using a three-dimensional radiative transfer code SKIRT (Baes et al., 2011), realized a bi-phase model in which the clumps are embedded in a continuos dust medium. Exploring the implications of clumpy and continuous dust distributions on the IR SEDs they found globally no significant dissimilarities in their full set of models.

Smooth models of Fritz et al. (2006), here after F06, and clumpy models of Nenkova et al. (2008a), here after N08, are two of the most popular models in the literature. They both succeed in reproducing different parts of the observed AGN SEDs, giving drawing of a conclusion on the still open dust distribution issue a hard time. In Section 5.1 we carry out a thorough *model-to-model* comparison, presented in Feltre et al. (2012), between two restricted grids of the aforementioned models in which the theoretical SEDs shapes provided by the models have been investigated looking for potential diagnostic of dust distribution. Then, as an extension of this work, in Section 5.2 we compare the physical parameters inferred when reproducing both the broad band features and the more detailed MIR spectral emission of AGN. Since along the next chapters we make an extensive use of the two aforementioned models, the next sections 3.4.2 and 3.4.3 provide a more detailed description of the two.

3.4.2 Smooth Dust Distribution of Fritz et al. 2006

The smooth models grid consists in a slightly updated grid of the original F06 models. The original models, together with the revised version, are the most used smooth models in the literature to date (see Rodighiero et al., 2007; Berta et al., 2007; Hatziminaoglou et al., 2008, 2009, 2010; Vignali et al., 2009; Agol et al., 2009; Pozzi et al., 2010; Natale et al., 2010; Pozzi et al., 2012; Feltre et al., 2012, 2013). What follows is a short summary of the models, but we refer to the original paper for a more detailed description.

F06 adopted a mixture of graphite (53%) and silicate (47%) grains with a MRN (Mathis et al., 1977) distribution for the grain sizes, which closely resembles that of the Milky Way. Absorption and scattering coefficients were taken from Laor & Draine (1993). The adopted geometry consists in a flared disc (see Fig. 3.3), whose sizes were defined by the outer and inner radii and by the full opening angle of the torus. The inner radius is calculated following the formula of Barvainis (1987):

$$\mathrm{R_{in}} \simeq 1.3 \times \left(\frac{\mathrm{L}}{10^{46}\mathrm{erg\ s^{-1}}}\right)^{1/2} \left(\frac{1500K}{T_{\mathrm{sub}}}\right)^{2.8} \qquad [pc] \tag{3.9}$$

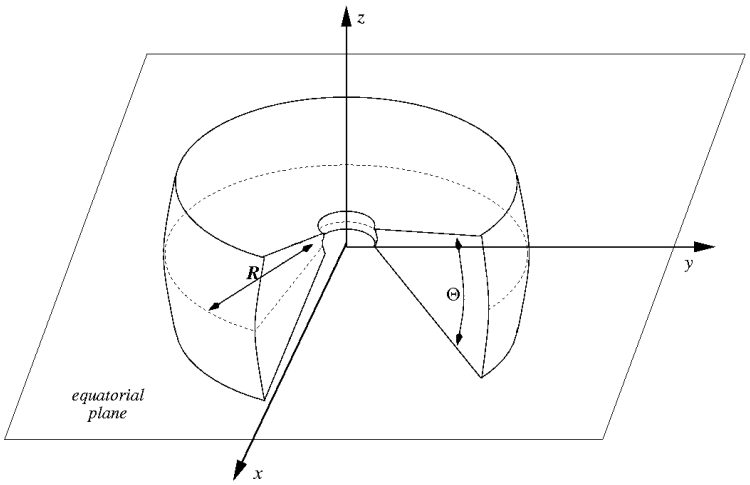

Figure 3.3: Geometry of the AGN torus model of F06. R indicates the radial size (R_{out} - R_{in} and Θ is the torus full opening angle.

where L is the bolometric optical/UV luminosity emitted by the central source and T_{sub} is the sublimation temperature of the dust grain. While the inner radius was naturally constrained by the sublimation temperature of graphite grains (1500K), both the outer radius and the torus flaring were parameters of the model. Two other parameters tune the dust density values within the torus, and allow for a density gradient along the radial and the polar coordinates (θ):

$$\rho\,(r,\theta) = \rho_0 \cdot r^{-q} \cdot e^{-\gamma \times |\cos(\theta)|} \tag{3.10}$$

The central source is assumed to be point-like and isotropic. Its spectral energy distribution is defined by means of a composition of power laws [i.e. $L(\lambda) \propto \lambda^i$] with different values for the spectral index i as a function of the spectral range. The original grid of F06 adopted values commonly found in the literature (e.g Granato & Danese, 1994; Nenkova et al., 2002). For this work we updated this component using the values described in Schartmann et al. (2005), namely:

$$L(\lambda) \propto \begin{cases} \lambda^{1} & \text{if} \quad 0.001 < \lambda < 0.03 \quad [\mu m] \\ \lambda^{-0.2} & \text{if} \quad 0.03 < \lambda < 0.125 \quad [\mu m] \\ \lambda^{-1.5} & \text{if} \quad 0.125 < \lambda < 10.0 \quad [\mu m] \\ \lambda^{-4} & \text{if} \quad \lambda > 10.0 \quad [\mu m]. \end{cases} \tag{3.11}$$

The radiative transfer problem is solved numerically, by means of the $\Lambda-$iteration technique (see Appendix C.1 for a detailed description), and includes also the scattering component. Furthermore, since the dust mixture includes both graphite and silicate grains, that have different sublimation temperatures ($\sim$ 1500 and $\sim$ 1000 K for graphite and silicate, respectively), the silicate grains sublimation radius is displaced further away from the central source with respect to that of graphite.

Hence, a new grid of $\sim$ 2400 models with a better sampling of the space parameters and a better wavelength resolution was obtained. The following discrete values have been explored:

- the torus full opening angle, Θ: 60°, 100° and 140°;

- the parameters of the dust distribution (see Eq. 3.10), namely q : 0.00, 0.25, 0.50, 0.75 and 1.0; and γ: 0.0, 2.0, 4.0 and 6.0;

- the equatorial optical depth at 9.7 μm, $\tau_{eq}(9.7)$: 0.1, 0.3, 0.6, 1.0, 2.0, 3.0, 6.0 and 10.0;

- the outer-to-inner radius ratio, Y= R_{out}/R_{in}: 10, 30, 60, 100 and 150.

A sixth parameter of the F06 models is the inclination. Indeed, the global model SEDs were computed at different angles of the line of sight with respect to the torus equatorial plane in order to account for both type 1 and type 2 object emission from 0° to 90°, in steps of 10°.

The dust configuration of F06 models (see Eq. 3.10), with the number of dust grains that decreases as the altitude on the equatorial plane increases, can be considered to mimic the "tapered torus" considered by Efstathiou & Rowan-Robinson (1995). Indeed, the bulk of the emission of F06 models with moderate values of the equatorial optical depth comes from those volume elements that are closer to the equatorial plane. As containing a smaller number of grains, the other elements of the geometrical grid providing a smaller contribution to the total emission. F06 found the models of Efstathiou & Rowan-Robinson (1995) to be those most resembling their modes.

As already mentioned, one of the main problems related to the AGN unified scheme was the observed absence of the emission of the silicate feature at 9.7 μm in type 1 AGN and the significant silicate absorption observed in type 2 AGN. Granato & Danese (1994) argued that, in order to reproduce the observations, a silicate depletion could be needed. In fact, they found that a dust mixture mainly composed by graphite grains is consistent with practically no silicate emission in type 1 AGN and with a moderate absorption at 9.7 μm in type 2. The interpretation was that the radiation pressure would induced shocks, with speeds of the order of $\sim$ 60 km/s, with a consequent destruction of the silicate grains in the innermost region of the torus. F06 found no need for such shock-depletion. In fact, F06 models allow for a silicate depletion due to sublimation of grains by the radiation field in the region of the torus closer to the primary source. Indeed, F06 takes into account the difference in the sublimation temperatures of graphite and silicate and the consequent discontinuity in the chemical composition of dust along the radial coordinate. In particular, F06 found models with a non-constant density profiles to display less pronounced silicate feature both in emission and in absorption.

Moreover, while trying to reproduce the main observed features of AGN, Manske & Henning (1998) found that the only way was to assume a non-isotropic central source. In particular, they argued that in such way their models were able to reproduce the silicate feature in type 1 and 2 objects. F06 did not find the need of such non-isotropic primary source. This can be due to the common sublimation temperature both for graphite and silicate grains (T∼1500K) assumed by Manske & Henning (1998). This choice not only leads for a stronger contribution from silicates due to their higher temperature, but also do not account for the fact that the innermost region of the torus should be free of silicate grains because of their lower sublimation temperature with respect to graphite grains.

3.4.3 Clumpy Dust Distribution of Nenkova et al. 2008

Nenkova et al. (2002) approached the issue of IR dust emission assuming that the dust is concentrated in clumps that are in turn distributed within a torus (see Fig. 3.4). They also assume a grain composition of 53% of graphite and 47% of silicate with a MRN law for grain size distribution, with the optical constants for both graphite and silicate from Draine (2003). In a later realisation Nenkova et al. (2008a,b), hereafter N08, further developed their clumpy models using as optical constants for silicate those from Ossenkopf et al. (1992) "cold" dust. The inner radius is set by the dust sublimation temperature, $T_{\rm sub}$:

$$\mathrm{R_{in}} \simeq 0.4 \times \left(\frac{\mathrm{L}}{10^{45}\mathrm{erg\ s^{-1}}}\right)^{1/2} \left(\frac{1500K}{T_{\rm sub}}\right)^{2.6} \qquad [pc], \tag{3.12}$$

similar to the value provided by the analogous equation in Barvainis (1987). In this case $\mathrm{R_{in}}$ is determined from the temperature of the illuminated face of the innermost optically thick cloud. The torus extends radially out to $\mathrm{R_{out}} = \mathrm{YR_{in}}$, with Y being one of the model parameters.

N08 assume a probabilistic approach for the distribution of the clumps. Assuming that the spatial distribution of the dusty clumps is a gaussian, the total number of clouds that can be found along a given direction at an angle β ($= 90^\circ - \theta$ using F06 notation) from the equator is provided by:

$$\mathcal{N}_T(\beta) = \mathcal{N}_0 \mathrm{e}^{(-\beta^2/\sigma^2)}, \tag{3.13}$$

where σ is the width of a gaussian angular distribution of the clouds and $\mathcal{N}_0$ is the average number of clouds along radial equatorial rays, where the clouds follow a Poisson distribution.

The number of clouds per unit length, $N_c(r, \beta)$, as a function of the angle β and of the radial distance r, is a separable function distribution with power law radial behaviour $r^{-\mathrm{q}}$ so that:

$$N_c(r, \beta) = C \frac{\mathcal{N}_T(\beta)}{\mathrm{R_{in}}} \left(\frac{\mathrm{R_{in}}}{r}\right)^q, \tag{3.14}$$

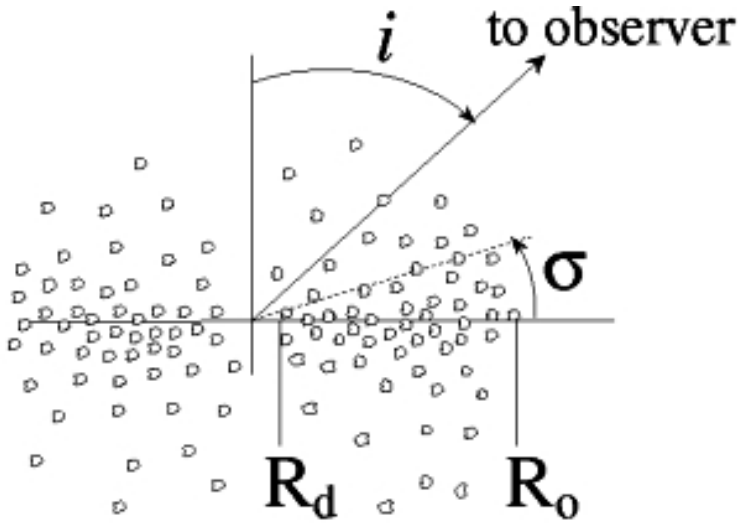

Figure 3.4: Schematic illustration of the AGN torus models of N08 (from Nenkova et al., 2008a). R_d and R_o are the R_{in} and R_{out} of this Thesis, respectively. i is the viewing angle measured from the torus axis and σ id the width of a Gaussian angular distribution of the clouds.

where $C = (\int_1^Y dy/y^q)^{-1}$ with $y = r/R_{in}$ is a dimensionless constant (for a given Y and σ) ensuring the normalization $\mathcal{N}_T(\beta) = \int N_c(r,\beta)dr$. For the primary source Nenkova et al. (2008a) employed a piecewise power law distribution following Rowan-Robinson (1995):

$$L(\lambda) \propto \begin{cases} \lambda^{0.2} & \text{if} \quad \lambda \leq 0.01 \quad [\mu m] \\ \lambda^{-1} & \text{if} \quad 0.01 < \lambda \leq 0.1 \quad [\mu m] \\ \lambda^{-1.5} & \text{if} \quad 0.1 < \lambda \leq 1 \quad [\mu m] \\ \lambda^{-4} & \text{if} \quad \lambda > 1 \quad [\mu m] \end{cases} \tag{3.15}$$

The total SED of such a configuration of clouds, is obtained by summing the emission of the clouds illuminated both directly and indirectly, and that of the primary source. In clumpy models the observed torus radiation is determined not only by the emission from individual clouds but it is also shaped by the fact that there is a non-zero probability that photons emitted from the AGN can freely escape without any interaction with the dusty medium. This probability, P_{esc}, for an overall number of clouds $\mathcal{N}$ along a path, are related to the optical depth: $P_{esc} \simeq e^{(-\mathcal{N}\tau_\lambda)}$ for wavelengths at which the optical depth of a single clouds obeys $\tau_\lambda < 1$, and $P_{esc} \simeq e^{-\mathcal{N}}$ where $\tau_\lambda > 1$ (Nenkova et al., 2008b).

The main parameters of the model and the values that are commonly explored can be summarised as follows:

- the width of a Gaussian angular distribution of the clouds, σ ranging from 15° to 70° in step of 5° determining the spatial distribution;

- the outer-to-inner radius ratio of the cloud distribution, Y: 5, 10, 20, 30, 40, 50, 60, 70, 80, 90, 100, 150, and 200;

- the average number of clouds along a given direction within the equatorial plane, $\mathcal{N}_0$, taking any integer value between 1 and 15;

- the power law index determining the radial distribution of clouds, q: 0.0, 1.0, 2.0 and 3.0;

- the optical depth of a single cloud τ_V =5.0, 10.0, 20.0, 30.0, 40.0, 60.0, 80.0, 100.0 and 150.0, calculated in the V band at 0.55 μm;

Again, the SEDs are created for different viewing directions with respect to the equatorial plane. The parameter representing the inclination spans the range from $\beta = 0^\circ$ to $\beta = 90^\circ$, in steps of 10°.

Two are the main difference among the various clumpy models. One concerns the range of parameter space for optical depth and volume filling factor occupied by various clumpy models. Indeed, he degree of clumpiness depends on the specific approach used. A probabilist approach, such as of N08 requires low volume filling factor, implying small and dense clouds, while Monte Carlo simulations favour higher volume filling factors with larger clouds (Hoenig, 2013). Another difference among clumpy models is the treatment of the surface of the clouds directly heated by the AGN. In the literature we find two distinct approach: one in which the cloud has a steep density gradient (e.g. Nenkova et al., 2008a,b; Stalevski et al., 2012), with the hot emission from optically thick clouds becoming a black body in the NIR and MIR, and another in which the gradient is smooth (Dullemond & van Bemmel, 2005; Hönig et al., 2006; Schartmann et al., 2008), corresponding to an emission which is optically thin in the IR and independent on the total density of the clouds.

Name	Reference	IMF	Spectral Library (number)	Range of Z (number)	Range of Ages	Availability of models
BC03	Bruzual & Charlot (2003)	Chabrier (2003)	STELIB	0.0001-0.05 (6)	0.0001-20 (221)	http://www.cida.ve/bruzual/bc2003
PEGASE-2.0	Fioc & Rocca-Volmerange (1997, 1999)	Kroupa (2001)	BaSeL2.0	0.0001-0.1 (7)	0.5-13 (25)	http://www2.iap.fr/users/fioc/PEGASE.html
STARBURST99	Vázquez & Leitherer (2005)	Kroupa (2001)	BaSeL2.0	0.0004-0.05 (5)	0.00001-15 (100)	http://www.stsci.edu/science/starburst99
GALEV	Anders & Fritze-v. Alvensleben (2003)	Kroupa (2001)	BaSeL2.0	0.0004-0.05 (5)	0.004-16 (51)	http://www.galev.org
SPEED	Jimenez et al. (1995, 2004)	Kroupa (2001)	Kurucz (1993)	0.001-0.05 (4)	0.001-14 (40)	http://www.ice.csic.es/personal/jimenez/speed/
BaSTI	Pietrinferni et al. (2004)	Kroupa (2001)	see Percival et al. (2009)	0.0003-0.04 (10)	0.03-15 (55)	http://albione.oa-teramo.inaf.it/
Maraston	Maraston (2005)	Kroupa (2001)	BaSeL2.0	0.0001-0.07 (6)	0.001-15 (40)	http://www.dsg.port.ac.uk/maraston c/

Table 3.1: Summary of the key parameters of some stellar population synthesis models, from (Carter et al., 2009).

4 | An *ad hoc* SED fitting tool

The analysis of the spectral energy distribution of galaxies (SEDs) allow the investigation of the different physical processes taking place during the life time of those same galaxies. As already seen in the previous chapter, when considering multi wavelength data, more than one component of emission needs to be taken into account. In particular, in the case of AGN, the AGN torus emission alone is not enough to account for the emission in all the electromagnetic spectra. It is then possible to get a complete view of the physical mechanisms taking place in active galaxies and their hosts. With this in mind, this chapter aims to provide a picture of the operating principles of the spectral energy distribution (SED) fitting method we further developed to reproduce the galaxies SED using a multi-component approach. Since the very first version of this code the goal has been to produce a tool as generic as possible, in order to be able to deal with different data sets as well as to use the widest spectral interval possible. This latter is actually between 10^{-2} and 10^{3} μm (restframe) and can be eventually extended through an extrapolation up to the X-ray range (2-10 KeV). At the moment the code accounts for three emission components:

- **stellar emission** which contributes mostly between ~ 0.3 μm and ~ 5 μm (restframe). It is introduced using Single Stellar Population (SSP) spectra with the addition of gas emission (which, in the younger SSP, appears as emissions lines).

- **AGN emission** which is due to thermal dust emission coming from the so-called "dusty torus" region surrounding the central source. For type 1 objects it dominates between 1 and $\sim 60 \div 80$ μm. In particular we consider two different AGN torus models characterized by two different spatial dust distributions. Both models also consider the accretion disc emission, visible in type 1 AGN (see Section 4.2.2 for more details).

- **FIR emission** mainly due to starburst phenomena, which contributes mostly between 5 and 10^{3} μm. Different models can be used to account for this contribution: empirical starburst galaxy templates or a grid of modified bodies (see Section 4.2.3 for more details).

The first versions of the code were presented in Fritz et al. (2006) and Hatziminaoglou et al. (2008) and, since then, the code has been widely used in the literature(Fritz et al., 2006; Rodighiero et al., 2007; Berta et al., 2007; Hatziminaoglou et al., 2008, 2009, 2010; Pozzi et al., 2010, 2012; Vignali et al., 2009, 2011), used in other works for comparison, or even went uncredited, e.g. Clements et al. (2009) and Dai et al. (2012), and tested within the "SED modeling group" of the HerMES consortium (see Section 4.7.3). Over the years the code has been improved with the goal to make it more flexible and tunable *ad hoc* on the basis of the individual user's aims. Among the improvements we can list: i) the possibility to use more than one AGN torus model; ii) the option to fit simultaneously photometric and MIR spectral information; and iii) the possibility to use a grid of modified black bodies to account for the FIR emission. As it will be extensively shown and explained both in this chapter and in Chapter 6, IRS spectra provide more constraints on the models and the modified black bodies allow for the estimation of the physical properties of the cold dust emission.

The next sections provide more detailed descriptions about the variety of the emission models used in the code, the methodology for the choice of the best fitting models and the physical properties that can be obtained applying this SED fitting procedure.

4.1 Data Input and Output

The fully automatic SED fitting tool presented here investigates the multi-band emission of galaxies with a multi-component approach making use of broad band photometry and MIR spectra. It has been written to be as flexible as possible in order to deal with different types of data. Indeed, the spectral information in the input catalogue can be expressed in different unit measures, and it is subsequently recognized in the appropriate way by the code through a label (see Appendix A for more details). Moreover, various input information to configure the fitting methodology, in turn the models, the prescriptions for the galactic and intergalactic absorption, the cosmology and the different fitting options to use, can be set up by the user on the basis of his own aims (see Appendix A). Once that all the files required have been settled, the code can run generating various output files (see Appendix B). These contain all the information that could be useful for the analysis of the SED, spanning from the parameters characterizing the model used to the information about the energy contribution of the different components as well as the complete SED better reproducing the data. An extensive description of the the data format and the main output file and calculations of AGN torus properties is provided in App. A, B and C.

4.2 Emission Components

4.2.1 The Stellar Component

We use SSP spectra constructed by using Padova (1994) evolutionary tracks (Bertelli et al., 1994) and a Salpeter IMF with mass in the interval between $0.15 \div 120$ $M_{\odot}$.

The stellar atmospheres library used to build up the optical spectra ($\sim 3500 \div 7500$ Å) are those from Jacoby et al. (1984) with spectral resolution of 4.5 Å and those from Kurucz (1993) with a spectral resolution of ~ 20 Å in the remaining part of the spectra ($90 \div 3500$ Å and $7500 \div 10^9$ Å). Note that these SSP models include the handling of dust emission from AGB stellar envelopes (Bressan et al., 1998). The nebular component, related to the younger stellar populations (typically up to 2×10^7 yr), is also added using the photoionization code CLOUDY (Ferland, 1996) assuming typical gas density and electronic temperatures (100 cm^{-3} and 10^4 K, respectively). The SSP grid contains 108 different ages starting from 10^5 to 2×10^{10} yr and 5 different metallicity values (Z=0.0004,0.008,0.004,0.02), although - at the moment - the default value is the solar one.

The evolutionary tracks are those from Padova (1994), while the stellar atmospheres are those observed by Jacoby, in the optical range, and from Kuruz in the UV, NIR and MIR ranges. The effect of the possible presence of extinction is also taken into account by choosing a specific attenuation law. The choice can be made among five different extinction curves, namely that of the Milky Way (with R_v=3.1, Cardelli et al., 1989), those with R=4.0 and 5.0, that of Calzetti et al. (1994) and the one of the SMC.

The stellar component can be introduced choosing between two different ways at the beginning of the run and it will be applied to all the objects in the catalogue in exams. This way the processing of this component will be homogeneous for all the objects SEDs. The two methods are:

1. a set of *stellar templates* representing the typical SFH of different Hubble types galaxies (Elliptical, S0, etc..), with the addition of a series of star formation histories typical of post-starburst, truncated star formation, and starburst of different intensities.

2. SFH purpose-built for each object, according to Schmidt's law:

$$SFR(t) = \left(\frac{T_G - t}{T_G}\right) \cdot \exp\left(-\frac{T_G - t}{T_G \cdot \tau_B}\right) \tag{4.1}$$

where T_G is the galaxy's age (or the age of formation of the first stellar populations), fixed on the basis of the redshift, and τ_B represents the duration of the starburst normalized at the age of the galaxy itself. The possible presence of an extinction effect is also considered. The best value for the two parameters, τ_B and E (B - V), is taken by the combination of the two best fits

of the observed SED (in this case the limits for E (B-V) are 0 and 0.5, while τ_B range from 0.05 to 1, in steps of 0.05).

It is worth highlighting that both the metallicity and the extinction law are fixed while running the code (see App. A.2 for the setting details), this mean that they do not vary and are not considered as free parameters.

4.2.2 The AGN Component

The hot dust emission, associated with the AGN torus and with the expected peak in the MIR regime, can be modelled in two distinct ways: by assuming the smooth dust distribution of F06 or the clumpy distribution developed by N08. The main characteristics of both models have been extensively described in Section 3.4.2 and 3.4.3, respectively.

4.2.3 The Cold Dust Emission

The peak of the thermal cold dust emission is expected to be around 100 μm (restframe). Two different options are scheduled to fit the FIR emission:

1. **Classical starburst galaxies templates**. The starburst component contributes mostly to the IR part of the total spectrum, in particular in the range between $\sim$ 5 a 1000 μm, with typical PAH emission features (6.2, 7.7, 8.6 e 11.3 μm bands) and silicate absorption feature at 9.7 μm. The choice is between some empirical templates representative of starburst galaxies, namely: Arp220, M82, M83, NGC1482, NGC4102, NGC5253, NGC7714. The templates of Arp220 and M82 were generated matching the SEDs from GRASIL and the observed spectra of ISO (Berta 2005 on which are based also the Polletta et al. 2007 template for the same objects). The templates of M83, NGC1482, NGC4102, NGC5253, NGC7714 were generated with the same procedure adopted for the previous ones (Berta, S. priv. comm.). Because of their empirical nature, the only information that can be derived accurately from these templates is the contribution of the starburst component to the total IR luminosity. Deriving the properties of the hot dust such as the temperature or the mass requires a more rigorous approach.

2. **Modified black bodies**. The code considers a grid of single-temperature modified black bodies with a temperature T spanning from 10 to 70 K and β as a free parameter (see Section 4.4.4 for further details). The advantage of this method is that the temperature and the mass of the cold dust are easy to derive. The modified black body is expressed in the analytic form:

$$S_\nu(\beta, T) = \frac{\mathrm{M}_c k_0}{d^2} \left(\frac{\nu}{\nu_0}\right)^\beta B_\nu\,(T) \tag{4.2}$$

where M_c is the mass of the (cold) dust, k_0 is the total mass absorption coefficient evaluated at a fixed frequency ν_0 (in this case k_0= 0.192 m^2 kg^{-1} at 350 μm, following Smith et al., 2010), d is the distance to the object, β is the dust emissivity index, and $B_\nu(T)$ is the Planck function.

4.3 Looking for the Best-Fit

The code first reads the data file, described in appendices A.3 and A.4, and checks whether any unit conversions have to be applied (e.g., from magnitudes to fluxes). The file is read one object (i.e., line) at a time. For each object it then calculates the luminosity distance assuming a ΛCDM cosmology with $\Omega_M = 0.3$, $\Omega_\Lambda = 0.7$ and a Hubble constant of 72 km/s/Mpc. These parameters can be modified in the setup file (see App. A.1). It then proceeds with the SED fitting.

The code checks the presence of observed data points at wavelengths longer than 24 μm (restframe)[1]: if such data are present the code takes into account the possible presence of a cold dust component. The models fitting the FIR are then normalized to all the IR point at wavelengths longer than 24 μm (restframe).

The next step consists in checking whether the presence of the stellar component is required or not. In type 1 AGN the optical/UV emission is often overwhelmed by the accretion disc continuum emission. The observed SED of the accretion emission is typically a power law and clearly distinguishable (if enough data points between 0.1 and 1 μm are available) from the stellar emission. The choice to include or not the stellar component is made by the code with a fit over all the photometric data points up to 1.6 μm (restframe). The research of the best fit exploits the available parameter space and if the reduced χ^2, χ^2_ν (that is the χ^2 divided for the number of the degrees of freedom[2], see Section 4.5) is lower than a given threshold value (set in the configuration file, see App. A.2) then the stellar component is taken into account.

Once the FIR emission models are normalized and the stellar component better reproducing the optical regime is fixed, the procedure starts looking for the best AGN model. The code exploits the entire grid of models (specified in the configuration file) accounting for all the inclinations of each model. It looks for the 30 models with the lowest values of χ^2 (the number can be modified in the configuration file, see App. A.1) that, combined with the other components, better reproduce the observed data points. The properties of these 30 models are kept in memory. The final step is an additional refinement, varying simultaneously the normalization constants of all the selected emission components (for more details we refer to Section 4.3.1).

In the presence of a stellar component, the normalization factor of the AGN component is calculated taking into account the part of the observed emission

[1] this value can be changed at will in the user setup file, see App. A.1

[2] The number of the degrees of freedom is the difference between the number of observed data points and the number of free parameters of the models

that has already been reproduced. In fact, the normalization is calculated after subtracting the stellar flux, already computed in the previous step, from the flux of the observed data points.

The fit is performed on the observed data points, resulting in the necessity to shift the model SED to the redshift of the object before starting with the fitting procedure. Then, in order to derive the intrinsic physical quantities, we accounted for the fact that data points need to be K-corrected in order to quantify the flux that the source would emit if observed at z=0. Since we perform the fit on the observed data frame, the K-correction is taken into account to calculate the flux of the model at the distance of the galaxy starting from the rest frame luminosity of the model:

$$S_{\nu_o} = \frac{L_{\nu_e}}{4\pi d_L^2} \cdot (1+z) \tag{4.3}$$

where L_{ν_e} is the intrinsic luminosity of the model, d_L is the luminosity distance of the object and S_{ν_O} is the flux at this distance.

In such a case this approach, on one hand, favours the other two emission mechanisms (stars and AGN), while on the other it reflects a physical scenario: the "purely stellar" emission contributes mostly at the UV wavelengths and at few μm, instead the AGN (dusty torus + accretion disk power law) dominates the emission from 1 to 60 μm in type 2 objects, while in the type 1 in general it dominates even below 1 μm up to the X-ray regime.

4.3.1 Normalization

The reproduction of an observed SED is very sensitive to the choice of the normalization of the different emission components. The normalization factors are calculated separately for each model, as described below, in order not to handle the normalization factors as completely free parameters while avoiding a strong dependence of the results on the normalization chosen. In a second instance and once the properties providing the best fits have been selected, the procedure looks for improvements of the best fit by "perturbing" the normalization constant values. The scale factors are iteratively and simultaneously varied from 0.6 to 1.1 in steps of 0.01, for the stars, from 0.4 to 1.1 in steps of 0.01 for the AGN component, while the starburst scale factor changes with respect to the initial phase in steps of 0.1, taking values from 0.6 to 1.1.

When a cold dust component is considered in the fit, it is the first to be normalized. The normalization is performed by matching the model SED and the observed fluxes at all the photometric points above a reference wavelength λ_n (this last can be changed at will, see App. A.1). The default value is $\lambda = 24$ μm (restframe). This procedure is repeated for all the FIR templates that will each have a proper normalization factor SB_{nrm} given by:

$$SB_{nrm} = \frac{\sum \mathrm{F}_O(\lambda_n)}{\sum \mathrm{F}_{SB}(\lambda_n)} \tag{4.4}$$

where λ_n is the reference wavelength (24 μm), F_O is the observed flux and F_{SB} is the flux calculated shifting the models at the redshift of the object in question.

When the stellar emission component is also included, it is normalized at the total emitted flux at $\lambda \leq 5$ μm (restframe), as follows:

$$ST_{nrm} = \frac{\sum \mathrm{F}_i^O(\lambda)}{\sum \mathrm{F}_i^M(\lambda)} \tag{4.5}$$

where ST_{nrm} is the normalization factor, F_i^O are the observed fluxes and and F_i^M the fluxes measured on the stellar models in the *i*-band once the K-correction has been applied to the model.

At this point the hot dust emission is introduced. The normalization of this component is performed in a way analogous to that described in Eq. 4.5 after having also accounted for the stellar and the cold dust emissions but using all the photometric data points available. Since a significant part of the observed flux can be reproduced well from other kinds of components (stars and cold dust emission) previously determined, the AGN normalization factor is calculated over the total sum AGN+stars+cold dust (or over all the components effectively used).

4.4 Recent Improvements

4.4.1 Data Format

Multi-band catalogues can contain photometric data with different units of measurement. With this in mind we made the code able to deal *simultaneously* with Vega or AB magnitudes as well as fluxes in units of μJy, with conversions dealt with internally. For details we refer to App. A.3 and A.4, where an example of the header of the photometric catalogue with a description for each column is given.

4.4.2 The FUV High Redshift Extinction

The view of extragalactic objects can be distorted by absorption due to intervening material located along the line of sight. Previous version of the code did not account for this attenuation effect, which I added during my PhD. To account for this attenuation effect we consider the common used prescription Madau (1995). They assessed the effects of the attenuation produced by intervening absorption systems as a function of redshift, constructing a detailed model of the HI opacity of a clumpy universe. Two aspects of the intergalactic obscuration have been considered: the attenuation of the FUV photometric properties of galaxies at high z due to the presence of intervening material and the distinctive absorption lines, called Lyman-α forest, in the UV spectra of background sources produced by the

presence of neutral hydrogen. Following the analytic form from Madau (1995) we corrected our input spectrum from the mean Lyman-α forest absorption. This last is calculated according to the observed flux deficities, D_A and D_B (see also Eqs. 17 and 18 of Madau, 1995), of a source emitting at redshift z_{em} and observed at wavelengths λ_{obs}:

$$\langle D_A \rangle = 1 - \frac{1}{\Delta\lambda_A} \int_{1050(1+z_{em})}^{1170(1+z_{em})} \exp\left[-A_2 \left(\frac{\lambda_{obs}}{\lambda_\alpha} \right)^{3.46} \right] d\lambda_{obs} \tag{4.6}$$

where $\Delta\lambda_A = 120(1+z_{em})$ and $A_2 = 3.6 \cdot 10^{-3}$, and

$$\langle D_B \rangle = 1 - \frac{1}{\Delta\lambda_B} \int_{920(1+z_{em})}^{1050(1+z_{em})} \exp\left[-\sum_{j=3,11} A_j \left(\frac{\lambda_{obs}}{\lambda_j} \right)^{3.46} \right] d\lambda_{obs} \tag{4.7}$$

where $\Delta\lambda_B = 95(1+z_{em})$. $A_j = (1.7 \cdot 10^{-3}, 1.2 \cdot 10^{-3}, 9.3 \cdot 10^{-4})$ and $\lambda_j = (1026, 973, 950)$ for Lyβ. Lyγ and Lyδ, respectively.

The model SEDs are then rescaled for the mean value of D_A and D_B at $1026 < \lambda < 1216$ and $\lambda < 1026$, respectively.

4.4.3 Addition of IRS Spectra

As already mentioned one of the most important improvements made to the SED fitting code during the course of this PhD thesis is the possibility to perform the SED fitting accounting *simultaneously* for photometric data points and MIR spectra. After having read the files with the MIR spectra information (see App. A) for each objects, each spectrum is rebinned in a prefixed number of bands (20). For each of this band the code calculates the mean flux and the relative error associated with the mean flux. This last, calculated following the theory of propagation of uncertainty, corresponds to the standard deviation of the flux for each bin of the spectrum. Mean fluxes and errors are subsequently handed in the same way as photometric points and the least square minimization is then performed as explained later in Section 4.5.

While running the code iteratively on more than one objects, it can be that in some cases the objects spectrum is not available. In such cases the code does not stop the run but the fit is performed on photometry only for those particular objects.

4.4.4 Modified Black Body

Another major improvement is the introduction of a modified black body component, to account for the emission at the longer wavelengths, which allows for the calculation of the temperature and the mass of the cold dust.

When performing the fit, we allow for the temperature to vary between 10 and 70 K while β is a free parameter. The default value is 2, which is consistent with the value commonly used in dust models (Draine & Lee, 1984; Li & Draine, 2001,

see also Davies et al. 2012 for observational evidence). At first, the temperature increases in steps of 1K in the predefined interval; once a first estimate is made, a fine-tuning is made around that value with a step of 0.1 K to derive the final best fitting value. The bottom panel of Fig. 4.1 shows an example where the best fit is obtained using a sum of SSPs, a smooth torus model of F06 and a modified black body with a temperature T=35.1 K and $\beta = 2.0$. When using the modified black body the IRS spectra information results redundant since the modified black body itself can not reproduce the characteristic emission features of a starburst galaxy.

4.5 The Best Fit

The determination of the models combination better reproducing the set of the observed data points is performed by *weighted least square*, better know as standard reduced χ^2 minimization, where the reduced χ^2 is given by the form:

$$\chi^2_\nu = \frac{1}{\mathrm{n} - \mathrm{p}} \sum_{i=1}^{\mathrm{n}} \left(\frac{\mathrm{F}_i^M - \mathrm{F}_i^O}{\sigma_i} \right)^2 \tag{4.8}$$

where n is the number of the observed data points (the sum of the photometric and spectral data points, when these last are available) and p the number of the free model parameters, taking into account all model components that are considered in each individual fit. F_i^O and F_i^M are the observed and model fluxes in the i-band, respectively, and σ_i the errors in the observed fluxes. The F_i^M are calculated through the convolution of the filter response curve with the model SED. The code is also able to deal with upper limits on the flux: if the models assume a flux value higher than that of the upper limits then the χ^2_i value, calculated specifically in the i-band, is automatically set to 10^5. Instead, if the request of the model flux being lower than the upper limits is observed, the χ^2_i is set equal to 1.

4.5.1 Fit Results

In addition to a synthetic SED best reproducing the data, the results coming from a run over an object consist of a set of 29 other combination of models (the number is configurable) reproducing the data in a more or less acceptable way. At each fit corresponds certain physical properties of the dusty torus, the stellar population and the cold dust.

The code outputs a set of files containing the results of the analysis:

- one file per object (`objname.OUT`), containing 10 columns reporting, for each one of the observed bands, the effective wavelength of the filter, the type of data (photometry or spectra, see App. A.3 and A.4 for more details), the observed flux, the error on the flux, the model flux, the χ^2 for that specific band and the percentage contributions of the 3 different components of emission in this specific band.

- one file per object (`objname.BST`), containing the characteristics of the top 30 best fitting models. The content and the order of the columns is that of the main output file (see next point).

- the *main output file*, `output.dat`, summarizing the results for the entire sample (one line per object). There could be 28, 30 and 32 columns depending on the models chosen to perform the fit (e.g a grid of modified black bodies instead of a set of empirical starburst galaxies templates and/or a single stellar template instead of SSPs) because the number of the resulting parameters and properties is different from a model to another. This file contains information about each object derived from the various emission components. All the output columns of this file and their explanations are summarized in App. B.

- one file per object (`objname.sed`), containing 5 columns reporting the information of the best model SED, in turn the wavelengths, the fluxes of the stellar, AGN and starburst components and then the total flux corresponding to the sum of the three components.

- one file per object (`objname.sfr`), containing 4 columns. The first specifying the file name identifying the SSP, then for each one are reported age, star formation rate and ΔT which is the interval of age difference between the subsequent SSP and the current one. This file is produced only when the stellar emission component is required and modelled with SSPs.

The output of the SED fitting (see App. B for more details) is not only the best fit model parameters or templates, but also a series of physical properties, derived from the best fit emission components, namely:

- the accretion luminosity, L_{acc}, i.e. the soft X-ray, UV and optical luminosity coming from the accretion disc.

- the IR luminosity, L_{IR}, defined as the flux integrated on the total model between 8 and 1000 μm.

- the contribution of the different emission components (AGN and starburst) to L_{IR};

- the innermost radius of the torus, R_{in}, set by the dust sublimation temperature, and defined in Eq. 3.12 for clumpy models and for smooth using Eq. 3.9.

- the outer radius of the torus, R_{out} derived from the outer-to-inner radius ratio that is an input parameter to both F06 and N08 models.

- the optical depth of the torus along the line of sight at 9.7 μm and in the V band, $\tau_{los}(9.7)$ and τ_{Vlos} respectively; for smooth models they are defined as:

$$\tau_{los}^{sm}(9.7) = \tau_{eq}(9.7) \cdot e^{-\gamma|\cos(\pi/2-\beta)|} \tag{4.9}$$

and

$$\tau_{Vlos}^{sm} = \tau_{eq}(0.55) \cdot e^{-\gamma|\cos(\pi/2-\beta)|} \tag{4.10}$$

while for clumpy models they take the form (see Nenkova et al., 2008a):

$$\tau_{los}^{cl}(9.7) = 0.07 \cdot \tau_{Vlos} \tag{4.11}$$

and

$$\tau_{Vlos}^{cl} = \tau_V(0.55) \cdot \frac{\mathcal{N}_0}{R_{in}} \cdot e^{\left(-\frac{\beta^2}{\sigma^2}\right)} \qquad \text{when} \qquad \beta < \sigma \tag{4.12}$$

where $\tau_{eq}(9.7)$ and $\tau_{eq}(0.55)$ is the equatorial optical depth calculated at 9.7 and 0.55 μm (V band), respectively, for smooth models, $\tau_V(0.55)$ is the optical depth of a single cloud and β is, in both cases, the viewing angle measured from the equatorial plane. The remaining parameters are defined in Section 3.4.2 and 3.4.3. In the case of $\beta > \sigma$, $\tau_{Vlos} = 0$.

- the hydrogen column density, N_H, along the line of sight. For smooth models the Galactic gas-to-dust ratio is implicitly assumed as a consequence of the use of the MRN distribution function. In clumpy models $N_H \sim 2 \cdot 10^{21} \tau_{Vlos}$ cm^{-2} (Elitzur, 2008).

- the effective amplitude of the torus, θ. For smooth models it is defined as that angle within which the optical depth at 0.33 μm is greater than 1.0 (see also App. C.2). For clumpy models it corresponds to twice the σ.

- the covering factor, CF, defined as the fraction of the nuclear emission covered by obscuring material. For smooth models CF depends on the opening angle of the torus, Θ:

$$CF^{sm} = 1 - \frac{1}{2} \cdot (1 - \cos(\pi - \Theta)), \tag{4.13}$$

while for clumpy models *CF* is given by the authors and is defined as:

$$CF^{cl} = 1 - \int_o^{\pi/2} e^{-\mathcal{N}_T(\beta)} \cos\beta d\beta \tag{4.14}$$

with parameters specified in Section 3.4.3.

- the mass of the torus (i.e. gas+dust), M_{torus}, which for smooth models is defined as the integral of all dust grains over all volume elements multiplied by the gas-to-dust ratio, while for clumpy models is the sum of the mass of gas of the single clouds. The gas-to-dust ratio considered is equal to 100, from Draine et al. (2007).

- the mass of the cold dust, in $M_\odot$, derived fitting FIR data with a modified black body and defined in Eq. 6.3.

- the temperature of the cold dust corresponding to that of the best modified black body.

- three different estimates of the mass associated to the stellar component (see e.g. Longhetti & Saracco, 2009), in turn the stellar mass of gas burned into stars from the epoch of galaxy formation to the time corresponding to its age,

$$\mathrm{M_{SFR}}(t) = \int_0^t \mathrm{SFR}(t^{'})dt^{'}, \tag{4.15}$$

the mass contained at any epoch inside stars accounting both for surviving stars and remnants,

$$\mathrm{M_{star}}(t) = \int_0^t \mathrm{SFR}(t')dt' - \int_0^t \mathrm{M}_{loss}(t')dt' \tag{4.16}$$

and the mass contained into still surviving stars at any epoch, where M_{loss} is the mass of gas returned to the interstellar medium from stars at any time t^i,

$$\mathrm{M_{alive}}(t) = \int_0^t \mathrm{SFR}(t')dt' - \int_0^t \mathrm{M}_{loss}(t')dt' - \mathrm{M}_r(t), \tag{4.17}$$

where M_r is the mass of dead remnants at the time t.

- the total extinction of the stellar population, E(B-V), and the extinction on the line of sight calculated in the V band (0.55 μm).

4.6 An illustrative example: AGN16

SST24 J171021.76+591854.7 (hereafter AGN16 following the identification number of Weedman & Houck, 2009) is classified as a Seyfert 1 galaxy, following the NED classification from optical spectra, at z=0.426. It was observed in the *Spitzer* extragalactic FLS which covers about 5 deg^2 centered on J2000.0 α = 17h18m, δ = +59°30′ and characterizes the extragalactic MIR sky at depths two orders of magnitude deeper than the IRAS survey (Condon et al., 2003). Indeed, Fadda et al. (2004) presented R-band images, observed using the Moisac-1 camera on the 4m Mayall Teelescope of the Kitt Peak National Observatory (KPNO), in preparation to the *Spitzer* extragalactic FLS (Fadda et al., 2006). Radio data at 1.4 GHz are also available (Marleau et al., 2007). The multi-band photometry used on the purpose of this section for AGN16 spans from the optical-UV to the FIR, in turn:

- u, g, r, i, z from SDSS.
- J, H, K from 2MASS.
- *Spitzer* IRAC at 3.6, 4.5, 5.8 and 8 μm.
- *Spitzer* MIPS at 24 and 70 μm.

- *Herschel* SPIRE at 250, 350 and 500 μm.

Additional information to these multi-wavelength data is the MIR spectra, from *Spitzer* IRS. I then ran the SED fitting procedure using the entire revised grid of F06 models (Section 3.4.2) consisting in $\sim$2400 models. Fig. 4.1 show examples for a best fit of the SED, from the optical to the FIR, of AGN16 (RA =17:10:21.76(his), Dec = +59:18:54.7(dms), Weedman & Houck, 2009). The three components contributing to the emission can be easily identified: a sum of SSP, a smooth torus model of F06 and a NGC7714-like starburst template. In the top left panel the photometric information is up to 24 μm and the starburst template is not required in order to reproduce the data in a satisfying way. Instead, once the information at longer wavelength, 70 μm (top left panel) and SPIRE 250, 350 and 500 μm (middle panel), are inserted a torus component alone does not account for the entire emission and a starburst template also need to be considered.

An improvement very recently introduced adds the possibility to fit simultaneously photmetric data and IRS spectra (Section 4.4.3). An example of this approach is shown on the bottom-left panel of Fig. 4.1. The inserted panel on the top-left shows how the shape of the best fit model (stars+AGN+starburst) is very well constrained by the presence of the IRS spectra. In particular, it is worth noting that the silicate feature at 9.7 μm of the torus model is very different from that of the best fit torus model obtained when using only photometric data (middle panel of Fig. 4.1). A more extensive discussion on this is presented in Section 6.3.1. Instead, the starburst component does not vary between the two and also in the top panel of Fig. 4.1 is still a NCG7714-like starburst template. Measurements on the spectra of AGN16 were made from Weedman & Houck (2009) and Hernán-Caballero & Hatziminaoglou (2011), which both found very low values for the equivalent width of the PAH feature at 6.2 μm : 0.02 and 0.03, respectively. This can be seen in the spectra (blue solid line) in the inserted top left panel at the bottom right of Fig. 4.1. This is also consistent with the results of the best fit, where it can clearly be seen that the AGN component dominates the MIR. Moreover, the best fit torus model shows a slightly absorbed silicate feature around 9.7 μm with a strength S=-0.11 (which is the logarithm between the observed flux and that of continuum), in agreement with the value -0.225 measured on the IRS spectra by Hernán-Caballero & Hatziminaoglou (2011).

4.7 A Potpourri of Applications and Examples

On our way to get the complete full-option final fitting procedure described in the previous sections, various intermediate, but at the same time self consistent, versions of the code have been used in different contexts, e.g. on different types of extragalactic sources or using different emission components. This section illustrates the most recent works where this code was used and reports on the different samples considered, on the fitting approaches chosen on the basis of the case in

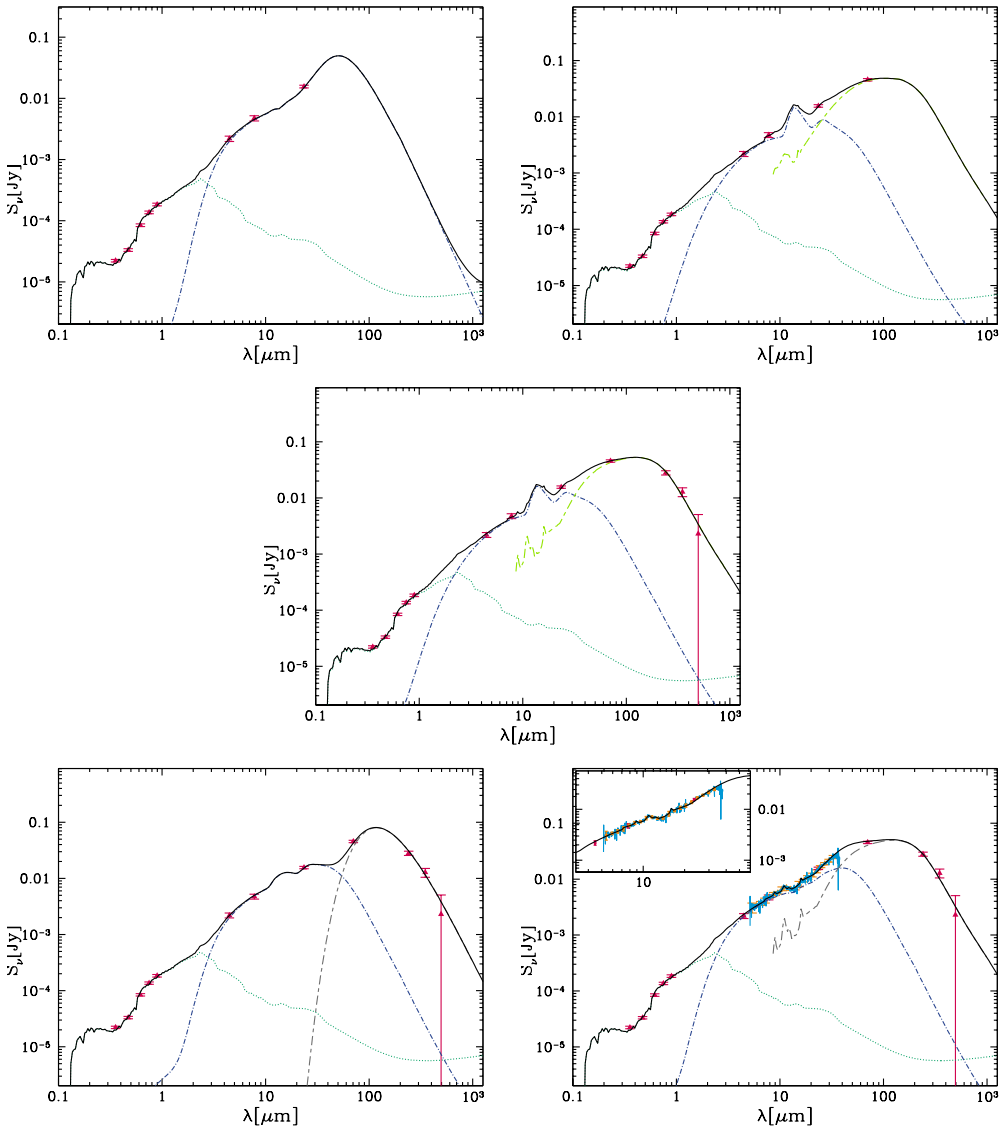

Figure 4.1: Best fits of AGN16 (RA =17:10:21.76(his), Dec = +59:18:54.7(dms), Weedman & Houck, 2009) considering only photometric data points up to MIPS 24 μm, MIPS 70 μm and SPIRE 500 μm (top left, top right and middle, respectively). Stellar, AGN and starburst component are in dotted dark green, dot-dashed blue and dashed light green, respectively. In the bottom left panel the fit to the FIR data is performed considering a grid of modified black bodies (dashed grey line), in this specific case the best fit black body is characterized by T=35.1K and $\beta = 2.0$. In the bottom right panel the fit is performed accounting simultaneously for the photometric data and IRS spectrum (blue solid line) information.

question and on the main results obtained. The goal is not to describe the details of the various works but to focus on the issues strictly related to this chapter, i. e. the fitting procedure and the results obtained in terms of models and their properties. Our SED fitting methodology was originally developed to reproduce the SED of active galaxies, which is the reason why the emission from an AGN component is taken into account. As extensively elucidated in the following sections this does not prevent the use of the procedure on different type of objects, such as ULIRGs or normal galaxies. Indeed, whereas the AGN component is not required the code does not insert it or fix its contribution to a negligible significance level. In respect to this, the next sections will show the results coming from the applications of our technique not only on active nuclei but also on various type of galaxies. Another goal of this section is to show the potential as well as the disadvantages, of our technique. In particular, the code was extensively used in the context of the HerMES "SED modeling group" where we carried out a comparison, reported in Section 4.7.3, with other SED fitting procedures with the goal of investigating the differences between some of the main physical properties that can be derived with different fitting approaches and emission models.

4.7.1 A MIR view of IRAS 09104+4109

IRAS 09104+4109 (I09104, hereafter) is a hyper luminous galaxy at z=0.442 optically classified as a type 2 AGN (Kleinmann et al., 1988). Various X-ray observations, e.g. *BeppoSAX* data (Franceschini et al., 2000) and 9.1 ks *Chandra* observations (Iwasawa et al., 2001) support the picture in which I09104 is a quasar with X-ray emission up to high energies consistent with being Compton thick. More recently, doubts on this scenario have arisen on the basis of 14-ks *XMM-Newton* observation (Piconcelli et al., 2007). To understand the real nature of I09104, i.e. wether it is a Compton thin or Compton thick AGN, Vignali et al. (2011) present an extensive analysis of X-ray long ($\sim$ 76 ks) and recent *Chandra* observations and an additional multi-wavelength analysis, from the optical to the FIR, as further support to investigate the real nature of the matter responsible for the X-ray absorption towards I09104.

My contribution to this work was related to using the SED fitting procedure presented in this chapter and carrying out detailed SED decomposition using photometric data and IRS spectra separately. Therefore, I focus only on my contribution to the work of Vignali et al. (2011), describing the multi-band analysis performed on IRAS 09104+4109 and paying particular attention to the details at IR wavelengths.

Data description

The multi-band photometry used by Vignali et al. (2011) is available in the literature, most of which in Table B.4 of Ruiz et al. (2010), and consists in:

- *XMM-Newton* Optical Monitor (OM) data, filters UVW2 and UVW1.

- SDSS magnitudes with the exclusion of the *i*-band magnitude due to its contamination from strong [O III] emission.
- *Spitzer*-IRAC data at 3.6 and 5.8 μm.
- *Spitzer*-MIPS data at 24 μm.
- IRAS detection at 60 μm.
- upper limits for IRAS at 100 μm and SCUBA at 450 and 850 μm.

Furthermore, the MIR *Spitzer* IRS spectra (5-38 μm) of I09104 is also available in the literature.

Methodology and results

In a first step we applied our SED fitting tool to photometric data alone considering SSP models of solar metallicity and empirical starburst galaxy templates to account for the emission of the host galaxy. We assumed as redshift for the stars to form z=4 (see App. A.1 for details on this option) and the attenuation law of Calzetti et al. (1994). Since the goal was to explore the nature of the obscuring material we performed the SED fitting using both smooth F06 and clumpy N08 models. For I09104, being it a type 2 AGN, we adopted the N08 models which are considered best suited to fit type 2 objects called "torus-only SED" where only the torus emission is considered (more detailed explanation is provided in Section 5.0.1). The best fits are reported in Fig. 4.2 (Figs. 3 and 4 of Vignali et al., 2011, respectively) where F06 and F08 models are the dashed blue lines, at the top and bottom, respectively. The red continuous line shows the IRS spectrum which has been fitted separately from the photometry using the procedure described in details in Section 5.2.5. While running the SED fitting code we used the $\sim$2400 models of the revised grid of F06 (Section 3.4.2).

It is worth noting that the starburst component is not required by the best fit due to lack of data at wavelength larger than 60 μm and in agreement with the lack of PAH features (which are star formation tracers) in the MIR spectra. Actually, recent *Herschel* data indicate the need for a starburst component. The lack of PAH is likely due to the strong radiation field of the quasar. One of the main result they obtained is that the same F06 best fit torus is able to reproduce both the photometric data and the IRS spectra, while the best fit N08 models is different when considering photometry or MIR spectra alone. Moreover, the best N08 torus model presented in the bottom panel of Fig. 4.2 is unable to reproduce the bulk of the multi-wavelength data. In particular it is worth nothing that, irrespective to the best fit solution for the stellar emission in the optical, the best N08 model presents some problems in reproducing the IRAC 3.6 μm data point. This problem of the N08 models is extensively discussed in Mor et al. (2009) where they claim the need of an additional hot component, possibly associated with graphite grains,

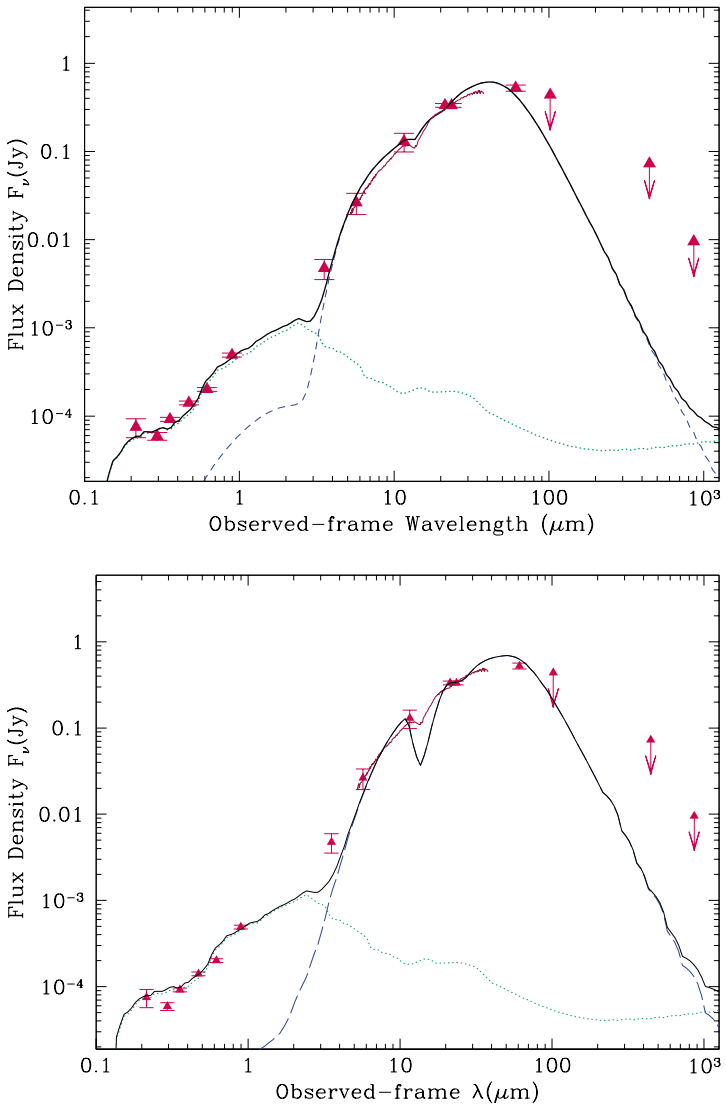

Figure 4.2: SED of I09104 (observed-frame) reproduced by stellar emission (green dotted lines) obtained using SSP models and AGN torus emission (blue dashed lines) obtained using F06 models (top) and N08 models (bottom). The black lines represent the total SED model. Top and bottom panel correspond to Fig. 3 and 4 of Vignali et al. (2011), respectively.

to reproduce the emission at short IR wavelengths. Furthermore, while the shape of the IRS spectra is well reproduced by the F06 models, N08 models appear to not be able to reproduce the shallow 9.7 μm absorption feature, even when trying to reproduce the IRS spectra alone. Note that the work of Vignali et al. (2011) was not aimed at comparing the two dust configurations (smooth and clumpy). Therefore, no definitive conclusion related to a possible comparison between the two models can be drawn. We refer to Chapter 5, which is an extended version of the work presented in Feltre et al. (2012), for a very detailed comparison between smooth F06 and clumpy N08 models.

4.7.2 Modelling ULIRGs and LIRGs

With the aim of investigating the AGN content in luminous IR galaxies, Pozzi et al. (2012) applied our multicomponent SED fitting procedure to 24 sources from the sample selected by Fadda et al. (2010). These luminous sources, with redshift between 1.75 and 2.4, lie in the *Chandra* Deep Field South (CDF-S) and are characterized by 24 μm flux density S_{24} $\sim$0.14-0.55 mJy and a typical total FIR luminosity between 8 and 1000 μm , L_{IR}, of $10^{12} L_{\odot}$, i.e. they are classified as ULIRGs.

The multi-wavelength photometry available for this sample consists in 70, 100 and 160 μm PACS data (from the PACS Evolutionary Probe, PEP, Lutz et al., 2011) for the FIR regime and data spanning from the UV to the MIR IRAC-*Spitzer* obtained by matching the sources with the GOODS-MUSIC photometric catalogue (Santini et al., 2009). Furthermore, all the objects have low resolution *Spitzer*-IRS spectroscopy in the 14-35 μm regime. This work represents the first attempt at simultaneous exploitation of photometric and spectral information, as described in Section 4.4.3. The fitting methodology considers the three standard components of emission: stellar emission by SSP, F06 AGN torus models ($\sim$ 2400, see Section 3.4.2) and empirical starburst galaxy templates. This approach of simultaneous fitting photometric data and IRS spectra is the most suitable to reach the author's aims and to achieve a full characterization of the source properties in terms of AGN, stellar and starburst emission. These are focused on the energy of the AGN component and on the investigation of the fraction of AGN which is well studied for local objects but still uncertain at higher redshifts. In this context, the presence of the MIR spectra plays a crucial role since it covers the MIR wavelengths where most of the difference between AGN and starburst activity can be found (see also Chapter 6). As mentioned also in Pozzi et al. (2012) the choice to use AGN torus models of Fritz et al. (2006) instead of the clumpy models of Nenkova et al. (2008a,b) does not affect or change the results, since they are mainly interested in investigating the energy budget and the infrared luminosity is well known to be very well constrained by the data (see Feltre et al., 2012, and Section 4.7.3).

The fits obtained by Pozzi et al. (2012) for all 24 ULIRGS are shown in Figs. 4.3 and 4.4.

The main SED fitting results obtained can be summarized as follows:

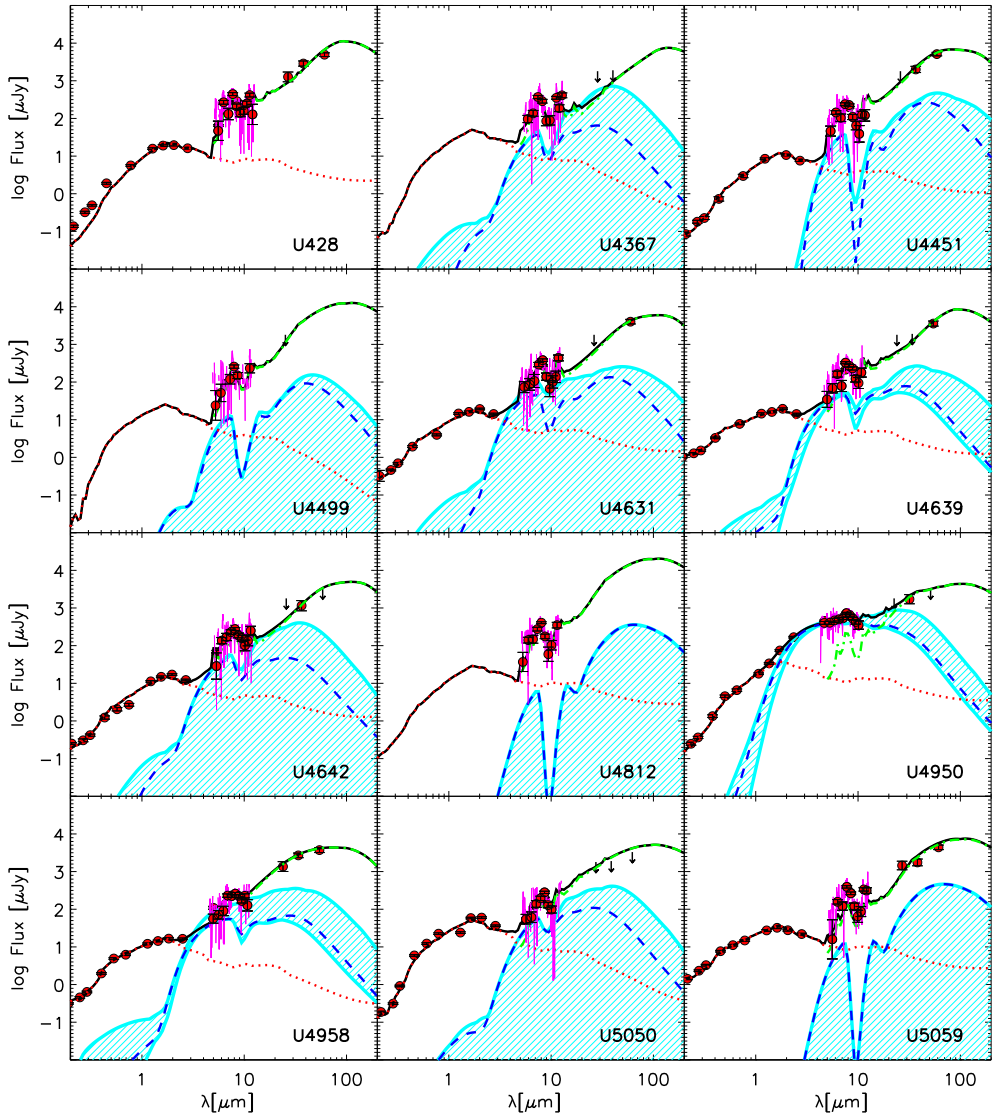

Figure 4.3: SED of part of the sample reproduced by Pozzi et al. (2012). The total SED (solid black line) is obtained as the sum of a stellar component (red dotted line), an AGN torus emission (blue dashed lines) and a starburst component (green dot-dashed lines). Red dots are the photometric points, black arrows the upper limits and the IRS spectra are shown in magenta. This figure correspond to Fig.1 in Pozzi et al. (2012).

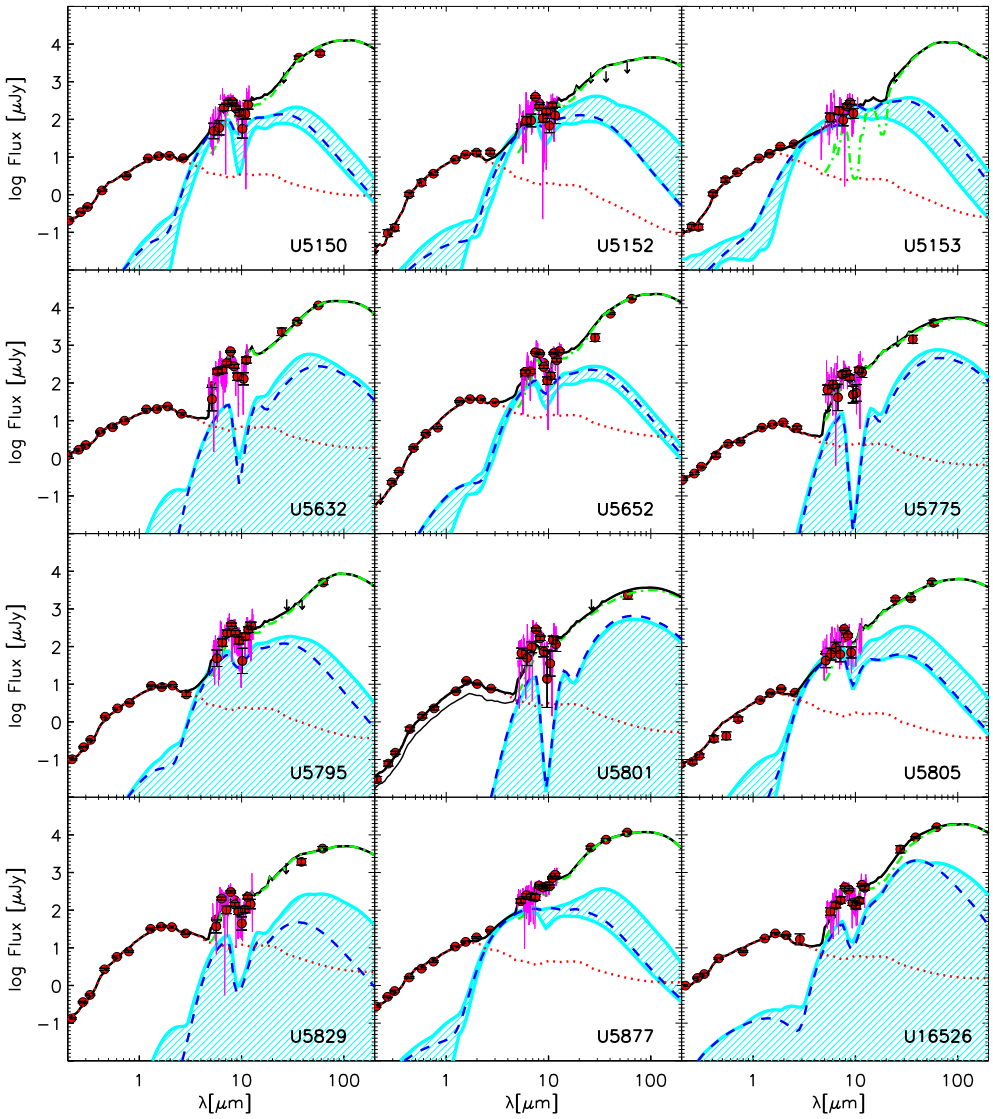

Figure 4.4: SED for the other 12 objects fitted by Pozzi et al. (2012). Color and symbols are the same of Fig. 4.3. This figure corresponds to Fig.1 in Pozzi et al. (2012).

- all the sources require both a stellar and a starburst component of emission;
- all but one (U428) require an AGN component, however, of low statistical significance for 14 sources;
- for the other nine sources the emission of the AGN was significant at least at the 3σ level and so they can be considered as AGN candidates;
- for these nine sources the total infrared emission and the MIR emission (5-30 μm) are dominated by the starburst component with the AGN contributing only for $\sim$23 % at maximum;
- only in the small spectral range between 2-10 μm, where the stellar emission from the host galaxy has a minimum, the AGN radiation overcomes the stellar and starburst component contributing to the energy budget for $\sim$60%.

4.7.3 Comparison of Infrared Luminosity and AGN fraction

Our procedure has been extensively tested within the SED modeling Working Group of the HerMES consortium. The objective of the group is to investigate the differences in the estimation of the basic galaxy parameter by comparing the results from different SED fitting codes and template libraries.

Of particular interest for us was exploiting the constrains that the IR data, from *Spitzer* (IRAC and MIPS) and *Herschel* (PACS and SPIRE), can provide to the L_{IR} and to the AGN fraction contributing to the L_{IR} itself.

Sample Description

The sample used for this comparison consists of 250 μm selected sources, with $S/N \geq 5$, in the Lockman North field (10h46m00s +59d01m00s, $35' \times 35'$) containing star-forming galaxies and, perhaps AGN, built by Véronique Buat and Denis Burgarella. From the 788 objects with $S/N \geq 5$ in the Lockman-North field, which was also explored by the SWIRE, 286 objects are uniquely identified inside a radius of 2 arcsec (based on *Spitzer*/IRAC coordinates, see also Buat et al., 2010) and 212 of these have a reliable redshift estimates. Fig. 4.5 shows the redshift, spanning from 0 to 3, of the 212 galaxies used in this comparison. Moreover, this sample is selected *ad hoc* to have a very good FIR coverage with the aims to investigate the IR properties of the galaxies. The photometric information spans from the UV (GALEX) to the FIR (*Herschel*, PACS-SPIRE), with

- 41 and 85 objects detected in FUV (1530 Åand 2310 Å) and NUV GALEX bands, respectively
- all 212 observed by the survey SWIRE in *u*, *g*, *r* ,*i*, *z*, J, H and 192 in K band
- 209, 208 176, 162 detected by IRAC/*Spitzer* (SWIRE survey) at 3.6, 4.5, 5.8 and 8.0 μm, respectively

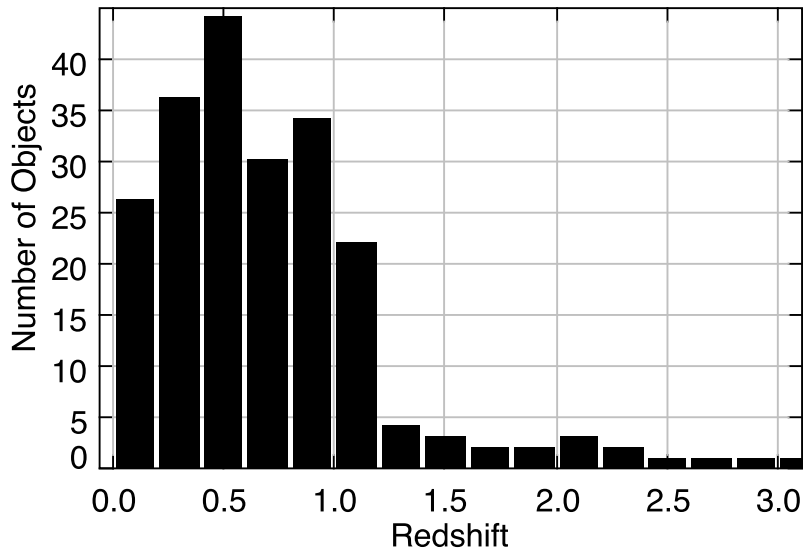

Figure 4.5: Redshift distribution of the sample of 212 galaxies selected at 250 μm in the Lockman-North field.

- all 212 detected by MIPS/*Spitzer* (SWIRE survey) at 24 μm and only 31 at 70 μm
- 174 and 163 detected by PACS/*Herschel* at 110 and 160 μm, respectively
- all 212 detected by by SPIRE/*Herschel* at 250 μm and only 41 and 2 at 350 and 500 μm, respectively.

SED Fitting Methods

The emission components considered when running our SED fitting procedure on the aforementioned sample consists of SSP models, the entire grid of the revised torus models of F06 (Section 3.4.2) and empirical templates for the stellar, AGN and starburst components, respectively.

As already introduced, one of the test that we carried out with the SED modeling Working group was a comparison of our results with those obtained with other SED fitting codes. In particular, with those obtained with the code GICALE by Elodie Giovannoli (EG here after) and with the code HyperZ by Lucia Marchetti (LM here after), both members of the HerMES consortium.

model	Θ	q	γ	$\tau_{eq}(9.7)$	Y	θ
1	140°	0.5	0.0	2	30	20°
2	140°	0.5	6.0	10	30	80°
3	60°	0.5	0.0	2	30	20°
4	140°	0.5	0.0	2	100	20°
5	60°	0.5	0.0	6	100	80°
6	140°	0.5	6.0	2	30	80°

Table 4.1: Model parameters value of the AGN torus models used by EG selected from the original grid of F06.

CIGALE

EG used the code CIGALE (Code Investigating Galaxy Emission) which extends the SED fitting algorithm written by Burgarella et al. (2005) [3]. The aim of CIGALE is to investigate the physical properties of galaxies reproducing photometric data from the UV to the FIR (restframe). The main difference of this code with our procedure is that CIGALE accounts for the energy balance between the stellar optical/UV emission and the emission in the FIR, relating in this way the dust attenuation with the dust emission. To derive the optimal galaxy parameters CIGALE applies a "Bayesian(-like) analysis". This last consists in a probability distribution functions analysis on the best fit models obtained with the χ^2 minimization method, as extensively described in Noll et al. (2009).

The models used to reproduce the data comprise in UV-to-IR SEDs of dust-attenuated complex stellar population models, IR dust emission models and spectral line templates. For the stellar components CIGALE allows both PEGASE (Fioc & Rocca-Volmerange, 1997) and Maraston (2005) SSP models to be used. Several dust emission models and templates can be used, such as Chary & Elbaz (2001); Dale & Helou (2002); Draine et al. (2007); Siebenmorgen & Krügel (2007).

In order to distinguish the contribution to IR emission due to the starburst activity and the one due to the active nucleus at the centre of the galaxies EG combined the models of the AGN with the starburst galaxy SEDs of CIGALE. EG selected, among the original grid of smooth torus models of F06, 6 AGN torus templates characterized by a less extreme shapes and suitable to the study of lower contributions from AGNs in starburst galaxies. The parameters of such models are summarized in Table 4.1. For this specific project of comparison, EG used the code CIGALE with the Maraston (2005) SSP models and the IR dust emission models of Dale & Helou (2002).

[3] http://www.oamp.fr/people/burgarella/cigale/

HyperZ

HyperZ (Bolzonella et al., 2000) [4] was originally developed to estimates the redshift of extragalactic source from broad-band photometry by applying a standard SED fitting procedure. The codes compares the fiducial photometry with that computed from the SED templates. Such templates are first redshifted (either observed and synthetic) and, then, are properly handled by applying the absorption of the Lyman forest (following the Madau's prescription as in our SED fitting code, see Section 4.4.2) and the reddening with the possibility to chose between different extinction laws. If required *HyperZ* computes the galactic dereddening on the real data. This is performed with a Seaton's law (Seaton, 1979, see Fig. 3.2) and color excess E(B-V) selected by the user.

HyperZ consists of three different applications:

- *HyperZ* is the original code developed to estimate the photometric redshift of the extragalactic sources.
- *Hyperzspec* is a modified version of the original *HyperZ* in which the redshift of the source is known. It produces an adjustments on the input photometry by using different SED templates and provides the best fitting template model and the respective physical parameters as output.
- *Hyperzmass* is also a modified version of the original *HyperZ* in which the redshift of the source is known. In this case the fitting is performed by using physical models (e.g. BC03, Maraston (2005) SSP models, etc.). The output comprises the best fit models, the stellar mass of the source and other physical parameters.

LM used an advanced version of the *HyperZ* code differing from the original for the introduction of IR SEDs templates. The template are constructed using the single stellar population models of BC03 plus the empirical templates libraries of normal galaxies, starburst galaxies and AGN of Polletta et al. (2007) and the slightly modified versions of few of them on the basis on PACS observations by (Gruppioni et al., 2010).

The Infrared Luminosity

The infrared luminosity L_{IR}, integrated between 8 and 1000 μm, is a fundamental parameter when studying the IR SED of galaxies. Indeed, it provides information about the energy emitted by obscured sources and contains information about the relative contribution of AGN and starburst. In Fig. 4.6 the comparison of the three different estimates of L_{IR} are color-coded as function of redshift. From the top to the bottom: our estimates, L_{IR} (AF), compared with those of EG and LM (L_{IR} (EG) and L_{IR} (LM), respectively) and L_{IR} (LM) compared with L_{IR} (EG). The

[4] http://webast.ast.obs-mip.fr/hyperz/

three estimates present a good agreement with correlations factor of 0.98, 0.99 and 0.98, respectively. The average L_{IR}, with the associate standard deviation, in all the sample is (0.77±1.7) $\times 10^{12}$ L⊙ (1.5±3.5) $\times 10^{12}$ $L_{\odot}$ and (0.96±2.07) $\times 10^{12}$ L⊙ for AF, EG and LM, respectively. While comparing L_{IR} (AF) with L_{IR} (EG) (top panel Fig. 4.6), we note a deviation for sources with $L_{IR} \geq 10^{12} L_{\odot}$, starting form z∼1, with L_{IR}(EG) taking systematically higher values. This does not happen while comparing our L_{IR} with L_{IR} (LM) showing a very tight correlation at all the redshift (middle panel of Fig. 4.6). As expected, L_{IR} (EG) presents a deviation from L_{IR}, starting at z∼ 1, from L_{IR} (LM) with the first taking higher values.

We can conclude that, for such sample, the three estimates are absolutely consistent and very well constrained, for objects with $L_{IR} \leq 10^{1}2$ $L_{\odot}$. Even though, when considering higher luminosity and z>2 a lower agreement is found with L_{IR} (EG), while the estimates of LM are still consistent with ours.

The AGN Fraction

The second parameter in which we are interested in is the AGN fraction contributing to the L_{IR}. The AGN fraction coming from our SED fitting procedure can be compared only with that of EG because the procedure used by LM does not account for a separate AGN emission component, which is in case contained in the SED templates used in *HyperZ*. Fig. 4.7 and 4.8 compare directly our AGN fraction, AGN fraction (AF), and that of EG, AGN fraction (EG) for all the 212 galaxies. We find a strong disagreement between the two estimates. This can be interpreted as a consequence of the use of different numbers of models between our procedure and that of EG. Indeed, we used the entire revised grid of F06 smooth models (∼ 2400) described in Section 3.4.2, while EG selected 6 models from the original grid of F06 as previously described. The higher the number of models used, the higher the probability of finding a model that approaches the observations, and then, the fraction of AGN contributing to the emission is more likely to increase.

The average value of AGN fraction (AF) is higher than that of EG, being such average values and the associated standard deviation, 0.095±0.011 and 0.077±0.015, for AF ad EG, respectively. The AGN fraction (EG) is influenced by the presence of some objects with best fit models characterized by high AGN emission. When only AGN fraction lower than 0.4 are considered, the average values become 0.084±0.091 and 0.052±0.097 for AF and EG, respectively. Fig. 4.8 shows the difference between the values for all the sample, with an average difference between the two AGN fractions equal to 0.018±0.165.

The reason of the difference can be attributed to the fit methodology. Indeed, our procedure, originally developed for AGN, inserts the AGN component first and, in a later stage, the starburst template. Consequently, our procedure is more likely to associate an higher weight to the AGN emission to the detriment of the starburst one. On the other end, EG insert the AGN *a posteriori* and this could

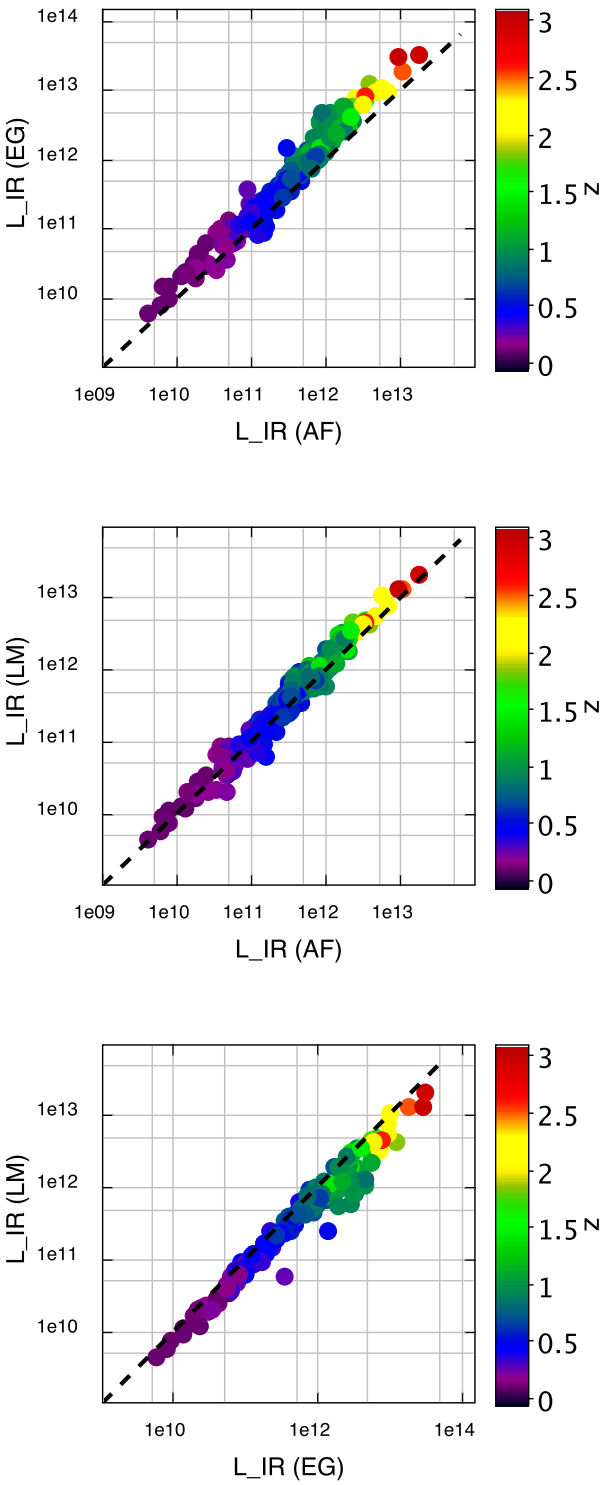

Figure 4.6: Comparison of the different estimates of L_{IR}, from top to bottom: L_{IR} (EG) vs L_{IR} (AF), L_{IR} (LM) vs L_{IR} (AF) and L_{IR} (LM) vs L_{IR} (EG). The dashed black line is the 1:1 line.

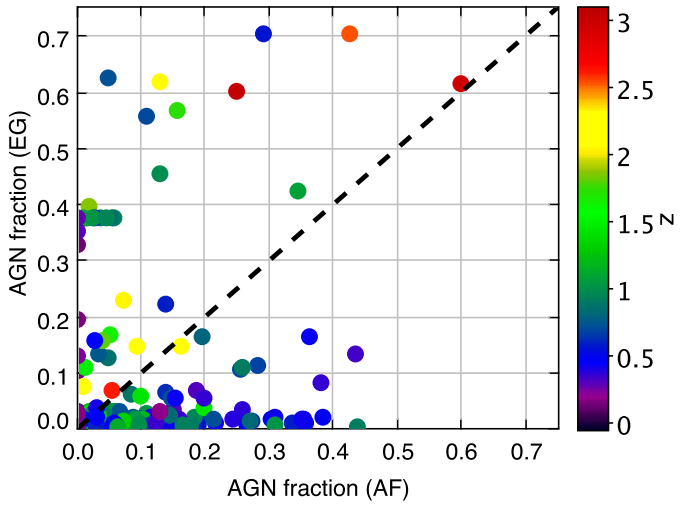

Figure 4.7: Comparison between the AGN fraction (AF), estimated with our procedure, and AGN fraction (EG), estimated adding AGN torus template to the CIGALE code.

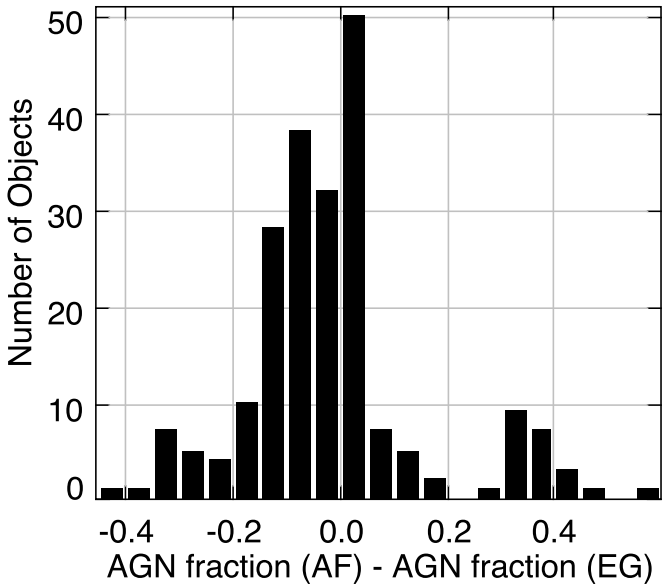

Figure 4.8: Histogram reporting the difference between AGN fraction (AF) and AGN fraction (EG).

result in an underestimation of the AGN fraction.

4.8 Discussion and Conclusions

Our SED fitting technique, presented in this chapter, turned out to be a very powerful tool, especially while investigating simultaneously the properties of starburst and AGN activity. Such procedure has several strengths:

- the capability to deal with multi-band data spanning a wide range from 0.1 μm and 1000 μm, with the possible extension to the radio and X-ray domain;
- the flexibility to simultaneously use multiple units of measurement for the flux, that is μJy, Vega magnitude and AB magnitude, as well as the use of different band filters;
- the possibility to chose the "favorite" combination of models to perform an *ad hoc* SED fitting decomposition on the basis of the user's aims, such as the possibility to chose between more than one AGN torus model or more than one model to reproduce the FIR emission. A detailed comparison between the two different torus models that can be used in the SED fitting procedure is provided in Chapter 5;
- the suitability to investigate simultaneously both the properties of AGN and the host galaxy;
- the flexibility to easily add further models;
- even if originally developed for AGN, our SED fitting procedure can be applied to all types of galaxies. Indeed, whenever the AGN component it is not necessary to reproduce the data the code does not consider it;
- the possibility to investigate objects at all the redshift. To make it possible I recently added the Madau's prescription to account for the FUV high redshift extinction;
- the possibility to simultaneously use both the spectral and photometric information that I recently introduced. This allows for better constraints on the AGN torus models as extensively discussed in Section 6.3.1;

At the same time, these strengths can translate into weaknesses. For example, the fact that the code was originally developed for AGN would result in a higher presence of the AGN component with respect to the necessary one as seen in Section 4.7.3. Moreover, this code does not consider the energy balance, as e.g. MAGPHYS of da Cunha et al. (2008) (Section 3.3) and CIGALE (sections 3.3 and 4.7.3). In our code the stellar and starburst components are not related to each other and this could result in a disadvantage in some cases. According with

FIR and sub-mm observations of normal spiral galaxies, the reprocessed radiation is roughly the 30% of the optical/UV emission (Popescu & Tuffs, 2002; Davies et al., 2012). However, some discrepancies have been found when studying individual edge-on spiral galaxies (Verstappen et al., 2013). A comparison between self-consistent radiative transfer models, successfully predicting the optical/UV extinction, found the prediction for FIR and sub-mm emission to provide an underestimates of the observed value by a factor 3 (Popescu et al., 2000; Misiriotis et al., 2001; Alton et al., 2004; Dasyra et al., 2005; Baes et al., 2010b; de Looze et al., 2012). The reason for such discrepancy is associated either with a FIR and sub-mm emissivity substantially underestimated (Alton et al., 2004; Dasyra et al., 2005) or with the geometrical distribution of stars and dust, which seems to have a crucial role in the observe IR radiation (Popescu et al., 2000; Misiriotis et al., 2004; Bianchi, 2008). In such cases the energy balance approach would not be the most suitable choice.

Furthermore, the procedure to look for the best fit is based on the χ^2 minimization making it impossible to have an estimate of the errors associated with the physical properties of the models and making hard a very detailed study of model degeneracy. Looking for best fitting models by using a Bayesian approach or boot strapping methods would provide more suitable information to carry out studies on model degeneracy and errors.

To conclude, our aims to investigate simultaneously the properties of the gravitational accretion and star formation activity are fully achieved by our code. Indeed, the possibility to use both photometry and the IRS spectra allow us to automatically reproduce the SED of large sample of objects to see whether the presence of an AGN could influence the MIR and FIR properties of the host galaxy, as presented in Chapter 6.

5 | Dust Distribution in AGN

[1]

The very elegant way to explain the differences between type 1 and 2 objects as due to an orientation effect, proposed for the first time by Rowan-Robinson (1977), set up the entire stage for the AGN Unified Model (Antonucci, 1993; Urry & Padovani, 1995). This scenario describes the interplay between the presence of dust around the central region of AGN and the line of sight. In fact, for certain lines of sight, the dust can obscure the central engine giving rise to a number of differences in the observed spectral energy distribution (SED) of AGN at almost all wavelengths: dust grains, present in an optically thick region surrounding the nucleus, absorb UV photons coming from the central region and re-radiate them in the IR.

At present the question "How is the dust distributed within the inner region of AGN?" is a very debated issue since the possibility to directly observe the internal structure of the torus is strongly hampered by observational limitations. During the last decades various radiative transfer models have been used to reproduce the observed IR emission coming from dust, and are roughly divided in two categories: those in which the dust uniformly occupies a toroidal region around the SMBH, customarily referred to as "smooth models", and those that consider the dust to be distributed in clumps or clouds surrounding the central source, and hence referred to as "clumpy models". Clumpy models are a more likely representation of the reality, as formerly claimed by Krolik & Begelman (1986, 1988), as in a smooth distribution the collisions between the grains would results in temperature too high for the dust to survive (see e.g. Krolik & Begelman, 1988). However, thanks to the simple treatment of the radiative transfer required by smooth models, they were the first to be developed and they obtained, in many aspects, a good success in reproducing the IR SED of AGN to be considered a good approximation of it.

But what can the models and the present day observations indirectly tell us about the dust distribution? In this chapter, entirely dedicated to this topic, we present our attempts to answer this question. At present, in the literature we can find only two investigations of the differences between model SEDs arising from

[1] This chapter is an extended version of the work of Feltre, A., Hatziminaoglou, E., Fritz, J., & Franceschini, A. 2012, presented in MNRAS, 426, 120

the two geometries. The first has been performed by Dullemond & van Bemmel (2005) which used their own multi-dimensional radiative transfer models of smooth and clumpy tori, concluding that it is not possible to distinguish between the two dust distributions based just on the observed broad-band SED. They compared various properties of the SEDs (i.e. the width of the SED, the strength of the silicate feature at 9.7 μm and the isotropy parameter defined as the linear ratio of the total integrated infrared flux at 90° inclination over the total integrated infrared flux at 20°) of smooth and clumpy models with the some global physical parameters. They concluded that both dust distributions produce broadly similar SEDs but, depending on the parameter values, some differences might appear in the 9.7 μm silicate feature and in the width of the IR bump. It was unclear, however, whether these differences were significant enough to be used as diagnostics. The comparison presented in Feltre et al. (2012) is the first comprehensive of such studies comparing two most representative torus models in the literature to date, each representative of one of the two classes. In particular the comparison, both from the purely modelling and from the observational points of view, concerns the analysis of the main IR SEDs properties of the smooth models of Fritz et al. (2006) and clumpy models of Nenkova et al. (2008a,b) with the aim to look for possible diagnostics between the two dust configurations. Our results prove that there are virtually no random parameter combinations that can produce the same SED shape. Even though both dust configurations provides equally good fits to the data and there is no way to distinguish between the two when broad band photometry or IRS spectra are considered.

5.0.1 Intrinsic Differences between the two Dust Distributions

As already pointed out by several authors the difference in the dust distribution between smooth and clumpy gives rise to a number of different effects on the dust emission and on its physical conditions (Hönig et al., 2006; Nenkova et al., 2008a,b; Elitzur, 2008).

Dust Temperature

The very nature of smooth models makes the dust temperature a continuous function of the distance from the central source: its fall off rate depends on the overall optical depth and the characteristics of its distribution. In a smooth model the dust temperature always follows a monotonic trend. When the dust density decreases not only along the radial coordinate but also with the angle from the equatorial plain, the temperature will be subject to a gradient along that direction, as well.

On the other hand, in clumpy models, characterized by dust-free space regions, the temperature will very strongly depend on the presence of optically thick clouds along a given direction. Without this shield the radiation from the primary source is able to heat the dust to high temperatures well inside the toroidal region. Similarly, the non-illuminated side of clouds, particularly those with high optical

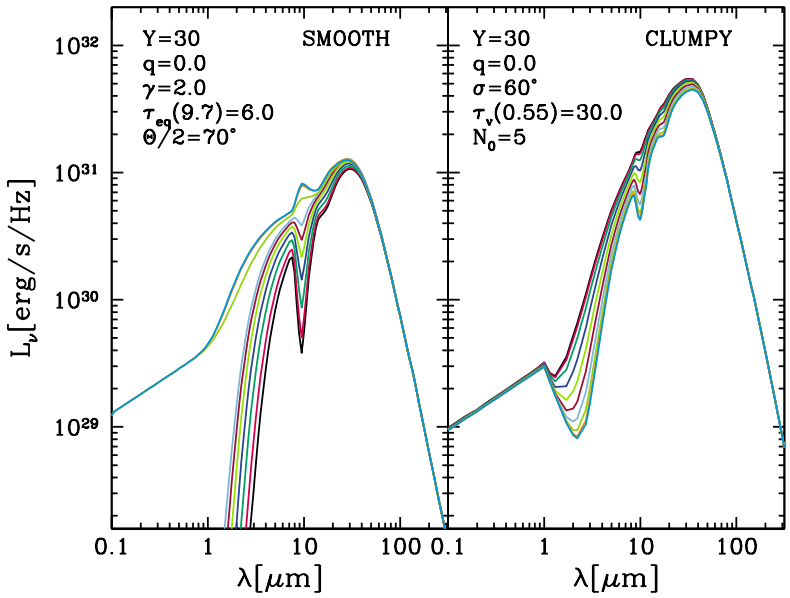

Figure 5.1: Example of smooth (left) and clumpy (right) model SEDs with comparable model parameter values, viewed at different inclinations (from Feltre et al., 2012).

depth, will be in general much colder with respect to their illuminated side. The net result is that a whole range of temperatures can coexist within the torus at a given distance from the primary source.

Schartmann et al. (2008) found a large spread in temperature, for a given distance from the central source for clumpy models with respect to smooth models. The dust within each individual cloud spans a wide range of temperatures, and therefore emits strongly at all wavelengths, from MIR to sub-mm. Therefore, in case of a clumpy medium we should observe the same emission at all infrared wavelengths. In contrast, as a consequence of the temperature gradient present in smooth models, the innermost warm dust should emit much more at MIR wavelengths, while colder dust located in the outer region should radiate in the larger wavelengths (Maiolino, 2008).

Type 1 and Type 2 Views

One of the most important implications of the AGN unified scheme, is that type 1 objects are those observed without the dust directly intercepting the line of sight, while type 2 objects are those in which the accretion disc is obscured by dust. In a clumpy representation this simplistic view is not strictly valid since, given the probabilistic nature of the dusty clouds distribution, the torus is no longer a well-defined space region that sharply divides the sources in type 1 and type 2. In

this picture, the chance of not seeing the central source is a matter of probability that the line of sight intercepts at least a cloud, and does not depend only on the viewing angle as in the case of a smooth torus. A side-effect of this aspect, is the fact that the SEDs of smooth and clumpy models behave in a different way, when different lines of sight are considered: in smooth models with high optical depths there is an abrupt change between the type 2 and type 1 SEDs, appearing when the line of sight starts intercepting the dust layer of the torus, and this might be described by a clear bimodality in the emission SED, in particular in the continuum shortwards of ~ 2 μm. On the other hand, a clumpy structure, with the dusty clouds positions being represented by a gaussian distribution function, naturally yields a smooth transition from the type 1 to type 2 observed emission at UV, optical and MIR wavelengths. Fig. 5.1 shows an example of the different SEDs in smooth (left panel) and clumpy AGN-added (right panel) models, as a function of the line of sight. An abrupt change is clearly observed in the smooth model shown here, that corresponds to the angle for which the dust no longer intercepts the line of sight (70° in this particular case), allowing for the bare emission from the primary source to be viewed directly. To simplify the study, in the comparison (see Section 5.1) only the two extreme inclinations are considered. For F06 this translates into an edge-on and a face-on inclination corresponding to a $\theta = 90°$ and $\theta = 0°$, respectively, while we consider as type 1 and 2 clumpy models those with a probability to see directly the AGN larger and lower than 0.5, respectively, for each model parameters combination.

Considering the chance to see or not the central source, N08 models are divided in models in which only the torus emission is considered (torus-only SED), and models with the AGN contribution added (AGN-added SED), identical to the former in the IR range but in which the central source is seen in the optical and UV wavelengths. An example of this separation between the two type is shown in the right panel of Fig. 5.2 where the range of the N08 type 1 and type 2 models are shown (AGN-added and torus-only, respectively). An example of the latter is shown, for 10 different inclinations, on the right panel of Fig. 5.1, where the break at $\lambda \sim 1$ μm is an artifact of the parameterization of the input spectrum (Nenkova et al., 2008b). As a general rule the torus only-SEDs are used to fit type 2 objects while the AGN-added SEDs for type 1 objects.

Note that, since in this work we deal either with MIR properties and spectra (see sections 5.1 and 5.2.5, where the AGN-added and torus-only SEDs are identical) or multi-wavelength photometric data of type 1 AGN (see Section 5.2.3), only AGN-added SED of N08 models have been considered.

Primary source

The revised grid of F06 models and N08 assume two different power laws to model the primary source (Eqs 3.11 and 3.14, respectively). By way of illustration they are reported in Fig. 5.3.

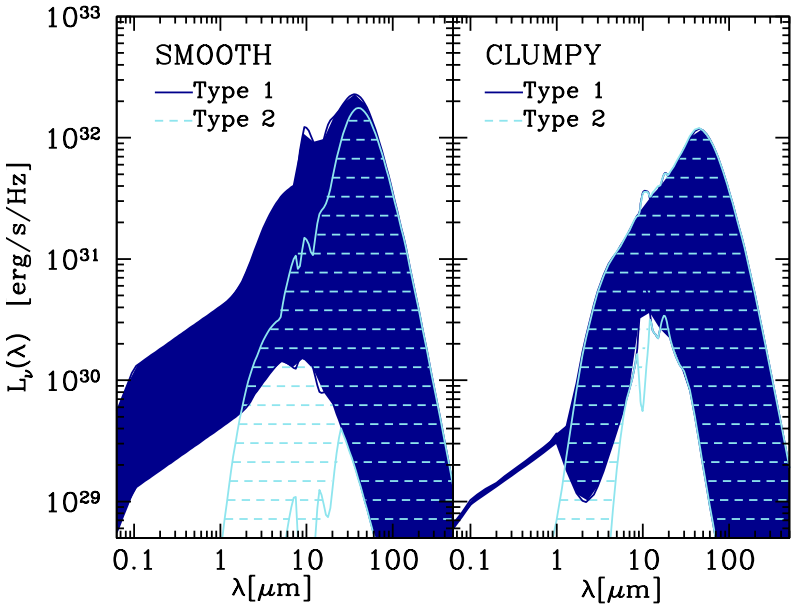

Figure 5.2: Range of intrinsic model SEDs for the smooth (left) and clumpy (right) dust configurations. Each panel shows the coverage for both type 1 (filled region) and type 2 (dashed) inclinations (from Feltre et al., 2012).

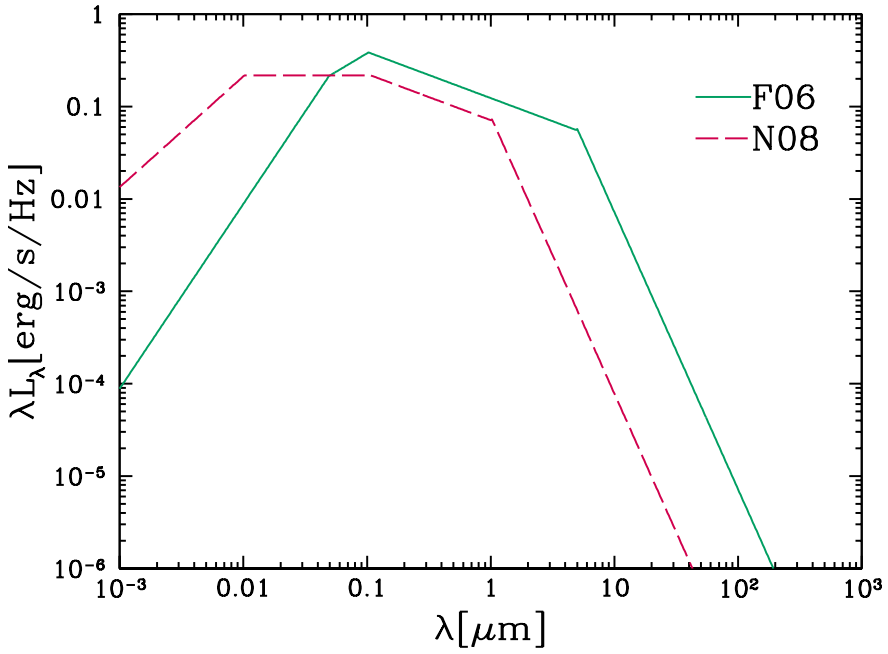

Figure 5.3: Primary sources of F06 (solid green line) and N08 (dashed red line) models, arbitrarily normalized.

Chemical Composition

As already mentioned in sections 3.4.2 and 3.4.3 both models consider a mixture of graphite and silicate grains but, while the F06 models use the silicate absorption and scattering coefficients given in Laor & Draine (1993), N08 makes use of values given in Ossenkopf et al. (1992). And while the absorption coefficient for the former peaks at 9.5 μm, that of the latter peaks at 10 μm.

The 9.7 and 18 μm Silicate Features

Silicates grains are one of the greater components of the interstellar medium. As already mentioned, they give rise to two features in the IR, one around 9.7 μm and the other around 18 μm. Emission or absorption due to silicate grains is one of the main properties of the IR spectra of the evolving stars with great mass loss, the interstellar clouds, the HII regions and the circumstellar discs surrounding young stars. The emission feature at 9.7 μm due to silicate grains has drawn the attention because its prominent appearance in all the smooth models did not match any observations for many years, laying the reliability of the AGN Unified Model on the line. As already mentioned in Section 3.4.1 the first clumpy models were designed to solve this issue (e.g. Nenkova et al., 2002) that remained controversial until the observations carried out with *Spitzer* IRS (Hao et al., 2005; Siebenmorgen et al., 2005; Sturm et al., 2005; Buchanan et al., 2006; Shi et al., 2006). By means of a smooth model, F06 were the first to successfully fit an observed MIR spectrum of an AGN. In fact, while it is in general true that smooth models are producing too strong emission feature and very deep absorption at 9.7 μm, F06 demonstrated that it is possible to achieve 9.7 μm features in only moderate emission in type 1 sources, as some observations were suggesting, even assuming a smooth distribution of the dust.

The feature of N08 models is smeared out when observed in indirect views, in spite of its prominence in emission when directly observed in single heated clouds. Furthermore, for edge-on viewing, there is a small range of clumpy model parameters that is able to produce a weak emission feature while other models present either a featureless SED or a weak absorption feature (Nenkova et al., 2008b). The same holds for smooth models: edge-on views of low optical depth models, present the silicate feature in emission, while face-on views of high optical depth models can show an absorption feature.

It is only recently that the attention has turned towards the nearby 18 μm silicate feature which, being broader and fainter, had almost escaped detection. Sirocky et al. (2008); Thompson et al. (2009) proposed that the comparison of the strengths of the two silicate features could be used as diagnostic of dust composition and, also, to discriminate between smooth and clumpy distributions.

The possible role played by these feature as diagnostic has been investigated in Feltre et al. (2012) where the results obtained are reported in Section 5.1.1.

	SMOOTH	CLUMPY
Y	10, 30, 60, 100, 150	10, 30, 60, 100, 150
q	0, 1	0, 1
γ	2, 4, 6	
σ		60°, 45°, 35°
$\tau_{9.7}$	0.3, 0.6, 1, 2, 3, 6, 10	
N_0		1 - 15
τ_V		5, 10, 20, 30, 40, 60, 80

Table 5.1: Matched model parameter considered in the comparative study.

5.0.2 The matched model parameter spaces

The two original model grids cover a large parameter space and produce SEDs with a considerable overlap when their parameters are "matched". The selection of the matched parameter space is of interest here, as it is not always straight forward given the different nature of the two models. However good analogies can be found, under a few reasonable assumptions. The inner-to-outer radius ratio, Y, is a parameter in common between the two models. The radial variation of the dust density or that of the clouds, q, can also be considered as equivalent between the two models. The relation between the optical depth at 9.7 μm and that in the V band is given by N08 as $\tau_{9.7} = 0.042 \times \tau_V$. The equatorial optical depth $\tau_{9.7}$ for clumpy models is then equal to $0.042 \times \tau_V \times N_0$. The resulting $\tau_{9.7}$ are not identical to those used in the smooth models, the values, however, are very close and the differences they introduce in the resulting SEDs negligible. Finally, considering only the two extreme lines of sights, the torus opening angle is of no relevance and γ (Eq. 3.10) and σ (Eq. 3.13) can be taken such that the distribution of dust and clumps match each other (see Tab. 5.1 for the exact values).

Table 5.1 summarizes the values of the models parameters that will be considered henceforth. Fig. 5.2 shows, for illustration purposes, the shapes of the model SEDs characterized by the above parameters, for type 1 and type 2 views.

In matching the models parameters as described above we significantly restrict the model grids and end up comparing a total of 614 smooth and 480 clumpy models. The difference in the numbers is due to the fact that often more than one combinations of N_0 and τ_V correspond to the same $\tau_{9.7}$. Furthermore, since we only consider the two extreme inclinations (smooth) and probabilities (clumpy), as already explained before Θ becomes of no relevance and hence three values shown in Table 5.1 are consider for each given γ and σ.

Note that in matching the models parameters, some parameter values were left out from both model grids and the comparison presented here only applies to the restricted grids. In effect what is left out from these grids are clumpy models with

very compact configuration (q$>$ 1) since there are no available equivalent smooth models, smooth models with very low optical depth ($\tau_{9.7} < 0.3$), as well as clumpy models with various combinations of N_0 and τ_V that do not correspond to any $\tau_{9.7}$ from the smooth grid.

5.1 A Model-to-Model Comparison

We use two different ways to directly compare the characteristics of the SEDs obtained from the two different dust distributions looking for possible diagnostics. First we measure and compare characteristic quantities of AGN SEDs, namely the width of the IR bump, the prominence or *strength* of the silicate feature, and the NIR slope or the peak of the emission. We then directly compare the overall shape of the SEDs looking for SEDs with similar global shapes. We compare the matched model grids of F06 and N08 models, described in Section 5.0.2, taking into account only the two extreme inclinations corresponding to type 1 and type 2 views.

5.1.1 The silicate features

Astronomical silicates give rise to two main features, one at ~ 9.7 μm and another at ~ 18 μm. The strength of the silicate feature is defined as the logarithm of the ratio between the flux F measured within the line profile over the continuum flux F_c at such wavelength, i.e.

$$S_\lambda = \ln \left[\frac{F(\lambda_m)}{F_c(\lambda_m)} \right] \tag{5.1}$$

where λ_m is the wavelength at which the feature's strength is an extremum with a value in the interval between 8.5 and 11.5 μm (for the computation of F_c see Sirocky et al., 2008). As already mentioned in Section 5.0.1, F06 and N08 models consider different absorption coefficients that peak at different wavelengths. In order to keep the notation of the paper simple but also consistent with other works in the literature, hereafter we will refer to this silicate feature as the "9.7 μm silicate feature", $S_{9.7}$, but the difference between the two should be kept in mind, as it could give rise to different results when the strengths of the silicate features are considered.

Fig. 5.4 compares the values of $S_{9.7}$ for matched smooth and clumpy models in a face-on inclination. The symbols are colour-coded according to the value of N_0. For small values of N_0 the values of the feature for the two models lie close to the 1:1 line (shown in black), however as N_0 takes larger values the points deviate from the line, with the clumpy models showing a weaker feature. This is due to increasing attenuation with increasing number of clouds, as dust is optically thick to itself. The distribution of $S_{9.7}$ for the two dust configurations can be seen in the two top histograms in Fig. 5.5, with the green (red) lines corresponding to smooth (clumpy) configurations.

Both Fig. 5.4 and the histograms at the top of Fig. 5.5 show that a large interval of $S_{9.7}$ values is covered by both dust configurations. The clumpy models with type 1 views can produce equally strong silicate features in emission (Fig. 5.5, top left histogram), despite repeated claims in the literature to the contrary. A large fraction of them, however, does extend to weaker $S_{9.7}$ values. The striking differences in the behaviour of $S_{9.7}$ (with means of 0.79 and 0.62 for type 1 smooth and clumpy, respectively, and -0.48 and 0.06 for type 2 views) have their origin in both the different chemical compositions used by the two models (see Section 5.0.1) and the fact that only the restricted model grids are being compared, leaving out a number of models (both smooth and clumpy) with parameters that can not be matched by the other dust distribution. On the other hand, the long standing issue of very deep silicate absorption produced by smooth models is confirmed, with the tail of the $S_{9.7}$ distribution for edge-on inclinations (Fig. 5.5, top right histogram) extending to large negative values. Both models can produce silicate emission in type 2 views. Since objects with such characteristics are rather uncommon (but not unheard of, see e.g. Sturm et al., 2006; Teplitz et al., 2006; Mason et al., 2009; Nikutta et al., 2009), the models that produce such features should also be seen as non-representative, yet realistic. Furthermore, silicate in absorption in type 1 views is also produced by both models, although only marginally.

Recently the attention has turned towards the 18 μm silicate feature which, being broader and fainter, had almost escaped detection. Its strength, S_{18}, is also computed from Eq. 5.1 with its extremum taking values in the interval between 17.0 and 19.5 μm. $S_{9.7}$ and S_{18} are shown in Fig. 5.5 for type 1 (left) and type 2 (right) views. Clumpy models show stronger S_{18} emission in type 1 views and span a larger range compared to the smooth models. For type 2 views, the values for S_{18} emerging from the two dust configurations are somewhat more similar, but again clumpy models extend to stronger features in emission while there are a few smooth models that show very deep absorption.

Thompson et al. (2009) proposed that the comparison of the strengths of the two silicate features could be used as a diagnostic of dust composition and, also, to discriminate between smooth and clumpy distributions. Fig. 5.5 shows indeed that the relative strength of the two features is very distinct between the two models, however as pointed out by Sirocky et al. (2008) this difference reflects the effect of the different chemical compositions used in the two models (discussed in Section 5.0.1; see also Figs 7 and 9 in Sirocky et al. 2008 showing the changing slope in the S_{18} vs $S_{9.7}$ distribution as a function of the dust chemistry).

The black squares shown in the top panel of Fig. 5.5 are spectral measurements of unobscured AGN, reported by (Thompson et al., 2009). Note that all the observed data lie in the common region of the feature-feature diagram and none occupy the region of intense silicate emission. The spectral measurements of optically classified narrow line AGN (Sirocky et al., 2008) are shown in the bottom panel of Fig. 5.5. Though some objects occupy the region common to both models, some marginally lie in the region populated by clumpy models alone and others

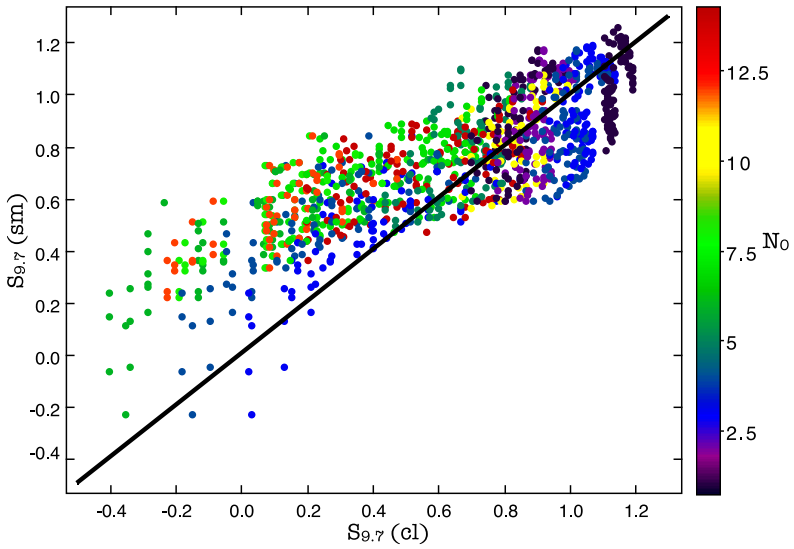

Figure 5.4: The values of $S_{9.7}$ for matched smooth and clumpy models. The points are colour-coded based on the value of N_0 (from Feltre et al., 2012).

in that of smooth models, while three lie in a region without any coverage. A part from the different chemical composition used in the two models (see Section 5.0.1), another reason for such differences is due to the fact that we are comparing two restricted grids both for the F06 and N08 models and, therefore, we are not exploring all the possible combination of parameters.

5.1.2 The characteristics of the SEDs in the infrared

The width of the IR bump

The width of the IR bump, W_{IR}, is defined as the $\log_{10}$ of the frequency range in which the spectrum is more than 1/3 of its peak value (expressed in F_ν) as in e.g. Granato & Danese (1994). While the mean of the distributions of W_{IR} is the same for smooth and clumpy models (12.88 for type 1 and 12.9 type 2 views), and the medians differing only slightly (12.86 versus 12.88 for type 1 views and 12.89 versus 12.9 for type 2 views), clumpy models produce, on average, wider IR bumps, as already noted by other authors (e.g. Dullemond & van Bemmel 2005; Nenkova et al. 2002). The reason behind this is due to the presence, in a clumpy configuration, of a range of temperatures coexisting at the same distance from the primary source (as already explained in Section 5.0.1). These give rise to a wider W_{IR} in clumpy models since they strongly emit at all wavelengths from the MIR to the sub-mm (as already explained in Section 5.0.1). The rms of the W_{IR} distribution of smooth models is twice as large as that of clumpy models

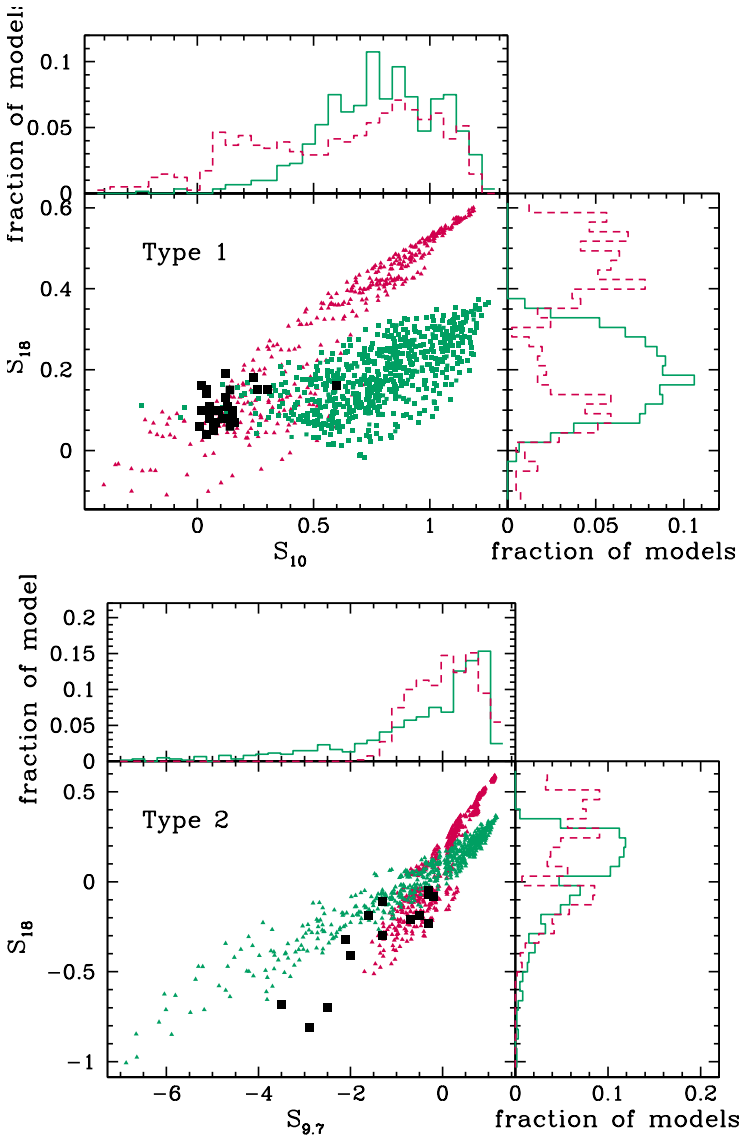

Figure 5.5: S_{18} versus $S_{9.7}$ for smooth (green squares) and clumpy (red triangles) models, and $S_{9.7}$ and S_{18} distributions for type 1 (top) and type 2 (bottom) views (from Feltre et al., 2012). The black squares are values obtained from measurements of real data, that is from a sample of unobscured AGN (from Thompson et al., 2009) and of optically classiffied narrow line AGN from a sample of ULIRGs (from Sirocky et al., 2008) for the top and bottom panel, respectively.

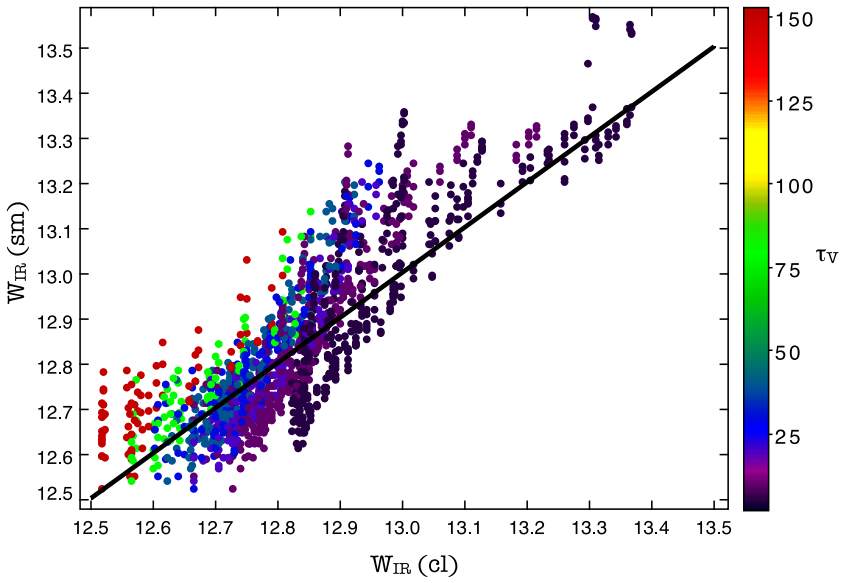

Figure 5.6: The values of W_{IR} for matched smooth and clumpy models for face-on inclinations. The points are colour-coded based on the value of τ_V.

and smooth models can also produce large W_{IR}. In fact, the largest ones in this study are indeed produced by the smooth models in the matched grids. Fig. 5.6 compares the values of W_{IR} for F06 and N08 SEDs of the restricted model grids as a function of τ_V. Though dispersions are observed, in general the points follow the 1:1 line (shown in black). Moreover, in both models W_{IR} increases with the decrease of the optical depth τ_V. This is due to the fact that for low optical depth the radiation coming from the accretion disc is able to heat the dust up to longer distances, resulting in a wider range of temperature.

The IR peak wavelength

The peak of the IR SEDs, λ_{peak}, measured on the continuum alone, excluding the silicate feature is shown in the middle panel of Fig. 5.7. Both sets of models peak at wavelengths typically between 10 and 30 μm, a fraction of smooth models, however, have their peak at very short wavelengths. For both views, the majority of clumpy models culminate at $\sim$30 μm, a behaviour related but not confined to the wider, on average, clumpy SEDs.

NIR spectral index

The spectral index at NIR wavelengths, α_{IR}, is defined as

$$\alpha_{IR} = \frac{\log_{10}(F_{4.5}) - \log_{10}(F_{3.6})}{\log_{10}(\lambda_{4.5}) - \log_{10}(\lambda_{3.6})} \tag{5.2}$$

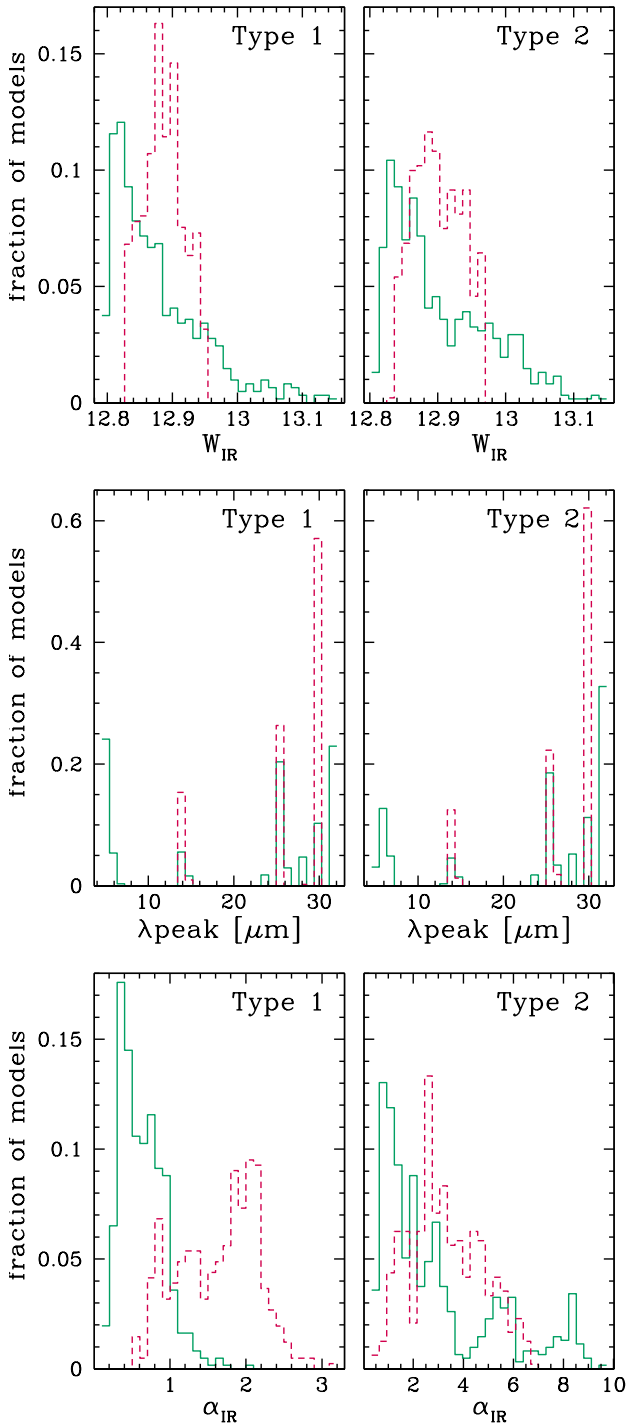

Figure 5.7: From top to bottom: W_{IR}, λ_{peak} and α_{IR}, for type 1 (left column) and type 2 (right column) views, for smooth (green continuous lines) and clumpy (red dashed lines) models (from Feltre et al., 2012).

The distribution of α_{IR} varies a lot depending on the dust morphology (Fig. 5.7, lower panel). For type 1 views in particular, the range of overlap is very small, with clumpy models producing, on average, steeper spectra. The mean (median) of the distributions for the smooth and clumpy models are 0.63 (0.58) and 1.63 (1.74), respectively. The same occurs for type 2 views but to a lesser extent, with a mean (median) of 2.98 (2.1) and 3.32 (3.18) for smooth and clumpy dust, respectively. Three components contribute to these differences: i) the lack of a very hot component in the clumpy models (see e.g. Deo et al. 2011), ii) the primary source (different power laws and different wavelength coverage for the two dust distributions), and, to a much lesser extent, iii) the scattering in the clumpy medium, which strongly depends on the distribution of the clouds. We calculated the average fractional contribution of the primary source to the flux at 3.6 and 4.5 μm to be of 1.5% and 0.7%, respectively, for clumpy models, while it is constant and $\sim$44% in smooth models in both bands. This would account for about 30% of the difference in the values of α_{IR} between the two dust configurations and, therefore, the remaining difference must be due to point i).

The luminosity at 12.3 μm

Some recent works indicate that the MIR emission, in particular the monochromatic luminosity at 12.3 μm, $L_{12.3}$, can be used as a diagnostic to distinguish between a smooth and a clumpy configuration. Horst et al. (2006) found that in a sample of eight Seyfert galaxies (a Seyfert 1, an 1.2 and six 1.5 or later), $L_{12.3}$ is tightly correlated with their X-ray $L_{2-10}keV$ luminosity, regardless of their type. This was interpreted as an evidence for the dust being optically thin at 12.3 μm, a characteristic which was reported to be typical of clumpy models, but incompatible with the smooth model of Pier & Krolik (1992).

We have checked the sets of clumpy and smooth models against this prediction, by computing the ratio of $L_{12.3}$ in type 2 over type 1 views, shown in Fig. 5.8. The solid black line, corresponding to $L_{12.3}^{type_2}/L_{12.3}^{type_1} = 1$, delimits the optically thin and the optically thick region with the first corresponding to value of $L_{12.3}^{type_2}/L_{12.3}^{type_1} > 1$ and viceversa. We note that, with the exception of 7% of clumpy models that are very close to the optically thin line, both sets of models always lie in the optically thick region, i.e. $L_{12.3}^{type_2}/L_{12.3}^{type_1} > 1$. This results shows that the $L_{12.3}^{type_2}/L_{12.3}^{type_1}$ ratio does not allow to distinguish between smooth F06 and clumpy N08 configurations and does not show any real evidence of the above claim.

Global SED shape

We have shown that even models with matched parameters can produce very different features (see Fig. 5.4). But could random parameter combinations result in very similar model SEDs? In order to answer this question, we introduce a measure of the dissimilarity of any two SEDs based on the properties discussed in the previous sections as follows:

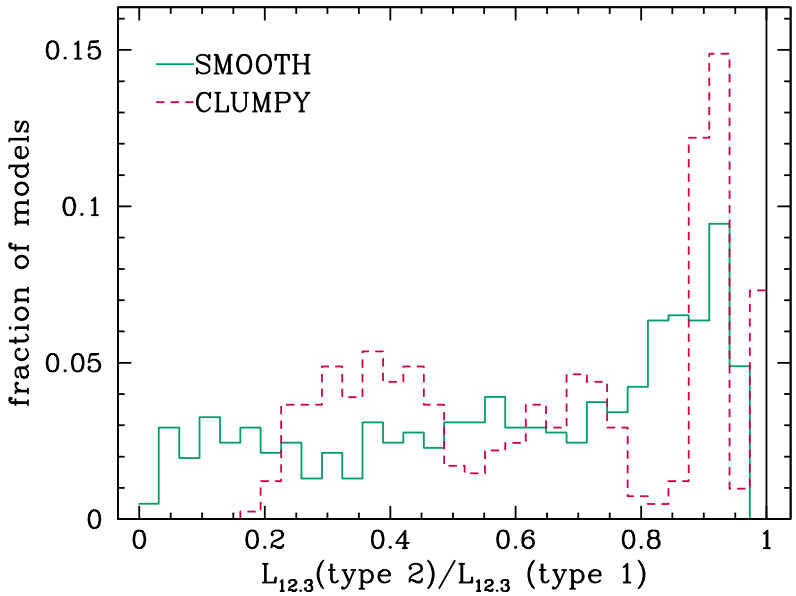

Figure 5.8: The distribution of the ratio of $L_{12.3}$ in type 2 over type 1 views, for smooth and clumpy models (from Feltre et al., 2012).

$$\bar{\Delta} = \frac{1}{6}\left(\left|\frac{S_{9.7}^{sm} - S_{9.7}^{cl}}{S_{9.7}^{sm}}\right| + \left|\frac{S_{18}^{sm} - S_{18}^{cl}}{S_{18}^{sm}}\right| + \left|\frac{W_{IR}^{sm} - W_{IR}^{cl}}{W_{IR}^{sm}}\right| + \left|\frac{\lambda_{peak}^{sm} - \lambda_{peak}^{cl}}{\lambda_{peak}^{sm}}\right| + \left|\frac{\alpha_{IR}^{sm} - \alpha_{IR}^{cl}}{\alpha_{IR}^{sm}}\right| + \left|\frac{C^{sm} - C^{cl}}{C^{sm}}\right|\right) \tag{5.3}$$

where *sm* and *cl* denote smooth and clumpy models, respectively, $C = F_{24}/F_{4.6}$ and $F_{4.6}$ and F_{24} are the fluxes at 4.6 and 24 μm respectively. C has been introduced to take into account the relative fluxes of the (normalised) models in addition to the IR spectral index, α_{IR}. Comparing the value of $\bar{\Delta}$ for each pair of matched models, we find that none of the pairs have a value lower than 0.1. Furthermore, we only find 6 combinations for type 1 views and 21 combinations for type 2 views with $\bar{\Delta} \leq 0.1$, with very different model parameters. We therefore conclude that there are virtually no random pairs of smooth and clumpy models in the matched grids that can produce very similar SEDs.

5.2 Fitting the Observed SEDs of AGN

To extend our analysis we investigate how the matched grids of F06 and N08 model SEDs, described in Section 5.0.2, behave when compared with observed photometric and spectroscopic datasets. We conduct this study in two distinct

steps, treating photometry and spectra separately and considering this time all the 10 inclinations for which the model SEDs are computed.

We use the type 1 quasars photometric catalogue presented in Hatziminaoglou et al. (2008). The entire sample consist of 278 spectroscopically confirmed SDSS type 1 quasars with redshift spanning $0.06 < z < 5.2$ and the SEDs comprise SDSS photometry (*u,g,r,i,z*), 2MASS (*J,H,K*, whenever available) and MIR data from SWIRE (Lonsdale et al., 2004) in IRAC 1-4 channel fluxes (3.6, 4.5, 5.8 and 8.0 μm) and MIPS 24-, 70- and 160-μm (whenever available). Restricting the study to type 1 AGN allows to better constrain the accretion luminosity, as the optical/UV data points are most of the times not significantly contaminated by stellar emission. The resulting best-fitting models are thus less likely to be affected by model degeneracies compared to type 2 objects.

5.2.1 Spectral data

We have also extracted a list of 97 objects, 58 type 1 and 39 type 2, with available IRS spectra covering the wavelength range between roughly $\sim$ 5 and $\sim$ 40 μm, from a larger compilation presented in Hernán-Caballero & Hatziminaoglou (2011). Namely, we made use of spectra taken from Netzer et al. (2007); Lutz et al. (2008); Sturm et al. (2006); Brand et al. (2008); Cao et al. (2008); Deo et al. (2007); Maiolino et al. (2007); Polletta et al. (2008); Tommasin et al. (2008); Weedman & Houck (2009). The sample consists of AGN of quasars and Seyfert galaxies spanning a large redshift range, between 0.009 to 2.793.

5.2.2 SED Fitting

SED fitting not only constrains the input model parameters but also the derived physical properties, described in details in Section 6.4. For the aims of this comparison the ones of interest are:

- the accretion luminosity, L_{acc}, i.e. is the soft X-ray, UV and optical luminosity coming from the accretion disc;
- the IR luminosity, L_{IR}, defined as the integrated flux between 8 and 1000 μm;
- the contribution of the different emission components (AGN and starburst) to the total IR luminosity;
- the outer radius, R_{out} derived from the outer-to-inner radius ratio that is an input parameter to both models;
- the optical depth along the line of sight;
- the covering factor, CF, defined as the fraction of the nuclear emission covered by obscuring material.

- the gas torus mass, M_{torus} computed as the mass of all the dust grains integrated over all volume elements and applying a gas-to-dust ratio of 100 (Draine et al., 2007) for F06 models, while for N08 models is the sum of the gas mass of the clouds.

Note that when fitting the type 1 AGN sample with available photometric datapoints, we are using the AGN-added clumpy models. When fitting the IRS spectra, we could used indiscriminately either the AGN-added or the torus-only SEDs because they are identical at IR wavelengths (as explained in Section 5.0.1).

Since all the torus emission models are calculated having $L_{acc} = 10^{46}$ or 10^{45} erg/s (for smooth and clumpy, respectively) the total SED (dust + accretion) will be in general rescaled to the intrinsic luminosity of the object. Once defined the optical depth and once it will be kept constant, due to a characteristic of the radiative transfer equation, the emission properties rescale in the same way without modify the shape of the SED itself. Consequently, given the inner radius (calculated from the torus model) the corresponding "physical" value for a certain object is obtained from Eq. 3.9 or Eq. 3.12, depending on the kind of models used, simply replacing the value of the accretion luminosity as calculated in the fit. The outer radius is calculated consequently. Another quantity scaling on the base of the normalization factor is the dust mass of the torus. Simple considerations bring to conclude that this scale linearly with the luminosity. Other properties, such as the optical depth, the extinction or the hydrogen column density or the SED shape itself, remain unchanged.

5.2.3 Fitting the UV-to-FIR Photometry

We first fit the broad band SEDs of the sample described at the beginning of Section 5.2. To compare models with the photometric data we use a fully automatic fitting procedure, described in Chapter 4, that considers three distinct contributions to the observed SED of an active galaxy from the UV to the FIR: a stellar component that would dominate the optical and UV emission in type 2 AGN but only plays a minimal role when fitting type 1 AGN, the hot dust (torus), that peaks in the MIR, and the emission due to the star formation activity which mainly contributes in the FIR. As explained in Chapter 4 the goodness of the fit is measured in terms of the reduced χ^2_ν of each fit. Note that, even though the χ^2_ν can reach high values, this does not undermine the confidence of our fits. The main reason for high χ^2_ν can be sought in the small photometric errors, as explained also in Hatziminaoglou et al. (2008). Indeed, both for SDSS and SWIRE catalogues the errors are very small (of the order of few percentage). Although the fits are proper weighted by using errors in the catalogues, the χ^2_ν could results in high values when the errors themselves are small. Others SED fitting codes (e.g. *HyperZ*) impose a minimum flux errors to overcome the problems of high χ^2_ν; such approach is not applied in our SED fitting procedure. Moreover, especially for this particular case, the SDSS optical/UV data, dominated by the accretion luminosity of

the AGN in type 1 objects, are reproduced with a simple power law instead the observed data are sensitive to the small blue bump and the broad emission lines. The convolution of the models with the transmission curve of the filters would lead more accurate results more accurate is the model representation of the real SED. However, this does not affect the estimation of the L_{acc} since data constrains very feel the optical/UV continuum (Hatziminaoglou et al., 2008).

Following Hatziminaoglou et al. (2008), where a first version of the procedure was presented, we consider acceptable fits those with $\chi^2_\nu < 16$ and the discussion that follows only makes use of the objects that fulfill this condition. This cut excludes 12% (33/278) and 28% (78/278) of objects when smooth and clumpy models are used, respectively. The distribution of the χ^2_ν are shown in Fig. 5.9, obtained using smooth (green) and clumpy (red) torus models. Five and 25 objects were found to have $\chi^2_\nu > 45$ when using F06 and N08 dust distributions, respectively, and are not shown here. When using F06 models, from the 245 objects with acceptable fits 202 required an AGN component alone for their broad band SED to be properly reproduced, 20 required an additional starburst component to account for the emission at longer wavelengths, another 20 needed a stellar component in order to recover the UV-to-optical part of their SED and finally 3 were better described by sets of all three components.

Similarly, clumpy models alone successfully reproduced 167 of the 200 SEDs with acceptable fits, 14 required an additional starburst component, 15 an additional stellar component and, finally, four more were sets of AGN, starburst and stellar components, three of which are the same as when using smooth models.

The reason for which many SEDs are reproduced by a torus component alone is the lack of photometric data at wavelengths longer than 24 μm. The lack of such observational data does not allow to properly constrain the contribution of the colder dust and, hence, does not allow for the use of a starburst template while performing the fit. Note, however, that while all objects with an additional starburst component have at least a 70 μm detection, with a datapoint at $\lambda > 24$ μm were assigned one.

Fig. 5.10 shows one of the best examples of a fit obtained using torus emission alone, for a smooth (top) and a clumpy (bottom) torus component. As a general trend not all the parameters of the two (smooth and clumpy) best models compare each other, in agreement with the conclusions of the model-to-model comparison (see Section 5.1). In this specific case the best fit smooth and torus models are both characterized by an outer-to-inner radius ratio Y= 150 and by a parameter ruling the dust distribution q= 1.0. The rest of the parameters' values are not consistent with the matched parameters in Table 5.1. The rest of the smooth model parameters are: $\Theta = 140^\circ$, an optical depth at 9.7 μm $\tau_{9.7} = 3.0$ and an index for the grains distribution along the vertical coordinate $\gamma = 2.0$. Those of the clumpy models are: an equivalent width of a Gaussian distribution of the clouds $\sigma = 35^\circ$, an optical depth of a single cloud $\tau_V = 5.0$ and an equatorial average number of clouds $\mathcal{N}_0 = 4$. Some of the physical parameters derived from the fits are

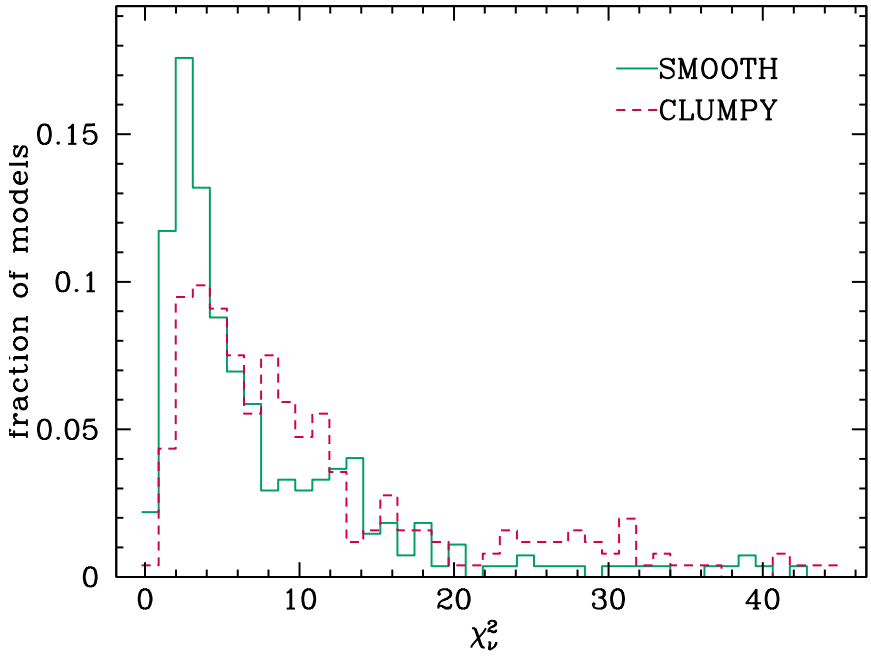

Figure 5.9: Distributions of the reduced χ^2_ν values resulting from the fitting to photometric data, using smooth (green solid line) and clumpy (red dashed line) models.

comparable, while others are very different when different dust distributions are considered. More precisely, the computed L_{acc} is 2.5×10^{46} and 3.3×10^{46} erg/s, for smooth and clumpy configurations, respectively, and the estimated outer torus radius, R_{out}, is of 33 and 347 pc, respectively (more than one order of magnitude of difference). The lower value of the smooth model compared to the clumpy one is due to the fact that R_{out} for F06 models does not correspond to the geometrical radius in the case of a density profile decreasing with the distance from the centre (q$>$ 0.0). Indeed, in these cases R_{out} correspond to the radius where the dust density is equal to 1/10 of the one calculated at the internal radius (see Appendix C.2 for more details on the calculations). The derived torus masses, M_{torus}, are more around one order of magnitude apart, with the smooth configuration yielding a value of 7×10^5 $M_\odot$ and its clumpy counterpart 9×10^6 $M_\odot$.

Fig. 5.11 shows an example of an object whose broad band SED was reproduced by the sum of a starburst and an AGN components. Both smooth and clumpy models have Y= 30. The rest of the parameters do not match each other. The smooth torus (top panel) has $\Theta = 140°$, $\tau_{9.7} = 2.0$ and a dust density profile that varies only along the vertical coordinate (q= 0.0 and $\gamma = 2.0$). The clumpy torus (bottom panel) has $\sigma = 45°$, $\tau_V = 5.0$, $\mathcal{N}_0 = 1$ and a power law index determining the radial distribution of the clouds $q = 1.0$. As for the case previously analysed, while the derived values of the accretion luminosity are consistent, other

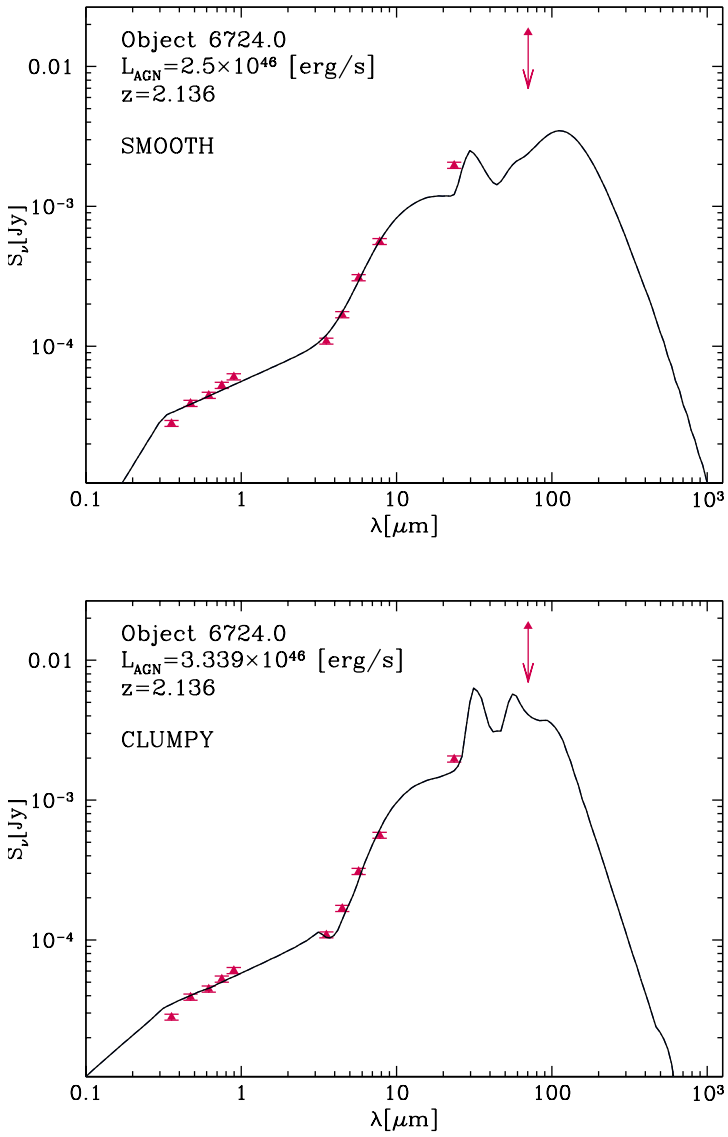

Figure 5.10: Object SDSS_6724 (RA = 16:40:39.31(hms), Dec = +40:31:35.1(dms), sequence number 267 in Table 4 of Hatziminaoglou et al., 2008) is reproduced by a single component, namely that of a type 1 AGN. The best fit in the top panel is obtained considering the emission by a smooth torus with a line of sight at 90° from the equatorial plane (type 1 viewing as expected) and with a full opening angle $\Theta = 140°$, an optical depth at 9.7 μm $\tau_{9.7} = 3.0$, an outer-to-inner radius ratio Y= 100 and a dust density profile that vary only along the vertical coordinates (q= 1.0 and $\gamma = 2.0$). The bottom panel shows the best fit provided by a clumpy torus with a line of sight at 90° from the equatorial plane and with an equivalent width of a Gaussian distribution of the clouds $\sigma = 35°$, an optical depth of a single cloud $\tau_V = 5.0$, an outer-to-inner radius ratio $Y = 150$, an equatorial average number of clouds $\mathcal{N}_0 = 4$ and a power law index determining the radial distribution of the clouds $q = 1.0$.

parameters such as R_{out} and M_{torus} are somewhat discrepant, taking larger values when a clumpy dust configuration is considered.

Even if Fig.5.9 shows χ_2 smaller, on average, for F06 than for N08 models, such difference is not to be consider significant. To conclude, we can consider the best fits produced using F06 and N08 models equally good: we have in this way demonstrated that fitting the spatially un-resolved broad-band SED is not a suitable tool to be used when trying to rule out a dust distribution in AGN, be it smooth or clumpy.

Note that the starburst template chosen in the two fits of Fig. 5.11 is the same, a NGC1482-like component. Nevertheless, it is worth highlighting that in many cases the starburst templates chosen is different when using smooth and clumpy configurations. This can give rise to larger discrepancies between the two fits, compared to the previous examples, in part due to the introduction of the additional (starburst) emission component, that influences the choice of the best fitting torus model. Note however, that the FIR emission is, in this case, very weakly constrained, by a single data point at 70 μm and an upper limit at 160 μm and, hence, this result should be considered with caution. The *Herschel* PACS (Poglitsch et al., 2010) and SPIRE (Griffin et al., 2010) instruments are now providing the much needed FIR data that already allow to better model the cold dust component and to re-iterate on the torus properties (Hatziminaoglou et al., 2010). Therefore, the use such data, being made publicly available by large surveys such as HerMES (Oliver et al., 2012) and H-ATLAS (Eales et al., 2010), are taken into account in chapters 4 and 6.

Results on the photometry fitting

We now explore and compare the physical properties (reported at the beginning of Section 5.2.2) derived from the SED fitting procedure (described in detail in Chapter 4) applied on the samples described in Section 5.2. We focus on the distribution of the physical properties that can be obtained from the best-fitting models and their distributions for models with acceptable χ^2_ν for both F06 and N08 dust configurations.

The accretion luminosity, L_{acc}, as computed from the best-fitting models is, as expected, very well constrained and shows a tight correlation, as it can be seen in the top right panel of Fig. 5.12. This is of course obvious as the primary source SED is seen directly in type 1 AGN, and it does not depend on the details of the radiative transfer modelling. Any difference, mostly in a form of an offset, is due to a different choice of this SED (see sections 3.4.2 and 3.4.3). A slightly higher dispersion is found when comparing the derived IR luminosities, L_{IR}, which are anyway in very good agreement (upper right panel of Fig. 5.12): this result confirms the findings by Hatziminaoglou et al. (2008) who already showed that this is one of the better constrained parameters, along with L_{acc}, when F06 models alone were considered. This somewhat higher scatter in the two sets of values is most

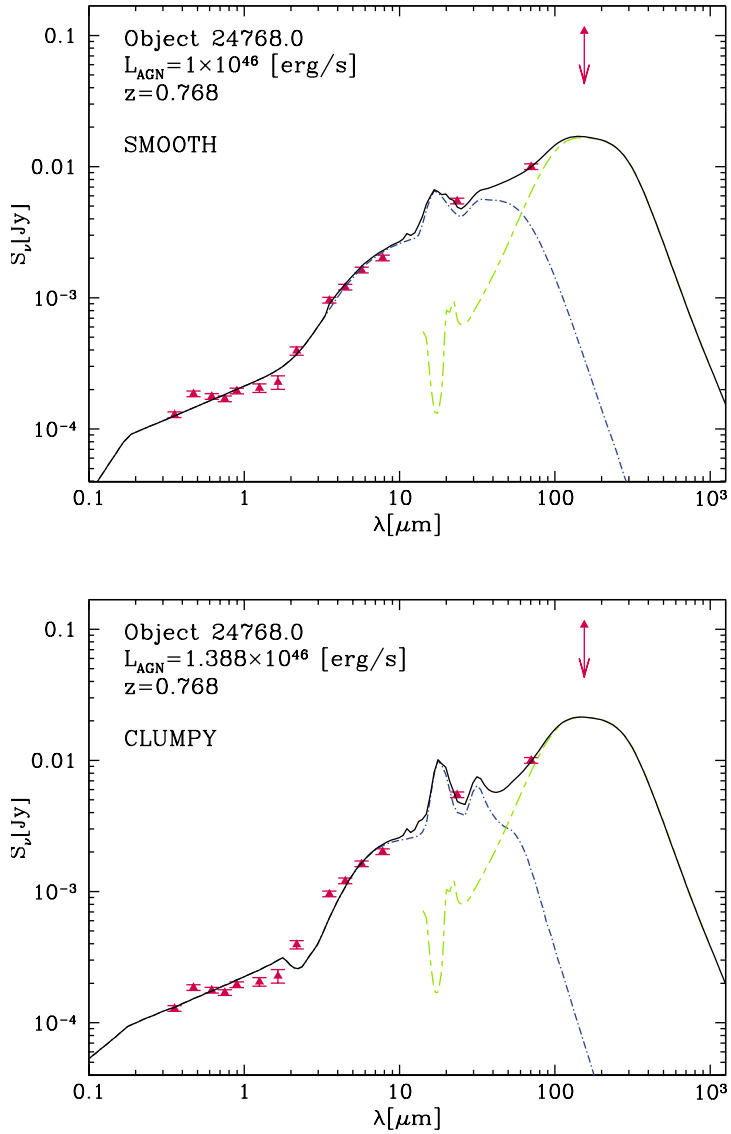

Figure 5.11: Object SDSS_24768.0 (RA = 10:51:06.12(hms), Dec = +59:16:25.2(dms), sequence number 138 in Table 4 of Hatziminaoglou et al., 2008) is reproduced using two components, namely AGN and starburst. On the top panel, the best fit obtained with a smooth torus (dotted dashed dark blue line) at a line of sight of 70° from the equatorial plane, $\Theta = 140°$, $\tau_{9.7} = 2.0$, Y= 30 and a dust density profile that varies only along the radial and the vertical coordinate (q= 0.0 and $\gamma = 2.0$). On the bottom panel, the best fit obtained with a clumpy torus (dotted dashed dark blue line) with a line of sight at 90.0° from the equatorial plane, $\sigma = 45°$, $\tau_V = 5.0$, Y= 30, $\mathcal{N}_0 = 1$ and q= 1.0. In both cases the starburst template (dashed light green line) is that of NGC 1482.

likely due to inherent differences between the two model configurations: F06 and N08 with very similar NIR to MIR SEDs can have longer wavelengths SED shapes that are distinct, and the lack of data points longward of $\lambda = 24$ μm would not allow constraining this particular part of the SED.

Since our sample consists of type 1 sources, we expect most best fits to be characterised by very low (or zero) optical depths along the line of sight. Indeed, 68% (188/245) of the fits obtained using smooth dust models have an optical depth $\tau_{los}(0.55) = 0.0$, with the remaining 32% having $\tau_{los}(0.55) < 0.7$. Instead, the use of clumpy models resulted in higher optical depths on average, with only 9% having $\tau_{los}(0.55) = 0.0$. Furthermore, when we compare the results obtained with the two sets of models, we find no correlation or similarities in the optical depth values. This is most likely reflecting the intrinsic difference in the dust distribution, with clumpy models allowing for much higher values.

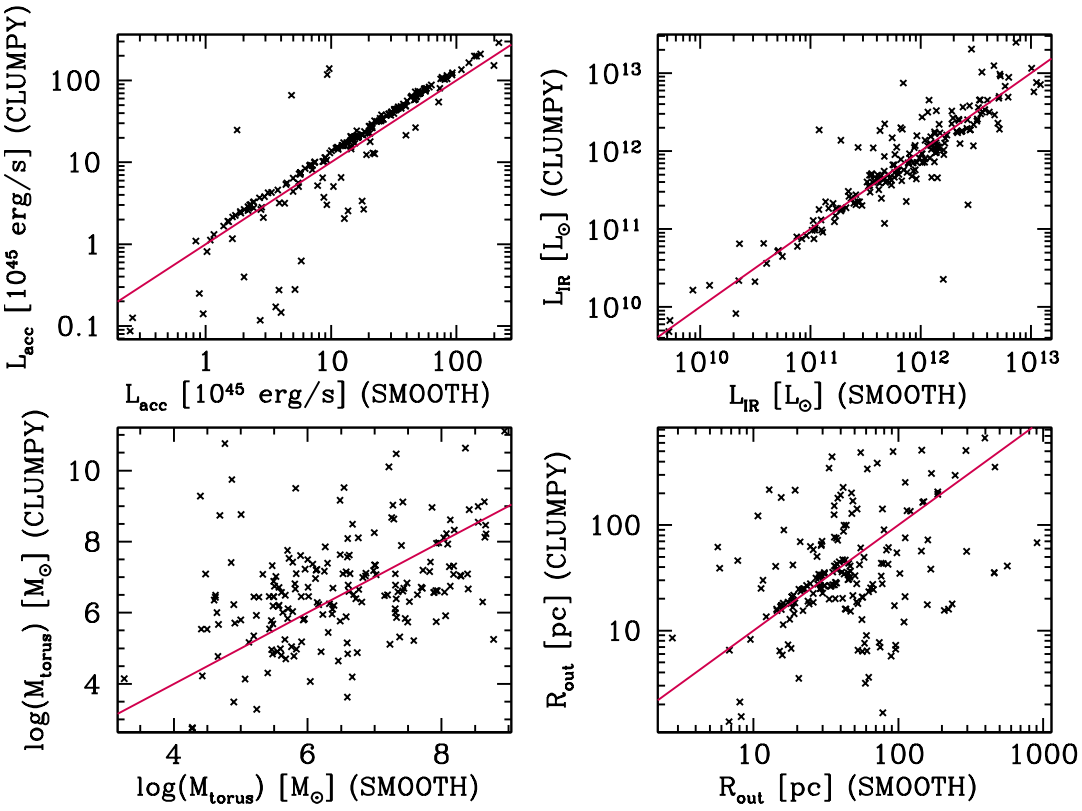

Figure 5.12: A comparison of the main physical properties of the sources under analysis, derived from SED-fitting by exploiting both smooth and clumpy models. On the x-axis we plot the results obtained with F06 model, while on the y-axis the same quantity is considered but from the N08 model application. The red continuous line represents the 1:1 relation in all plots.

The lower left panel of Fig. 5.12 shows the comparison for the derived values of the torus mass: in both cases it spans several order of magnitude and, despite the large dispersion, the two estimates show a broad agreement.

It is generally claimed (e.g. Elitzur & Shlosman, 2006) that smooth models cannot reproduce the small torus sizes that are observed in local, low-luminosity AGN (see, for example, Jaffe et al., 2004; Tristram et al., 2007). In F06 it was already shown that, at least as far as NGC1068 and Circinus were considered, this was not the case. Here, even though the values derived for the physical outer radius with smooth and clumpy models for the single objects are not in agreement (see lower right panel of Fig.5.12), we show that there is no specific tendency towards more compact tori when clumpy SEDs are used to fit an observed SED.

Finally, if we consider the derived values for the covering factor of each single object, we find no good agreement. Smooth models tend to have high torus opening angle, with 62% of objects requiring $\Theta = 140^{\circ}$, while about 67% of clumpy models favour a distribution of the clouds occupying an angle equal to 30° ($\sigma = 15^{\circ}$). Despite this, smooth models tend to have low covering factors, with $\sim 63\%$ of them having a covering factor below 0.5, while the minimum value for clumpy models is 0.3. This is due to the fact that all smooth models in the selected grid have a dust profile which varies along the vertical coordinate. Subsequently, it can be that the opening angle of the torus that *effectively* obscures the central source is the lower part of the torus with an optically thin transition region. This reflect the interplay between the different parameters constituting the models, such as the indices ruling the dust distribution profile, the torus opening angle and the optical depth, and their mutual dependence which can give rise to a similar SEDs.

A relatively small number of clouds in the equatorial coordinate, $\mathcal{N}_0 < 5$, is in general preferred with around 92% of clumpy models satisfying this criteria. Moreover, 55% of best fits clumpy models have Y= 10 and 72% have $\tau_V = 5.0$. It is worth noting that clumpy models favour tori in which the amount of clouds decreases as a function of the distance from the central source. In fact, about the 94% of clumpy best models has q= 1, meaning a declining number of clouds along the radial coordinate. Contrary, smooth models do not show any preference between a constant radial distribution of the dust and a decreasing one, with 50% of the models having q= 0.0 and the other 50% with q=1.0. This, together with clumpy models favoring small Y values, is an indication that when considering clumpy models, data are better reproduced by the more compact clumpy configurations.

5.2.4 Model degeneracies

We can not neglect the model and/or parameter degeneracies that are usually involved in multi-component SED-fitting, due to the various combinations of model parameters that can result in very similar model SEDs, providing thus equally good results in reproducing the observed data. Degeneracies are also a result of

the interdependencies and correlations among some of the model parameters. We investigated the possible correlations that may exist between the physical properties, derived from fitting the observed SEDs, i.e. M_{torus}, L_{acc}, CF, $\tau_{eq}(0.55)$ and R_{out}. We report example results obtained for a few selected sources; however, the tests we performed on all other objects produce very similar results.

To study the degeneracies, we take into account fits with χ^2_ν smaller or equal to 1.5 times the minimum χ^2_ν, $\chi^2_{\nu,min}$, for each object. Figs. 5.13 shows the variations of M_{torus} as a function of L_{acc} (upper left panel) and R_{out} (lower right panel), and those of the optical depth along the line of sight, $\tau_{los}(9.7)$ versus the covering factor (upper right panel) and R_{out} (lower left panel), for fits with $\chi^2_\nu \leq 1.5 \times \chi^2_{\nu,min}$, for SDSS_15814 (objects with sequence numbers 200 (RA = 16:05:23.11 (hms), Dec =+54:56:13.4 (dms)), Table 2 in Hatziminaoglou et al., 2008).

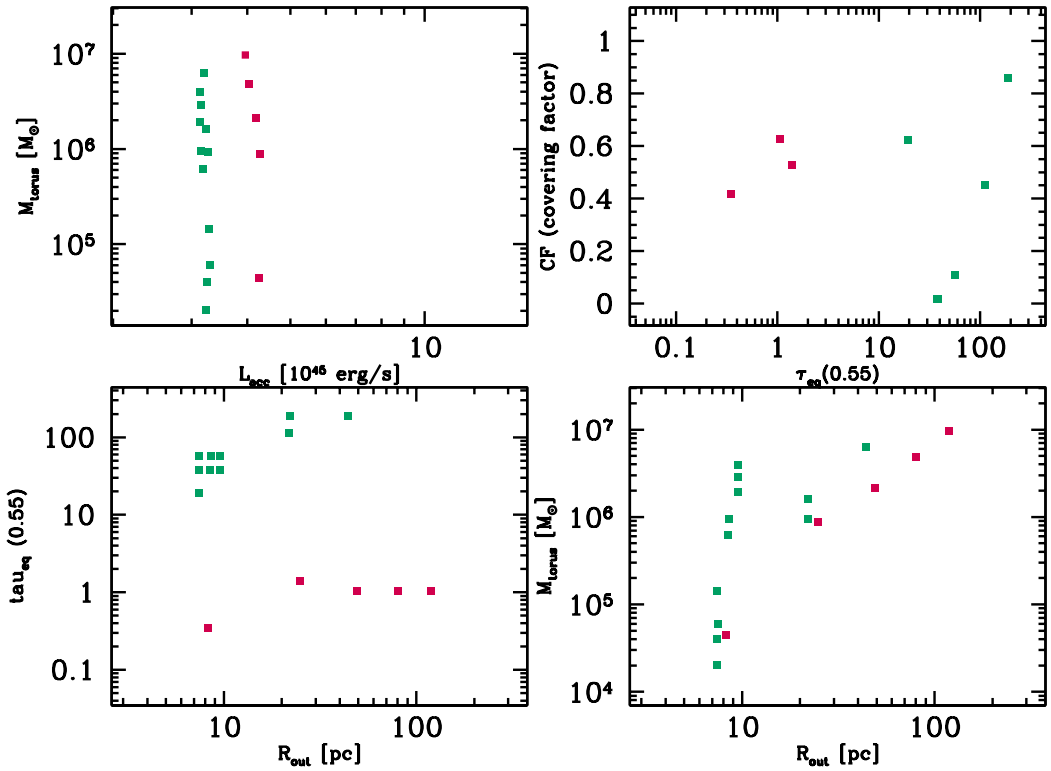

Figure 5.13: Diagrams with the physical properties of the tori models that provide fits with a χ^2_ν less that 1.5 times the minimum χ^2_ν for the source SDSS_15814.0. The parameters shown are as follows: M_{torus} versus L_{acc} (top left panel); M_{torus} versus R_{out} (bottom right panel); CF versus $\tau_{eq}(9.7)$ (top right panel) and CF versus R_{out} (bottom left panel). Green and red squares indicate smooth and clumpy models, respectively.

As already reported in Hatziminaoglou et al. (2008), L_{acc} is not affected by model degeneracies meaning that, once the characteristics of the primary source SED are defined, the values derived from the SED fitting are quite robust. In fact, for type 1 quasars, L_{acc} is directly constrained by the observed UV and optical data. Other physical properties are, however, more affected and hence, their values estimated based on the best-fitting models are not well constrained. In fact, the torus mass spans a large range of values, as it does not only depend on the accretion luminosity (see Section 3.3 of F06) but also on the parameters that define the dust distribution (q and γ) and the outer radius, with values spanning about an oder of magnitude. In fact R_{out} has a weak correlation with M_{torus}, as seen in the bottom-right panels of Fig. 5.13. In this case, interestingly enough, both the torus mass and the physical outer radius show a similar dispersion when F06 and N08 models are used. Similarly, the values of $\tau_{eq}(9.7)$ not only span almost an order of magnitude for each kind of model but there is no overlap in the derived values, either. Clumpy models favour high values of $\tau_{eq}(9.7)$ by an order of magnitude. This difference reflects the two distinct approaches of the radiative transfer problem: in clumpy models the intra-cloud scattering has to be taken into account and that plays an important role.

The equatorial optical depth does not correlate neither with R_{out} nor with CF. In fact, the latter seems to be better constrained by the use of clumpy models models, reflecting its dependence on the probability for the line of sight to intersect a cloud.

Figs. 5.14 and 5.15 show how smooth and clumpy torus models with extreme values of M_{torus} provide equally good fits for the same object (SDSS_15814.0).

5.2.5 Fitting the IRS spectra

We fit the sample of AGN with IRS spectra described at the beginning of Section 5.2 using two components: torus and starburst emission. To reproduce the latter component we adopt a set of starburst templates, namely Arp220, M82, M83, NGC1482, NGC4102, NGC5253 and NGC 7714 (see Section 4.2.3). This starburst component was introduced mainly because most spectra show evidence of Polyciclic Aromatic Hydrocarbons (PAHs), typical indication of star formation activity. We compare the flux of the observed spectra with the flux of the models in some specific wavelength intervals chosen *a priori*. Specifically we use a maximum number of predefined spectral bands in the rest frame range from 0.5 to 59 μm, the spectral coverage of these bands depending of course on the redshift of the source. The wavelength included between 6.8 and 13.9 μm, which is of crucial importance to our study as it samples the 9.7 μm silicate feature, was more accurately sampled, making sure that emission bands from PAHs were avoided. Once the model SEDs are moved to the observed frame, we perform an automatic search for the best combination of AGN and starburst template that minimizes the differences between the observed spectrum and the total (AGN+starburst) theoretical SED.

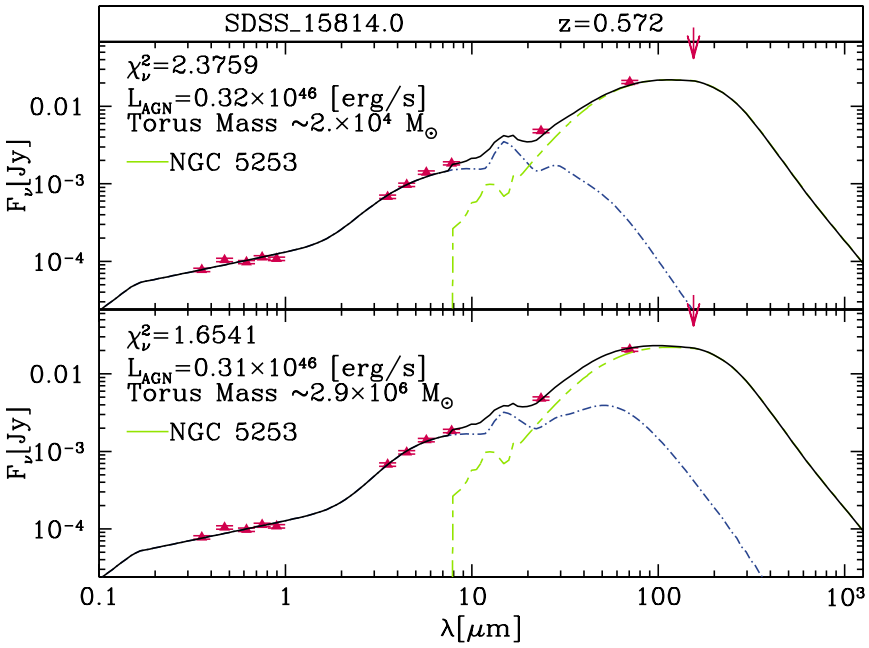

Figure 5.14: SED fitting for source SDSS_15814, obtained using two smooth models (blue lines) characterised by very different torus mass, namely $\sim 2 \cdot 10^4$ and $\sim 2.9 \cdot 10^6$ $M_\odot$ for the top and bottom fits, respectively.

This is done by χ^2_ν minimization.

As a general rule, both smooth and clumpy models can reproduce an observed spectrum in equally satisfying ways. Some examples are given below. The two top panels of Fig. 5.16 shows how the IRS spectrum of the type 1 object SBS_1408+567 (Lutz et al., 2008) is reproduced by smooth (top left panel, green line) and clumpy (top right panel, red line) models, with the contribution of an NGC 5253-like and NGC 4102-like starburst template, respectively. The smooth model predicts a torus with an amplitude $\Theta = 100°$, an optical depth $\tau_{9.7} = 6.0$, an outer-to-inner radius ratio Y= 30 and a viewing angle of 20° from the equatorial plane. Moreover, it is important to note that parameters that rule the spatial density behaviour (see Eq. 3.10) are q= 0.0 and $\gamma = 6.0$, respectively. This means that the dust distribution could be concentrated around the equatorial plane. The clumpy model predicts a torus with a Gaussian distribution of the clouds $\sigma = 60°$, an optical depth of a single cloud $\tau_V = 20.0$, an outer-to-inner radius ratio Y= 10, an equatorial average number of clouds $\mathcal{N}_0 = 10$ and a power law index determining the radial distribution of the clouds q= 1.0. The viewing angle, in this case, is 90° from the equatorial plane. It is worth noting that no one of the parameters of a smooth models is consistent with the value of the correspondent (see Section 5.0.2) clumpy parameter but the SED shape of both best models reproduce the

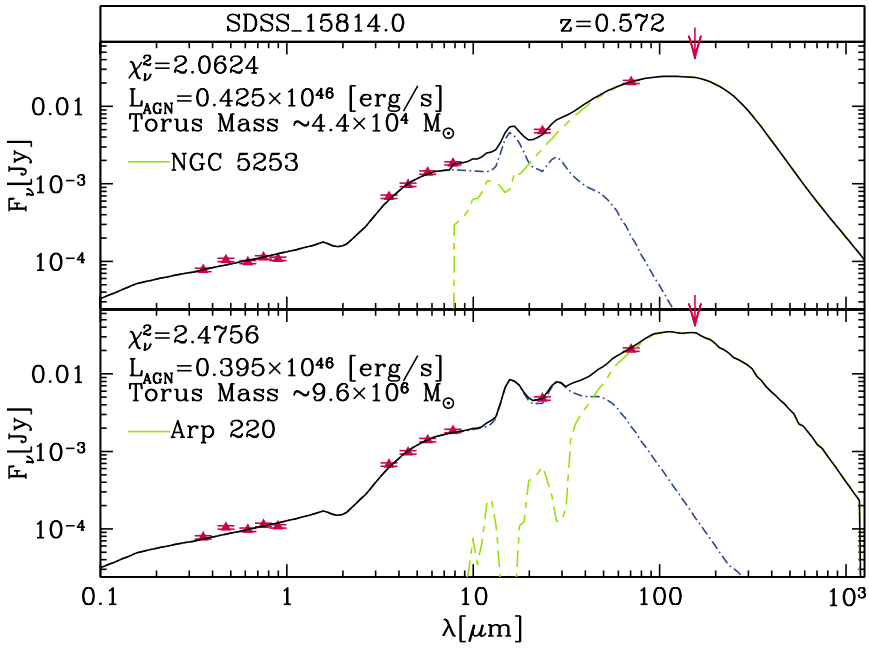

Figure 5.15: SED fitting for source SDSS_15814, obtained using two clumpy models (blue lines) characterised by very different torus mass, namely $\sim 4.4 \cdot 10^4$ and $\sim 9.6 \cdot 10^6$ $M_\odot$ for the top and bottom fits, respectively.

data equally well. Similarly, the two bottom panels of Fig. 5.16 shows the fit of the IRS spectrum of the type 2 object IRAS00198-7926 from Tommasin et al. (2008) with a NGC5253 SED both in the case of smooth (bottom left panel, green line) and clumpy models (bottom right panel, red line). The result as estimated by the χ^2_ν values, are excellent in both cases. The starburst component is required only to reproduce the longer wavelengths, which are dominated by emission from colder dust, and it actually could be replaced, for this almost featureless spectrum, by a grey body spectrum.

Some objects show preference towards smooth models while others are better reproduced by clumpy models. An example where a good fit is obtained using clumpy model while no good fit results from the use of smooth models is shown in the bottom panels of Fig. 5.17. Here the most relevant problem is reproducing the silicate feature at 9.7 μm in the spectrum of AGN (from Weedman & Houck, 2009), that is in fact underestimated when fitting it with smooth models.

It is worth to note that among the spectra studied here there are those of Netzer et al. (2007) which are already used in the work of Mor et al. (2009). The authors, after subtracting the spectrum of the starburst galaxy M82, were not able to reproduce the observations using the clumpy dusty torus from Nenkova et al. (2002). For this reason they consider two additional components for the SED fitting: a

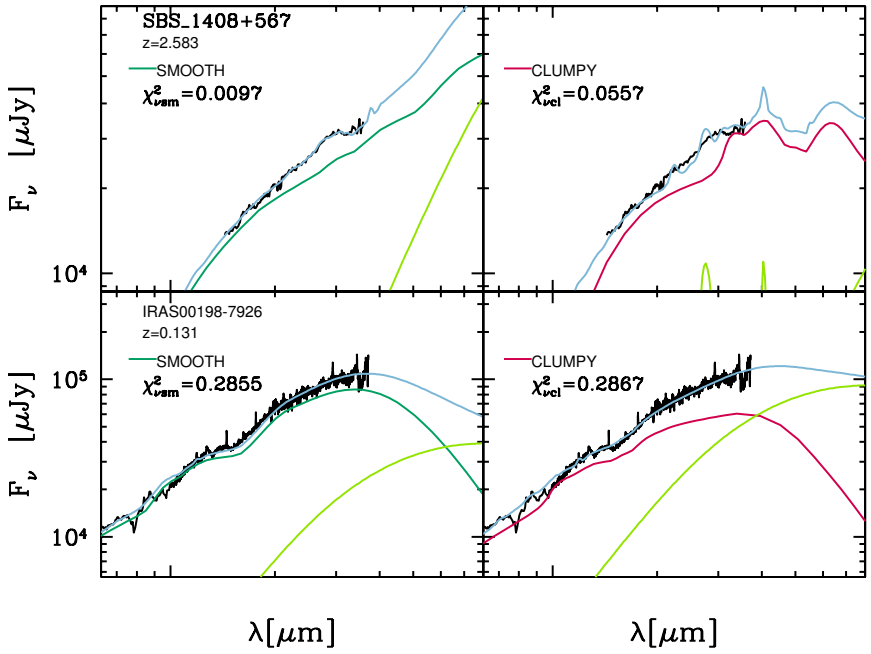

Figure 5.16: Two top panels: SED fitting of the IRS spectrum of the type 1 object SBS_1408+567 (from Lutz et al., 2008) using smooth (left, green line) and clumpy (right, red line) models. Two bottom panel: the same for the IRS spectrum of the type 2 object IRAS00198-7926 (from Tommasin et al., 2008). In all the panels the spectrum is shown as a black line, the total model in light blue and the starburst template in light green. See text for the parameters of the models and for the characteristics of the fits.

Broad Line Region (BLR) clouds and a black body representing the emission of hot dust. Here, however, we show that the use of both smooth and clumpy models provide good fits of the spectra. The additional starburst component not only fits, in most cases, the PAH features but is also necessary for both models to reproduce the emission due to colder dust.

The bottom panels of Fig. 5.17 show the example of PG1004+130 from Netzer et al. (2007). This difference, relative not only to the number and the nature of the components utilized but also to the goodness of the best-fitting model, is difficult to quantify, as not many details on the exact fitting procedure used by Mor et al. (2009) are available. A possible explanation to this is that the subtraction of one single starburst SED component (M82) for all objects, as carried out in that work, biases the procedure, making the introduction of a further very hot component necessary. All other objects of the Netzer et al. (2007) sample are equally well reproduced by both models using either a combination of an AGN a starburst component or by an AGN component alone.

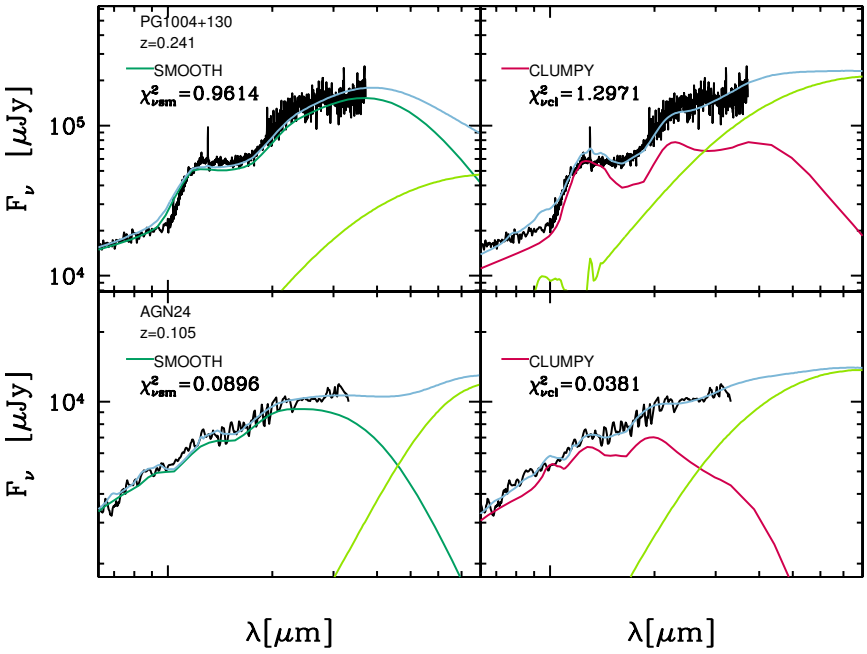

Figure 5.17: The same in Fig. 5.16 for the IRS spectrum of the type 1 object PG1004+130 (from Netzer et al., 2007) and the type 2 object AGN24 (from Weedman & Houck, 2009) on the top and bottom panels, respectively.

Results of IRS spectral fitting

We consider as acceptable those fits with a reduced χ^2_ν values less than 1.5, excluding thus 16% (16/97) and 25% (73/97) of the fits obtained with smooth and clumpy models, respectively. When only MIR spectra are considered, the goodness of fit between model and observations is not significantly affected by the choice of model (smooth or clumpy). Fig. 5.18 illustrates the distribution of the χ^2_ν values provided by spectral fits, for both smooth and clumpy models. We remind that the probabilities associated with the χ^2 can not be taken as a face value. In this case the χ^2 can be overestimated due to same spectra with more noise than others. Indeeed, the IRS spectra used in this work, as explained in Section 5.2.1, have been collected from various authors and then processed with different reduction procedure and wavelength binning.

As in Section 5.2.3, we now investigated the various physical properties derived from the fitting procedure. A first observation is that most clumpy models yield larger $\tau_{eq}(0.55)$ with respect to smooth models, something that could be due to the effect of scattering among clouds.

On the upper panels of Fig. 5.19 we compare accretion luminosity and FIR luminosity as calculated from the spectral fitting with our two sets of models. While the derived infrared luminosities are independent from the adopted model,

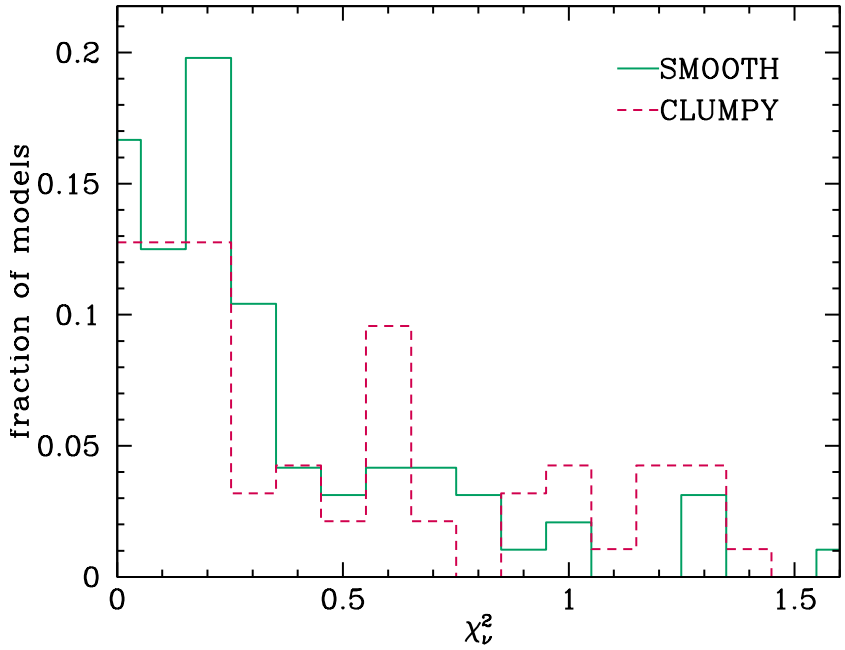

Figure 5.18: Distributions of the reduced χ^2_ν for the best fits to the IRS spectra, using smooth (green solid line) and clumpy (red dashed line) models.

the accretion luminosity values are systematically higher by ~ 0.2 dex.

Comparing the derived values for M_{torus} and R_{out} (lower panels of Fig. 5.19), we found that mass values, even though with a large dispersion, show a better agreement with respect to the same comparison made from the photometry fitting. The values of the physical radius of the torus are also less dispersed compared to the photometry fit.

As already found for the broad band photometry fitting, in Section 5.2.3, none of the values in the model parameters can be excluded. For type 1 views 70% of best smooth models present tori with large opening angle ($\Theta = 40°$), 60% with the dust concentrated on the equatorial plane (γ=6.0) and 70% have $\tau_{9.7} > 6.0$. The 85% of best smooth models has a constant density profile along the radial coordinate (q=0.0), while 65% of best clumpy has q=1.0. Considering best clumpy models for type 1 objects: 50% has $\mathcal{N}_0 < 10.$, 65% has compact size (Y$\leq$10) and 80% has low optical depth (t_V < 10.0). Also for type 1 objects the best smooth models (60%) favor large opening angle. $\sim$ 60% of best smooth has q=0.0 and the 84% has high optical depth. For type 2 views, best clumpy models do not show preferences for $\mathcal{N}_0$ and q, with an uniform distribution of these two values. 40% has Y=10 and another 40% has Y=150. The 85% has t_V20.0. The 60% of best clumpy, for both type 1 and 2 objects, has $\sigma = 60°$.

We also estimated the contribution of the AGN to the integrated flux of the spectra for each of the objects in the sample, shown in Fig. 5.20. For each object,

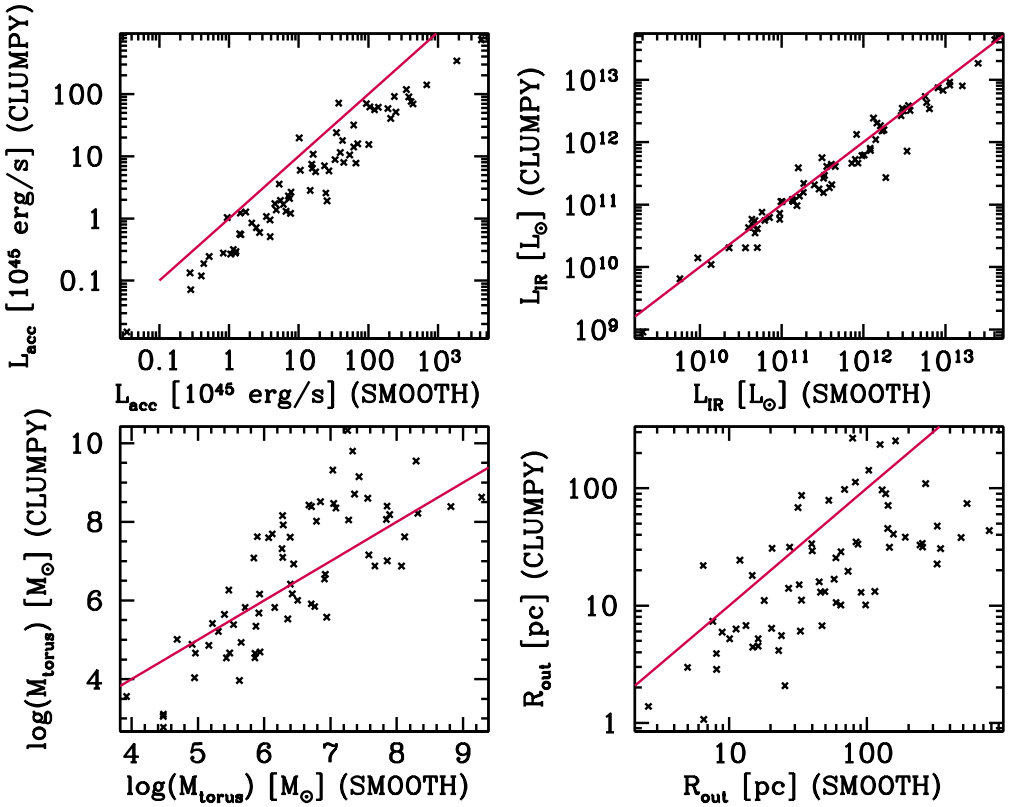

Figure 5.19: The same as in Fig. 5.12. In this case the physical properties are obtained from the best fits to the IRS spectra.

we calculated the integrated fluxes for the AGN component and for the total spectrum, obtained combining the AGN and the starburst emission, that give the best fit. We find that ∼91% and the ∼79% of smooth and clumpy models, respectively, provide a contribution to the spectrum luminosity greater than or equal to 50%, while there are very few cases where the emission is dominated by the starburst component. This result does not apply on the total L_{IR} because the fit relies only on the MIR spectra. This was of course to be expected, as the objects under study were selected to be AGN but also because the IRS spectral coverage leaves out the wavelengths where the starburst emission dominates (λ ∼60-200 μm).

5.2.6 Model degeneracies

For each IRS spectrum with at least one good fit there are very often more than one combinations of AGN and starburst components able to produce other, equally good fits, giving once again rise to degeneracies. As for the photometric data fitting, we consider fits with $\chi^2_\nu \leq 1.5$ times the minimum χ^2_ν. Figs. 5.21 and 5.22 illustrate two examples of properties degeneracies when fitting two IRS spectra from the sample of Tommasin et al. (2008): IRASF15091-2107 and IRASF22017+0319,

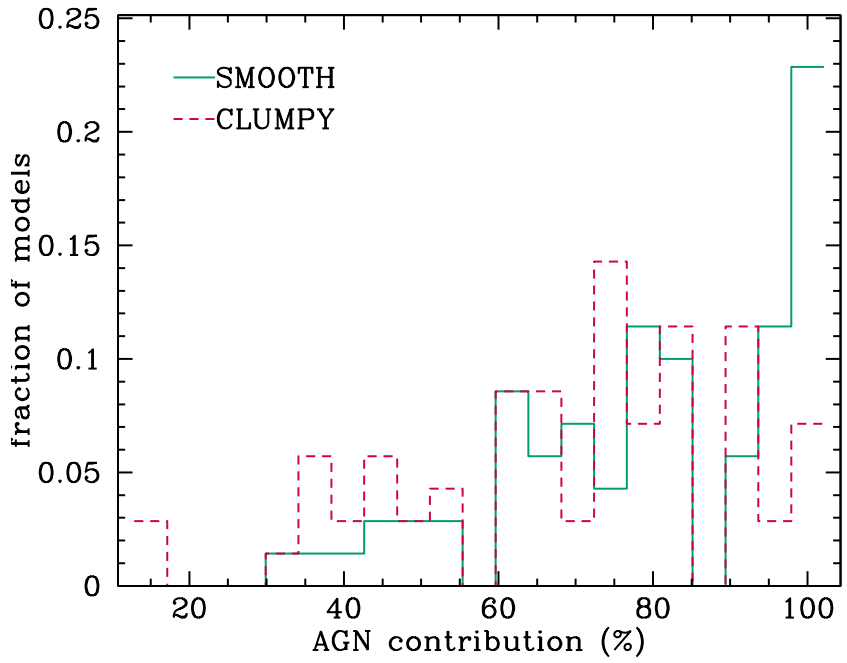

Figure 5.20: Distribution of the AGN contribution to the total flux of the spectra, for smooth (green solid line) and for clumpy (red dashed line) models.

a Seyfert 1 and a Seyfert 2, respectively. Again, models with very different physical properties can reproduce equally well the observed spectra. Other than the intrinsic torus models degeneracies, another factor that may add to the effect is the relatively narrow spectral coverage available that does not allow to constrain neither all the torus properties nor the starburst template. The choice of the latter in turn influences the choice of the torus model.

The accretion luminosity, that was very well constrained by photometric data, now spans a larger range of values. This was to be expected when fitting only the MIR part of the SED, as $L_{\rm acc}$ can best be constrained when UV and/or optical data are available. The large spread in the values of $M_{\rm torus}$ and $R_{\rm out}$ is due, as noted in Section 5.2.4, to their interdependency and to their dependence on the parameters that rule the dust distribution. In this case the equatorial optical depth, calculated at 0.55 μm, presents a very high level of degeneracy with $\tau_{eq}(0.55)$ being more than about one order of magnitude larger.

5.3 Discussion and Conclusion

Within the paradigm of the AGN unified scheme, the different properties of the various types of AGN are attributed to the interception of the line of sight by an axisymmetric molecular dust distribution encircling the nucleus, likely in the

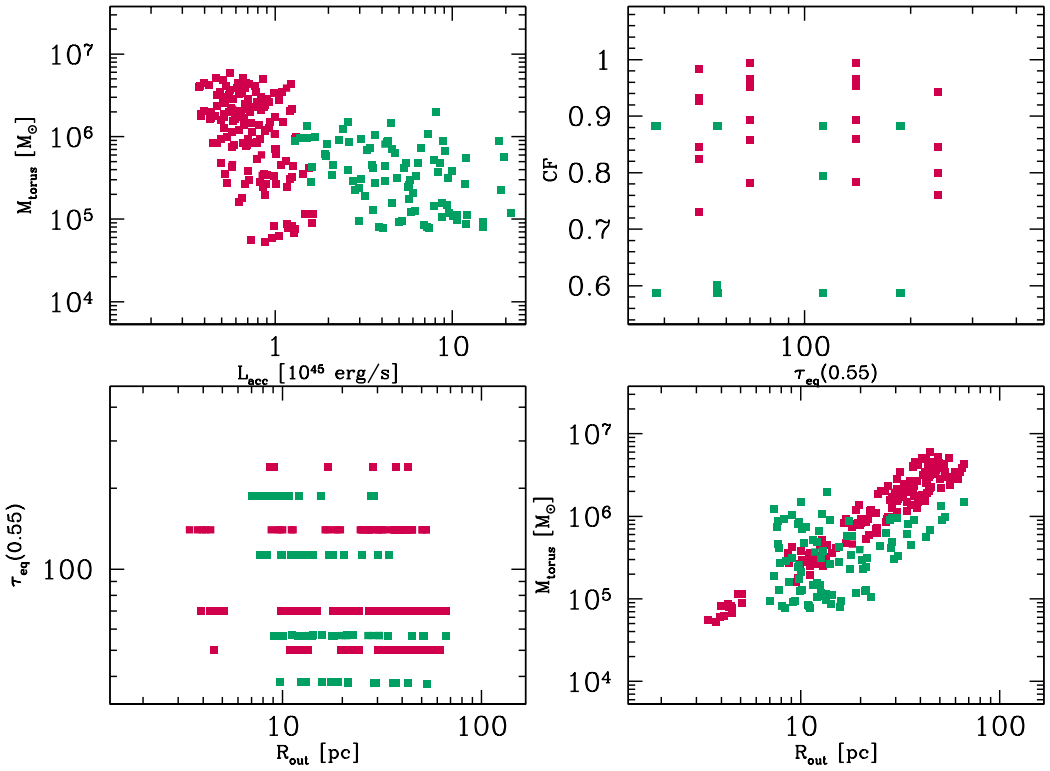

Figure 5.21: Same as in Fig. 5.13, fitting the IRS spectrum of the Seyfert 1 object IRASF15091-2107. In this case the equatorial optical depth, $\tau_{eq}(0.55)$ is calculated in the visible band, at 0.55 μm. Green and red squares denote smooth and clumpy models, respectively.

form of a torus. Direct and indirect observational evidence, such as the dichotomy of the AGN population in obscured and unobscured objects, the ionization cones for the NLR, the MIR bump present in the SEDs of all known AGN attributed to emission by dust heated by the primary source, but also IR interferometry that directly resolved the inner parsec of the nucleus of the prototype Seyfert 2 galaxy NGC 1068 (Wittkowski et al., 2004; Jaffe et al., 2004), all support the existence of a toroidal absorbing structure. As there is evidence favouring both a clumpy distribution (e.g. Risaliti et al., 2002; Wittkowski et al., 2004; Tristram et al., 2007) and a smooth distribution (e.g. Ibar & Lira, 2007), both smooth and clumpy models are still equally widely used to explain the observed SEDs of AGN, counting both successes and shortcomings.

In this chapter we compared two of the most popular sets of models currently available in the literature, namely an extension of the smooth model grid based

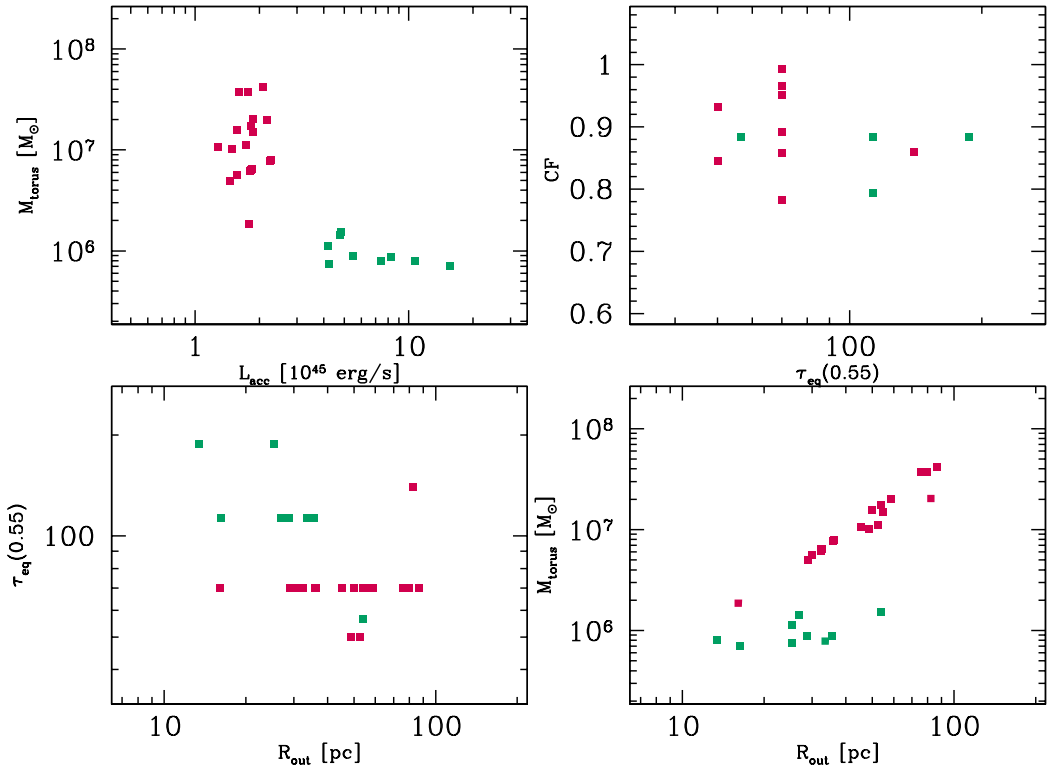

Figure 5.22: Same as in Fig. 5.13, fitting the IRS spectrum of the Seyfert 2 source IRASF22017+0319. In this case the equatorial optical depth, $\tau_{eq}(0.55)$ is calculated in the visible band, at 0.55μm.

on the code by Fritz et al. (2006) and a clumpy model grid by Nenkova et al. (2008a). Our study is complementary to previous work by Dullemond & van Bemmel (2005), who investigated the differences in the model SEDs produced by their own multi-dimensional radiative transfer smooth and clumpy models, characterised by the same global parameters. In order to compare as similar models as possible and despite the intrinsic differences between the two configurations, we matched the two sets of parameters building thus restricted grids, and compared only the models within these grids. This approach has the limitation of not exploring the full parameter space for either of the two models. Furthermore, and to avoid complications arising from the probabilistic nature of viewing an AGN as a type 2 object through a clumpy medium, we consider, when comparing the model SEDs (see Section 5.1) two extreme inclinations i.e. edge on and face-on, for smooth models, and take as equivalent type 1 and 2 clumpy models those with a probability to see directly the central engine greater and lower than 0.5,

respectively. Our findings can be summarised as follows:

- Even after matching the model parameters there is not a one-to-one correspondence. For each smooth model of the restricted grid there can be several clumpy models with matched Y, q, and σ, but different combinations of N_0 and τ_V that finally produce a given value of $\tau_{9.7}$. Additionally, and since we only consider the two extreme inclinations (face-on and edge-on), the torus opening angle can not be matched and for each clumpy model we consider all smooth counterparts, irrespective of the value of Θ.

- The distribution of the various features of the IR model SEDs differs when smooth and clumpy dust configurations are considered. The very different behaviour of the silicate features is due more to the different chemical compositions assumed by F06 and N08 and less to the actual dust morphology. We confirm the occurrence of broader, on average, IR SEDs in clumpy configurations, with a larger fraction of clumpy models peaking at long wavelengths ($\sim$30 μm). The infrared spectral index, especially for type 1 views, is the quantity that changes the most between the two dust configurations, owing to the differences in the primary source assumed in the two models as well as the lack of the hotter dust component in the treatment of the clumpy medium.

- The relative strengths of the silicate features at 9.7 and 18 μm are of particular interest, as they could in principle distinguish between smooth and clumpy configurations. The situation is, however, rather complex. Recent *Spitzer*/IRS observations show this feature in absorption in many type 1 AGN or in emission in type 2 AGN. We showed that the parameter space covered by the two configurations largely overlap, with type 1 observations providing virtually no constraints, while some type 2 objects tend to marginally reside in areas covered by the clumpy models alone (Fig. 5.5).

- The same holds for the use of $L_{12.3}$ as a discriminator between clumpy and smooth models, as previously reported in the literature. Our study showed no palpable differences in the behaviour of this quantity between the two model configurations, with a large fraction of both clumpy and smooth models resulting in a ratio of $L_{12.3}^{type_2}/L_{12.3}^{type_1}$ close to 1 when comparing the values between type 1 and type 2 views.

- Models with matched parameters within the restricted model girds do not produce similar SEDs (similar either by eye or based on the value of $\bar{\Delta}$ introduced in Section 5.1.2). Additionally, only a very limited number of random parameter combinations can result in seemingly identical SEDs, though the dust configuration differs.

- Due to their distinct nature, the two grids of models under scrutiny here are governed by some intrinsic differences and some of their parameters de-

scribe similar but not identical properties and are not always straightforward to compare. Despite these differences, we found that the physical properties of the models cover a significant range of common values and that both dust distributions are able to reproduced the observed photometric and spectroscopic MIR data in equally satisfying ways.

– Both dust configurations provide equally good fit when compared either with photometry or IRS spectra. Even if the global shape of the SEDs of F06 and N08 models can be similar, since it is constrained from the data, best models can result in very different parameters and physical properties. All this do not allow to use the SED fitting technique as a tool to distinguish between smooth and clumpy configurations, both for type 1 and 2 objects.

– Degeneracies are often an issue when comparing observations with models, with many factors entering the game. The present study is not free of degeneracies, either. Different model parameter combinations can easily result in remarkably similar SED shapes, virtually indistinguishable from one another, with often significantly different underlying physical properties. The combination of two or three emission components contributing to the total SED is an additional source of degeneracies.

From the above we conclude that, even though the two dust models produce distinct SEDs, most of the differences arise from the model assumptions (e.g. primary source, dust chemical composition) and not from the dust morphology (smooth or clumpy). To summarise, the properties of dust in AGN as measured by matching observation (be it broad band IR photometry or IR spectra) with models will strongly depend on the choice of the dust distribution. The possibility to discriminate between a smooth and a clumpy medium based on the various SED features may exist, but ambiguities are more common than not.

The lack of long wavelength data also limits a proper constraint of the cold dust emission, hence of the relative contribution of the AGN and starburst components to the overall SED. Despite these caveats, overall our results are consistent with those of Dullemond & van Bemmel (2005).

In addition to considering a variety of model SED properties, we also attempted a systematic comparison of the models with observed MIR and FIR photometric and spectroscopic data. We used two large AGN samples, one with available UV-to-FIR photometry and one observed with *Spitzer* IRS, in order to test the validity of smooth and clumpy models, and showed that, globally, both model dust distributions provide equally good fits with the data.

SED fitting is a widely used tool to derive physical parameters. Comparing the results obtained by adopting the two different models, we find parameters such as the accretion luminosity and the infrared luminosity to be well in agreement. The comparison between the derived masses of dust shows instead very large scatter. Concerning the physical radius of the dusty torus, as calculated from the

model, although the values obtained by smooth and clumpy models do not agree in general, we see no systematic trends. The two main differences are apparently in the values of the optical depth, with clumpy tori providing higher values in general, and in the covering factor that tends to assume smaller values in clumpy models.

To summarize, despite previous reports in the literature, we did not find any significant difference in the model parameters, silicate features and MIR luminosity, that could be exploited as a diagnostic to discriminate between the two dust distributions. A conclusion of our study is that a SED fitting procedure alone is not a reliable tool for distinguishing between smooth and clumpy dust distributions, whether we are dealing with photometric or with spectroscopic IR data.

If from one side, SED fitting technique is not the correct tool to investigate the dust distribution in AGN tori, from the other it is the most suitable tool to compare physical properties of the different emission components that contribute in built up the observed SEDs. For example, the infrared luminosity L_{IR} and the accretion luminosity of the AGN, L_{acc} as well as the stellar mass have been found to be well constrained when reproducing the data. To do this, more suitable data are necessary, such as photometry spanning a wider range of wavelengths and comprehensive of FIR coverage together with additional constraints provided by MIR spectra information (see Chapter 6).

6 | AGN and Star Formation in 250 μm Selected HerMES Sources with IRS Spectra

[1]

There is now both observational and theoretical evidence for an intimate link between the growth of galaxies and the SMBHs residing at their centres. On the theoretical front, cosmological simulations and semi-analytic models find it necessary to include feedback from AGN to suppress star formation in massive galaxies (e.g. Bower et al., 2006; Croton et al., 2006; Booth & Schaye, 2009) in order to account for the observed galaxy mass function simultaneously at low and high redshifts. Observations have shown that the masses of SMBHs, and those of the bulges in galaxies, follow a tight proportionality (Magorrian et al., 1998; Ferrarese & Merritt, 2000; Tremaine et al., 2002), and that the peak of the quasar number density (e.g. Boyle & Terlevich, 1998; Richards et al., 2006) coincides with that of the star formation history of the universe (e.g. Madau et al., 1998; Heavens et al., 2004). Moreover, AGN and circumnuclear star formation are often found to co-exist in galaxies at all redshifts (e.g. Farrah et al., 2003; Alexander et al., 2005), usually in systems with significant dust obscuration, and some authors have claimed evidence for direct links between the two phenomena (e.g. Farrah et al., 2012).

The most important issue to establish now is whether a causal relationship exists between star formation and AGN activity, specifically, to determine how the two phenomena regulate each other, and the overall impact of an AGN on its host galaxy. In contrast to observations at a single wavelength band, multi-wavelength studies of the incidence of AGN and star formation in dusty galaxies can provide extensive information on the manner in which the two phenomena coexist, as they are in general sensitive to nuclear activity over a wide range in obscurations (for recent works in the literature see e.g. Kirkpatrick et al., 2012; Sajina et al., 2012; Snyder et al., 2012). Selection in the IR favours sources with intense AGN or star-

[1] This chapter is an extended version of the work of Feltre, A., Hatziminaoglou, E., Hernán-Caballero, A., Fritz, J., & Franceschini, A. 2013, published in MNRAS

burst activity, as IR SEDs are likely to be dominated by these two processes: strong MIR continua imply AGN activity with hot dust reradiating optical/UV photons (e.g. Laurent et al., 2000; Hatziminaoglou et al., 2005) while strong PAHs in the MIR are signatures of intense star formation (e.g. Lutz et al., 1998; Rigopoulou et al., 1999; Farrah et al., 2008; Fadda et al., 2010). Silicate absorption at 9.7 μm is an ambiguous feature, since it can be attributed to both phenomena, although type 1 (i.e., unobscured) AGN are likely to have this feature in emission, or to have featureless continua at this wavelength. While the relative contributions of the two mechanisms can sometimes be quantified on the basis of broad band photometry alone, individual features can be smeared out, making MIR spectroscopy indispensable for accurate studies.

The combination of the *Spitzer* (Werner et al., 2004) and *Herschel* (Pilbratt et al., 2010) observatories, especially deep surveys, tracing low and high redshift objects over wide ranges in luminosity, has the potential to make dramatic advances in the study of the AGN-starburst connection. In this work we explore the impact of the presence of an AGN on the MIR and FIR properties of dusty galaxies and how simultaneous AGN and starburst activities affect these properties. We do so using a sample extracted from the HerMES (*Herschel* Multi-tiered Extragalactic Survey[2]; Oliver et al. 2012) population, using HerMES/SPIRE (Griffin et al., 2010) data as well as a wealth of publicly available ancillary data, including *Spitzer*/IRS spectra (Houck et al., 2004), of hundreds of extragalactic sources lying in the HerMES fields. The paper is structured as follows: Section 6.1 describes the sample of HerMES objects with IRS spectra and the populations it represents. The spectral decomposition technique and measurements applied to the IRS spectra are elucidated in Section 6.2. Section 6.3 describes the multi-component SED fitting method used, detailing the novelties introduced with respect to previous versions of the code as well as describing the impact that inclusion of the IRS spectra spectra has on the SED fitting of AGN. Section 6.4 discusses our principal results on the AGN and starburst components in the MIR, the various SFR estimates and the hot and cold dust components. Finally, Section 6.5 summarizes our approach and findings. Throughout this work we assume a ΛCDM cosmology with $\Omega_\Lambda = 0.7$ and Ω_M=0.3, and a Hubble constant, H_0, of 72 km/s/Mpc.

6.1 HerMES sources with IRS spectra

For the purpose of this work, we select a sample consisting of 375 sources, each detected at $> 3\sigma$ at 250 μm , and with an IRS spectrum and spectroscopic redshift measurement (either from an optical or the IRS spectrum) available. As explained in Roseboom et al. (2010), the σ value considered here includes both the instrumental noise, $\sigma_{\rm inst}$, which is between $\sim$8 and 15.5 mJy depending on the fields (for more details see Table 5 of Oliver et al., 2012) at the $3\sigma_{\rm inst}$ noise level, and the con-

[2]http://hermes.sussex.ac.uk

fusion noise, $\sigma_{\rm conf}$ equal to 3.8 mJy at 250 μm with a $3\sigma_{\rm conf}$ cut (for more details, see Nguyen et al., 2010). All sources lie in the four northern HerMES fields, namely Bootes HerMES, FLS, Lockman Swire (LS) and ELAIS N1 SWIRE (EN1), covered by the first data release[3] (for a detailed description of the fields and their coverage see Oliver et al. 2012). HerMES is a legacy survey conceived to cover about 380 deg^2 of nested fields in the most commonly observed extragalactic areas in the sky: fields were chosen among those with the best ancillary data. We therefore have at least six photometric points for each source with which to build the SEDs from optical to the FIR wavelengths.

The IRS spectra used over all this work are taken from the Cornell AtlaS of *Spitzer*/Infrared Spectrograph project (CASSIS[4]; Lebouteiller et al. 2011), which recently made available the reduced low resolution spectra (in two low-resolution modules with a resolving power of R $\sim$ 60-120) of about 11000 sources ever observed with the *Spitzer*/IRS. Henceforth, we refer to this sample as the HerMES/IRS sample. The entire sample has IRAC 3.6 and 4.5 μm, and MIPS 24 μm counterparts: $\sim$90 % of the objects have been detected at 5.8 and 8.0 μm, and 77 and 43 % of them were also detected at the MIPS 70 and 160 μm, respectively. SPIRE (containing a imaging photometer operating at 250, 350 and 500 μm on board the *Herschel* Space Observatory) fluxes are estimated from scan maps via linear inversion methods, using the positions of known 24 μm sources as priors (see Roseboom et al., 2010). As mentioned above, sources are included in the HerMES/IRS sample only if the 250 μm flux value, S_{250}, is greater than 3σ. No other cut is imposed based on the SPIRE fluxes: 350 and 500 μm non-zero fluxes are available for 98 and 84 % of the HerMES/IRS sample (72 and 35 % above 3σ, respectively). Finally, *ugriz* photometry from the Sloan Digital Sky Survey Data Release 7 (SDSS DR7; Abazajian et al. 2009) is available for 73 % of the sample, with the remaining objects being undetected by SDSS.

Fig. 6.1 shows the redshift distribution of the HerMES/IRS sample in black, spanning the range from z$\sim$ 0.014 to 2.99. The various peaks in the distribution reflect the different selection criteria of each of the subsamples present in CASSIS; dashed and shaded regions correspond to the starburst- and AGN-dominated subsamples and will be discussed in the next section.

The IRS spectra come from a compilation of various small and larger *Spitzer* programmes with objects including dusty galaxies, LIRGs and ULIRGs, normal star-forming galaxies and AGN. The details of programmes contributing with more than 10 objects to the final sample are summarized in Table 6.1. The majority of sources ($\sim$ 56 % of the entire sample) are selected at 24 μm, with a flux cut at 24 μm, S_{24}, depending on the details of the individual programmes: $S_{24} > 0.5, 0.7, 0.9, 1.0$ mJy or higher for the $\sim$ 15, 16, 7, 4 and 4 % of the sources of the total sample, respectively. Another $\sim$ 13 % of the entire sample is selected at 70 μm. Note that most of the IRS samples are flux limited. A notable exception

[3]http://hedam.oamp.fr/HerMES/release.php
[4]http://cassis.astro.cornell.edu/atlas/

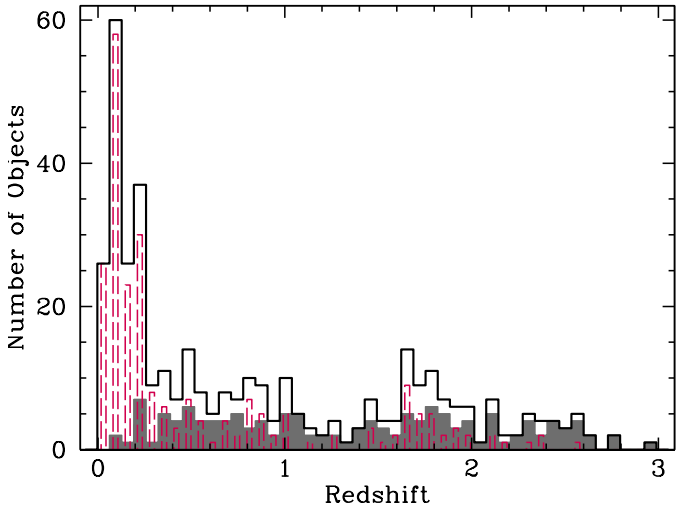

Figure 6.1: Redshift distribution of the sample. The red dashed and grey shaded histograms correspond to the starburst- and AGN-dominated subsamples: the definition of these subsamples will be described in detail in Section 6.2.2.

is the sample of Yan et al. (2007), where both 24 μm flux and a 8-24 μm colour cuts are applied. This selection biases the sample in favour of AGN type and MIR bright sources, avoiding also objects with strong silicate absorption features. Due to its selection criteria, the sample of Weedman & Houck (2009) is not complete, with sources classified as starburst by optical spectra not being detected by IRS. The sample of Farrah et al. (2008) is biased towards ULIRGs with ongoing star formation to the detriment of those containing luminous AGN. Instead, the sample of Houck et al. (2007) represents a complete distribution of IR extragalactic sources including those with featureless spectra and those with strong PAH and/or silicate features. The flux-selected samples at 70 μm, as that of Farrah et al. (2009), are less affected by biases with the selection being sensitive both to starburst and AGN sources. Even though the presence of possible different small selection biases in the different subsamples, the HerMES/IRS sample is a large sample, spanning several orders of magnitude in luminosity, and the properties of its sources match the entire range of the IR bright HerMES population. Fig. 6.2 shows the S_{24} μm (top), S_{250} μm (middle) and S_{24}/S_{250} (bottom) distributions of the full HerMES population in the four fields (solid line) and as well as those of the HerMES/IRS sample (shaded region).

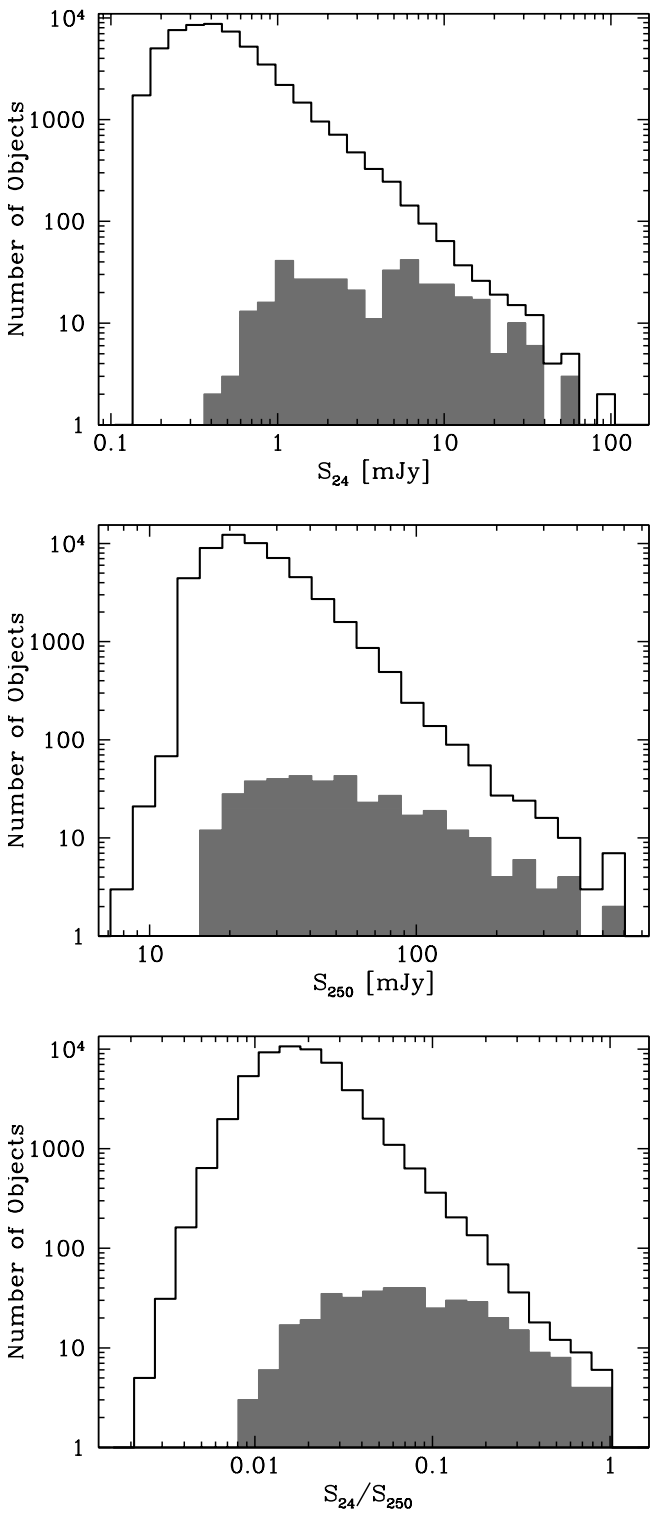

Figure 6.2: S_{24} μm (top), S_{250} μm (middle) and S_{24}/S_{250} (bottom) distributions of the full HerMES population in the four fields (solid line) and those of the HerMES/IRS sample (shaded region).

ID	PI	Selection	Reference	Field	Number of Sources
15	Houck	S_{24} >0.7 mJy		LS, Bootes, FLS, EN1	47
16	Houck	S_{24} >0.7 mJy		Bootes	14
3748	Yan	S_{24} >1 mJy		FLS	15
20113	Dole	70μm-selected		Bootes	15
20128	Lagache	24μm-selected	e.g. Weedman & Houck (2009)	Bootes, FLS	21
20629	Yan	S_{24} >0.9 mJy	Yan et al. (2007)	FLS	28
30364	Houck	S_{24} > 0.5 mJy	Farrah et al. (2008)	LS	25
40038	Houck	S_{24} > 6 & mJy S_{24} > 10 mJy	Houck et al. (2007)	Bootes, FLS	14
40539	Helou	0.5 mJy <S_{24} <100 mJy	e.g. Weedman & Houck (2009)	LS, FLS, EN1	30
50666	Farrah	S_{70} >20 mJy	Farrah et al. (2009)	LS	32

Table 6.1: Major contributors to the HerMES/IRS sample. Shown are the *Spitzer* programme ID, the PI of the proposal, the primary selection criteria and the reference, whenever available, the corresponding fields and number of sources.

6.2 IRS spectral analysis

6.2.1 IRS spectral decomposition

MIR emission from active and star-forming galaxies arises mostly from photodissociation regions (PDR) and from HII regions, the sum of which represents the contribution from star formation, and emission from hot dust heated by the AGN. To quantify the contribution of each of the components, we preform a spectral decomposition of the IRS spectra, fitting the 5-15 μm rest-frame wavelength range of each spectrum to a parametrized $F_\lambda(\lambda)$ of the form:

$$F_\lambda(\lambda) = e^{-b\tau(\lambda)}(\alpha_1 f_{AGN}(\lambda) + \alpha_2 f_{HII}(\lambda) + \alpha_3 f_{PDR}(\lambda)) \quad (6.1)$$

where f_{AGN} is represented by the IRS spectrum of PG QSO 3C273 (Wu et al., 2009), f_{PDR} by the ISOCAM spectrum of a PDR in the reflection nebula NGC 7023 (Cesarsky et al., 1996b), and f_{HII} by the ISOCAM spectrum of M17 in the vicinity of OB stars (Cesarsky et al., 1996a). We then quantify the contribution, r, of each spectral component to the MIR luminosity as the ratio of its integrated luminosity to the total luminosity in the 5-15 μm rest-frame range. For more details see Hernán-Caballero et al. (2009).

From the 510 sources with redshifts, 430 have a reliable, non-zero MIR AGN component, r_{AGN}, as defined from the spectral decomposition. Note that the spectral decomposition method uses an AGN template with a fixed slope and therefore only objects with the exact same slope as the template (a blue quasar), will have $r_{AGN} \sim 1$. As a consequence, r_{AGN} should rather be seen as a lower limit of the contribution of the AGN component to the MIR. The combination, however, of varying the contribution of the AGN and HII templates allows for a reasonable fit of the spectrum for a wide range of MIR slopes. The distribution of r_{AGN} is shown in the Fig. 6.3.

6.2.2 IRS spectral measurements

An additional set of measurements was performed on the IRS spectra, namely measurements of the intensities of PAH and silicate features, and MIR monochro-

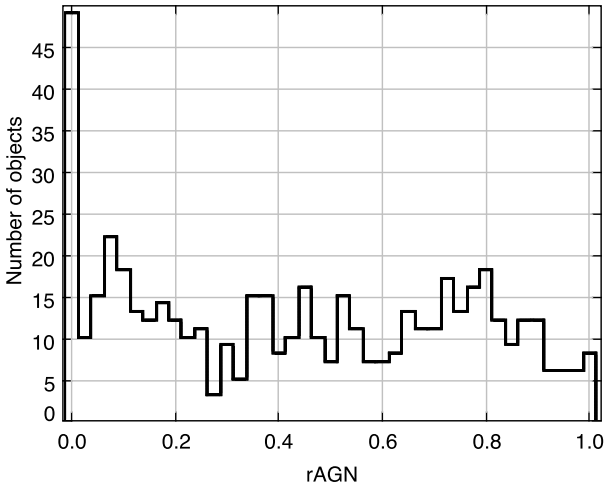

Figure 6.3: Distribution of the MIR AGN component, r_{AGN}, derived from IRS spectral decomposition.

matic luminosities, that we use to characterise the objects (for details on the measurement procedure see Hernán-Caballero & Hatziminaoglou, 2011).

We measured the equivalent widths of the PAH features, EW_{PAH}, at 6.2 and 11.3 μm, as well as their luminosities from the IRS spectra using the procedure described in Hernán-Caballero & Hatziminaoglou (2011). Briefly, we select continuum bands 0.2 μm wide at both sides of each PAH feature (centred at 5.9 and 6.6 μm for the 6.2 μm PAH feature; 10.88 and 11.78 μm for the 11.3 μm one) and interpolate linearly between them to estimate the continuum under the feature. We subtract the linear continuum and integrate the residual in a band of width 0.5 μm centred at the nominal wavelength of the feature to obtain the flux in the PAH band. As explained in Hernán-Caballero & Hatziminaoglou (2011), our selection of a narrow integration band and nearby continuum bands help to maximize the signal-to-noise (S/N) and to reduce the uncertainty in the underlying continuum. Flux lost in the wings of the PAH bands and contamination to the continuum are corrected for by assuming that the PAH feature has a Lorentzian profile with a full width at half-maximum (FWHM) of 0.2 μm. Simulations indicate that a 10 % increase in the FWHM causes a 5 or 6 % drop in the PAH flux, with no observable dependency on the EW_{PAH} or S/N of the spectrum. Uncertainties in the PAH flux and the underlying continuum for each source are estimated by performing Monte Carlo simulations.

Extinction has complex interactions with the PAH features: in highly obscured sources, the 6.2 μm band is often attenuated or even entirely suppressed due to a water ice absorption band at 6 μm (e.g. Spoon et al., 2004; Imanishi et al., 2007; Sajina et al., 2009). The 11.3 μm band is embedded inside the much wider silicate

feature at 9.7 μm (see Section 6.3.1), and the effect of extinction on it depends on whether the obscuration producing the silicate feature affects only the AGN or also the starburst component. In the first case, continuum emission from the AGN gets diminished, and the EW_{PAH} of the feature at 11.3 μm is accordingly boosted. In the second, both the continuum and the feature are equally suppressed, and therefore the EW_{PAH} remains unchanged. Since most of the sources in the sample have moderate to low values of the strength of the silicate feature (see Fig. 6.7), our results are largely unaffected by extinction. The distribution of EW_{PAH} is shown in Fig. 6.4, where the grey histogram corresponds to the feature at 11.3 μm.

The strength of the silicate feature at 9.7 μm, $S_{9.7}$ is defined by Pier & Krolik (1992) as:

$$S_{9.7} = ln[F(\lambda_p)/F_C(\lambda_p)] \tag{6.2}$$

Where $F(\lambda_p)$ and $F_C(\lambda_p)$ are the feature's peak flux density and the underlying continuum respectively. It follows from this that a negative value of $S_{9.7}$ indicates that the silicate feature is in absorption. The distribution of $S_{9.7}$ for the sample is shown in Fig. 6.7.

6.2.3 MIR AGN- and starburst-dominated objects

PAH features are commonly used to quantify AGN and star formation activity, as well as the relative contribution of the two physical processes to the energy output of dusty galaxies in the MIR (Lutz et al., 1996; Genzel et al., 1998; Rigopoulou et al., 1999; Armus et al., 2006; Veilleux et al., 2009). Indeed, the luminosity of PAH, L_{PAH}, allows for an estimate of the star formation rate, SFR_{PAH} (Brandl et al., 2006; Houck et al., 2007; Pope et al., 2008; Hernán-Caballero et al., 2009, see Section 6.4 for more details). Previous work has established that the EW_{PAH} of the 6.2 and 11.3 μm bands correlate with the relative contributions of the AGN and starburst to the bolometric output of the galaxy (e.g. Laurent et al., 2000; Spoon et al., 2007). Hernán-Caballero & Hatziminaoglou (2011) estimated that EW_{PAH}=0.2 μm represents roughly equal contributions from the AGN and starburst to the bolometric luminosity (valid for either of the two PAH features), with the AGN dominating at lower values and the starburst dominating at higher values. For the purpose of this work, we use the 11.3 μm PAH feature, and use that 6.2 μm only in the absence of the former (necessary in $\sim$ 10 % of the objects).

As shown in Fir. 6.4, in the HerMES/IRS sample we found 45% and 55% MIR AGN- and starburst- dominated objects, i.e. with $EW_{PAH} < 0.2$ and > 0.2, respectively. Hereafter, when reporting to AGN-dominated ($EW_{PAH} < 0.2$) or starburst-dominated ($EW_{PAH} > 0.2$) objects, we refer to the distinction made based on the calculated values of EW_{PAH}.

Returning to the redshift distribution of the HerMES/IRS sample (Fig. 6.1), we note that very low redshift sources may have angular sizes larger than the width of the slits used for IRS spectroscopy (3.6 and 10.5 arc sec wide for the short- and long-wavelength modules, respectively). As a consequence, a fraction

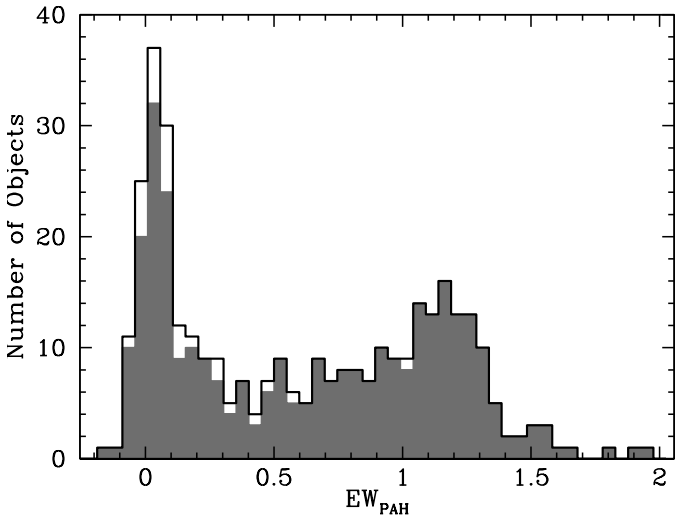

Figure 6.4: Distribution of EW_{PAH} (that at 11.3 μm shown in grey; PAH at 6.2 μm used when the 11.3 μm data were not available), measured from the IRS spectra.

of the emission from the outer regions of these galaxies may be missed by the IRS observations. This, in principle, could result in an overestimation of the AGN contribution to the galaxy's measured emission, which would translate to an excess of AGN-dominated objects at very low redshifts. As seen in the figure, the more nearby objects ($z \leq 0.3$) are almost exclusively starburst-dominated (red dashed histogram) with only 10 objects being AGN-dominated. The effects of slit width can be assessed by comparing the MIPS 24 μm flux with that evaluated at 24 μm from the IRS spectra. We find consistent values for all low-redshift sources in the HerMES/IRS sample, and conclude that aperture effects do not significantly affect our results and conclusions. We note that almost all HerMES/IRS galaxies at $z > 2$ (Fig. 6.1) are AGN-dominated (shaded histogram): this is not a physical result but is due to the selection of the IRS targets that constitute the various subsamples of our HerMES/IRS sample.

It is well known that AGN-dominated sources tend to concentrate in a particular region of the IRAC colour-colour diagram (e.g. Lacy et al., 2004, 2007; Stern et al., 2005; Donley et al., 2012). In fact, Fig. 6.5 shows the (observed) IRAC colours of the HerMES/IRS sources, colour-coded based on the value of EW_{PAH}, justifying the use of the latter to separate between AGN- and starburst-dominated objects. Hatziminaoglou et al. (2009) showed that the position of AGN on this colour-colour diagram depends on the relative contribution of their starburst content to the MIR, going from the diagonal locus (defined by the MIR AGN continuum) for pure AGN to the vertical $S_{5.8}/S_{3.6}$ locus, as the starburst contribution increases. They also showed that the position of AGN is almost independent of redshift up to a redshift of ~ 3 (see their Fig. 2), a value corresponding to the most distant object in our HerMES/IRS sample. AGN-dominated objects in the HerMES/IRS

sample, as classified by the value of EW_{PAH}, show the same behaviour and lie on or around the power-law slope; as the starburst component becomes increasingly dominant, the position of sources moves towards the vertical $S_{5.8}/S_{3.6}$ locus. The black points denote objects in one of the selected fields (FLS), with stars clustering in the lower left corner of the plot (see e.g. Sajina et al., 2005; Hatziminaoglou et al., 2009).

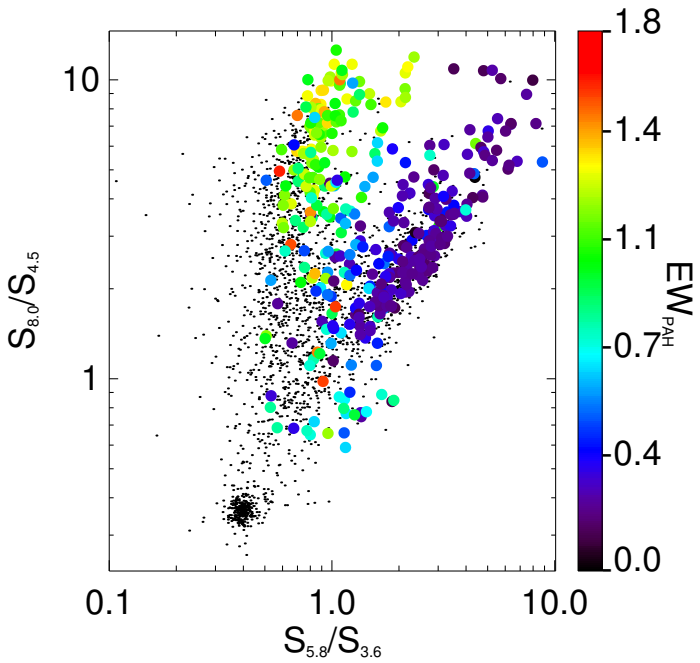

Figure 6.5: IRAC colours of the HerMES/IRS sources. The points are colour-coded as a function of EW_{PAH}. Black points show the density of objects in the FLS field, with stars clustering in the lower left corner of the plot.

6.3 SED fitting

We use the routine presented in Chapter 4 to fit SEDs to the HerMES/IRS sample data. The observed SED of each object is compared to a set of model SEDs by means of a standard χ^2 minimisation. An addition to the original code is the possibility to simultaneously fit photometry *and* an IRS spectrum for each object, as described in Section 4.4.3 and summarized in Section 6.3.1. As shown in Fig. 6.6, the model SEDs (black line) are the sum of three components: a stellar (dotted dark green), an AGN (dot dashed blue) and a starburst (dashed light green) component. The stellar component is itself the sum of Simple Stellar Population (SSP) models of different age, all having a common (solar) metallicity, and is built up using the Padova evolutionary tracks (Bertelli et al., 1994), a Salpeter initial mass

function (0.15-120 $M_{\odot}$) and the Jacoby et al. (1984) library of observed stellar spectra in the optical domain. The AGN component consists of the emission from the primary source and the emission reprocessed by dust, distributed in a continuous fashion (as opposed to clumps) in a toroidal or flared-disk shaped region around the primary source and described in detail in Fritz et al. (2006). In this work, we use the updated AGN torus model grid presented in Feltre et al. (2012). Finally, the starburst component is represented by a library of starburst templates that are used to reproduce the detailed PAH features of the IRS spectra. Sources in the library include Arp220, M82, M83, NGC1482, NGC4102, NGC5253 and NGC7714. Due to their empirical nature, the starburst templates cannot be used to compute accurate values of physical quantities such as the mass of cold dust and its temperature. For this reason, and as a second step, we fit the FIR data points ($\lambda > 100\mu$m) of the SEDs to a modified black body emission, as described in detail in Section 6.3.2.

The SED fitting procedure described above also takes into account the interstellar dust and the extragalactic flux attenuations. Extinction by dust in the interstellar medium is modelled as a uniform slab in front of the stars. It is parameterised by an E(B-V) value and an assumed galactic extinction curve taken from (Cardelli et al., 1989). We checked whether adopting other prescriptions for the dust extinction, e.g. the extinction curve as proposed by Calzetti et al. (1994) and widely used in studies of actively star-forming objects, would alter our results: we are only fitting five broad band optical data points (SDSS) and found that using the Calzetti model neither changed significantly the stellar masses estimations, nor provided a better fit to the data (as quantified by the value of χ^2). Finally, we model attenuation by the intergalactic medium using the Madau (1995) law.

6.3.1 Spectrophotometric fitting

We perform the SED fitting using photometric data points (typically SDSS *urgiz*, *Spitzer* IRAC and MIPS, and *Herschel* SPIRE fluxes: red points in Fig. 6.6) and the IRS spectra simultaneously, and use standard χ^2 minimization to determine the best fit. Each IRS spectrum (shown in turquoise in Fig. 6.6) is divided in a predefined number of bands (20), with the mean flux and the respective error calculated in each band. These fluxes are then handled in the same way as the photometric data points. The best-fit model comprises the combination of the models providing the lowest values of the reduced χ^2, χ^2_ν, which is by definition the χ^2 divided by the number of degrees of freedom, in turn the number of data points - the number of model parameters.

An AGN component was required to reproduce the observed SED for about 96 % of the HerMES/IRS sources. For the $\sim$25 % of these, no stellar component was needed because in these objects the light of the AGN outshines that of the host galaxy in the UV/optical, and the sources are therefore characterised as unobscured AGN. Inconspicuous PAH features ($\mathrm{EW_{PAH}} < 0.2$) further demonstrate

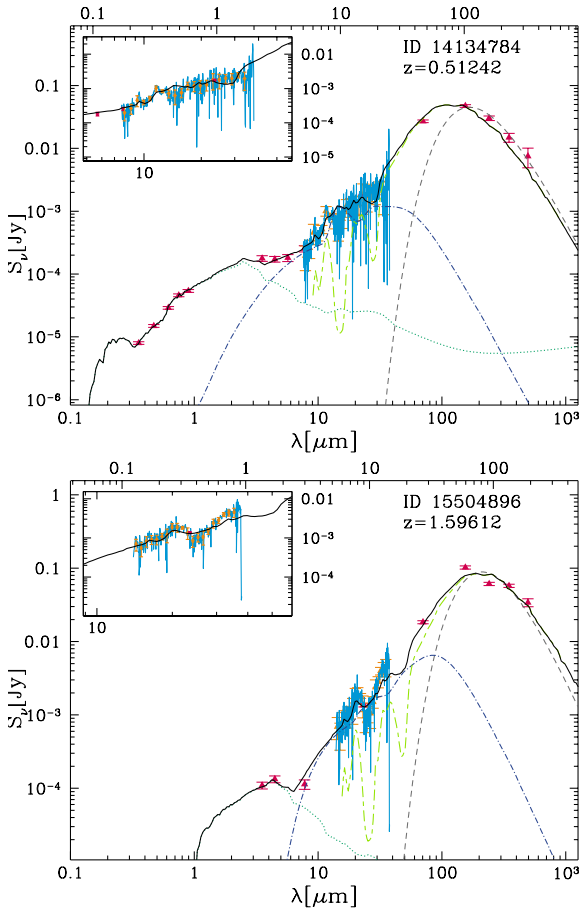

Figure 6.6: Example of a best-fit to a low (top) and a high (bottom) redshift object (*Spitzer* ID 14134784 and 11867904, respectively). The IRS spectrum (turquoise; see also the insert figure) and photometric data (red symbols) are reproduced using the three emission components: SSPs (dotted dark green line), AGN torus (dot dashed blue line) and starburst (dashed light green line), giving the total model emission (in black). The dashed grey lines show the best-fit modified black body emission, fitted at a second step. The top x-axis shows the rest-frame wavelength.

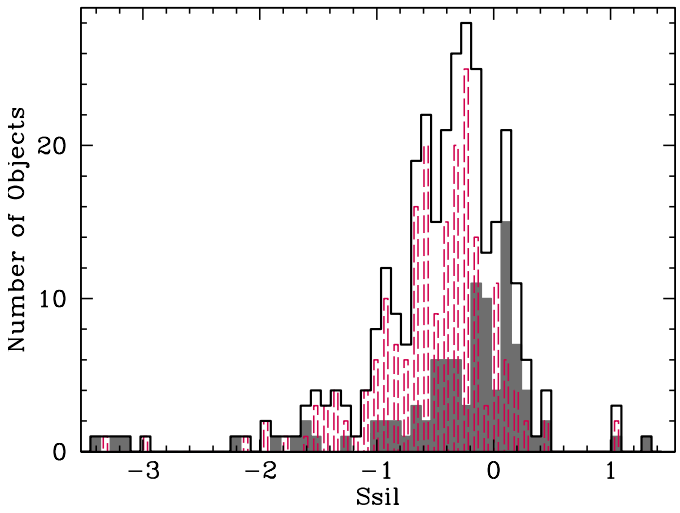

Figure 6.7: Distribution of the strength of the silicate feature at ∼9.7 μm. The grey shaded and red dashed histograms illustrate AGN- and starburst-dominated sub-samples, defined as such by EW$<$ 0.2 and EW$\geq$ 0.2, respectively.

that the AGN dominates the MIR emission of such sources (for more details see Section 6.4).

Important physical quantities can be derived from the SED fitting including the AGN accretion luminosity, L_{acc}, i.e. the soft X-ray, UV and optical luminosity coming from the accretion disc, the infrared luminosity, L_{IR}, defined as the integrated flux between 8 and 1000 μm, and the relative contribution of the AGN and the starburst, L_{SB}. The latter quantity can be used to estimate the obscured star formation rate, SFR_{FIR}, using the calibration derived in Kennicutt (1998), in which the bolometric luminosity of stars younger than 100 Myr is assumed to be re-emitted in the IR (see Kennicutt, 1998; Leitherer & Heckman, 1995, and Section 6.4 for more details).

On the effects of the IRS spectra on the SED fitting

A large fraction (75 %) of the objects with the feature in emission are AGN-dominated based on calculated values of EW_{PAH}.

$S_{9.7}$ is a property of the hot dust that relates to its opacity and geometry and cannot be constrained with photometric data points alone. In the following we determine the impact of including the IRS spectra in the evaluation of $S_{9.7}$. We measure this quantity using the best-fit torus model for all the objects, with and without including the IRS spectra in the SED fitting (S and S', respectively). We then compare the values, S and S' with the values of $S_{9.7}$ measured directly from the IRS spectra, as shown in Fig. 6.8, top and middles panels, respectively. In the presence of both AGN and starburst components, the SED fitting has to reproduce the silicate feature by adding the two components, hence measuring S on the

best fit torus model alone might be irrelevant, especially for objects with strong starburst contribution. Indeed, in this case, S has to be measured on the total (i.e., AGN+starburst) model (S_{tot}, shown as a function of $S_{9.7}$ in the bottom panel of Fig. 6.8). The circles correspond to all the AGN-dominated objects ($EW_{PAH} < 0.2$), with the open (filled) symbols representing objects with (without) a stellar component. Finally, the stars indicate starburst-dominated objects ($EW_{PAH} > 0.2$).

Fig. 6.8 shows several interesting consequences of including IRS spectra in SED fitting. A simple comparison between the top and middle panels shows that the cluster of points at $S' \sim 0.0$ for objects with a stellar component and $S_{9.7} < 0.0$ to vanish. For these objects including IRS spectra in the fit returns torus models with a silicate feature whose strength matches more closely that measured in the IRS spectra. Since S depends strongly on the model parameters, a more accurate measurement, as in the presence of the IRS spectra, implies better constraints on the model parameters. Furthermore, the clustering of unobscured AGN around the 1:1 line becomes tighter, although SED fitting still tends to favour torus models with silicate emission that is stronger than observed. In starburst-dominated objects the IRS spectra do not improve the constraints on the silicate feature of the torus models, as can be seen in the top and middle panels of Fig. 6.8, where both S and S' present very deep absorption ($\sim$ -8.0). Indeed, as the starburst component starts becoming important, the points disperse even in the presence of IRS spectrum and S_{tot} has to be considered instead (bottom panel of Fig. 6.8). Despite a non-negligible scatter, likely due to the noise of the spectra, model and spectral measurements now cluster around the 1:1 line, particularly tightly for unobscured AGN (filled circles). Our findings show that including the IRS spectra in the SED fitting helps to better constrain the AGN component for objects whose optical/MIR SEDs are dominated by the AGN; as a consequence, better constraints on the starburst component are obtained as well.

6.3.2 Fitting a modified black body to the FIR points

The starburst templates used to fit the observed emission, due to their empirical nature, cannot be used to derive accurate estimates of the physical properties of the cold dust component, such as mass and temperature. For this reason data at $\lambda > 100$ μm are fitted separately, assuming that dust is emitting as a single-temperature, modified black-body. Dust emissivity is modelled as power law $k_\nu = k_0 \nu^\beta$, with k_0 a normalization factor such that $k_{350\mu m} = 0.192$ m^{2}kg^{-1} (Draine, 2003). The modified black body is then expressed in the analytic form:

$$S_\nu(\beta, T) = \frac{M_c k_0}{d^2} \left(\frac{\nu}{\nu_0}\right)^\beta B_\nu(T) \tag{6.3}$$

where M_c is the mass of the (cold) dust and d is the luminosity distance. The only two free parameters in the fitting procedure are the dust temperature and mass: we chose to fix the value of β at 2, which is consistent with the value commonly

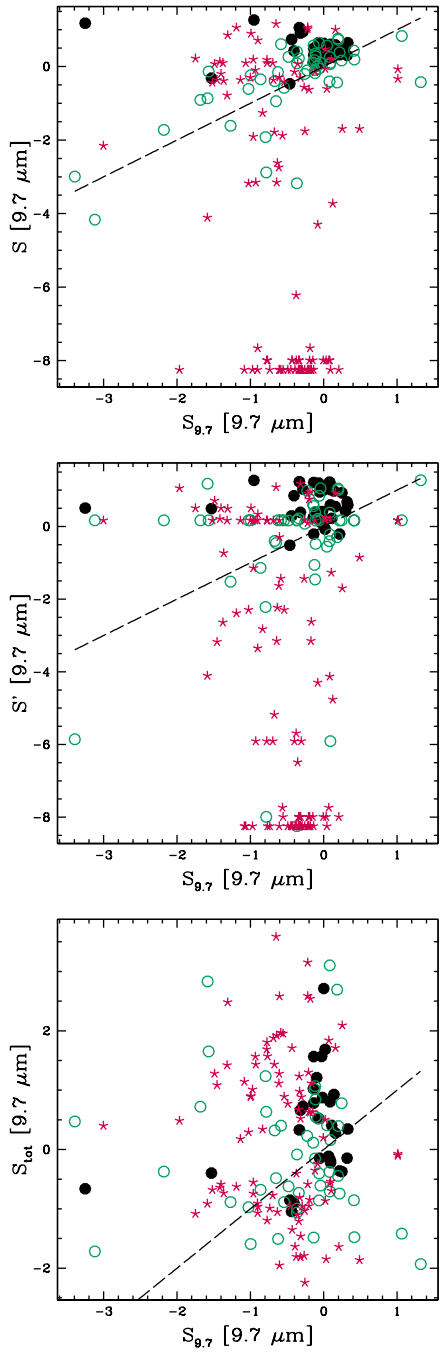

Figure 6.8: The strength of the silicate feature at 9.7 μm measured from the best-fit model versus that measured from the IRS spectra. In the top panel, S' was measured on the best-fit torus models obtained by fitting photometry alone, while S (middle panel) was measured from the best-fit torus model when fitting simultaneously photometric data and IRS spectra. In the bottom panel, S_{tot} is the measured strength of the silicate feature on the total model, i.e. the sum of the AGN and the starburst component. The filled black (open green) circles correspond to AGN-dominated objects without (with) a stellar component (SSPs), while red stars correspond to starburst-dominated objects.

used in dust models (Draine & Lee, 1984; Li & Draine, 2001, see also Davies et al. 2012 for observational evidence).

The best fit temperatures are found by means of a gradient search method following Fritz et al. (2012). A well-sampled SED with photometry that spans the IR peak is required to properly constrain the properties of the cold dust (Kirkpatrick et al., 2012): fitting using the modified black body has therefore only been applied to objects with at least two SPIRE band detections as well as MIPS 160 μm, jointly available for $\sim$30% of the HerMES/IRS sample.

6.4 AGN and star formation in the MIR and FIR

We use EW_{PAH} to distinguish between AGN- and starburst-dominated objects in the MIR, with the AGN-dominated objects being characterized by values lower than the threshold value, $EW_{PAH} = 0.2$. An important question is how this measure compares to the absolute AGN and starburst contributions to the overall emission from the galaxies. Fig. 6.9 shows EW_{PAH} measured from the IRS spectra as a function of the AGN fractional contribution, r'_{AGN}, to L_{IR}, in turn derived from the SED fitting (as already mentioned, an AGN component was necessary to reproduce the SEDs for 85 % of the HerMES/IRS sample). The green open circles denote the AGN with a stellar component while the black filled circles AGN without one (see Section 6.3.1). The two quantities are not expected to be correlated, as the contribution of the AGN component to the MIR is not necessarily representative of its contribution to the total energy output, there is clearly an avoidance zone, however: objects with a high fractional AGN contribution to the L_{IR} do not exhibit any PAH features ($EW_{PAH} \sim 0$). Furthermore, $\sim$75 % of the unobscured AGN (filled circles) also have $EW_{PAH} < 0.2$. At the same time, 40 % of the AGN with a stellar optical component (open circles) also have $EW_{PAH} < 0.2$. Last but not least, some sources present large EW_{PAH} (with values between 1 and 1.5) and, at the same time, a relatively high AGN contribution (between 0.4 and 0.6). These objects are characterized by values of $S_{9.7}$ that are around zero, or slightly negative due to absorption suppressing the continuum around the PAH features, and by best fit torus models with large size and high optical depth giving rise to a significative AGN contribution even at longer wavelength. The presence of a starburst emission component is necessary to account for the total FIR emission. Indeed, it is worth highlighting the presence of a cluster of objects ($\sim$ 37 %) with very low EW_{PAH} (AGN-dominated in the MIR) and very low AGN fraction, meaning that the total IR luminosity is dominated by the starburst mechanisms. Sajina et al. (2012) find a class of composite objects ($\sim$ 47 % of their sample of 191 24-μm bright sources in FLS field) showing similar properties, that is high starburst contribution to the L_{IR} along with a very low value of the EW of the PAH feature at 7.7 μm. Moreover, we found very few objects ($\sim$8%) having a fractional contribution of the AGN to L_{IR} of more than 50%, confirming once again that the source of the bulk of the IR emission, even in AGN-dominated systems, is star formation. The 53% of

the HerMES/IRS sample objects presenting a fractional contribution of the AGN to L_{IR} of less then 50% also presents $EW_{PAH} > 0.2$ (all but three MIR starburst-dominated sources), i.e. starburst emission dominates both the MIR and the FIR. Our findings are in agreement with those of Kirkpatrick et al. (2012) where they analyze a sample of 151 24 μm selected galaxies in the GOODS-N and ECDFS fields. They found most of the starburst-dominated sources in the MIR have a negligible AGN contribution to the FIR, while MIR AGN-dominated objects show various levels of contribution by star formation activity.

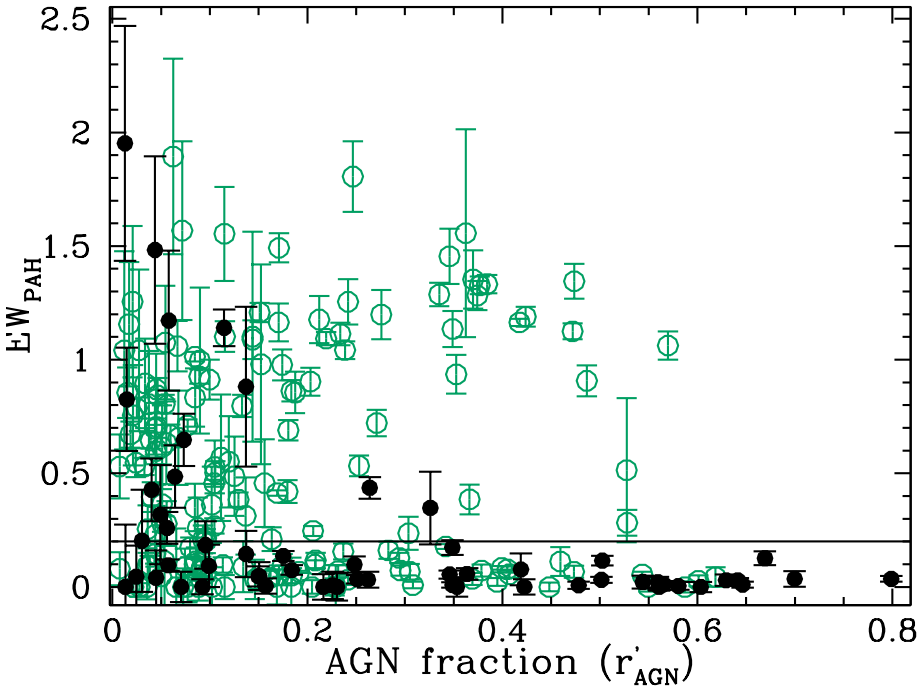

Figure 6.9: EW_{PAH} as a function of the fractional contribution of the AGN component to the total IR luminosity for all objects to which the SED fitting assigned an AGN component. The filled (open) symbols are objects without (with) an optical stellar component. The black line (EW_{PAH} = 0.2) delimits the MIR AGN- and starburst dominated objects, with the first taking lower values.

Measurements on IRS spectra provide also estimates of $S_{9.7}$. Spoon et al. (2007) presented a diagnostic diagram for MIR spectra of IR galaxies based on the EW_{PAH} and $S_{9.7}$ values. They found their objects to mainly distribute in two branches of the diagram: an horizontal one, mainly populated by Seyfert galaxies, quasar and ULIRGs and a diagonal one occupied mostly by ULIRGs and starburst galaxies. Note that ULIRGs have been found in both branches, indicating the composed nature of the objects. Interesting is to see where our HerMES/IRS sources are collocated in such diagram, reported in Fig. 6.10, where the green open circles denote the AGN with a stellar component while the black filled circles AGN with-

out one (see Section 6.3.1). Most of the AGN-dominated objects ($EW_{PAH} < 0.2$) of our sample occupy an horizontal region and, moreover, all the sample sources do not significantly populate the region between the two branches, in agreement with the findings of Spoon et al. (2007). The diagonal locus of Fig. 6.10 is not very well sampled by the HerMES/IRS sources, with a lack of objects with high silicate absorption and weak EW_{PAH} which were supposed to occupy the top left bottom part in the Spoon et al. (2007) diagram. However, we see a conspicuous bulk of sources in the extreme right tips of the two branches that has been found to be populated by starburst galaxies Spoon et al. (2007).

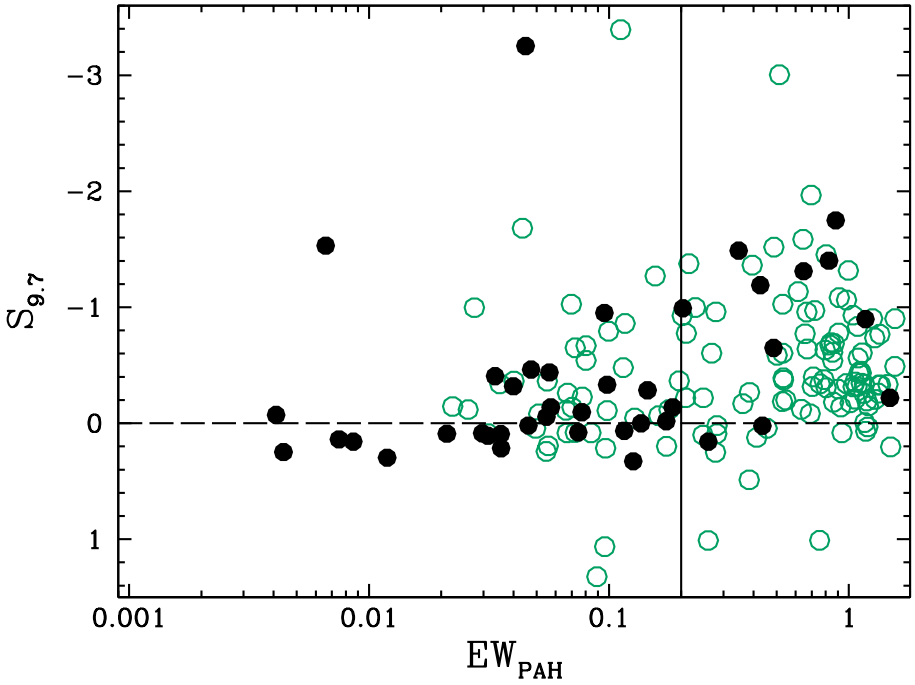

Figure 6.10: Spoon et al. (2007) diagnostic diagram for the HerMES IRS sample, reporting $S_{9.7}$ and EW_{PAH} as measured on the IRS spectra. The black solid line (EW_{PAH} = 0.2) delimits the MIR AGN- and starburst dominated objects, with the first taking lower values. The dashed black lines denotes the horizontal branch found, from Spoon et al. (2007), to be mainly populated from AGN and ULIRGs. The filled (open) symbols are objects without (with) an optical stellar component.

6.4.1 The contribution of the AGN at the various wavelengths

The presence of an AGN in the centre of a galaxy will leave a distinct signature at different wavelengths. A type 2 AGN will be completely obscured in the optical/UV and its broad band photometry at these wavelengths will be indistinguishable from that of luminous red galaxies (Zakamska et al., 2003). Obscured or not, an AGN is expected to contribute the most in the MIR wavelengths where the hot

dust emission peaks. On the other hand, it has been shown that the starburst emission dominate in the FIR even in the presence of a bright AGN (Hatziminaoglou et al., 2010).

From the IRS spectral decomposition we already derived the fraction of the AGN contribution to the 5-15 μm range, r_{AGN} (see Section 6.2.1 for details). From the SED fitting procedure we can also derive the fractional contribution of the AGN to the total IR luminosity, L_{IR}, integrated between 8 and 1000 μm, r'_{AGN}. As explained before, the two are tracing the AGN signature in different parts of the electromagnetic spectrum and are, hence, not expected to correlate. Indeed, plotting the two quantities against each other results in an almost complete scatter plot, as shown in Fig. 6.11. Despite the huge dispersion, such a comparison is still meaningful: the requirement for a SPIRE detections ensures that these objects have a prominent starburst component. In a more general case though, the IR emission of the bulk of bright quasars is dominated by the actual AGN activity, while in luminous and ultra-luminous IR galaxies the starburst is the dominant component. Fig. 6.11 is shown here to stress the fact that the definition of an "AGN-dominated" object is strongly wavelength dependent. It is, however, worth pointing out the lack of objects with $r'_{AGN} > 0.5$ and $r_{AGN} < 0.4$, which suggests that objects for which the AGN component is dominating the FIR SED will also be dominated by the AGN component in the MIR but, of course, not the other way round.

If we explore the AGN contribution r'_{AGN} to the 5-15 μm regime, the wavelength interval in which r_{AGN} is defined, we can directly compare the two quantities and we start seeing something of a trend (Fig. 6.12). The dispersion is still large, however objects with $r_{AGN} > 0.5$ also tend to have $r'_{AGN} > 0.5$ and vice versa. The scatter is now due to the differences in the methods used to derive the two quantities: spectral decomposition uses, as already mentioned, a single quasar template with a blue MIR slope, while the SED fitting considers a full grid of torus models, better constrained when fitting a much larger wavelength range.

6.4.2 AGN and the star formation rate from MIR and FIR

The combination of spectral measurements and SED fitting allows us to estimate the *obscured* SFR in the objects of our sample in two different ways, as already described in sections 6.2.2 and 6.3.1:

i) SFR_{FIR}, the obscured star formation rate, is calculated using Kennicutt (1998), converting L_{SB} into a value for SFR using $SFR_{FIR} = 4.5 \times 10^{-44} \times L_{SB}$, with L_{SB} in erg/sec.

ii) SFR_{PAH}, derived from the luminosity of the PAH features as measured from the IRS spectra (see Section 6.2.2), and defined as $SFR_{PAH} = 1.4 \times 10^{-8} \times L_{PAH[6.2]}$, $SFR_{PAH} = 1.52 \times 10^{-8} \times L_{PAH[11.3]}$, where PAH luminosities are expressed in erg/sec (Hernán-Caballero et al., 2009). We verified that the infrared luminosity derived from the luminosities of the PAH features at 6.2

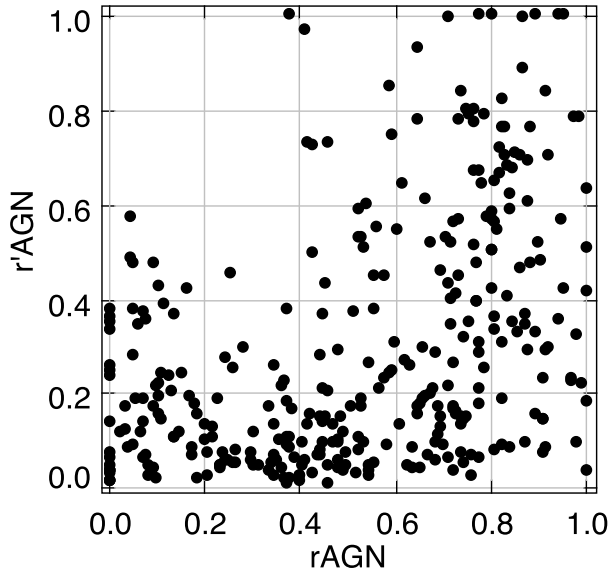

Figure 6.11: Comparison between the contribution of the AGN derived from the IRS spectral decomposition calculated in the 5-15 μm range, r_{AGN}, and the AGN torus model contribution to the L_{IR} [8-1000 μm] derived from the SED fitting procedure, $r^{'}_{AGN}$.

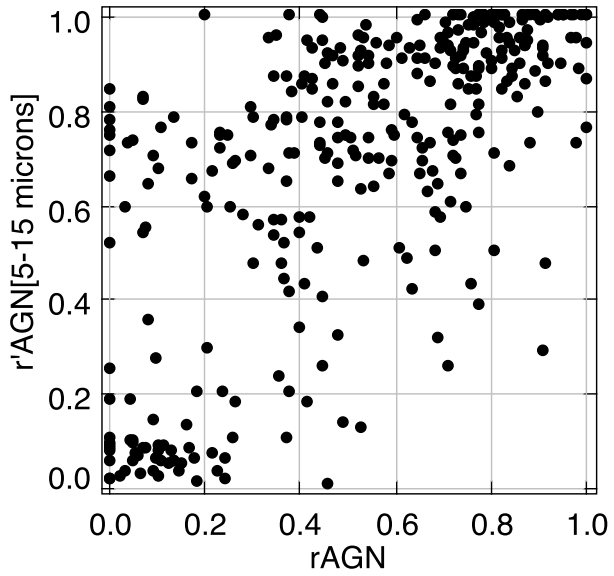

Figure 6.12: Comparison between r_{AGN} and $r^{'}_{AGN}$, but now integrated between 5 and 15 μm.

μm and 11.3 μm are comparable, and adopted the value derived for the PAH feature at 11.3 μm as it is less affected by extinction. We use the PAH luminosity at 6.2 μm only for objects for which a measurement at 11.3 μm is not available (about 10% of the objects, as already mentioned in Section 6.2.2.

As other authors have previously pointed out (Schweitzer et al., 2006; Netzer et al., 2007; Lutz et al., 2008), SFR_{FIR} and SFR_{PAH} correlate with each other (Fig. 6.4.2, top panel). Unobscured AGN-dominated objects (black circles) show a shallower slope and a loose correlation ($r = 0.64$). AGN-dominated objects with an optical stellar component (open circles) show a tighter correlation ($r = 0.82$) and a steeper slope that is almost parallel to the 1:1 line, but with systematically larger SFR_{FIR} than SFR_{PAH} by about an order of magnitude. Finally, starburst-dominated objects (stars), have a very tight ($r = 0.95$) correlation lying close to the 1:1 line at low SFR, with the SFR_{FIR} deviating from their SFR_{PAH} counterparts with increasing SFR. To exclude the possibility of these trends being a statistical effect, we ran the following test: we modelled a population lying on the 1:1 line with the scatter of the starburst-dominated objects and applied a random offset for the PAH luminosity of each object, drawn from a Gaussian distribution with σ equal to the error on the PAH luminosity. We then recalculated the SFR_{PAH} and related EWs. The behaviour shown in the top panel of Fig. 6.4.2 was not reproduced and the AGN-dominated objects were distributed randomly, implying a physical origin of the observed SFR trend. The reason of this can be sought in the fact that the ratio of L_{PAH} to L_{SB} depends on L_{SB} (Smith et al., 2007). For example the ratio L_{PAH}/L_{IR} has been found to be significantly smaller for local ULIRGs (Armus et al., 2007) compared to that of regular local and low-luminosity starburst galaxies (Brandl et al., 2006; Smith et al., 2007). Moreover, high redshift ULIRGs, being on the whole less obscured than the local ones, present stronger PAH feature (Pope et al., 2008; Fadda et al., 2010).

While comparing distant quasars with samples of local quasars and ULIRGs of Schweitzer et al. (2006) and Netzer et al. (2007), Lutz et al. (2008) reported a constant L_{PAH}/L_{SB} (and hence a constant SFR_{FIR}/SFR_{PAH}, if we assume a constant SFR_{PAH}/L_{PAH} ratio), with luminosities spanning almost four orders of magnitude. Analogously, Pope et al. (2008) found that sub-millimetre galaxies (SMGs) at z$\sim$ 2 allow to extend the relation between L_{IR} and L_{PAH} of the local starburst galaxies. In contrast, we find L_{PAH}/L_{SB} to clearly decrease with L_{SB} for starburst-dominated objects (Fig. 6.4.2, middle panel) while AGN-dominated objects have a close-to-constant L_{PAH}/L_{SB}, but with a large scatter. Furthermore, we find a decreasing L_{PAH}/L_{SB} with increasing of redshift for starburst-dominated objects.

To see whether the presence of an AGN has an effect on the obscured SFR, we also looked at the behaviour of SFR_{FIR} as a function of the accretion luminosity, L_{acc}, that is the normalisation of the AGN component to the observed data points (Fig. 6.14, top panel). As already seen in the recent literature, brighter AGN also exhibit higher SFRs (e.g. Serjeant & Hatziminaoglou, 2009; Hatziminaoglou et al., 2010; Serjeant et al., 2010; Bonfield et al., 2011). Focusing on the brightest objects

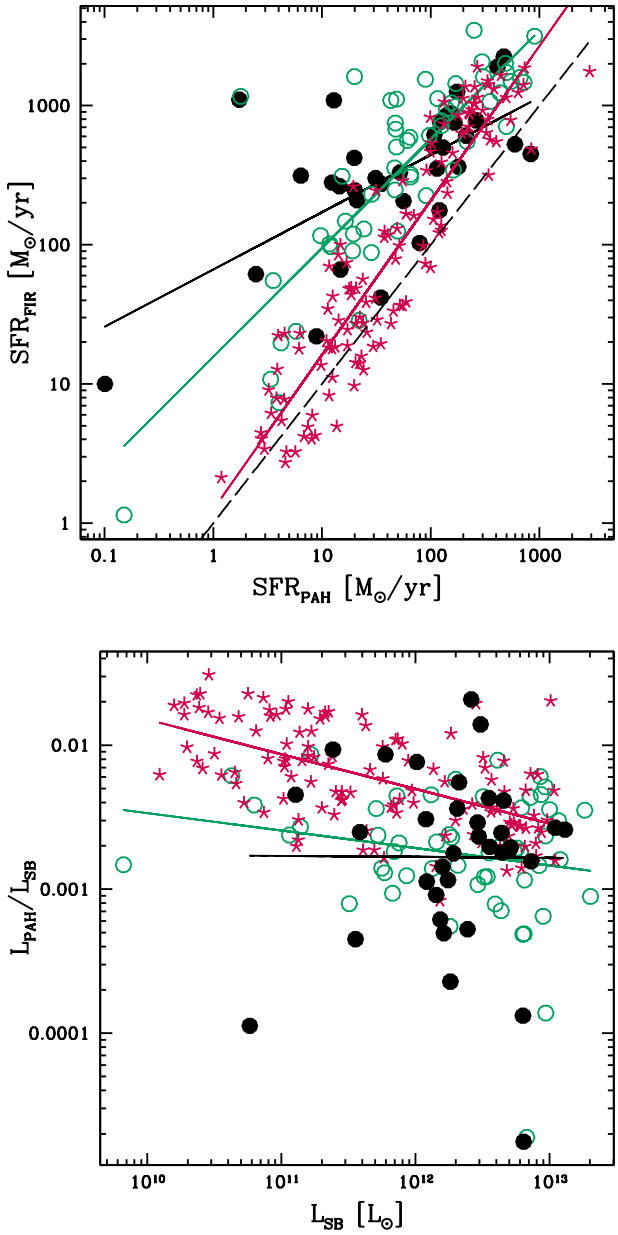

Figure 6.13: SFR_{FIR} versus SFR_{PAH} (top) and L_{PAH}/L_{SB} as a function of L_{SB} (bottom) for unobscured AGN-dominated objects (filled circles), AGN-dominated objects with an optical stellar component (open circles) and starburst-dominated objects (stars). The continuous lines mark the respective linear correlations, the dashed line (top panel) the 1:1 relation.

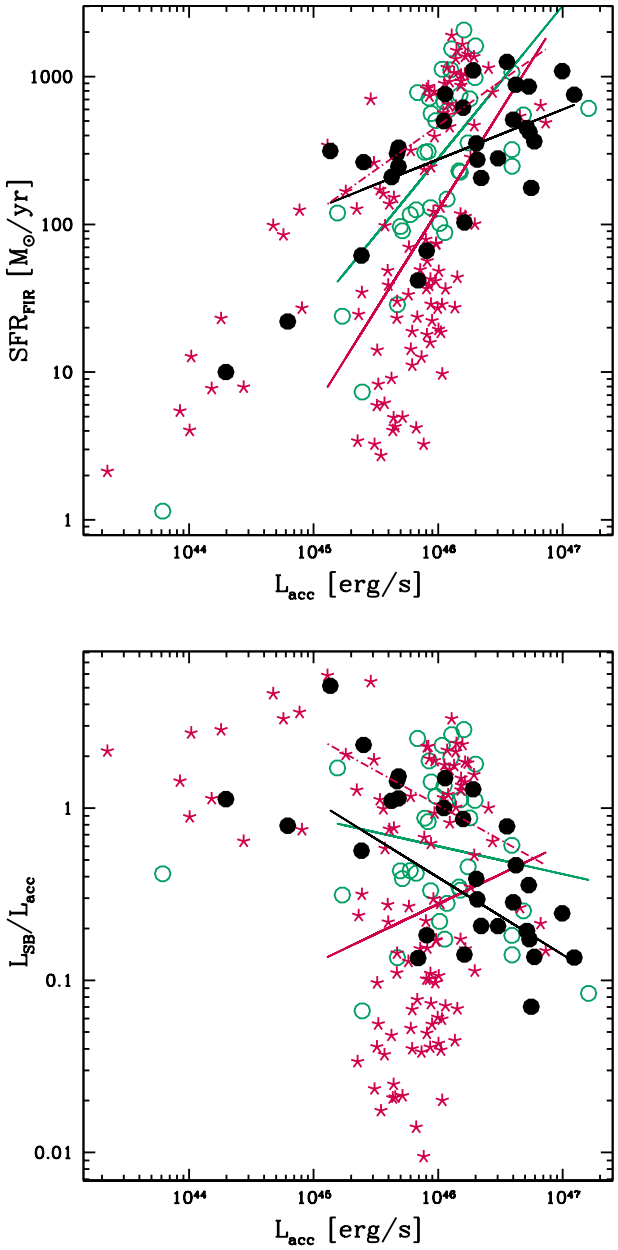

Figure 6.14: SFR_{FIR} versus L_{acc} and L_{SB}/L_{acc} as a function of L_{acc} for unobscured AGN-dominated objects, AGN-dominated objects with an optical stellar component and starburst-dominated objects. The symbols-code is the same of Fig. 6.4.2. The linear correlations shown here are computed for objects with $L_{acc} > 10^{45}$ erg/sec alone. The dotted-lines represent the correlation for starburst-dominated objects when discarding sources with N_H of the best torus model $< 3 \cdot 10^{23}$ cm^{-2}.

of the sample, i.e. objects with $L_{acc} > 10^{45}$ erg/sec, we see that unobscured AGN-dominated objects have a somewhat flatter distribution although the large scatter renders the correlation very weak (r=0.44). The increase of SFR seems to be less prominent for the very bright ($L_{acc} > 10^{46}$ erg/sec) unobscured AGN but the low number of objects makes the derivation of any firm conclusion impossible. There is a tail of starburst-dominate objects with $SFR_{FIR} < 100$ and $L_{acc} \sim 10^{46}$ erg/s for which the best fit torus models provide a quite high hydrogen column density, $N_H > 3 \times 10^{23}$ cm^{-2}. This means that such objects are potentially heavily obscured in the optical band bringing more uncertainties in the estimation of the accretion luminosity. The dotted-line in both panels of Fig. 6.14 represents the correlation of the starburst-dominated objects while excluding starburst-dominated sources with $N_H > 3 \times 10^{23}$ cm^{-2}. The behavior of the starburst-dominated objects now resembles more that of AGN-dominated ones, albeit presenting a higher SFR. When comparing L_{SB} with L_{acc} we find their ratio decreasing with increasing L_{acc} for AGN-dominated objects but not for starburst-dominated ones. Analogously, when discarding starburst-dominated sources with high N_H, the dotted-line in the bottom panel of Fig. 6.14 is parallel to that of unobscured AGN, with the starburst-dominated objects having higher L_{SB} at same values of L_{acc}.

6.4.3 The cold and hot dust components

The fit of the MIPS and SPIRE data with a grid of modified black bodies (as described in Section 6.3.2) returns the temperature of the cold dust component, heated by the starburst, as well as its mass. As already mentioned, we only fit a modified black body to objects with at least three data point at $\lambda > 100$ μm, one of which has to be MIPS 160 μm. The reason behind this choice is to sample both sides of the peak of the cold dust emission in order to avoid the introduction of possible biases (Shetty et al., 2009a,b) and the under/over estimate of the cold dust temperature/mass (Smith et al., 2012). The mass of the hot dust is that of the torus models, defined as the integral of all dust grains over all volume elements.

The masses of the cold (starburst-heated) and hot (AGN-heated, that is the sum of all dust grains integrated over the torus volume elements) dust components do not correlate with each other, as seen in Fig. 6.15. These two components occupy very different physical scales: the hot dust, heated by the accretion disk surrounding the central engine, extends out to a few tens of pc, while the cold dust, heated mostly by young stars in star-forming regions, extends to much larger distances from the central source, reaching kpc scales. Star formation is known to occur in individual or combinations of morphological features (such as spiral arms, central or extended starbursts, rings, etc) that are driven by gravitational instabilities, interactions and/or mergers. The lack of correlation between the masses of the hot and cold dust components therefore suggests that the gravitational effects that drive star formation do not divert a fixed fraction of the gas to the AGN center while the starburst is ongoing.

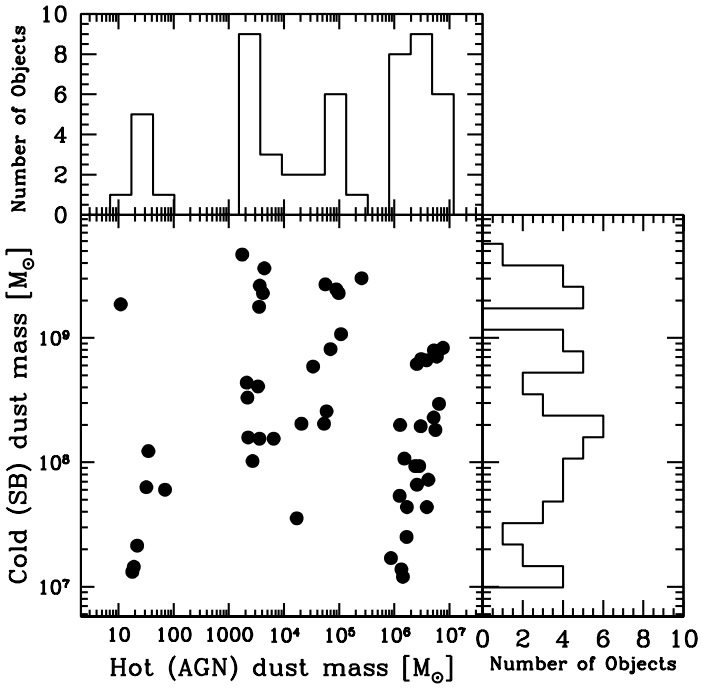

Figure 6.15: Cold (starburst-heated) dust mass versus hot (AGN-heated) dust mass.

To check whether the presence of an AGN has an impact on the heating of the dust at large scales, we check the correlation between the derived black body temperatures and the AGN accretion luminosity, L_{acc}, as shown in Fig. 6.16. Unfortunately, the requirement for a 160 μm detection to constrain the shape of the SED at $\lambda < 200$ μm limits the number of objects for which the temperature of the cold dust can be determined as the 160 μm data are very shallow: this affects many AGN-dominated objects (open and filled circles). Due to the small number of available data points we used a single-temperature modified black body component to account for the emission at FIR wavelengths where both warm and cold dust can contribute. The range of temperatures, reported in Table 6.4.3, that we fit is consistent with temperatures found by (e.g. Kirkpatrick et al., 2012) using a multi-temperature modified black body approach that considers two modified black bodies to account for the warm and cold dust components: the majority of the temperatures derived for the cold dust component span the range between 20 and 40 K, with a mean temperature of 28.5 K. Even though the majority of objects shown in this figure are starburst-dominated in the MIR, many harbour an AGN with high L_{acc} values. With the above caveats in mind, we find no evidence that the cold dust temperature is affected by the presence of an underlying AGN. This can also be seen from the average temperature of the different L_{acc} bins (reported in in Table 6.4.3).

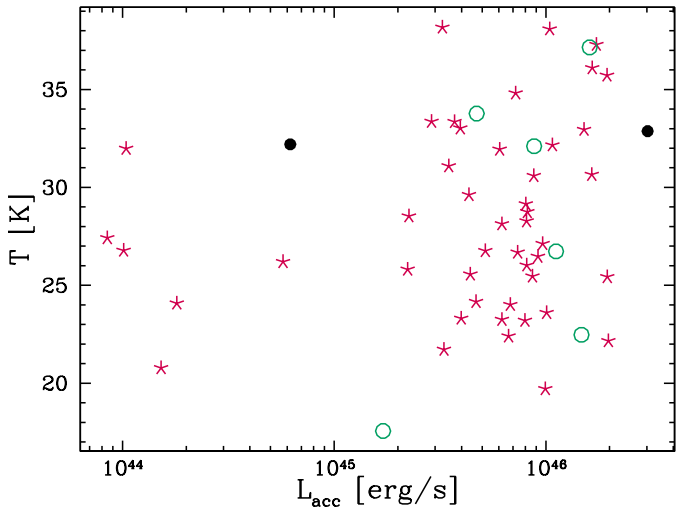

Figure 6.16: Cold dust temperature as a function of L_{acc} (circles and stars mark AGN- and starburst-dominated objects, respectively).

$L_{acc}[erg/s]$	#	$\langle T \rangle [K]$	σ_T [K]	T_{min} [K]	T_{max} [K]
total	53	28.5	5	17.6	38.2
$\leq 10^{45}$	7	27.1	3.8	20.8	32.2
$10^{45} - 10^{46}$	33	27.7	4.6	17.6	38.2
$> 10^{46}$	14	30.9	5.6	22.2	38.1

Table 6.2: Results of the temperature of the cold dust both for all the objects with MIPS 160 and for different bins of L_{acc}. From the left-most to the right-most column: range of Lacc, number of sources, mean temperature, $\langle T \rangle$, standard deviation, σ_T, and minimum and maximum temperature, T_{min} and T_{max}, respectively.

6.5 Conclusions

Assessing the effects of the presence of an active nucleus in the centre of a galaxy is of paramount importance to the understanding of the evolution of the galaxy and the coevolution of the activity processes occurring during the galaxy's lifetime. In this paper we present the analysis of a sample of 375 extragalactic sources in the northern HerMES fields of Bootes, FLS, Lockman and ELAIS N1 with available broad-band photometry spanning the optical (SDSS) to the FIR (*Herschel*), and *Spitzer*/IRS spectra, with the aim to investigate the observational signatures of AGN in the MIR and FIR wavelengths and their impact on the properties of their hosts. The IRS spectra impose constraints on the AGN torus models while the SPIRE photometry is essential for the measurement of the cold dust properties of the host galaxies. Spectrophotometric multi-band and multi-component SED fitting, in combination with EWs and luminosities of the PAH features measured from the IRS spectra, allows us to investigate the source properties as a function of AGN content.

We find SFR_{FIR}, the obscured star formation rate derived from the IR luminosity of the starburst component, and SFR_{PAH}, derived from the luminosity of the PAH features, to correlate with MIR AGN- and starburst-dominated populations presenting different correlations. Moreover, we note that, as a general trend, the SFR_{FIR} takes systematically higher values than SFR_{PAH}, with the possibility of this being due to statistical errors excluded. We find L_{PAH}/L_{SB} to be almost constant for AGN-dominated objects but to decrease with increasing L_{SB} for starburst-dominated objects, contrary to what has been reported by other authors (Lutz et al., 2008, and references therein). Furthermore, we observe an increase in SFR with increasing L_{acc}, with the increase less prominent for the very bright, unobscured AGN-dominated sources.

We find no noticeable effect of the presence of an AGN on the FIR properties of the host galaxy: SFR_{FIR} increases with increasing L_{acc}, as already reported in the recent literature (e.g. Serjeant & Hatziminaoglou, 2009; Hatziminaoglou et al., 2010; Serjeant et al., 2010; Bonfield et al., 2011). We find the ratio L_{SB}/L_{acc} to decrease with increasing of L_{acc}. No significant dependence of the temperature of the cold dust on L_{acc} is observed, even for sources harbouring bright AGN components with $L_{acc} > 10^{46}$ erg/sec.

The cold dust, heated by young stars in star-forming regions, extends to several kpc from the central source. The hot dust emission, on the other hand, arises from the pc-size region surrounding the central black hole and could, in principle, serve as the reservoir that feeds the black hole during the high energy accretion phase of a galaxy. We find the masses of the two dust components to be completely uncorrelated and interpret this lack of correlation as an indication that the fraction of gas funnelled to the AGN as a result of gravitational effects that also drive the starburst activity is not constant.

To summarize, our findings are in agreement with there being no evidence for

the AGN significantly influencing star formation processes of the host galaxy. This is consistent with the fact that most models predict an extremely brief feedback phase: when considering large IR samples, an average effect is expected to be observed. This implies that a correlation between the hot and cold dust properties is not expected to be seen, even with a feedback itself being very strong.

Our findings are based on spectral synthesis techniques that are methodology-dependent, and the models considered not completely free from degeneracy. Nonetheless, they do not support the scenario in which the AGN in a galaxy's center has an impact on the star formation of the host (as also found by e.g. Hatziminaoglou et al., 2010; Harrison et al., 2012; Santini et al., 2012; Rosario et al., 2012) but show, instead, that the two phenomena coexist in a variety of both AGN- and starburst-dominated sources spanning more than four orders of magnitude in both L_{acc} and L_{IR}.

7 | Conclusions

The recent progress of IR surveys offers a widely complementary view to the classical optical surveys allowing to extensively probe the dusty structures in the Universe. In fact, IR observations enabled conspicuous studies of the origin of galaxies and AGN and provided substantial amount of information about the evolutionary history of star formation and gravitational accretion. Indeed, both the two main activity phases of extragalactic sources, namely intense starburst episodes and accretion on a SMBH, strongly emit in the IR making a thorough analysis of such wavelengths essential for quantifying their relative contribution.

This Thesis was devoted to contributing new studies on the multi-band emission of active galaxies, with a special consideration for the possible relationship between star formation and gravitational accretion activity. For this purpose, we also carried out detailed spectral energy fitting decomposition trying to make the best use of the unprecedented high resolution *Spitzer* and *Herschel* data.

Multi-wavelength approach

We presented in this Thesis a SED fitting procedure aimed to reproduce the UV-to-IR SED of active galaxies accounting simultaneously AGN and the host galaxy emission. Briefly, the code considers three components of emission to construct the total best-fitting SED, namely SSP models to account for the stellar component, AGN torus models for the bulk of the MIR emission and starburst galaxy templates or a modified black body for cold dust emission. Since the galaxy SEDs are the main source of information about the physical processes taking place in the extragalactic sources, our procedure turned out to be a powerful tool to investigate the dusty emission from the AGN torus and the AGN-starburst connection. As already elucidated in chapters 3, 5 and 6, the code have been extensively used and applied to various samples at all the redshifts in order to achieve different goals. Our SED fitting procedure is appropriate to investigate the origin of the emission of single objects, as in the case of IRAS 09104+4109 (Section 4.7.1), to analyse the energy budget of the IR sources, as done with the sample of Fadda et al. (2010), and to investigate the physical properties of the various components contributing to the total emission, as done with the HerMES/IRS sample (Chapter 6). In addition, the code can make use of different models, chosen *a priori* by the

user, for the same components.

This results to be very useful when the aim is to carry a comparison between such models (e.g. Section 5.2). Various are the new improvements I made to the SED fitting code during my PhD, among with the opportunity to use a catalogue with data having different units of measurement, the possibility to account for the FUV extinction at high redshift and the choice between the use of an empirical starbust galaxy template or a modified black body, with this last used to have estimates of the mass and temperature of the cold dust. Finally, including of the IRS spectra in the fitting procedure, where is now possible to fit MIR spectra and photometric data simultaneously, provides much more constrains on the torus models, in particular for AGN-dominated objects. Consequently, the starburst models is more constrained as well. Furthermore, the SED fitting code is very flexible, in particular for what concerns the possibility to add new state-of-the-art model SEDs for the different components.

Future perspectives

Besides the addition of other models, such as the bi-phase models of Stalevski et al. (2012), further changes and improvements can be introduced in the SED fitting code. As already discussed, in our SED fitting procedure the stellar component is not connected with the starburst one. An approach accounting for the fact that the same optical/UV radiation, which is absorbed by dust, is also reprocessed in the IR would be, in same cases, more physical and more representative of the physical processes related to the host galaxy. From the other side, this energy balance approach, have been found not to be suitable for all the objects, e.g. spiral galaxies.

Future plans include the addition of an option, set by the user, concerning the use or not of such energy balance between optical/UV and IR. The idea is to relate the two emission components, the stellar and the cold dust ones, computing, upon appropriate assumptions, the optical/UV extinction and, then, estimating the correspondent emission of the interstellar dust grains heated by photons in a way similar to DustEM (Compiègne et al., 2010). This last is a numerical tool providing SEDs with a default spectra range between 0.04 and 10^5 μm, in which the dust emission is calculated in the optically thin limit, that is without radiative transfer.

Moreover, despite the least square minimization, on which our SED fitting technique is based, have been widely used in the astronomical community, there are important limitations to use it in model selection and fitting. In particular, the least square minimization strongly depends on Gaussian assumptions and it fails when the errors are non-Gaussian. Moreover, it does not provide clear procedure for adjudicating between models with different number of parameters or between different acceptable models (Feigelson & Babu, 2013). This limitations can be overcome by using more suitable methods, such as a bayesian approach

or by applying a boot strapping technique. This improvement will also provide errors associated to the physical properties, allowing for more detailed statistical studies.

Dust models in Active Galactic Nuclei

A large part of this Thesis is devoted to compare the two main classes of AGN torus models, differing from each other in the dust distribution approach adopted. Along the years both smooth models, characterised by a continuos dust distribution, and clumpy models, with dust concentrated in clumps or clouds, have been developed. Several were the claims supporting the possibility to discriminate between these two approaches by using SED fitting.

In Chap. §5 we report an extensive comparison between two of the most widely used torus models in the literature and both successful in reproducing different parts of the electromagnetic spectra, namely a revised version of smooth models of Fritz et al. (2006) (presented in Feltre et al., 2012) and the clumpy models of Nenkova et al. (2002, 2008a,b). After a thorough model-to-model comparison in which the main properties of the IR SEDs are extensively investigated with the aim to look for possible diagnostics, the model are compared with observed data including both photometry and MIR (*Spitzer*/IRS) spectra. We do not find any of the properties of the IR SEDs to be used as diagnostic between the two dust configurations and conclude that most of the differences found are due to different model assumptions, such as the chemical compositions of dust grains or the power law of the central source. Moreover, we show that both smooth and clumpy models can reproduce the same set of observations equally well, without any particular indication favoring one of the two models; however never for the same set of matched parameters. Indeed, we find virtually no random parameter combinations can resulting in seemingly identical SEDs.

In addition, degeneracies are often an issue when comparing observations with models, with many factors entering the game. The present study is not free of degeneracies, either. Different model parameter combinations can easily result in remarkably similar SED shapes, virtually indistinguishable from one another, with often significantly different underlying physical properties. Nevertheless, the combination of two or three emission components contributing to the total SED is an additional source of degeneracies.

Future perspectives

Since SEDs fitting results not to be the appropriate tool to distinguish between smooth and clumpy dust distributions, independent estimates of physical parameters, such as the optical depth, the size of the torus or the mass of the gas are needed in order to further constrain the models. In particular, X-ray observations could, for instance, provide an *upper limit* of the optical depth, integrated along

the line of sight and high resolution HI maps of known nearby AGN could put constraints on the gas content within the circumnuclear region. Furthermore, a detailed studies of X-ray variability of AGN monitored over a wide range of years could provide essential information on the possible presence of clouds along with their number and their size.

MIR interferometry, providing the brightness distribution of the torus emission projected onto the plane of the sky, is also an important source of information. Up to know, in this sense, such study have been made only on NGC 1068, the Circinus galaxy, and NGC 3783 (Hönig et al., 2006; Schartmann et al., 2008; Hönig et al., 2010). A step forward in this direction could be made with interferometric instruments of next generation, such as MATISSE (the *Multi Aperture mid-Infrared SpectroScopic Experiment*) and GRAVITY Eisenhauer et al. (2008, 2011), which will provide additional data to those already available.

Eventually, interferometry with the sub-mm and radio antennas of ALMA (the *Atacama Large Millimeter Array*) will permit to indirectly determine the morphology of the obscuring material by allowing the comparison between the MIR and sub-mm emission of the structure (see e.g. Maiolino 2008) or even to directly resolve the obscuring torus, making use of its very high angular resolution (sub-pc scale at the distances of nearby AGN at high frequencies).

Star Formation and Nuclear Gravitational Activity

Mounting are the evidence for a connection between starburst and gravitational accretion activity. In Chapter 6 we present our effort to investigate wether this coexistence between the two emission mechanisms can translate in a causal relation (Feltre et al., 2013). With this in mind, we selected a sample (see Section §6.1) representative of the MIR bright fraction of the HerMES population, the HerMES/IRS sample. We applied our SED fitting procedure to study simultaneously the properties of the AGN and the starburst, investigating the SFR in connection with the presence of an AGN and comparing the properties of the hot (AGN) and cold (starburst) dust components. Our sources show, in different levels, both AGN activity and star formation. Asserting which of the two mechanisms dominates the emission strongly depends on the wavelength range considered, since an active nucleus mainly contributes in the MIR and the starburst emission, due to colder dust, manifests the bulk of its emission at larger wavelengths. We find the SFR measured in the FIR, and hence the starburst luminosity, to increase with increasing of the AGN accretion luminosity with no clear sign of star formation suppression for the highest luminosity considered. Indeed, no significant trend between the temperature of the could dust and the AGN luminosity is also found suggesting that the influence of the AGN does not reach the scales on which dust is heated by star formation. This was interpreted as no evidence that the presence of an AGN could affects the properties of the host galaxy. Indeed, this was not expected to be seen since, when dealing with large samples, an average effect is

expected to be observed. Moreover, we interpret the lack of correlation between the masses of the cold and hot dust with the fact that a non-costant fraction of gas is diverted, by the gravitational effects, towards the centre of the nucleus while the starburst is ongoing.

Future perspectives

The debate in this field is still open, with different results from various SED fitting decompositions applied to sample of different fields in the sky and selected with different criteria. Lots of work still need to be done to see whether the black hole at the centre of the AGN plays a role in galaxy formation or not. To make step forwards in this context, it is essential to have large statistical samples of galaxies, including also rare but cosmologically important populations, that reach into the peak epochs of star formation and AGN activity. Additional information coming from other parts of the UV-to-IR spectrum are also important. In particular, radio observations can directly probe intensively star forming galaxies without dust biases and provide a direct test to investigate the radio AGN feedback, a process essential in understanding galaxy formation.

ALMA observations are expected to bring huge progress in this scenario, helping to expand our understanding about the AGN-starburst connection out to the first galaxies. Star formation activity is expected to heat the dust on kpc scales, while AGN should light up the dust only on pc scales. ALMA will allow to investigate the scale of dust heating by the two mechanisms by spatially resolving the dust reservoirs of galaxies. In particular, ALMA studies of sub-millimeter galaxies will allow us to investigate whether such sources are exclusively powered by dust heating of young massive stars or if an AGN is substantially contributing to their emission.

Complementary studies to that of SED decomposition concern the study of gas excitation using observations of CO transitions, in particular to investigate the circum-nuclear star formation. Eventually, the study of the AGN-induced kinematics in the ionized gas via integral field spectroscopy will put further constrains on the underlying physics.

Appendices

A Input files

A.1 User Setup

The user has to edit a file with the definition of different variables and flags that will be used along all the entire run over a sample of objects, namely:

homedir home directory where the code run and all the input/output data are saved

sf_flag can be set to `true` or `false`. If `true`, a file `objectname.sfr` containing the values of the SFR and corresponding details is created (for testing purposes)

torus_disable can be set to `true` or `false`. If `true`, the AGN emission in the fit is turned off

madau can be set to `true` or `false`. If `true`, the prescription of Madau (1995) for the intergalactic absorption is taken into account

nbest_mod integer number of best models saved in the file `objname.BST` (see Sec. 6.4)

l_sb real number corresponding to the wavelength over which the cold dust emission is inserted in the fit (see Sec. 4.5). The default value is 24 μm

H_0 Hubble constant

OmegaL real double number corresponding to the ratio between the energy density due to the cosmological constant and the critical density of the universe, Ω_λ

OmegaM real double number corresponding to the ratio between the energy density due to the matter in the universe and the critical density of the universe, Ω_M

Below and example of a `user_setup` file:

```
'/Users/lapguest/SEDFIT12/'              !homedir home directory
```

```
.true.    !sf_flag
.false.   !torus_disable
.true.    !if true uses the Madau 95 prescription
2         !nbest_mod
2.40d1    !l_sb
72.000     !H0 in km/s/Mpc
7.00d-1    !OmegaL
3.00d-1    !OmegaM
```

A.2 Configuration File

The input to the code can be given either interactively (option "0") or be included in a configuration file (option "1"). The input parameters/variables required are:

- the name of the catalogue with photometric points (in the format described in Sec. A.3)
- value used in the catalogue to denote missing data
- a second value in case of absent data
- choice of the models to fit the stellar components [`T` or `t` = stellar template, `S` or `s` = SSP models with Schmidt's law]
- choice of the stellar metallicity ["1", "2" or "3" correspond to a metallicity of 0.5 (Super Solar), 0.02 (Solar) or 0.004 (Sub Solar), respectively]
- choice of the extinction's law ["1", "2", "3", "4" or "5") correspond to a total-to-selective extinction ratio $R_v = 3.1$ (Cardelli et al., 1989, the one the Milky Way), 4.0, 5.0, the one of the attenuation's law of Calzetti et al. (1994) and the one of the Small Magellanic Cloud, respectively]
- choice for the behavior of the E(B-V) [`0` or `1` correspond to a constant E(B-V) or a E(B-V) with an exponential increase with the SSP, respectively]
- choice of the methodology to calculate the age of the galaxies: [1] it is calculated on the basics of the galaxy's redshift; [2] the age of the oldest SSP for each object is required as an input,; [3] a common redshift of formation for all the objects is required; and [4] the code requires a redshift of formation for each object
- threshold value for the χ^2 of the fit of the stellar component (see Sec. **??** for the details about the fitting methodology)
- choice of the grid of AGN torus models (1= smooth models of F06, = clumpy models of N08)

- value of the optical-to-X ratio (used only if observed L_x(2-10 keV) are available)

- choice of the model to be used to fit far-IR data (`sb` = starburst template, `gb` = grid of modified black bodies)

Here is an example of a configuration file

```
sample_paper2_1.cat # catalogue name
-99.0 # absent data value
99.0 # absent data value (2)
s # models for the star (s=Schmidt law)
2 # ssp metallicity
2 #  option for the extinction file
0 #  option selective extinction
1 # option to calculate galaxy age
5. # chi2 over which the code DO NOT fit the stars
1 # torus model type
1.45 # AlphaOX
sb # FIR flag
```

A.3 Photometric catalogue Format

The photometric catalogue is an ascii file that lists all available photometric data points per object, one object per row. This SED fit program was conceived to deal with data as generic as possible and with an arbitrarily large number of objects. The format of the catalogue is close to the SExtractor output catalogue: a header consisting in a series of rows starting with a symbol (usually '#'), the number of the column, one label and an integer specifying the data type for each column (see below). On the basis of this last integer number, the corresponding data will be treated in the opportune way by the code.

The data type can take the following values:

0 data not used in the procedure and it will not appear in the final output

1 name or ID of the object

2 flux, in μJy

3 error on flux, in μJy

4 Vega magnitude

5 percentage error on Vega magnitude

6 AB magnitude

7 percentage error on the AB magnitude

8 X luminosity emitted between 2 and 10 keV (restframe) and dereddened, in erg/s

10 Right Ascension (RA), used only on the final output table

11 Declination (Dec), used only on the final output table

12 z, the redshift column

A fifth column should include the name of the filter (`bandname`) corresponding to the flux of a given column, e.g. "B", "irac1", "mips24". The code requires the filter response curves corresponding to each fluxes and magnitude column. Each of these response curves should be in a file named (`bandname.dat`), with the wavelength expressed in μm.

When the observed errors in fluxes or in magnitudes are lower than 5%, their value will be recalculated and fixed equal to the 5% of the corresponding flux. Missing fluxes and/or magnitudes are recognized by assigning to them a negative value, e.g. in the form of -99.99, -999.00, etc. Upper limits are used anyway and they need to be indicated with a negative sign.

One objects without a redshift determination (identifying with the value for absent data, e.g. -99.0) will be skipped and will not appear on the final table.

A typical header with the first couple of rows of the catalogue looks like the following:

```
#1 ObjID                          1
#2 RA                            10
#3 Dec                           11
#4 zspec                         12
#5 AB_u                         2       u_sdss
#6 AB_g                         2       g_sdss
#7 AB_r                         2       r_sdss
#8 AB_i                         2       i_sdss
#9 AB_z                         2       z_sdss
#10 Vega_j                        2       J_2MASS
#11 Vega_h                        2       H_2MASS
#12 Vega_k                        2       Ks_2MASS
#13 flux_irac1                    2       irac1
#14 flux_irac2                    2       irac2
#15 flux_irac3                    2       irac3
#16 flux_irac4                    2       irac4
#17 flux_mips24                   2       mips24
#18 err_flux_u                    3
#19 err_flux_g                    3
#20 err_flux_r                    3
#21 err_flux_i                    3
#22 err_flux_z                    3
#23 err_flux_j                    3
#24 err_flux_h                    3
#25 err_flux_k                    3
#26 err_flux_irac1                3
#27 err_flux_irac2                3
#28 err_flux_irac3                3
#29 err_flux_irac4                3
#30 err_flux_mips24               3
# ID                 ra             dec           z          flux_u_sdss   ...
  25777152_0  0.18188   162.47214    56.764288     20.29640007019043  ...
  17418240_0  1.93      160.637117   57.909498     -99.0 ...
```

A.4 IRS spectra format

The code was originally developed to deal only with photometric data. A recent update allows also the simultaneous use of photometric data and IRS spectra (if available).

The files containing the information about the IRS spectra should be in the format `objectname.spec` and saved in `/SEDFIT/data/spectra/`, where the `objectname`

is the name identifying the object also in the photometry catalogue. The files should contain 3 columns: wavelength (expressed in μm), the flux and the error (both expressed in μJy). The code checks for the presence of a file containing the spectral information: if it is there, it will deal with them as explained in Sec. §4.4.3. If not, it will go ahead taking into account only the photometric information.

B | Main Output File

The main output file, `output.dat`, summarize in columns (28, 30 and 32 columns depending on the options used) the properties and characteristics of the sources in the sample and their best fit models. A detailed description of the meaning of all the columns with the correspondent label is given below.

ID identifying the name of the object, taken from the input catalogue

z redshift of the object, taken as input from the catalogue

Ld luminosity distance calculated after assuming a cosmology (usuallly a "standard" cosmology $H_0 = 72$, $\Omega_\Lambda = 0.70$ and $\Omega_M = 0.30$, even though it can be changed at will in the user setup file (see Appendix A.1))

RedChi2 reduced χ^2 value, χ^2_ν, defined in Sec.. 4.5

TorusModel name (and eventually path) of the best fit torus model

Rin torus inner radius, in pc

Rout effective torus outer radius, in pc. In the case in which the dust density is independent on the radial coordinate, this can be easily calculated using the ratio R_{in}/R_{out}. [For F06 models] In case of radial dependence (usually, decreasing density with the increasing of the distance from the center), some models can present a particularly low density in the outer regions of the torus, resulting in a negligible dust density for such regions. The physical size of the torus is truncated at the point in which the equatorial density is 1/10 of the one calculated from the inner radius (see Appendix C.2 for further details)

DustMass for F06 models is the dust mass of the torus, in solar masses. For N08 models it refers to gas mass. In order to compare the two an assumption on the gas/dust ratio need to be taken into account.

Vang integer identifying, inside the best fit torus models, the viewing angle respect which the model is calculated (NB: for F06 models 1 corresponds to the equatorial plane, 10 corresponds to a completely face-on view of the toroidal geometry, and viceversa for N08 models)

bestvang is the value of the viewing angle of the best fit model, expressed in degrees, calculated starting from the equatorial plane for F06 models and from the torus axis for N08 models

NHv Hydrogen column density along the line of sight

Vextv V band (0.55 μm) extinction calculated along the line of sight

tau_eqV optical depth calculated in the V band (0.55 μm) along a radial direction within the equatorial plane

tau97v or tauv optical depth along the line of sight calculated at 9.7 μm (tau97v) for F06 models and in the V band at 0.55 μm (tauv) for N08 models

EffAng [only when the F06 torus models are considered] effective amplitude of the torus (in deg): when the models has a constant behaviour of the density respect to the altitude on the equatorial plane, it corresponds to the nominal opening angle of the model. When a non constant density profile along the vertical coordinate ($\gamma \geq 0$ in the Eq. 3.10) is assumed, there is the need to take into account the possibility for the density to reach, at certain altitude on the equatorial plane, such a low value to allow a view of the system very close to that of a type 1. In this case the nominal value of the torus opening angle could be not particularly significative. Then, the value of the angle θ for which the optical depth, calculated at 0.3 μm, is equal to 1 is calculated (for more details see Appendix C.2).

Pesc [only when the N08 torus models are considered] probability to see the central source for the respective inclination of the best fit model (if Pesc>0.5 we are dealing with a type 1 and viceversa)

CF covering factor, that is the dust free fraction of solid angle (see Sec. 6.4 for details on calculation)

Lacc is the bolometric luminosity due to accretion in unit of 10^{46} and 10^{45} erg/s for F06 and N08 models respectively. It represents the model input energy, that is the primary source of dust heating

LX(mod) the luminosity in the interval $2 - 10$ keV resulting from the fit. It is calculated starting from the accretion luminosity. This option is not well tested so it has been left out from the content of this thesis

rho_in the dust density at the inner torus radius

StarScaling is the normalization of the stellar component scale factor. It is the stellar mass of gas burned into stars from the epoch of galaxy formation to the time corresponding to its age (i.e. the stellar mass) in units of solar masses.

Mstar [only when using SSPs] is the mass, in solar mass unity, contained at any epoch inside stars. It concerns both surviving stars and dead remnants

Mlum [only when using SSPs] is the mass contained into still surviving stars at any epoch

StarTempl [only when the stellar option is the one with templates] name identifying the template used for stellar emission (e.g. ELLIPTICAL, Sa, Sb, Sc, etc...)

Tgal [only when using SSPs] time of galaxy formation (that is the age of the oldest stellar population), T_{gal}

tau [only when using SSPs] duration time of the initial star formation burst, in units of T_{gal}

E(B-V) total extinction of the stellar population

SBTempl name of the starburst template used (or `nostarburst` when the cold dust emission component is not used). In the case of a modified black body instead of the SB template the name is identified by the value of the temperature T and the dust emissivity index β (e.g. `te`40.00`be`2.0 for T=40 K and $\beta = 2.0$)

SBScale starburst template normalization factor

Lir(8-1000) total infrared luminosity, calculated as the integral of the model between $8 - 1000$ μm (rest-frame)

AGNfrac percentage AGN contribution to the total infrared luminosity

C | Note on the Model Calculations

C.1 Λ-iteration Method

The Λ-*iteration* method to solve the radiative transfer equation (used by Granato & Danese 1994 and Fritz et al., 2006) consists in choosing as lower limit for the incident radiation that of the accretion primary source alone, i.e. without accounting for the thermal emission and the scatter of the dust. These two are introduced in the later iterations. The equilibrium temperature of each species of grain in each element (in which the geometrical shape of the torus is divided) is obtained solving the thermal equilibrium equation:

$$\int_{\lambda_m}^{\lambda_M} Q_{abs,id}(\lambda) \cdot I_{AGN}(ik,\lambda) d\lambda - \int_{\lambda_m}^{\lambda_M} Q_{em,id}(\lambda) \cdot B(\lambda, T_{id,ik}) d\lambda = 0 \tag{C.1}$$

whew id refers to the grain species and $B(\lambda, T)$ is the black body emission:

$$B(\lambda, T_{id,ik}) = \frac{2hc^2/\lambda^5}{e^{(hc/\lambda k T_{id,ik})} - 1}. \tag{C.2}$$

$T_{id,ik}$ is the temperature of the grain species of the $ik-$element. $I_{AGN}(ir,\lambda)$ is the specific intensity emitted buy the AGN:

$$I_{AGN}(ik,\lambda) = \frac{1}{4\pi} \cdot \frac{L(\lambda)}{4\pi r_{ik}^2} e^{-\tau_{ik}(\lambda)} \tag{C.3}$$

where $\tau_{ik}(\lambda)$ is the optical depth of the region between the central source and the $ik-$element, r_{ik} is the distance from the centre and L(λ) is the input AGN spectra (in $ergs^{-1}\,\mu m^{-1}$).

Once estimated the temperature for each grain species, it is possible to include the thermal emission and the scattering. Then 3.3 becomes:

$$J^{ik}(\lambda) = I^{ik}_{AGN}(\lambda) + \frac{1}{4\pi} \cdot \cdot \sum_{e=1}^{N-1} \left\{ \frac{\sum_{id}^{N_{dust}} [4\pi \cdot \pi a_{id}^2 Q_{id}^{em}(\lambda) B(\lambda, T_{e,id}) + 4\pi \cdot \pi a_{id}^2 Q_{id}^{sca}(\lambda) J_{tot}^{e}(\lambda)] e^{-\tau_{ik,e}(\lambda)}}{4\pi \cdot r_{ik,e}^2} \right\}$$

where e is the generic volume element, N is the total number of volume elements and ik indicated the element. J^e_{tot} is the total specific intensity heating the e-element and coming both from the AGN and the torso dust (thermal dust emission and dust scattering). Note that these two components are unknown at the beginning, so they are not included in the first calculation of the temperature estimate.

Such calculations are iteratively repeated until the difference between the temperatures of 2 consecutive iterations is lower than a prefixed value. In specific, F06 chose 1 K as maximum temperature difference allowed.

C.2 Note on the Calculations of the Effective Angle and Radius

In the case of smooth models of F06, as already mentioned in Sec. 6.4, under the assumption of a constant spatial density profile of the dust, is straightforward to define the geometrical sizes of the torus. The density inside the torus is expressed with the law (see also Eq. 3.10):

$$\rho\left(r,\theta\right) = \alpha \cdot r^{-q} \cdot e^{-\gamma \cdot |\cos(\theta)|} \tag{C.4}$$

where, in a polar coordinate system centered on the centre of the object, r is the radial coordinate, θ the angular one and a constant density imply $q = 0.0$ and $\gamma = 0.0$. Models with $q > 0.0$ will have decreasing density towards the external parts, while $\gamma > 0.0$ imply a decreasing of the density with the altitude respect to the equatorial plane. In the case of models with optical depth particularly low it can happen that the density in the external parts, or in region far from the equatorial plane, is effectively low with the consequence that the torus "get blured" with the interstellar medium. This needs to be taken into account when the aim is to deal with the torus as an independent entity and when defining its geometrical properties. For this reason, in models with $q > 0.0$ the point for which the dust density is equal to $1/10$ of the one calculated at the internal radius can be else defined:

$$\rho\left(r,\theta = \pi/2\right) = \alpha \cdot r^{-q} \qquad \rho_{lim} = \frac{1}{10}\rho\left(r_{in},\pi/2\right) = \frac{\alpha \cdot R_{in}^{-q}}{10} \tag{C.5}$$

where R_{in} is the inner radius and ρ_{lim} is the lower limit of the density previously defined and it can also be written as:

$$\rho_{lim} = \rho\left(r_{lim},\pi/2\right) = \alpha \cdot r_{lim}^{-q} \tag{C.6}$$

which is the definition of external radius looked for. From this last and from C.5

$$r_{lim} = 10^{1/q} \cdot R_{in}. \tag{C.7}$$

The opening angle of the torus in the case in which $\gamma > 0.0$, that is a decreasing of the density with the increasing of the altitude respect to the equatorial plane, can be derived in analogous way. In this case at some point the density of the dust can be considered negligible meaning that the torus is "not significative" anymore when θ is that for which the optical depth at 0.3 μm is equal to 1. Taking the expression for the density, Eq. C.4, and writing the expression valid on the equatorial plane, we obtained:

$$\rho_{eq} = \rho\left(r = R_{out}, \theta = \pi/2\right) = \alpha \cdot R_{out}^{-q} \tag{C.8}$$

where R_{out} is the outer radius of the torus. In this way the expression for the total density, that is the one calculated on the external surface, as a function of the altitude on the equatorial plane is:

$$\rho_{\theta} = \alpha \cdot R_{out}^{-q} \cdot e^{-\gamma \cdot |\cos(\theta)|} = \rho_{eq} \cdot e^{-\gamma \cdot |\cos(\theta)|} \tag{C.9}$$

The expression defining the optical depth along the radial coordinate, that is at fixed θ:

$$\tau_{eq}(\lambda_{ref}) = \int_{R_{in}}^{R_{out}} \sum_{id=1}^{Ndust} \left\{ \left[Q_{id}^{A}(\lambda_{ref}) + Q_{id}^{S}(\lambda_{ref}) \right] a_{id}^{2} \pi \cdot Nd_{id} \right\} \cdot \rho_{H}(r, \theta) dr \tag{C.10}$$

where Q_{id}^{A} and Q_{id}^{S} are the coefficients of absorption (emission) and scattering for the $i-$ dust grain, respectively. a_{id}^{2} is the external dust grain radius (in the calculations of the coefficients, see Weingartner & Draine, 2001, , the dust grains are supposed to have a spherical shape) and Nd_{id} s the number of the grain of $i-$kind normalized to the Hydrogen density, $\rho_{H}(r, \theta)$. The sum is made over the total number of sizes and species of the grains, while the integral is calculated between the minimum R_{in} and maximum radius R_{out} of the torus. Since the dust properties as well as their distribution function do not vary along the radial coordinate, it is possible to derive C.10 as follows:

$$\tau_{eq}(\lambda_{ref}) = \sum_{id=1}^{Ndust} \left\{ \left[Q_{id}^{A}(\lambda_{ref}) + Q_{id}^{S}(\lambda_{ref}) \right] a_{id}^{2} \pi \cdot Nd_{id} \right\} \cdot \int_{R_{in}}^{R_{out}} \alpha \cdot r^{-q} dr \tag{C.11}$$

Generalizing it for each line of sights, that is to a generic angle $\theta \neq \pi/2$, and taking into account this last one, the C.10 becomes:

$$\tau(\lambda_{ref}) = \tau_{eq}(\lambda_{ref}) \cdot e^{-\gamma \cdot |\cos(\theta)|} \tag{C.12}$$

where it is possible to isolate the part dependent on the polar angle because it does not enter directly in the integration. For this reason the properties such as the optical depth, the extinction A_V, the Hydrogen column density N_H along a certain line of sights, can be easily calculated when $\gamma \neq 0$. Indeed, analogues expression

to the C.12 exist for N_H and A_V. As already mentioned for models with low equatorial optical depths and certain angles θ the dust density, and consequently the optical depth, can decrease, even thought an intersection between the torus and the ling of sight, till at the point in which a view similar to a type 1 view is allowed. Following the definition given above to truncate, when necessary, the torus aperture, an "effective" opening angle θ_e as well as a covering factor can be calculated.

The angle θ_e is calculated imposing:

$$\tau_\theta(\lambda = 0.3) = 1 \tag{C.13}$$

which can be translated in a condition on the Hydrogen density:

$$\rho(r,\theta) = \alpha \cdot r^{-q} \cdot e^{-\gamma \cdot |\cos(\theta)|} = \rho_{eq} \cdot e^{-\gamma \cdot |\cos(\theta)|}. \tag{C.14}$$

Since, as can be deducted from Eqs. C.11 e C.12, a linear correspondence between the Hydrogen density and the optical depth exists (defined for less than a constant which depend on the geometry and on the optical properties of the dust grains), the following equivalence can be defined:

$$\rho_{\theta_e} : \rho_{eq} = 1 : \tau_{eq} \tag{C.15}$$

where θ_e is the angle for which the optical depth at a certain wavelength is equal to 1. Using the angle for which the optical depth (at a prefixed wavelength) is equal to 1 and using the C.14 we can write:

$$\frac{\rho_{eq} \cdot e^{-\gamma \cdot |\cos(\theta_e)|}}{\rho_{eq}} = \frac{1}{\tau_{eq}} \tag{C.16}$$

from which the expression for the "threshold" angle is obtained:

$$\theta_e = acos\left[\frac{1}{\gamma} \cdot \ln(\tau_{eq})\right]. \tag{C.17}$$

D | Best fitting models of the HerMES/IRS sample

I report in this Appendix some of the best fitting models obtained by applying the SED fitting procedure described in Chapter 4 to the 250 μm selected sources with IRS spectra in four of the HerMES fields, referred to us the HerMES/IRS sample. The best fitting models showed here are representative of the results for all the sample. In all the following panels photometric data are shown with red symbols, the IRS spectra in turquoise and the average flux for each band in which the IRS spectra was divided are represented with orange symbols. A sum of three components SSP models (dotted dark green line), AGN torus model (blue dashed line) and the starburst components (dotted light green line) give total best fitting models (black continuous line).

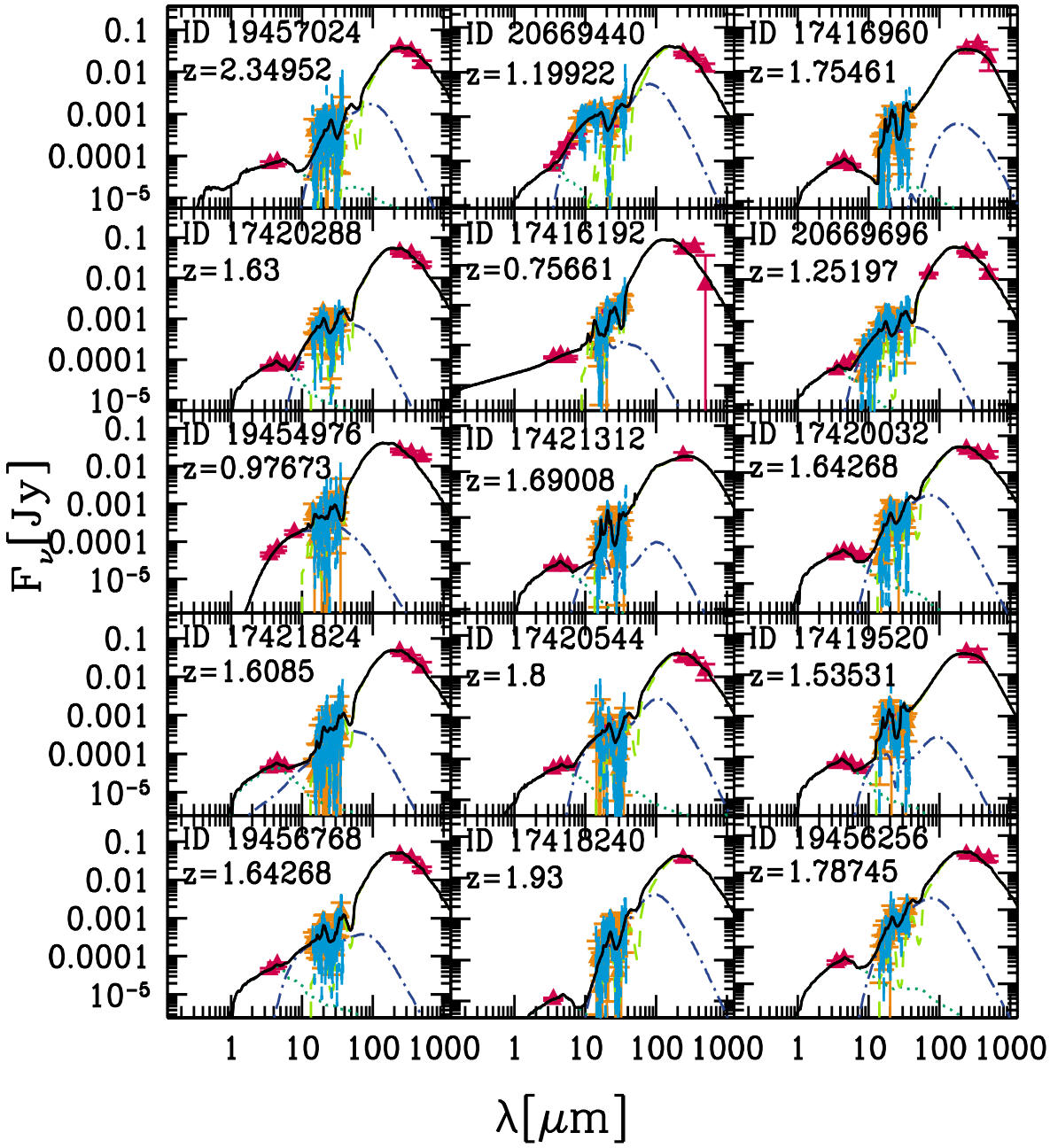

Figure D.1: Examples of a best-fit to the HerMES/IRS sample. The IRS spectrum (turquoise) and photometric data (red symbols) are reproduced using three emission components: SSPs (dotted dark green line), AGN torus (dot dashed blue line) and starburst (dashed light green line), giving the total model emission (in black).

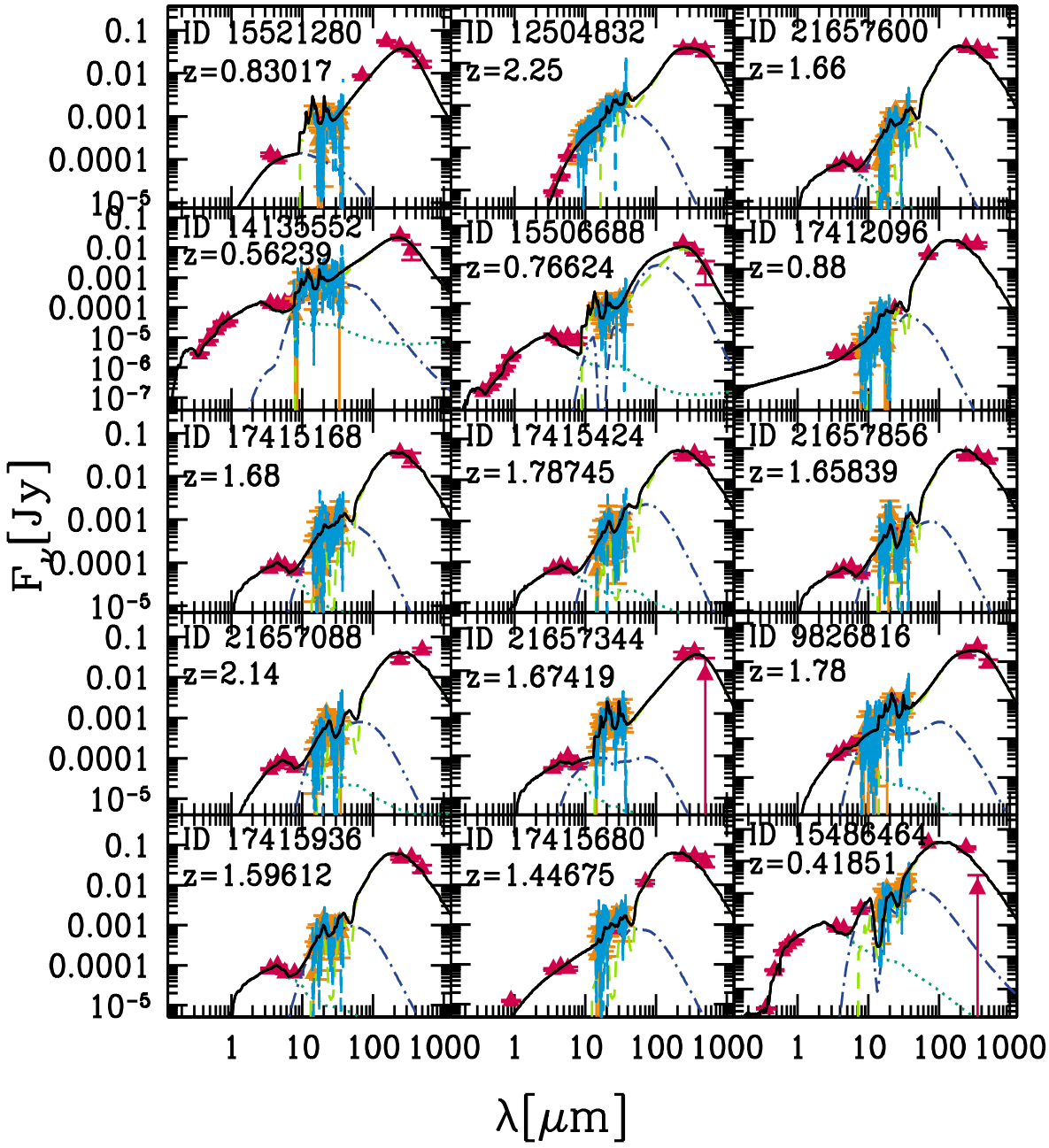

Figure D.2: Other examples of a best-fit to the HerMES/IRS sample. Symbols and colors code are the same of Fig. D.1.

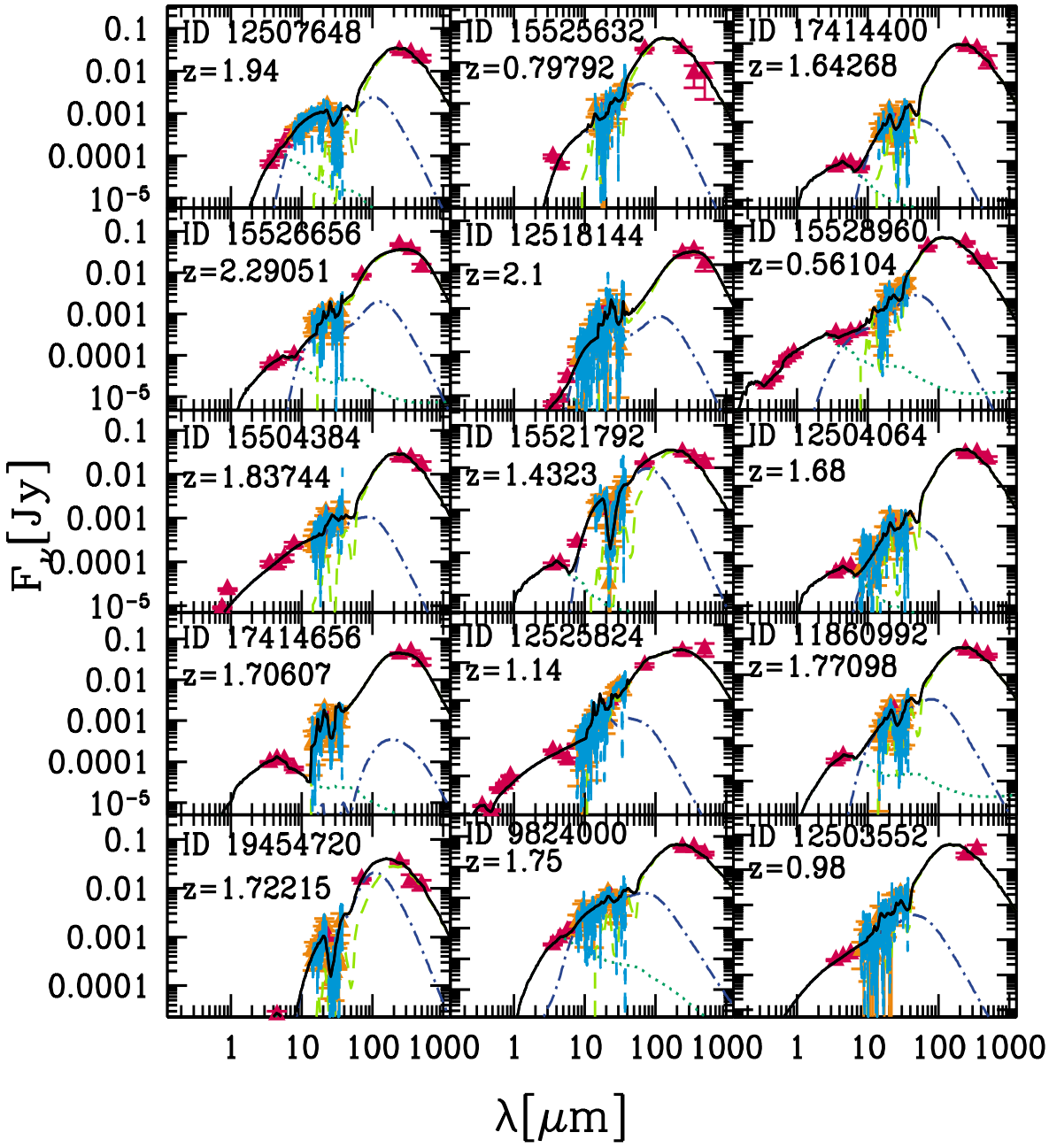

Figure D.3: Other examples of a best-fit to the HerMES/IRS sample. Symbols and colors code are the same of Fig. D.1.

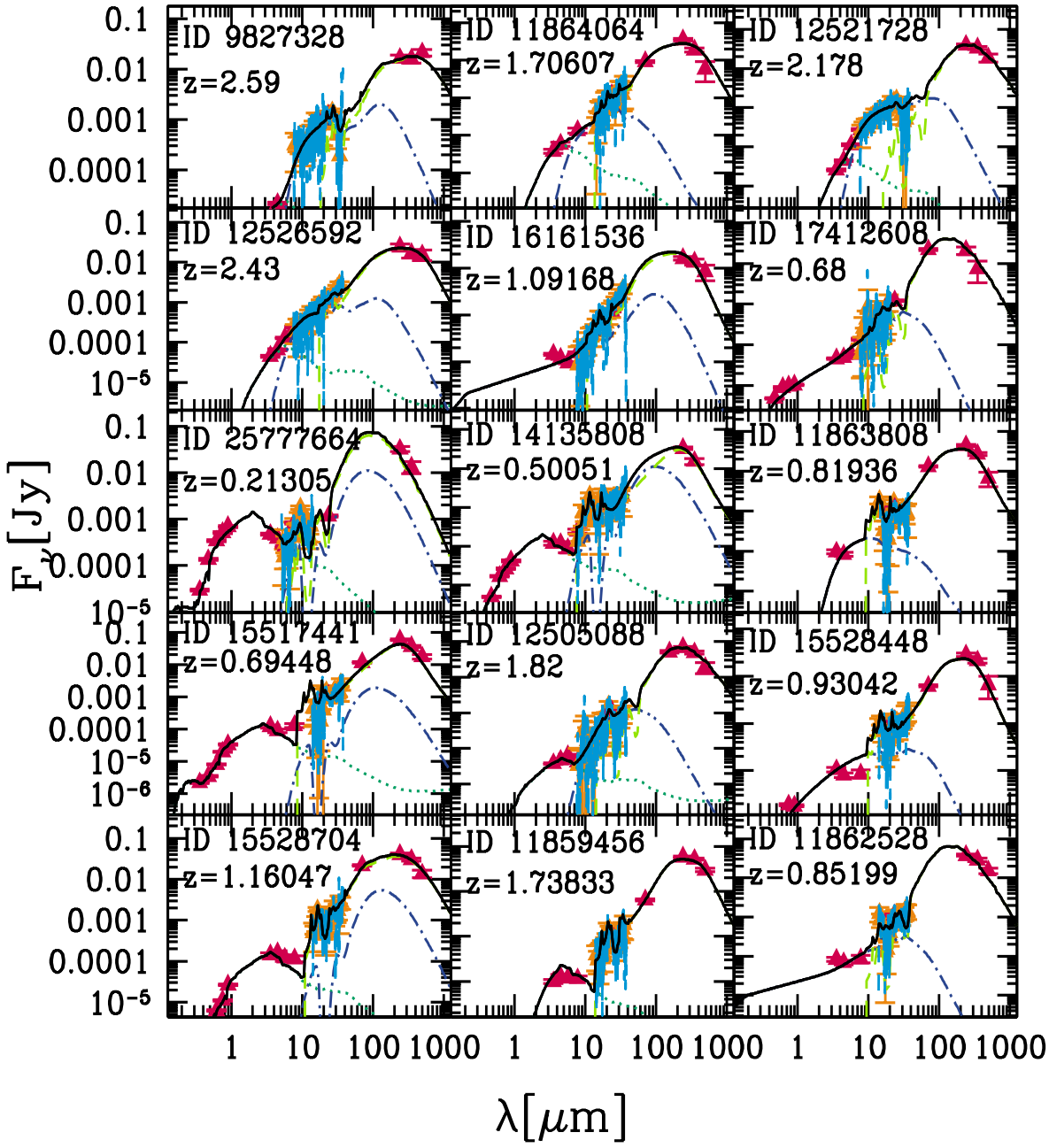

Figure D.4: Other examples of a best-fit to the HerMES/IRS sample. Symbols and colors code are the same of Fig. D.1.

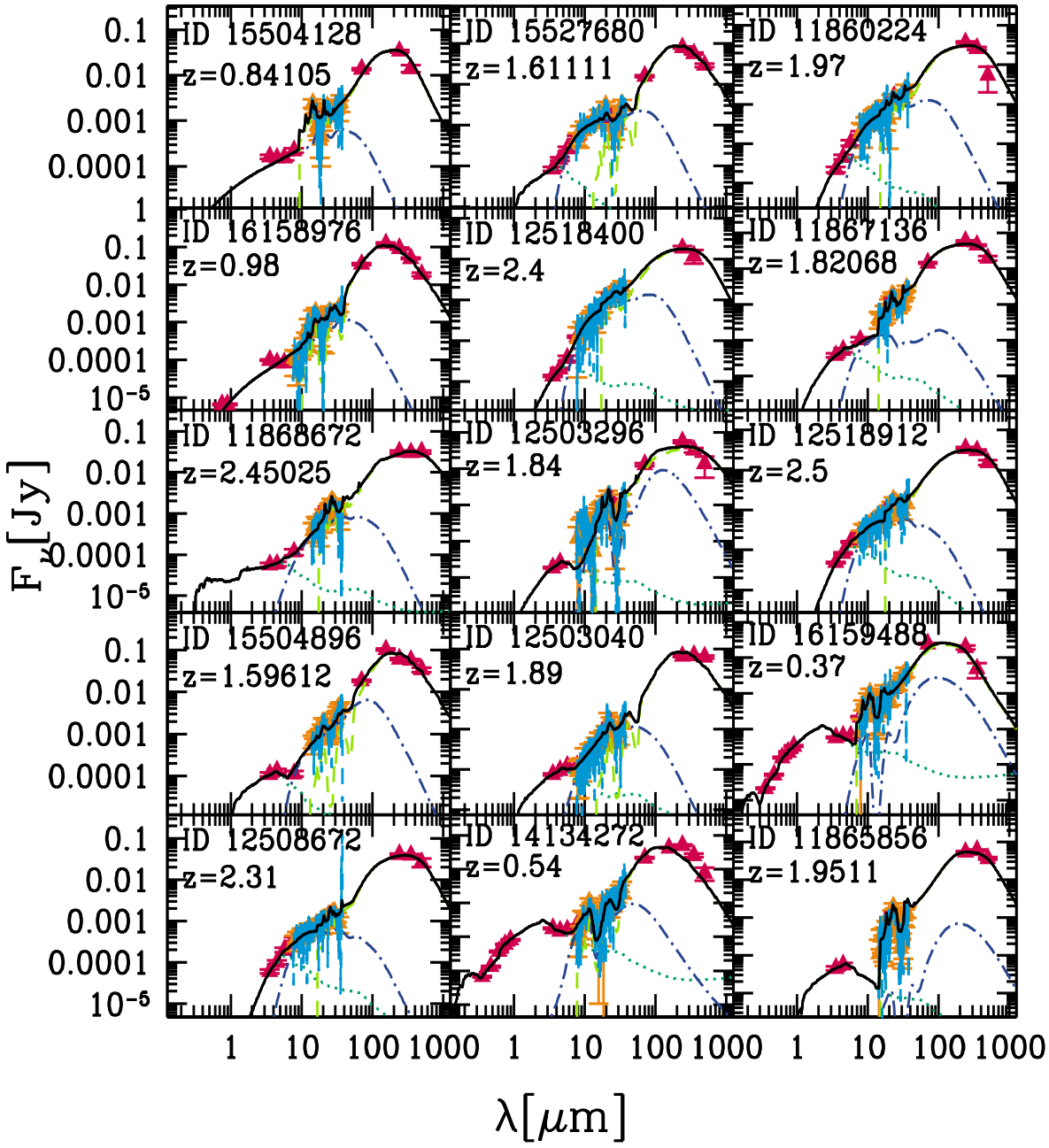

Figure D.5: Other examples of a best-fit to the HerMES/IRS sample. Symbols and colors code are the same of Fig. D.1.

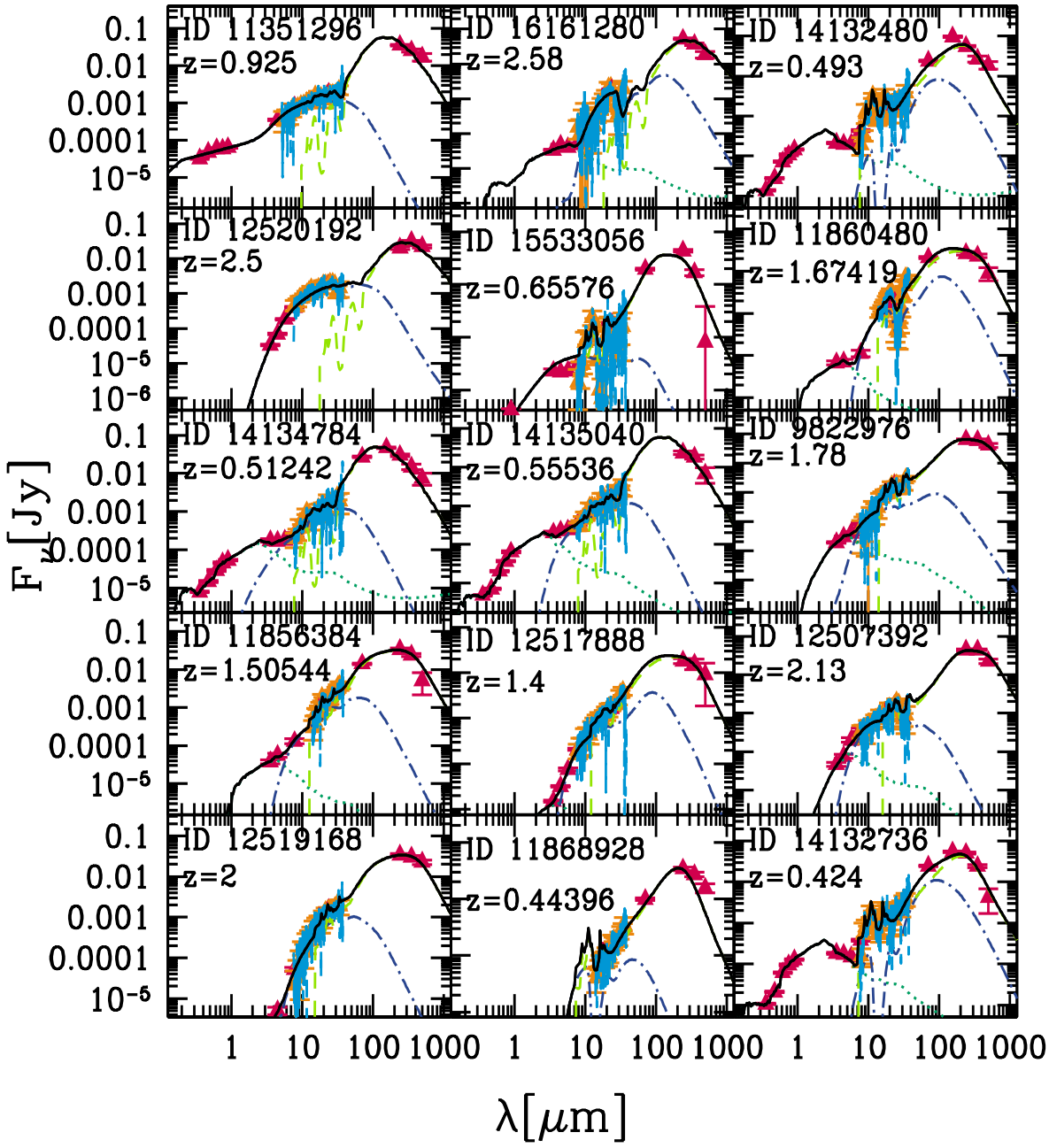

Figure D.6: Other examples of a best-fit to the HerMES/IRS sample. Symbols and colors code are the same of Fig. D.1.

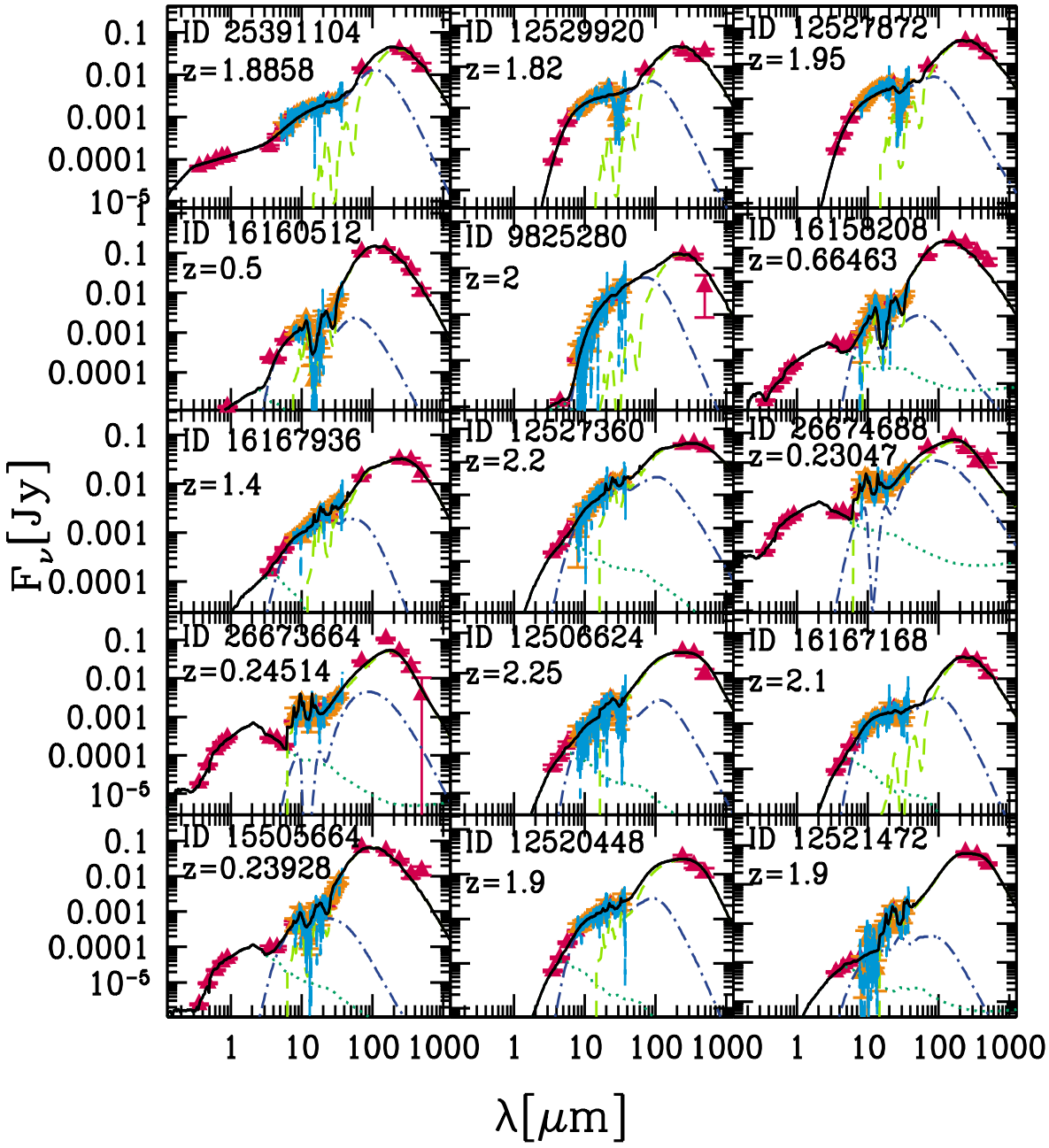

Figure D.7: Other examples of a best-fit to the HerMES/IRS sample. Symbols and colors code are the same of Fig. D.1.

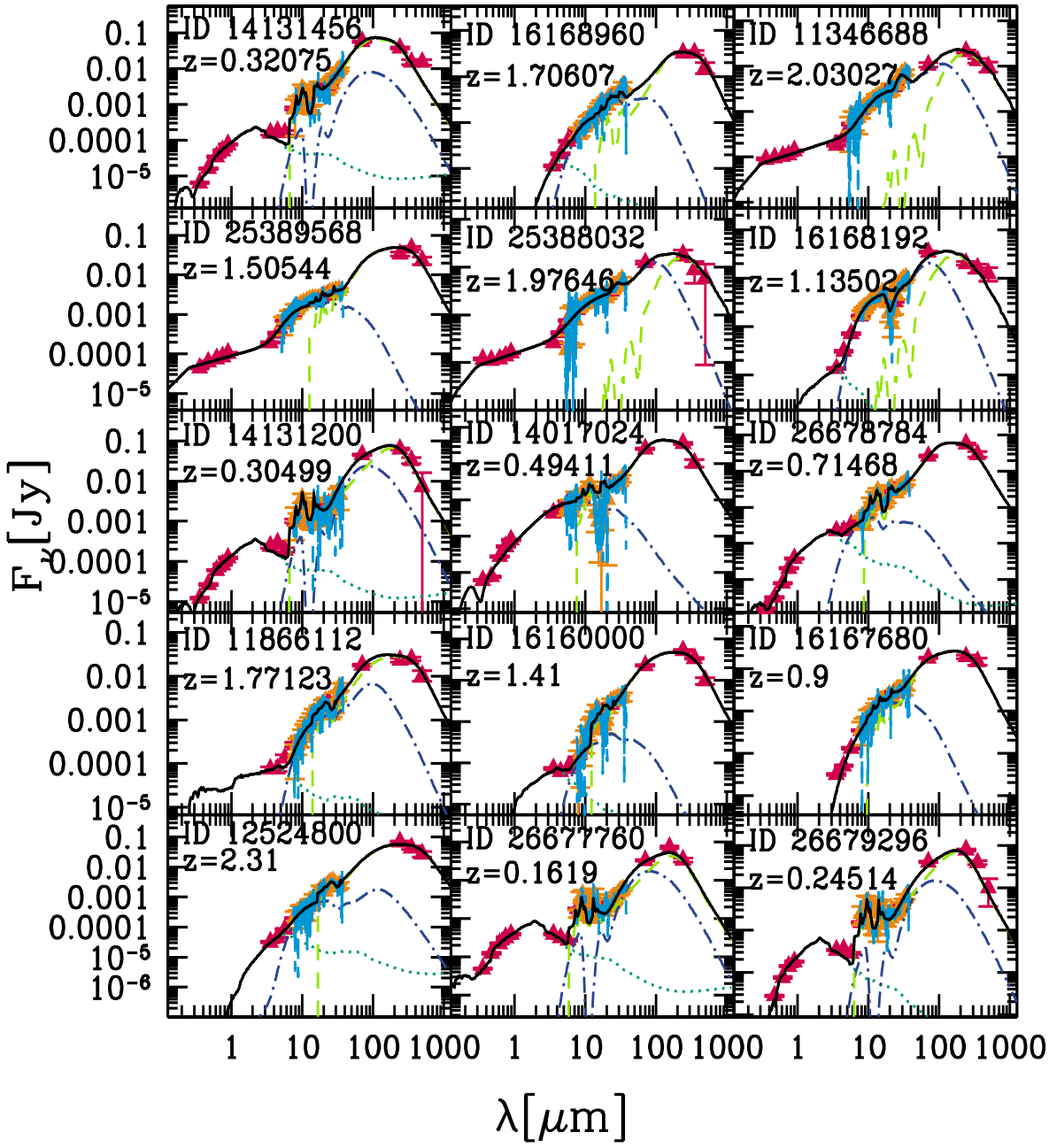

Figure D.8: Other examples of a best-fit to the HerMES/IRS sample. Symbols and colors code are the same of Fig. D.1.

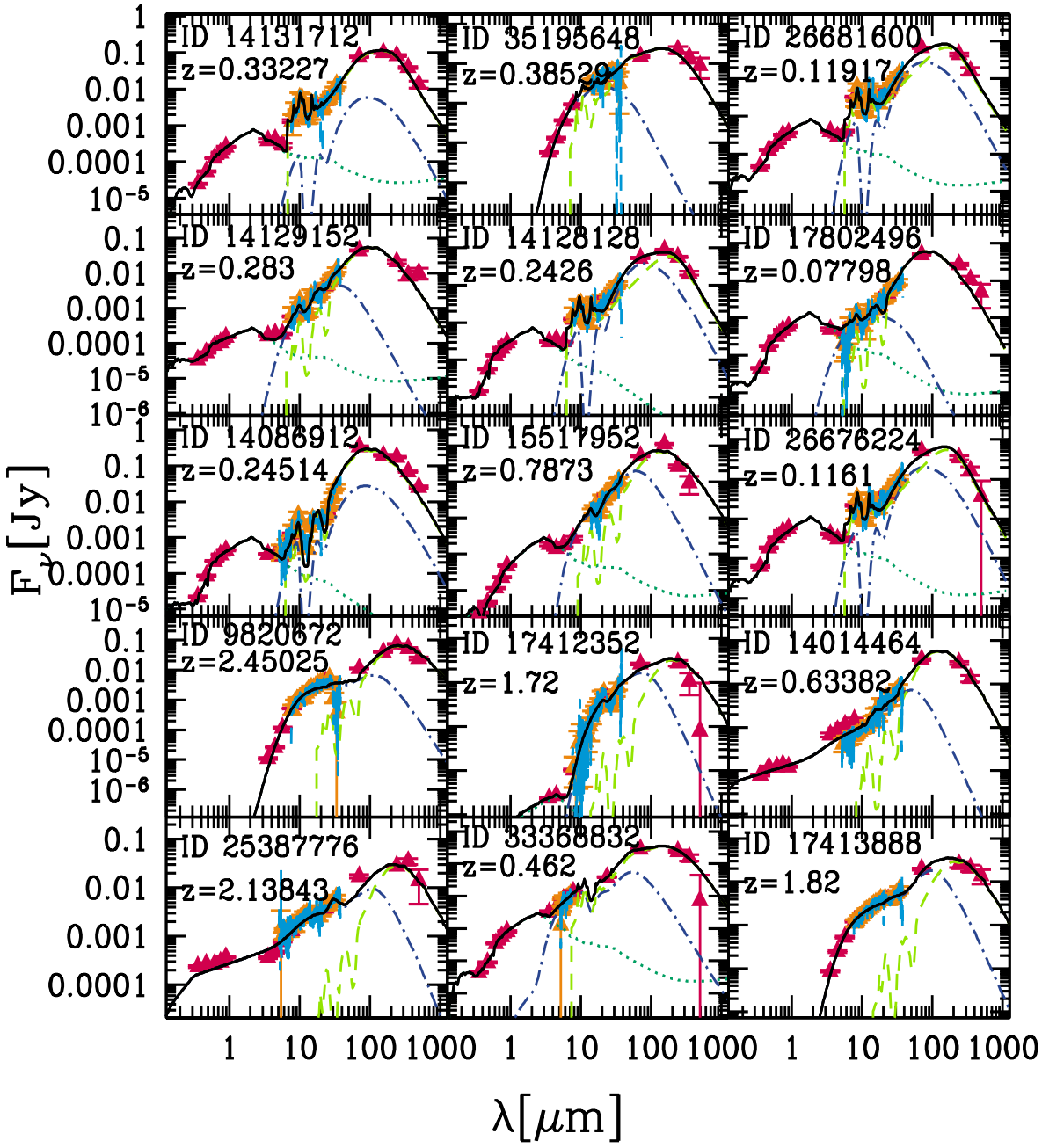

Figure D.9: Other examples of a best-fit to the HerMES/IRS sample. Symbols and colors code are the same of Fig. D.1.

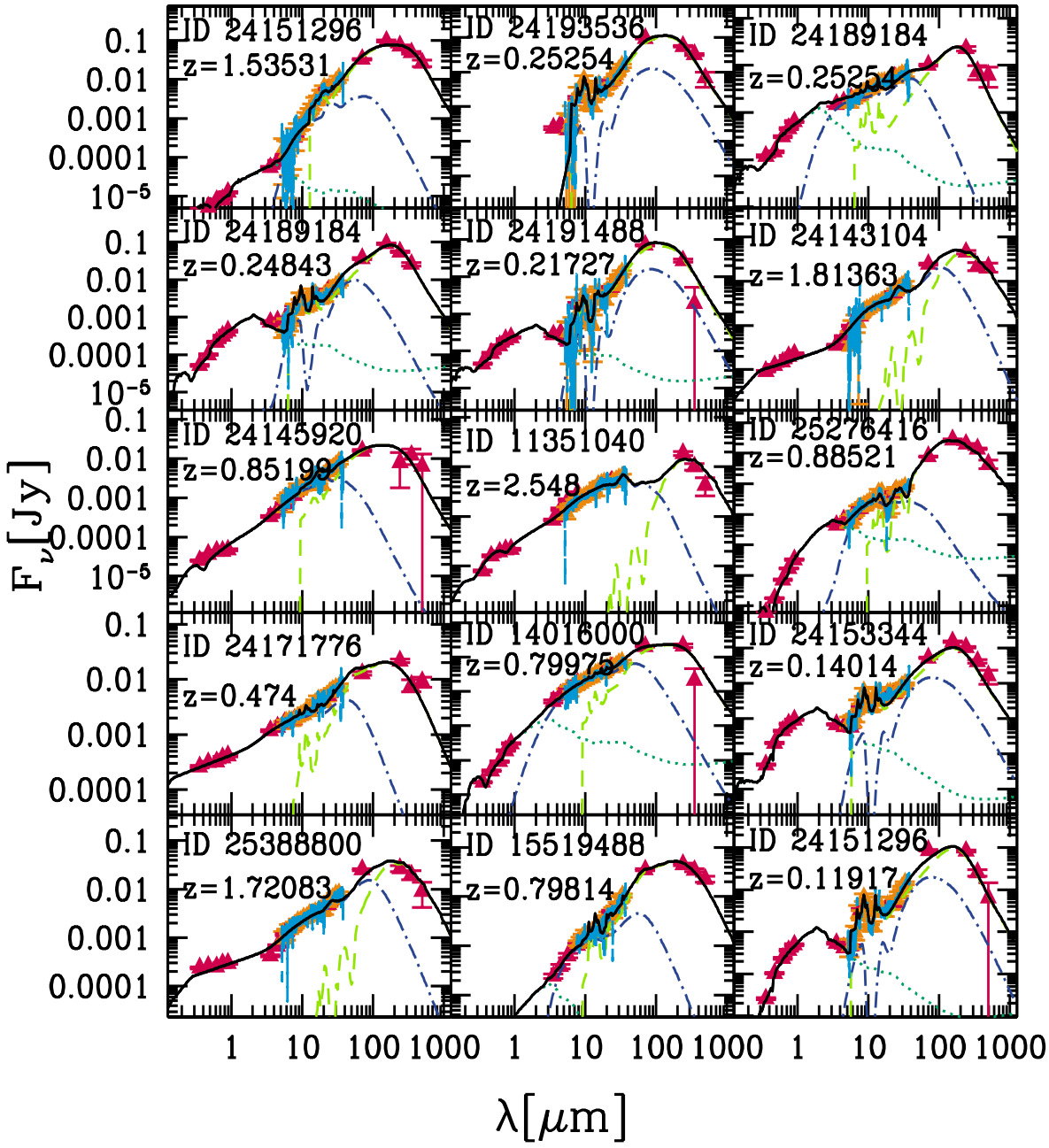

Figure D.10: Other examples of a best-fit to the HerMES/IRS sample. Symbols and colors code are the same of Fig. D.1.

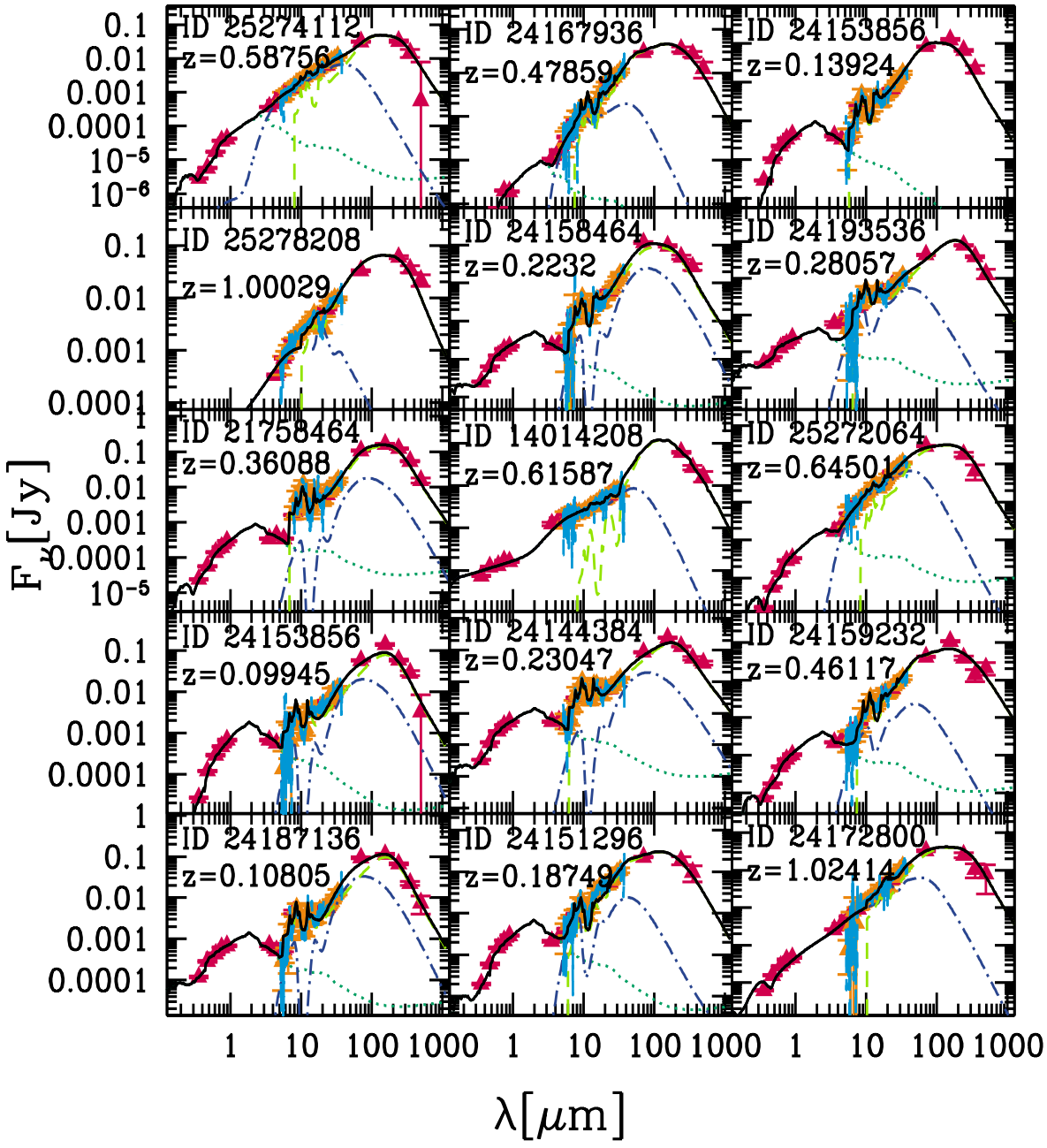

Figure D.11: Other examples of a best-fit to the HerMES/IRS sample. Symbols and colors code are the same of Fig. D.1.

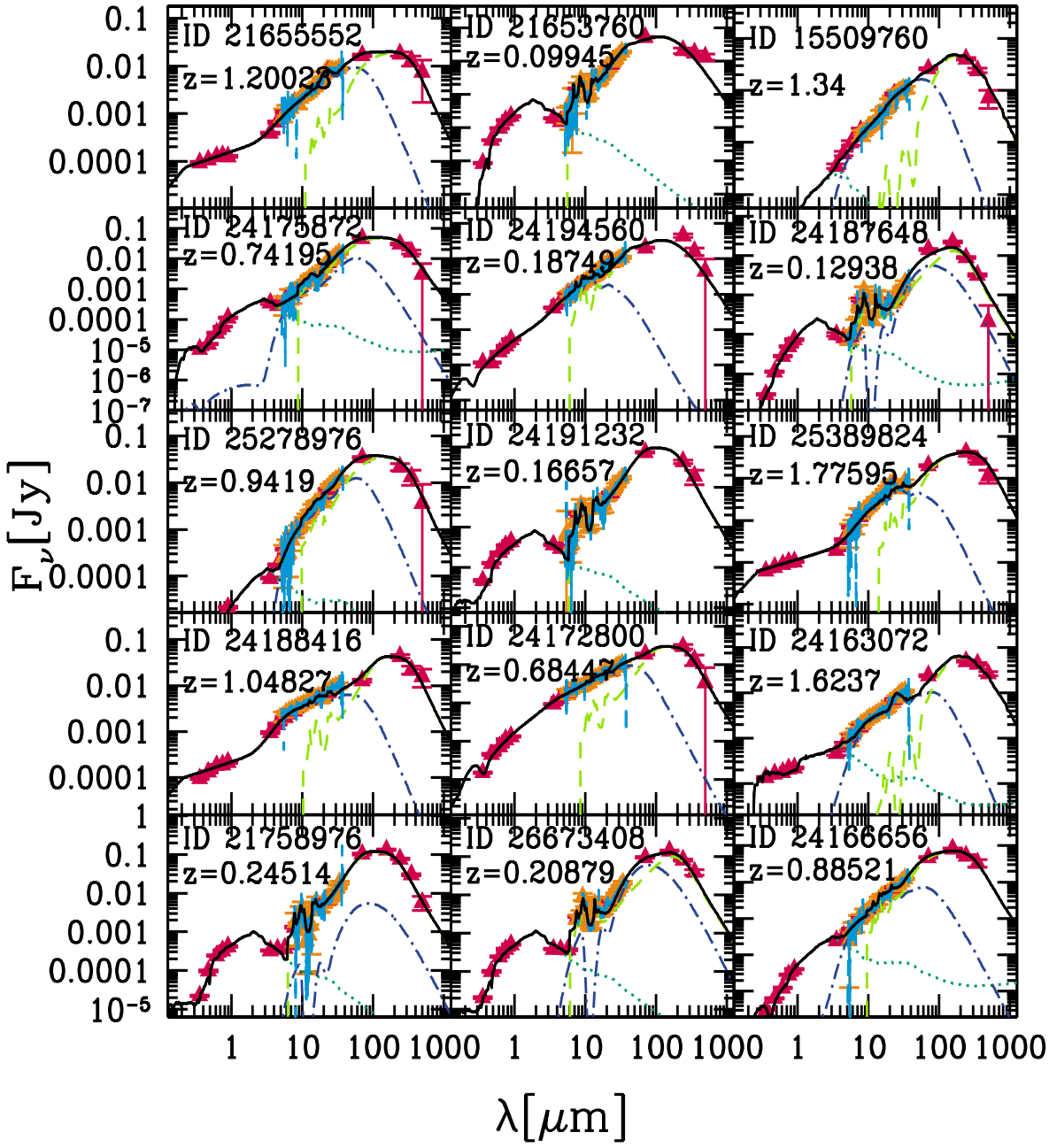

Figure D.12: Other examples of a best-fit to the HerMES/IRS sample. Symbols and colors code are the same of Fig. D.1.

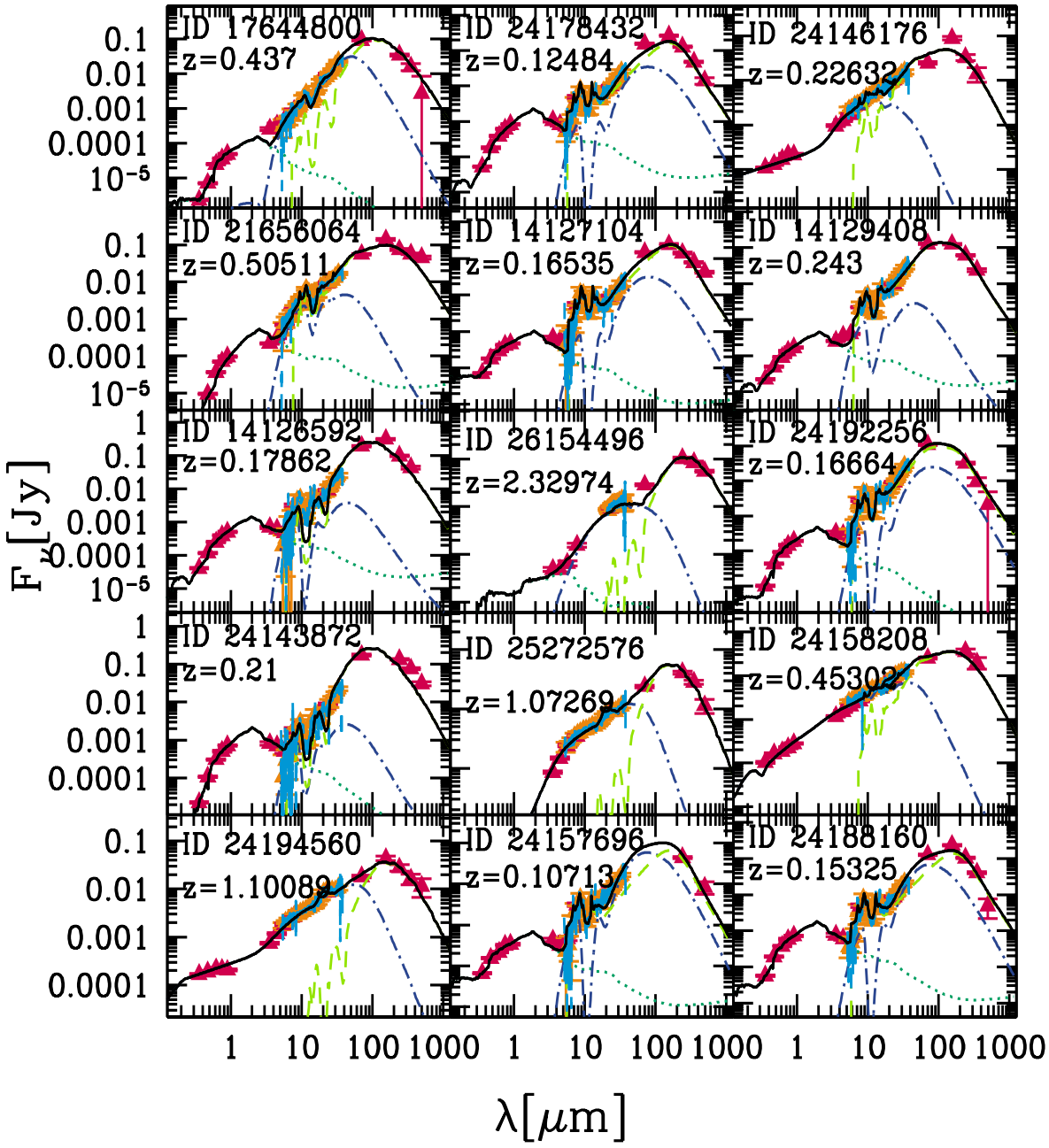

Figure D.13: Other examples of a best-fit to the HerMES/IRS sample. Symbols and colors code are the same of Fig. D.1.

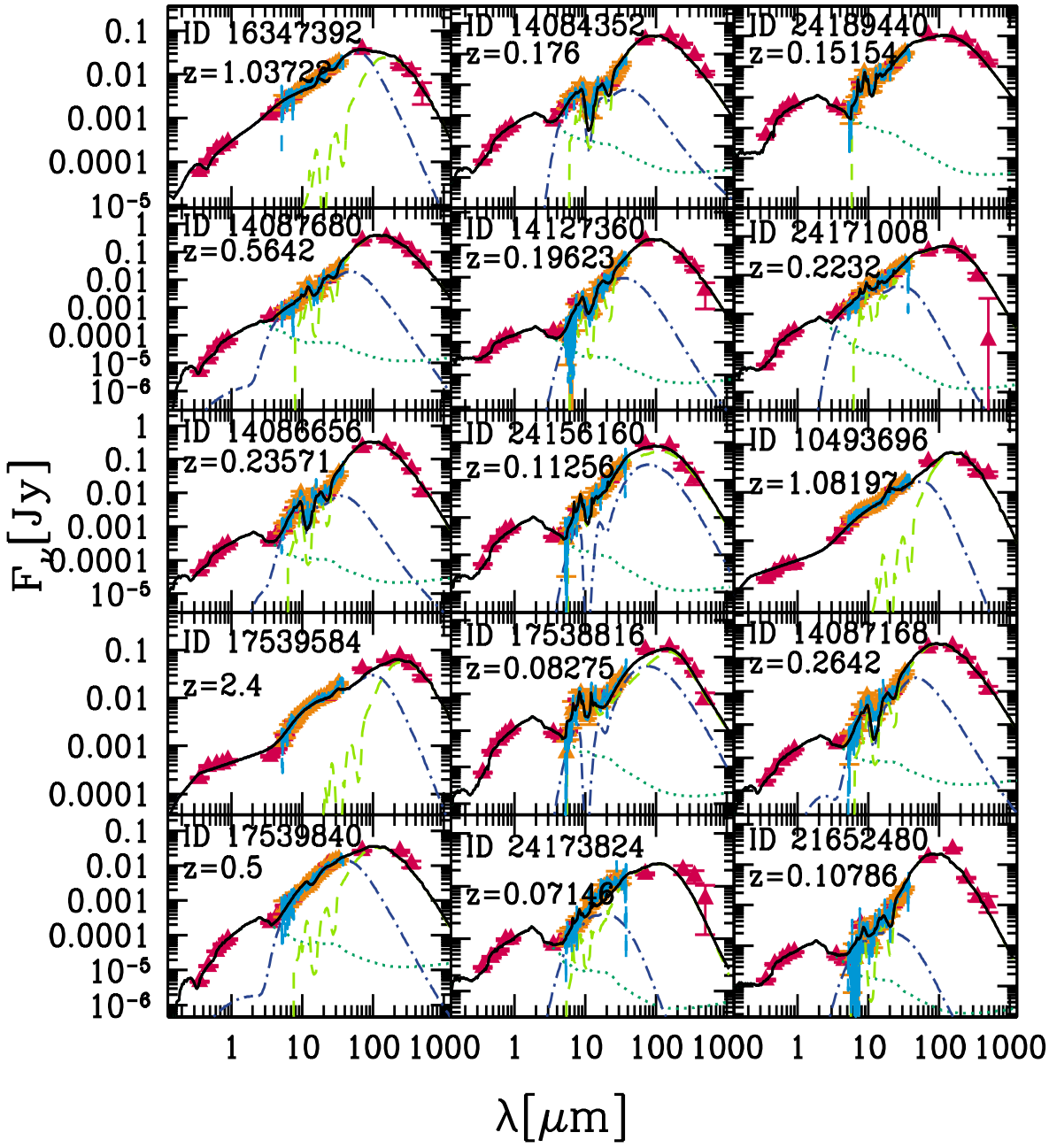

Figure D.14: Other examples of a best-fit to the HerMES/IRS sample. Symbols and colors code are the same of Fig. D.1.

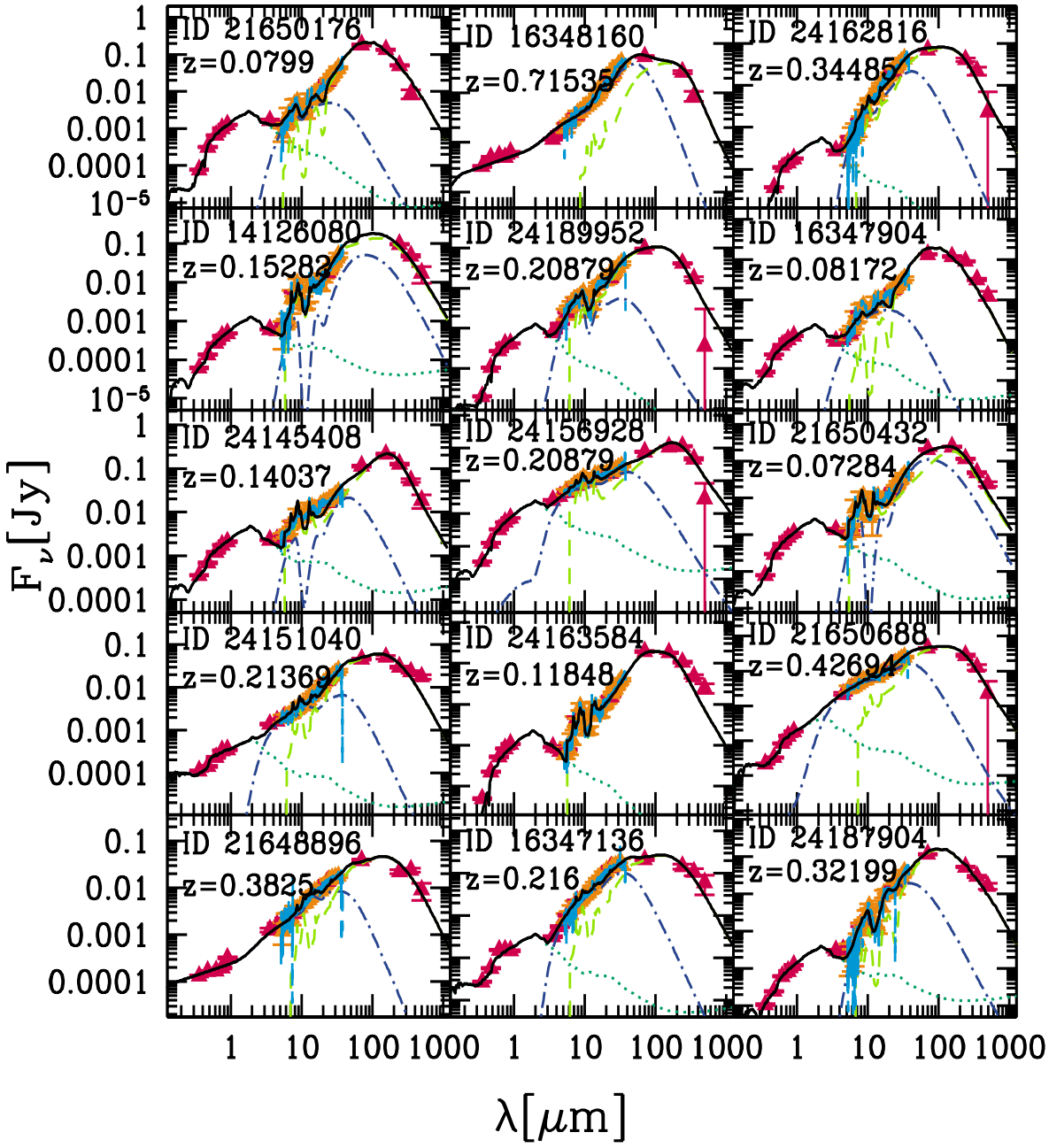

Figure D.15: Other examples of a best-fit to the HerMES/IRS sample. Symbols and colors code are the same of Fig. D.1.

Bibliography

Abazajian, K., Adelman-McCarthy, J. K., Agüeros, M. A., et al. 2004, *AJ*, 128, 502

Abazajian, K. N., Adelman-McCarthy, J. K., Agüeros, M. A., et al. 2009, *ApJS*, 182, 543

Agol, E., Gogarten, S. M., Gorjian, V., & Kimball, A. 2009, *ApJ*, 697, 1010

Alexander, D. M., Bauer, F. E., Chapman, S. C., et al. 2005, *ApJ*, 632, 736

Alongi, M., Bertelli, G., Bressan, A., et al. 1993, *A&AS*, 97, 851

Altieri, B., Berta, S., Lutz, D., et al. 2010, *A&A*, 518, L17

Alton, P. B., Xilouris, E. M., Misiriotis, A., Dasyra, K. M., & Dumke, M. 2004, *A&A*, 425, 109

Anders, P. & Fritze-v. Alvensleben, U. 2003, *A&A*, 401, 1063

Antonucci, R. 1993, *ARA&A*, 31, 473

Antonucci, R. R. J. 1984, *ApJ*, 278, 499

Antonucci, R. R. J. & Miller, J. S. 1985, *ApJ*, 297, 621

Arav, N., Barlow, T. A., Laor, A., Sargent, W. L. W., & Blandford, R. D. 1998, *MNRAS*, 297, 990

Armus, L., Bernard-Salas, J., Spoon, H. W. W., et al. 2006, *ApJ*, 640, 204

Armus, L., Charmandaris, V., Bernard-Salas, J., et al. 2007, *ApJ*, 656, 148

Aussel, H., Cesarsky, C. J., Elbaz, D., & Starck, J. L. 1999, *A&A*, 342, 313

Baes, M., Clemens, M., Xilouris, E. M., et al. 2010a, *A&A*, 518, L53

Baes, M., Davies, J. I., Dejonghe, H., et al. 2003, *MNRAS*, 343, 1081

Baes, M., Fritz, J., Gadotti, D. A., et al. 2010b, *A&A*, 518, L39

Baes, M., Verstappen, J., De Looze, I., et al. 2011, *ApJS*, 196, 22

Barvainis, R. 1987, *ApJ*, 320, 537

Beckmann, V. & Shrader, C. R. 2012, Active Galactic Nuclei

Bendo, G. J., Boselli, A., Dariush, A., et al. 2012, *MNRAS*, 419, 1833

Berta, S. 2005, PhD thesis, Dipartimento di Astronomia, Univ. di Padova, Vicolo dell'Osservatorio 2, I-35122, Padova, Italy

Berta, S., Lonsdale, C. J., Siana, B., et al. 2007, *A&A*, 467, 565

Berta, S., Magnelli, B., Lutz, D., et al. 2010, *A&A*, 518, L30

Berta, S., Magnelli, B., Nordon, R., et al. 2011, *A&A*, 532, A49

Bertelli, G., Bressan, A., Chiosi, C., Fagotto, F., & Nasi, E. 1994, *A&AS*, 106, 275

Béthermin, M., Le Floc'h, E., Ilbert, O., et al. 2012, *A&A*, 542, A58

Bianchi, S. 2008, *A&A*, 490, 461

Bianchi, S., Davies, J. I., & Alton, P. B. 2000, *A&A*, 359, 65

Bianchi, S., Ferrara, A., & Giovanardi, C. 1996, *ApJ*, 465, 127

Bidelman, W. P. 1988, Bulletin d'Information du Centre de Donnees Stellaires, 35, 52

Bolzonella, M., Miralles, J.-M., & Pelló, R. 2000, *A&A*, 363, 476

Bonfield, D. G., Jarvis, M. J., Hardcastle, M. J., et al. 2011, *MNRAS*, 416, 13

Booth, C. M. & Schaye, J. 2009, *MNRAS*, 398, 53

Bournaud, F., Dekel, A., Teyssier, R., et al. 2011, *ApJ*, 741, L33

Bower, R. G., Benson, A. J., Malbon, R., et al. 2006, *MNRAS*, 370, 645

Boyle, B. J. & Terlevich, R. J. 1998, *MNRAS*, 293, L49

Brand, K., Weedman, D. W., Desai, V., et al. 2008, *ApJ*, 680, 119

Brandl, B. R., Bernard-Salas, J., Spoon, H. W. W., et al. 2006, *ApJ*, 653, 1129

Bressan, A., Fagotto, F., Bertelli, G., & Chiosi, C. 1993, *A&AS*, 100, 647

Bressan, A., Granato, G. L., & Silva, L. 1998, *A&A*, 332, 135

Brusa, M., Fiore, F., Santini, P., et al. 2009, *A&A*, 507, 1277

Bruzual, G. & Charlot, S. 2003, *MNRAS*, 344, 1000

Bryant, P. M. & Scoville, N. Z. 1999, *AJ*, 117, 2632

Buat, V., Giovannoli, E., Burgarella, D., et al. 2010, *MNRAS*, 409, L1

Buchanan, C. L., Gallimore, J. F., O'Dea, C. P., et al. 2006, *AJ*, 132, 401

Burgarella, D., Buat, V., & Iglesias-Páramo, J. 2005, *MNRAS*, 360, 1413

Buzzoni, A. 1989, *ApJS*, 71, 817

Calzetti, D., Kinney, A. L., & Storchi-Bergmann, T. 1994, *ApJ*, 429, 582

Camenzind, M. 1995, in Reviews in Modern Astronomy, Vol. 8, Reviews in Modern Astronomy, ed. G. Klare, 201–234

Cano-Díaz, M., Maiolino, R., Marconi, A., et al. 2012, *A&A*, 537, L8

Cao, C., Xia, X. Y., Wu, H., et al. 2008, *MNRAS*, 390, 336

Cardamone, C. N., Urry, C., van Dokkum, P., et al. 2009, in Bulletin of the American Astronomical Society, Vol. 41, American Astronomical Society Meeting Abstracts 213, 334.05

Cardelli, J. A., Clayton, G. C., & Mathis, J. S. 1989, *ApJ*, 345, 245

Carter, D., Smith, D. J. B., Percival, S. M., et al. 2009, *MNRAS*, 397, 695

Cassisi, S., Castellani, M., & Castellani, V. 1997a, *A&A*, 317, 108

Cassisi, S., Castellani, V., Ciarcelluti, P., Piotto, G., & Zoccali, M. 2000, *MNRAS*, 315, 679

Cassisi, S., degl'Innocenti, S., & Salaris, M. 1997b, *MNRAS*, 290, 515

Cen, R. 2012, *ApJ*, 755, 28

Cesarsky, D., Lequeux, J., Abergel, A., et al. 1996a, *A&A*, 315, L309

Cesarsky, D., Lequeux, J., Abergel, A., et al. 1996b, *A&A*, 315, L305

Chabrier, G. 2003, *PASP*, 115, 763

Chakrabarti, S. & Whitney, B. A. 2009, *ApJ*, 690, 1432

Charbonnel, C., Däppen, W., Schaerer, D., et al. 1999, *A&AS*, 135, 405

Charbonnel, C., Meynet, G., Maeder, A., & Schaerer, D. 1996, *A&AS*, 115, 339

Charlot, S. & Bruzual, A. G. 1991, *ApJ*, 367, 126

Charlot, S. & Fall, S. M. 2000, *ApJ*, 539, 718

Charmandaris, V., Armus, L., Houck, J. R., et al. 2004, in Bulletin of the American Astronomical Society, Vol. 36, American Astronomical Society Meeting Abstracts 204, 702

Chary, R. & Elbaz, D. 2001, *ApJ*, 556, 562

Chiosi, C., Bertelli, G., & Bressan, A. 1988, *A&A*, 196, 84

Cisternas, M., Jahnke, K., Inskip, K. J., & Inskip. 2010, in IAU Symposium, Vol. 267, IAU Symposium, ed. B. M. Peterson, R. S. Somerville, & T. Storchi-Bergmann, 326–326

Clements, D. L., Petitpas, G., Farrah, D., et al. 2009, *ApJ*, 698, L188

Compiègne, M., Flagey, N., Noriega-Crespo, A., et al. 2010, *ApJ*, 724, L44

Condon, J. J., Cotton, W. D., Yin, Q. F., et al. 2003, *AJ*, 125, 2411

Cordier, D., Pietrinferni, A., Cassisi, S., & Salaris, M. 2007, *AJ*, 133, 468

Cox, P. & Mezger, P. G. 1989, *A&ARv*, 1, 49

Croton, D. J., Springel, V., White, S. D. M., et al. 2006, *MNRAS*, 365, 11

da Cunha, E., Charlot, S., & Elbaz, D. 2008, *MNRAS*, 388, 1595

Dabringhausen, J., Hilker, M., & Kroupa, P. 2008, *MNRAS*, 386, 864

Daddi, E., Alexander, D. M., Dickinson, M., et al. 2007, *ApJ*, 670, 173

Dai, Y. S., Bergeron, J., Elvis, M., et al. 2012, *ApJ*, 753, 33

Dale, D. A. & Helou, G. 2002, *ApJ*, 576, 159

Dasyra, K. M., Xilouris, E. M., Misiriotis, A., & Kylafis, N. D. 2005, *A&A*, 437, 447

Davies, J. I., Bianchi, S., Cortese, L., et al. 2012, *MNRAS*, 419, 3505

de Graauw, T., Helmich, F. P., Phillips, T. G., et al. 2010, *A&A*, 518, L6

de Grijp, M. H. K., Lub, J., & Miley, G. K. 1987, *A&AS*, 70, 95

de Grijp, M. H. K., Miley, G. K., Lub, J., & de Jong, T. 1985, *Nature*, 314, 240

de Looze, I., Baes, M., Bendo, G. J., et al. 2012, *MNRAS*, 427, 2797

De Lucia, G., Springel, V., White, S. D. M., Croton, D., & Kauffmann, G. 2006, *MNRAS*, 366, 499

Demarque, P., Woo, J.-H., Kim, Y.-C., & Yi, S. K. 2004, *ApJS*, 155, 667

Deo, R. P., Crenshaw, D. M., Kraemer, S. B., et al. 2007, *ApJ*, 671, 124

Deo, R. P., Richards, G. T., Nikutta, R., et al. 2011, *ApJ*, 729, 108

Desert, F.-X., Boulanger, F., & Puget, J. L. 1990, *A&A*, 237, 215

Devriendt, J. E. G., Guiderdoni, B., & Sadat, R. 1999, *A&A*, 350, 381

Dey, A., Soifer, B. T., Desai, V., et al. 2008, *ApJ*, 677, 943

Di Matteo, P., Montuori, M., Lehnert, M. D., Combes, F., & Semelin, B. 2011, in IAU Symposium, Vol. 277, IAU Symposium, ed. C. Carignan, F. Combes, & K. C. Freeman, 246-249

Dietrich, M. 1999, in IAU Symposium, Vol. 194, Activity in Galaxies and Related Phenomena, ed. Y. Terzian, E. Khachikian, & D. Weedman, 317

Dole, H., Lagache, G., Puget, J.-L., et al. 2006, *A&A*, 451, 417

Donley, J. L., Koekemoer, A. M., Brusa, M., et al. 2012, *ApJ*, 748, 142

Donley, J. L., Rieke, G. H., Pérez-González, P. G., Rigby, J. R., & Alonso-Herrero, A. 2007, *ApJ*, 660, 167

Dopita, M. A., Fischera, J., Sutherland, R. S., et al. 2006a, *ApJS*, 167, 177

Dopita, M. A., Fischera, J., Sutherland, R. S., et al. 2006b, *ApJ*, 647, 244

Dopita, M. A., Groves, B. A., Fischera, J., et al. 2005, *ApJ*, 619, 755

Downes, D. & Solomon, P. M. 1998, *ApJ*, 507, 615

Draine, B. T. 2003, *ApJ*, 598, 1017

Draine, B. T., Dale, D. A., Bendo, G., et al. 2007, *ApJ*, 663, 866

Draine, B. T. & Lee, H. M. 1984, *ApJ*, 285, 89

Draine, B. T. & Li, A. 2001, *ApJ*, 551, 807

Driver, S. P., Popescu, C. C., Tuffs, R. J., et al. 2008, *ApJ*, 678, L101

Dullemond, C. P. & van Bemmel, I. M. 2005, *A&A*, 436, 47

Dwek, E., Arendt, R. G., Hauser, M. G., et al. 1998, *ApJ*, 508, 106

Eales, S., Dunne, L., Clements, D., et al. 2010, *PASP*, 122, 499

Edge, D. O., Shakeshaft, J. R., McAdam, W. B., Baldwin, J. E., & Archer, S. 1959, *MemRAS*, 68, 37

Efstathiou, A. & Rowan-Robinson, M. 1991, *MNRAS*, 252, 528

Efstathiou, A. & Rowan-Robinson, M. 1995, *MNRAS*, 273, 649

Efstathiou, A., Rowan-Robinson, M., & Siebenmorgen, R. 2000, *MNRAS*, 313, 734

Eggleton, P. P. 1971, *MNRAS*, 151, 351

Eggleton, P. P. 1972, *MNRAS*, 156, 361

Eisenhauer, F., Perrin, G., Brandner, W., et al. 2011, The Messenger, 143, 16

Eisenhauer, F., Perrin, G., Brandner, W., et al. 2008, in Society of Photo-Optical Instrumentation Engineers (SPIE) Conference Series, Vol. 7013, Society of Photo-Optical Instrumentation Engineers (SPIE) Conference Series

Elbaz, D., Aussel, H., & Baker, A. C. 1998, in ESA Special Publication, Vol. 429, LIA Colloq. 34: The Next Generation Space Telescope: Science Drivers and Technological Challenges, ed. B. Kaldeich-Schürmann, 47

Elbaz, D., Daddi, E., Le Borgne, D., et al. 2007, *A&A*, 468, 33

Elbaz, D., Dickinson, M., Hwang, H. S., et al. 2011, *A&A*, 533, A119

Elitzur, M. 2008, *NewAR*, 52, 274

Elitzur, M. & Shlosman, I. 2006, *ApJ*, 648, L101

Elvis, M., Wilkes, B. J., McDowell, J. C., et al. 1994, *ApJS*, 95, 1

Erb, D. K., Steidel, C. C., Shapley, A. E., et al. 2006, *ApJ*, 647, 128

Faber, S. M., Tremaine, S., Ajhar, E. A., et al. 1997, *AJ*, 114, 1771

Fadda, D., Jannuzi, B. T., Ford, A., & Storrie-Lombardi, L. J. 2004, *AJ*, 128, 1

Fadda, D., Marleau, F. R., Storrie-Lombardi, L. J., et al. 2006, *AJ*, 131, 2859

Fadda, D., Yan, L., Lagache, G., et al. 2010, *ApJ*, 719, 425

Fagotto, F., Bressan, A., Bertelli, G., & Chiosi, C. 1994a, *A&AS*, 104, 365

Fagotto, F., Bressan, A., Bertelli, G., & Chiosi, C. 1994b, *A&AS*, 105, 29

Farrah, D., Afonso, J., Efstathiou, A., et al. 2003, *MNRAS*, 343, 585

Farrah, D., Lonsdale, C. J., Weedman, D. W., et al. 2008, *ApJ*, 677, 957

Farrah, D., Urrutia, T., Lacy, M., et al. 2012, *ApJ*, 745, 178

Farrah, D., Weedman, D., Lonsdale, C. J., et al. 2009, *ApJ*, 696, 2044

Fath, E. A. 1909, Lick Observatory Bulletin, 5, 71

Fazio, G. G., Hora, J. L., Allen, L. E., et al. 2004, *ApJS*, 154, 10

Feigelson, E. D. & Babu, G. J. 2013, Statistical Methods for Astronomy, ed. T. D. Oswalt & H. E. Bond, 445

Feltre, A., Hatziminaoglou, E., Fritz, J., & Franceschini, A. 2012, *MNRAS*, 426, 120

Feltre, A., Hatziminaoglou, E., Hernán-Caballero, A., et al. 2013, *MNRAS*

Ferland, G. J. 1996, Hazy, A Brief Introduction to Cloudy 90

Ferland, G. J., Korista, K. T., Verner, D. A., et al. 1998, *PASP*, 110, 761

Ferrara, A., Pettini, M., & Shchekinov, Y. 2000, *MNRAS*, 319, 539

Ferrarese, L. & Merritt, D. 2000, *ApJ*, 539, L9

Ferrière, K. M. 2001, Reviews of Modern Physics, 73, 1031

Fioc, M. & Rocca-Volmerange, B. 1997, *A&A*, 326, 950

Fioc, M. & Rocca-Volmerange, B. 1999, ArXiv Astrophysics e-prints

Fiore, F., Brusa, M., Cocchia, F., et al. 2003, *A&A*, 409, 79

Fisher, K. B., Strauss, M. A., Davis, M., Yahil, A., & Huchra, J. P. 1992, *ApJ*, 389, 188

Fixsen, D. J., Dwek, E., Mather, J. C., Bennett, C. L., & Shafer, R. A. 1998, *ApJ*, 508, 123

Flores, H., Hammer, F., Thuan, T., et al. 1998, ArXiv Astrophysics e-prints

Franceschini, A., Aussel, H., Cesarsky, C. J., Elbaz, D., & Fadda, D. 2001, *A&A*, 378, 1

Franceschini, A., Bassani, L., Cappi, M., et al. 2000, *A&A*, 353, 910

Franceschini, A., Danese, L., de Zotti, G., & Xu, C. 1988, *MNRAS*, 233, 175

Franceschini, A., Mazzei, P., de Zotti, G., & Danese, L. 1994, *ApJ*, 427, 140

Fritz, J., Franceschini, A., & Hatziminaoglou, E. 2006, *MNRAS*, 366, 767

Fritz, J., Gentile, G., Smith, M. W. L., et al. 2012, *A&A*, 546, A34

Gabor, J. M., Impey, C. D., Jahnke, K., et al. 2009, *ApJ*, 691, 705

Gebhardt, K., Bender, R., Bower, G., et al. 2000, *ApJ*, 539, L13

Genzel, R., Burkert, A., Bouché, N., et al. 2008, *ApJ*, 687, 59

Genzel, R., Lutz, D., Sturm, E., et al. 1998, *ApJ*, 498, 579

Genzel, R., Tacconi, L. J., Eisenhauer, F., et al. 2006, *Nature*, 442, 786

Georgakakis, A., Coil, A. L., Laird, E. S., et al. 2009, *MNRAS*, 397, 623

George, I. M. & Fabian, A. C. 1991, *MNRAS*, 249, 352

Girardi, L., Bressan, A., Bertelli, G., & Chiosi, C. 2000, *A&AS*, 141, 371

Girardi, L., Bressan, A., Chiosi, C., Bertelli, G., & Nasi, E. 1996, *A&AS*, 117, 113

Glenn, J., Conley, A., Béthermin, M., et al. 2010, *MNRAS*, 409, 109

Gordon, K. D., Misselt, K. A., Witt, A. N., & Clayton, G. C. 2001, *ApJ*, 551, 269

Graham, A. W. & Driver, S. P. 2007, *ApJ*, 655, 77

Graham, A. W., Erwin, P., Caon, N., & Trujillo, I. 2001, *ApJ*, 563, L11

Granato, G. L. & Danese, L. 1994, *MNRAS*, 268, 235

Graves, G. J. & Schiavon, R. P. 2008, *ApJS*, 177, 446

Greenstein, J. L. 1963, *Nature*, 197, 1041

Griffin, M. J., Abergel, A., Abreu, A., et al. 2010, *A&A*, 518, L3

Groenewegen, M. A. T. & de Jong, T. 1993, *A&A*, 267, 410

Grogin, N. A., Conselice, C. J., Chatzichristou, E., et al. 2003, in Bulletin of the American Astronomical Society, Vol. 35, American Astronomical Society Meeting Abstracts, 1297

Groves, B., Dopita, M. A., Sutherland, R. S., et al. 2008, *ApJS*, 176, 438

Gruppioni, C., Pozzi, F., Andreani, P., et al. 2010, *A&A*, 518, L27

Gruppioni, C., Pozzi, F., Rodighiero, G., et al. 2013, *MNRAS*, 432, 23

Guiderdoni, B., Bouchet, F. R., Puget, J.-L., Lagache, G., & Hivon, E. 1997, *Nature*, 390, 257

Gunn, J. E. & Peterson, B. A. 1965, *ApJ*, 142, 1633

Haardt, F. & Maraschi, L. 1993, *ApJ*, 413, 507

Haas, M., Chini, R., Meisenheimer, K., et al. 1998, *ApJ*, 503, L109

Hao, L., Spoon, H. W. W., Sloan, G. C., et al. 2005, *ApJ*, 625, L75

Häring-Neumayer, N., Cappellari, M., Rix, H.-W., et al. 2006, *ApJ*, 643, 226

Harrison, C. M., Alexander, D. M., Mullaney, J. R., et al. 2012, *ApJ*, 760, L15

Harwit, M. & Pacini, F. 1975, *ApJ*, 200, L127

Hatziminaoglou, E., Fritz, J., Franceschini, A., et al. 2008, *MNRAS*, 386, 1252

Hatziminaoglou, E., Fritz, J., & Jarrett, T. H. 2009, *MNRAS*, 399, 1206

Hatziminaoglou, E., Omont, A., Stevens, J. A., et al. 2010, *A&A*, 518, L33

Hatziminaoglou, E., Pérez-Fournon, I., Polletta, M., et al. 2005, *AJ*, 129, 1198

Hauser, M. G. & Dwek, E. 2001, *ARA&A*, 39, 249

Hazard, C., Mackey, M. B., & Shimmins, A. J. 1963, *Nature*, 197, 1037

Heavens, A., Panter, B., Jimenez, R., & Dunlop, J. 2004, *Nature*, 428, 625

Hernán-Caballero, A. & Hatziminaoglou, E. 2011, *MNRAS*, 414, 500

Hernán-Caballero, A., Pérez-Fournon, I., Hatziminaoglou, E., et al. 2009, *MNRAS*, 395, 1695

Hoenig, S. F. 2013, ArXiv e-prints

Hogg, D. W. 2001, *AJ*, 121, 1207

Hollenbach, D. J. & Tielens, A. G. G. M. 1997, *ARA&A*, 35, 179

Hönig, S. F., Beckert, T., Ohnaka, K., & Weigelt, G. 2006, *A&A*, 452, 459

Hönig, S. F., Kishimoto, M., Gandhi, P., et al. 2010, *A&A*, 515, A23

Hopkins, P. F., Hernquist, L., Cox, T. J., & Kereš, D. 2008, *ApJS*, 175, 356

Hopkins, P. F., Somerville, R. S., Hernquist, L., et al. 2006, *ApJ*, 652, 864

Horst, H., Smette, A., Gandhi, P., & Duschl, W. J. 2006, *A&A*, 457, L17

Houck, J. R., Roellig, T. L., van Cleve, J., et al. 2004, *ApJS*, 154, 18

Houck, J. R., Weedman, D. W., Le Floc'h, E., & Hao, L. 2007, *ApJ*, 671, 323

Hoyle, F. 1966, Galaxies, nuclei and quasars

Hunter, D. A., Gillett, F. C., Gallagher, III, J. S., Rice, W. L., & Low, F. J. 1986, *ApJ*, 303, 171

Ibar, E. & Lira, P. 2007, *A&A*, 466, 531

Imanishi, M., Dudley, C. C., Maiolino, R., et al. 2007, *ApJS*, 171, 72

Ishibashi, W. & Courvoisier, T. J.-L. 2011, *A&A*, 525, A118

Iwasawa, K., Fabian, A. C., & Ettori, S. 2001, *MNRAS*, 321, L15

Jacoby, G. H., Hunter, D. A., & Christian, C. A. 1984, *ApJS*, 56, 257

Jaffe, W., Meisenheimer, K., Röttgering, H. J. A., et al. 2004, *Nature*, 429, 47

Jahnke, K. & Macciò, A. V. 2011, *ApJ*, 734, 92

Jimenez, R., Jorgensen, U. G., Thejll, P., & MacDonald, J. 1995, *MNRAS*, 275, 1245

Jimenez, R., MacDonald, J., Dunlop, J. S., Padoan, P., & Peacock, J. A. 2004, *MNRAS*, 349, 240

Johnson, H. L. 1962, *ApJ*, 135, 975

Jones, A. P., Tielens, A. G. G. M., & Hollenbach, D. J. 1996, *ApJ*, 469, 740

Jonsson, P. 2006, *MNRAS*, 372, 2

Jonsson, P., Groves, B. A., & Cox, T. J. 2010, *MNRAS*, 403, 17

Joseph, R. D. 1999, *Ap&SS*, 266, 321

Kellermann, K. I., Sramek, R. A., Schmidt, M., Green, R. F., & Shaffer, D. B. 1994, *AJ*, 108, 1163

Kennicutt, R. C. & Evans, N. J. 2012, *ARA&A*, 50, 531

Kennicutt, Jr., R. C. 1992, *ApJ*, 388, 310

Kennicutt, Jr., R. C. 1998, *ApJ*, 498, 541

Kennicutt, Jr., R. C., Armus, L., Bendo, G., et al. 2003, *PASP*, 115, 928

Kessler, M. F., Steinz, J. A., Anderegg, M. E., et al. 1996, *A&A*, 315, L27

Kewley, L. J., Geller, M. J., Jansen, R. A., & Dopita, M. A. 2002, *AJ*, 124, 3135

Kirkpatrick, A., Pope, A., Alexander, D. M., et al. 2012, *ApJ*, 759, 139

Kirkpatrick, A., Pope, A., Charmandaris, V., et al. 2013, *ApJ*, 763, 123

Kleinmann, S. G., Hamilton, D., Keel, W. C., et al. 1988, *ApJ*, 328, 161

Kocevski, D., Mozena, M., Koekemoer, A. M., et al. 2011, in American Astronomical Society Meeting Abstracts 218, 317.01

Kormendy, J., Bender, R., & Cornell, M. E. 2011, *Nature*, 469, 374

Kormendy, J. & Richstone, D. 1995, *ARA&A*, 33, 581

Krolik, J. H. 1999, *Nature*, 398, 678

Krolik, J. H. & Begelman, M. C. 1986, in Bulletin of the American Astronomical Society, Vol. 18, Bulletin of the American Astronomical Society, 903

Krolik, J. H. & Begelman, M. C. 1988, *ApJ*, 329, 702

Kroupa, P. 2001, *MNRAS*, 322, 231

Kroupa, P., Tout, C. A., & Gilmore, G. 1993, *MNRAS*, 262, 545

Krugel, E. & Siebenmorgen, R. 1994, *A&A*, 282, 407

Kurucz, R. L. 1993, SYNTHE spectrum synthesis programs and line data

Kylafis, N. D. & Bahcall, J. N. 1987, *ApJ*, 317, 637

La Franca, F., Fiore, F., Comastri, A., et al. 2005, *ApJ*, 635, 864

Lacy, M., Petric, A. O., Sajina, A., et al. 2007, *AJ*, 133, 186

Lacy, M., Storrie-Lombardi, L. J., Sajina, A., et al. 2004, *ApJS*, 154, 166

Lagache, G., Dole, H., Puget, J.-L., et al. 2004, *ApJS*, 154, 112

Lagache, G., Puget, J.-L., & Dole, H. 2005, *ARA&A*, 43, 727

Laor, A. & Draine, B. T. 1993, *ApJ*, 402, 441

Larson, R. B. & Tinsley, B. M. 1978, *ApJ*, 219, 46

Lastennet, E., Lejeune, T., Oblak, E., Westera, P., & Buser, R. 2002, *Ap&SS*, 280, 83

Laurent, O., Mirabel, I. F., Charmandaris, V., et al. 2000, *A&A*, 359, 887

Le Borgne, J.-F., Bruzual, G., Pelló, R., et al. 2003, *A&A*, 402, 433

Lebouteiller, V., Barry, D. J., Spoon, H. W. W., et al. 2011, *ApJS*, 196, 8

Leger, A. & Puget, J. L. 1984, *A&A*, 137, L5

Lehnert, M. D. & Heckman, T. M. 1996, *ApJ*, 472, 546

Leitherer, C. & Heckman, T. M. 1995, *ApJS*, 96, 9

Lejeune, T. & Schaerer, D. 2001, *A&A*, 366, 538

Leung, C. M. 1975, *ApJ*, 199, 340

Levenson, L., Marsden, G., Zemcov, M., et al. 2010, *MNRAS*, 409, 83

Li, A. & Draine, B. T. 2001, *ApJ*, 554, 778

Lo Faro, B., Franceschini, A., Vaccari, M., et al. 2013, *ApJ*, 762, 108

Longhetti, M. & Saracco, P. 2009, *MNRAS*, 394, 774

Lonsdale, C., Polletta, M. d. C., Surace, J., et al. 2004, *ApJS*, 154, 54

Lonsdale, C. J., Farrah, D., & Smith, H. E. 2006, Ultraluminous Infrared Galaxies, ed. J. W. Mason, 285

Lonsdale, C. J. & Hacking, P. B. 1987, in Bulletin of the American Astronomical Society, Vol. 19, Bulletin of the American Astronomical Society, 1074

Lonsdale, C. J., Hacking, P. B., Conrow, T. P., & Rowan-Robinson, M. 1990, *ApJ*, 358, 60

Lonsdale, C. J., Smith, H. E., Rowan-Robinson, M., et al. 2003, *PASP*, 115, 897

Lu, N., Helou, G., Werner, M. W., et al. 2003, *ApJ*, 588, 199

Lusso, E., Comastri, A., Vignali, C., et al. 2011, *A&A*, 534, A110

Lutz, D., Genzel, R., Sternberg, A., et al. 1996, *A&A*, 315, L137

Lutz, D., Mainieri, V., Rafferty, D., et al. 2010, *ApJ*, 712, 1287

Lutz, D., Poglitsch, A., Altieri, B., et al. 2011, *A&A*, 532, A90

Lutz, D., Spoon, H. W. W., Rigopoulou, D., Moorwood, A. F. M., & Genzel, R. 1998, *ApJ*, 505, L103

Lutz, D., Sturm, E., Tacconi, L. J., et al. 2008, *ApJ*, 684, 853

Madau, P. 1995, *ApJ*, 441, 18

Madau, P., Pozzetti, L., & Dickinson, M. 1998, *ApJ*, 498, 106

Maeder, A. & Meynet, G. 1988, *A&AS*, 76, 411

Magnelli, B., Popesso, P., Berta, S., et al. 2013, *A&A*, 553, A132

Magorrian, J., Tremaine, S., Richstone, D., et al. 1998, *AJ*, 115, 2285

Mainieri, V., Bongiorno, A., Merloni, A., et al. 2011, *A&A*, 535, A80

Maiolino, R. 2008, *NewAR*, 52, 339

Maiolino, R., Marconi, A., Salvati, M., et al. 2001, *A&A*, 365, 28

Maiolino, R., Shemmer, O., Imanishi, M., et al. 2007, *A&A*, 468, 979

Manske, V. & Henning, T. 1998, *A&A*, 337, 85

Maraston, C. 1998, *MNRAS*, 300, 872

Maraston, C. 2005, *MNRAS*, 362, 799

Marconi, A. & Hunt, L. K. 2003, *ApJ*, 589, L21

Marconi, A., Pastorini, G., Pacini, F., et al. 2006, *A&A*, 448, 921

Marigo, P. & Girardi, L. 2007, *A&A*, 469, 239

Marigo, P., Girardi, L., Bressan, A., et al. 2008, *A&A*, 482, 883

Marleau, F. R., Fadda, D., Appleton, P. N., et al. 2007, *ApJ*, 663, 218

Martel, A. R., Baum, S. A., Sparks, W. B., et al. 1999, *ApJS*, 122, 81

Martin, D. C., Fanson, J., Schiminovich, D., et al. 2005, *ApJ*, 619, L1

Mason, R. E., Levenson, N. A., Shi, Y., et al. 2009, *ApJ*, 693, L136

Mathis, J. S., Rumpl, W., & Nordsieck, K. H. 1977, *ApJ*, 217, 425

Meurer, G. R., Heckman, T. M., Lehnert, M. D., Leitherer, C., & Lowenthal, J. 1997, *AJ*, 114, 54

Mihalas, D., Auer, L. H., & Mihalas, B. R. 1978, *ApJ*, 220, 1001

Miley, G. K., Neugebauer, G., & Soifer, B. T. 1985, *ApJ*, 293, L11

Minkowski, R. 1960, *ApJ*, 132, 908

Misiriotis, A., Papadakis, I. E., Kylafis, N. D., & Papamastorakis, J. 2004, *A&A*, 417, 39

Misiriotis, A., Popescu, C. C., Tuffs, R., & Kylafis, N. D. 2001, *A&A*, 372, 775

Misselt, K. A., Gordon, K. D., Clayton, G. C., & Wolff, M. J. 2001, *ApJ*, 551, 277

Miyoshi, M., Moran, J., Herrnstein, J., et al. 1995, *Nature*, 373, 127

Moorwood, A. F. M. 1999, in ESA Special Publication, Vol. 427, The Universe as Seen by ISO, ed. P. Cox & M. Kessler, 825

Mor, R., Netzer, H., & Elitzur, M. 2009, *ApJ*, 705, 298

Moshir, M., Kopan, G., Conrow, T., et al. 1990, in Bulletin of the American Astronomical Society, Vol. 22, Bulletin of the American Astronomical Society, 1325

Mullaney, J. R., Alexander, D. M., Goulding, A. D., & Hickox, R. C. 2011, *MNRAS*, 414, 1082

Natale, G., Tuffs, R. J., Xu, C. K., et al. 2010, *ApJ*, 725, 955

Nenkova, M., Ivezic, Z., & Elitzur, M. 1999, LPI Contributions, 969, 20

Nenkova, M., Ivezić, Ž., & Elitzur, M. 2002, *ApJ*, 570, L9

Nenkova, M., Sirocky, M. M., Ivezić, Ž., & Elitzur, M. 2008a, *ApJ*, 685, 147

Nenkova, M., Sirocky, M. M., Nikutta, R., Ivezić, Ž., & Elitzur, M. 2008b, *ApJ*, 685, 160

Netzer, H., Lutz, D., Schweitzer, M., et al. 2007, *ApJ*, 666, 806

Netzer, H. & Marziani, P. 2010, *ApJ*, 724, 318

Neugebauer, G., Oke, J. B., Becklin, E. E., & Matthews, K. 1979, *ApJ*, 230, 79

Nguyen, H. T., Schulz, B., Levenson, L., et al. 2010, *A&A*, 518, L5

Nikutta, R., Elitzur, M., & Lacy, M. 2009, *ApJ*, 707, 1550

Noeske, K. G., Weiner, B. J., Faber, S. M., et al. 2007, *ApJ*, 660, L43

Noll, S., Burgarella, D., Giovannoli, E., et al. 2009, *A&A*, 507, 1793

Norman, C., Hasinger, G., Giacconi, R., et al. 2002, *ApJ*, 571, 218

Oliver, S., Mann, R. G., Carballo, R., et al. 2002, *MNRAS*, 332, 536

Oliver, S. J., Bock, J., Altieri, B., et al. 2012, *MNRAS*, 424, 1614

Oliver, S. J., Rowan-Robinson, M., & Saunders, W. 1992, *MNRAS*, 256, 15P

Oliver, S. J., Wang, L., Smith, A. J., et al. 2010, *A&A*, 518, L21

Ossenkopf, V., Henning, T., & Mathis, J. S. 1992, *A&A*, 261, 567

Osterbrock, D. E. 1981, *ApJ*, 249, 462

Padmanabhan, T. 2002, Theoretical Astrophysics, Volume III: Galaxies and Cosmology

Page, M. J., Symeonidis, M., Vieira, J. D., et al. 2012, *Nature*, 485, 213

Pascale, E., Ade, P. A. R., Bock, J. J., et al. 2009, *ApJ*, 707, 1740

Patanchon, G., Ade, P. A. R., Bock, J. J., et al. 2009, *ApJ*, 707, 1750

Pearson, C. & Rowan-Robinson, M. 1996, *MNRAS*, 283, 174

Percival, S. M., Salaris, M., Cassisi, S., & Pietrinferni, A. 2009, *ApJ*, 690, 427

Peters, W. 2002, PhD thesis, University of Groningen

Peterson, B. M. 1997, An Introduction to Active Galactic Nuclei

Pettini, M. 2000, in Royal Society of London Philosophical Transactions Series A, Vol. 358, Astronomy, physics and chemistry of H^+_3, 2035

Piconcelli, E., Fiore, F., Nicastro, F., et al. 2007, *A&A*, 473, 85

Pier, E. A. & Krolik, J. H. 1992, *ApJ*, 401, 99

Pierce, C. M., Lotz, J. M., Laird, E. S., et al. 2007, *ApJ*, 660, L19

Pietrinferni, A., Cassisi, S., Salaris, M., & Castelli, F. 2004, *ApJ*, 612, 168

Pilbratt, G. L., Riedinger, J. R., Passvogel, T., et al. 2010, *A&A*, 518, L1

Poggianti, B. M., Bressan, A., & Franceschini, A. 2001, *ApJ*, 550, 195

Poglitsch, A., Waelkens, C., Geis, N., et al. 2010, *A&A*, 518, L2

Polletta, M., Tajer, M., Maraschi, L., et al. 2007, *ApJ*, 663, 81

Polletta, M., Weedman, D., Hönig, S., et al. 2008, *ApJ*, 675, 960

Pope, A., Chary, R.-R., Alexander, D. M., et al. 2008, *ApJ*, 675, 1171

Pope, E. C. D., Mendel, J. T., & Shabala, S. S. 2012, *MNRAS*, 419, 50

Popescu, C. C., Misiriotis, A., Kylafis, N. D., Tuffs, R. J., & Fischera, J. 2000, *A&A*, 362, 138

Popescu, C. C. & Tuffs, R. J. 2002, *MNRAS*, 335, L41

Pozzi, F., Vignali, C., Comastri, A., et al. 2010, *A&A*, 517, A11

Pozzi, F., Vignali, C., Gruppioni, C., et al. 2012, *MNRAS*, 423, 1909

Puget, J.-L., Abergel, A., Bernard, J.-P., et al. 1996, *A&A*, 308, L5

Rees, M. J., Silk, J. I., Werner, M. W., & Wickramasinghe, N. C. 1969, *Nature*, 223, 788

Reimers, D. 1975, Memoires of the Societe Royale des Sciences de Liege, 8, 369

Renzini, A. & Buzzoni, A. 1986, in Astrophysics and Space Science Library, Vol. 122, Spectral Evolution of Galaxies, ed. C. Chiosi & A. Renzini, 195–231

Richards, G. T., Strauss, M. A., Fan, X., et al. 2006, *AJ*, 131, 2766

Rieke, G. H., Alonso-Herrero, A., Weiner, B. J., et al. 2009, *ApJ*, 692, 556

Rieke, G. H. & Lebofsky, M. J. 1979, *ARA&A*, 17, 477

Rieke, G. H., Lebofsky, M. J., Thompson, R. I., Low, F. J., & Tokunaga, A. T. 1980, *ApJ*, 238, 24

Rieke, G. H., Young, E. T., Engelbracht, C. W., et al. 2004, *ApJS*, 154, 25

Rigby, E. E., Maddox, S. J., Dunne, L., et al. 2011, *MNRAS*, 415, 2336

Rigopoulou, D., Spoon, H. W. W., Genzel, R., et al. 1999, *AJ*, 118, 2625

Risaliti, G., Elvis, M., & Nicastro, F. 2002, *ApJ*, 571, 234

Roche, N. & Eales, S. A. 1999, *MNRAS*, 307, 111

Rodighiero, G., Cimatti, A., Franceschini, A., et al. 2007, *A&A*, 470, 21

Rodighiero, G., Cimatti, A., Gruppioni, C., et al. 2010, *A&A*, 518, L25

Rodighiero, G., Daddi, E., Baronchelli, I., et al. 2011, *ApJ*, 739, L40

Rosario, D. J., Santini, P., Lutz, D., et al. 2012, *A&A*, 545, A45

Roseboom, I. G., Oliver, S. J., Kunz, M., et al. 2010, *MNRAS*, 409, 48

Rowan-Robinson, M. 1977, *ApJ*, 213, 635

Rowan-Robinson, M. 1980, *ApJS*, 44, 403

Rowan-Robinson, M. 1995, *MNRAS*, 272, 737

Rowan-Robinson, M., Babbedge, T., Oliver, S., et al. 2008, *MNRAS*, 386, 697

Rowan-Robinson, M., Broadhurst, T., Oliver, S. J., et al. 1991, *Nature*, 351, 719

Rowan-Robinson, M. & Crawford, J. 1989, *MNRAS*, 238, 523

Rowan-Robinson, M. & Harris, S. 1982, *MNRAS*, 200, 197

Ruiz, A., Miniutti, G., Panessa, F., & Carrera, F. J. 2010, *A&A*, 515, A99

Rybicki, G. B. & Lightman, A. P. 1979, Radiative processes in astrophysics

Sajina, A., Lacy, M., & Scott, D. 2005, *ApJ*, 621, 256

Sajina, A., Spoon, H., Yan, L., et al. 2009, *ApJ*, 703, 270

Sajina, A., Yan, L., Armus, L., et al. 2007, *ApJ*, 664, 713

Sajina, A., Yan, L., Fadda, D., Dasyra, K., & Huynh, M. 2012, *ApJ*, 757, 13

Salim, S., Rich, R. M., Charlot, S., et al. 2007, *ApJS*, 173, 267

Salpeter, E. E. 1955, *ApJ*, 121, 161

Sandage, A. 1986, *A&A*, 161, 89

Sanders, D. B. & Mirabel, I. F. 1996, *ARA&A*, 34, 749

Sanders, D. B., Soifer, B. T., Elias, J. H., et al. 1988, *ApJ*, 325, 74

Sanders, D. B., Soifer, B. T., Scoville, N. Z., Neugebauer, G., & Elias, J. H. 1986, in Bulletin of the American Astronomical Society, Vol. 18, Bulletin of the American Astronomical Society, 1034

Santini, P. 2011, Journal of Physics Conference Series, 280, 012007

Santini, P., Fontana, A., Grazian, A., et al. 2009, VizieR Online Data Catalog, 350, 40751

Santini, P., Rosario, D. J., Shao, L., et al. 2012, *A&A*, 540, A109

Sargent, M. T., Béthermin, M., Daddi, E., & Elbaz, D. 2012, *ApJ*, 747, L31

Sargent, M. T., Daddi, E., Béthermin, M., et al. 2013, ArXiv e-prints

Sargsyan, L. A. & Weedman, D. W. 2009, *ApJ*, 701, 1398

Saunders, W., Rowan-Robinson, M., Lawrence, A., et al. 1990, *MNRAS*, 242, 318

Saunders, W., Sutherland, W. J., Maddox, S. J., et al. 2000, *MNRAS*, 317, 55

Savage, B. D. & Mathis, J. S. 1979, *ARA&A*, 17, 73

Schaller, G., Schaerer, D., Meynet, G., & Maeder, A. 1992, *A&AS*, 96, 269

Schartmann, M., Meisenheimer, K., Camenzind, M., Wolf, S., & Henning, T. 2005, *A&A*, 437, 861

Schartmann, M., Meisenheimer, K., Camenzind, M., et al. 2008, *A&A*, 482, 67

Schawinski, K., Urry, M., Virani, S., et al. 2011, in American Astronomical Society Meeting Abstracts 218, 206.04

Schlegel, D. J., Finkbeiner, D. P., & Davis, M. 1998, *ApJ*, 500, 525

Schmidt, M. 1963, *Nature*, 197, 1040

Schoenberner, D. 1983, *ApJ*, 272, 708

Schulz, B., Clavel, J., Altieri, B., et al. 1998, in Astronomical Society of the Pacific Conference Series, Vol. 146, The Young Universe: Galaxy Formation and Evolution at Intermediate and High Redshift, ed. S. D'Odorico, A. Fontana, & E. Giallongo, 88

Schweitzer, M., Lutz, D., Sturm, E., et al. 2006, *ApJ*, 649, 79

Seaton, M. J. 1979, *MNRAS*, 187, 73P

Serjeant, S., Bertoldi, F., Blain, A. W., et al. 2010, *A&A*, 518, L7

Serjeant, S. & Hatziminaoglou, E. 2009, *MNRAS*, 397, 265

Shakura, N. I. & Sunyaev, R. A. 1973, *A&A*, 24, 337

Shapiro, J. N. 1993, Black holes, ed. G. G. Fazio & R. Silberberg, 310

Shetty, R., Kauffmann, J., Schnee, S., & Goodman, A. A. 2009a, *ApJ*, 696, 676

Shetty, R., Kauffmann, J., Schnee, S., Goodman, A. A., & Ercolano, B. 2009b, *ApJ*, 696, 2234

Shi, Y., Rieke, G. H., Hines, D. C., et al. 2006, *ApJ*, 653, 127

Shields, G. A. 1978, *Nature*, 272, 706

Sibthorpe, B., Ivison, R. J., Massey, R. J., et al. 2013, *MNRAS*, 428, L6

Siebenmorgen, R., Haas, M., Krügel, E., & Schulz, B. 2005, *A&A*, 436, L5

Siebenmorgen, R. & Krügel, E. 2007, *A&A*, 461, 445

Silva, L., Granato, G. L., Bressan, A., & Danese, L. 1998, *ApJ*, 509, 103

Sirocky, M. M., Levenson, N. A., Elitzur, M., Spoon, H. W. W., & Armus, L. 2008, *ApJ*, 678, 729

Skrutskie, M. F., Cutri, R. M., Stiening, R., et al. 2006, *AJ*, 131, 1163

Slipher, V. M. 1917, Lowell Observatory Bulletin, 3, 59

Smith, D. J. B., Dunne, L., da Cunha, E., et al. 2012, *MNRAS*, 427, 703

Smith, J. D. T., Draine, B. T., Dale, D. A., et al. 2007, *ApJ*, 656, 770

Smith, M. W. L., Vlahakis, C., Baes, M., et al. 2010, *A&A*, 518, L51

Snyder, G. F., Hayward, C. C., Sajina, A., et al. 2012, ArXiv e-prints

Soifer, B. T. & Neugebauer, G. 1991, *AJ*, 101, 354

Soifer, B. T., Sanders, D. B., Madore, B. F., et al. 1987, *ApJ*, 320, 238

Spoon, H. W. W., Armus, L., Cami, J., et al. 2004, *ApJS*, 154, 184

Spoon, H. W. W., Marshall, J. A., Houck, J. R., et al. 2007, *ApJ*, 654, L49

Springel, V., Di Matteo, T., & Hernquist, L. 2005, *MNRAS*, 361, 776

Stalevski, M., Fritz, J., Baes, M., Nakos, T., & Popović, L. Č. 2012, *MNRAS*, 420, 2756

Stenholm, L. 1994, *A&A*, 290, 393

Stern, D., Eisenhardt, P., Gorjian, V., et al. 2005, *ApJ*, 631, 163

Stern, D., Moran, E. C., Coil, A. L., et al. 2002, *ApJ*, 568, 71

Sturm, E., Hasinger, G., Lehmann, I., et al. 2006, *ApJ*, 642, 81

Sturm, E., Schweitzer, M., Lutz, D., et al. 2005, *ApJ*, 629, L21

Suganuma, M., Yoshii, Y., Kobayashi, Y., et al. 2006, *ApJ*, 639, 46

Surace, J. A., Shupe, D. L., Fang, F., et al. 2005, in Bulletin of the American Astronomical Society, Vol. 37, American Astronomical Society Meeting Abstracts, 1246

Takagi, T., Arimoto, N., & Hanami, H. 2003, *MNRAS*, 340, 813

Teplitz, H. I., Armus, L., Soifer, B. T., et al. 2006, *ApJ*, 638, L1

Thomas, D., Maraston, C., Bender, R., & Mendes de Oliveira, C. 2005, *ApJ*, 621, 673

Thompson, G. D., Levenson, N. A., Uddin, S. A., & Sirocky, M. M. 2009, *ApJ*, 697, 182

Tinsley, B. M. 1972, *ApJ*, 178, 319

Tommasin, S., Spinoglio, L., Malkan, M. A., et al. 2008, *ApJ*, 676, 836

Tremaine, S., Gebhardt, K., Bender, R., et al. 2002, *ApJ*, 574, 740

Tristram, K. R. W., Meisenheimer, K., Jaffe, W., et al. 2007, *A&A*, 474, 837

Trumpler, R. J. 1930, *PASP*, 42, 267

Tuffs, R. J., Popescu, C. C., Völk, H. J., Kylafis, N. D., & Dopita, M. A. 2004, *A&A*, 419, 821

Urry, C. 2004, in Astronomical Society of the Pacific Conference Series, Vol. 311, AGN Physics with the Sloan Digital Sky Survey, ed. G. T. Richards & P. B. Hall, 49

Urry, C. M. & Padovani, P. 1995, *PASP*, 107, 803

Vaccari, M., Marchetti, L., Franceschini, A., et al. 2010, *A&A*, 518, L20

van Bemmel, I. M. & Dullemond, C. P. 2003, *A&A*, 404, 1

Vassiliadis, E. & Wood, P. R. 1993, *ApJ*, 413, 641

Vassiliadis, E. & Wood, P. R. 1994, *ApJS*, 92, 125

Vázquez, G. A. & Leitherer, C. 2005, *ApJ*, 621, 695

Veilleux, S. & Osterbrock, D. E. 1987, *ApJS*, 63, 295

Veilleux, S., Rupke, D. S. N., Kim, D.-C., et al. 2009, *ApJS*, 182, 628

Verstappen, J., Fritz, J., Baes, M., et al. 2013, ArXiv e-prints

Vignali, C., Piconcelli, E., Lanzuisi, G., et al. 2011, *MNRAS*, 416, 2068

Vignali, C., Pozzi, F., Fritz, J., et al. 2009, *MNRAS*, 395, 2189

Walcher, J., Groves, B., Budavári, T., & Dale, D. 2011, *Ap&SS*, 331, 1

Walmsley, C. M., Bertout, C., Combes, F., et al. 2010a, *A&A*, 518, 1

Walmsley, C. M., Bertout, C., Combes, F., et al. 2010b, *A&A*, 521, 1

Weedman, D. W. 1988, Astrophysical Letters and Communications, 27, 117

Weedman, D. W., Feldman, F. R., Balzano, V. A., et al. 1981, *ApJ*, 248, 105

Weedman, D. W. & Houck, J. R. 2008, *ApJ*, 686, 127

Weedman, D. W. & Houck, J. R. 2009, *ApJ*, 693, 370

Weingartner, J. C. & Draine, B. T. 2001, *ApJS*, 134, 263

Weiss, A. & Schlattl, H. 2008, *Ap&SS*, 316, 99

Welty, D. E. & Fowler, J. R. 1992, *ApJ*, 393, 193

Werner, M., Fazio, G., Rieke, G., Roellig, T. L., & Watson, D. M. 2006, *ARA&A*, 44, 269

Werner, M. W., Roellig, T. L., Low, F. J., et al. 2004, *ApJS*, 154, 1

Wild, V., Heckman, T., Sonnentrucker, P., et al. 2010, in IAU Symposium, Vol. 267, IAU Symposium, ed. B. M. Peterson, R. S. Somerville, & T. Storchi-Bergmann, 96–102

Williams, D. A. 2005, Journal of Physics Conference Series, 6, 1

Wittkowski, M., Kervella, P., Arsenault, R., et al. 2004, *A&A*, 418, L39

Wu, Y., Charmandaris, V., Huang, J., Spinoglio, L., & Tommasin, S. 2009, *ApJ*, 701, 658

Xilouris, E. M., Alton, P. B., Davies, J. I., et al. 1998, *A&A*, 331, 894

Xilouris, E. M., Byun, Y. I., Kylafis, N. D., Paleologou, E. V., & Papamastorakis, J. 1999, *A&A*, 344, 868

Xue, Y. Q., Brandt, W. N., Luo, B., et al. 2010, *ApJ*, 720, 368

Yan, L., Sajina, A., Fadda, D., et al. 2007, *ApJ*, 658, 778

York, D. G., Adelman, J., Anderson, Jr., J. E., et al. 2000, *AJ*, 120, 1579

Yorke, H. W. 1977, *A&A*, 58, 423

Young, J. S. & Scoville, N. Z. 1991, *ARA&A*, 29, 581

Zakamska, N. L., Strauss, M. A., Krolik, J. H., et al. 2003, *AJ*, 126, 2125

Zitelli, V., Trevese, D., & Vagnetti, F. 2004, Baltic Astronomy, 13, 661

Acknowledgements

I would like to thank my supervisor, Prof. Alberto Franceschini, for the fundamental guidance and advice he has provided throughout my time as his student. I am sincerely grateful to my supervisor, Dott. Evanthia Hatziminaoglou, for her invaluable support during the two years spent at ESO which contributes to make this work successful. A particular thank to Dott. Jacopo Fritzfor the constant encouragement and for the prompt responding to my questions and queries. Thanks to the University of Padova and, in particular, to ASI (Agenzia Spaziale Italiana) for financially supporting my PhD. Last but not least, thanks to the European Southern Observatory, for the stimulating scientific environment, which is, for a PhD student, one of the most exciting places to "grow up" and network in astronomical research.